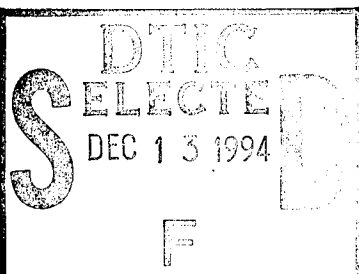


REPORT DOCUMENTATION PAGE

Form Approved
OMB No. 0704-0788

Public reporting burden for this collection of information is estimated to average 1.5 hour per response, including the time for reviewing instructions, searching existing data sources, gathering and maintaining the data needed, and completing and reviewing the collection of information. Send comments regarding this burden estimate or any other aspect of this collection of information, including suggestions for reducing this burden, to Washington Headquarters Services, Directorate for Information Operations and Reports, 1215 Jefferson Davis Highway, Suite 1204, Arlington, VA 22202-4302, and to the Office of Management and Budget, Paperwork Reduction Project (0704-0188), Washington, DC 20503.

1. AGENCY USE ONLY (Leave blank)			2. REPORT DATE	3. REPORT TYPE AND DATES COVERED	
			Sep 1994		
4. TITLE AND SUBTITLE			5. FUNDING NUMBERS		
A Study of Magnetic Activity Effects on the Thermosphere winds in the Low Latitude Ionosphere					
6. AUTHOR(S)			7. PERFORMING ORGANIZATION NAME(S) AND ADDRESS(ES)		
Ricardo Cruz Davila			AFIT Students Attending:		
8. SPONSORING/MONITORING AGENCY NAME(S) AND ADDRESS(ES)			9. PERFORMING ORGANIZATION NAME(S) AND ADDRESS(ES)		
DEPTMENT OF THE AIR FORCE AFIT/CI 2950 P STREET WRIGHT-PATTERSON AFB OH 45433-7765			Utah State University		
11. SUPPLEMENTARY NOTES					
12a. DISTRIBUTION/AVAILABILITY STATEMENT			12b. DISTRIBUTION CODE		
Approved for Public Release IAW 190-1 Distribution Unlimited MICHAEL M. BRICKER, SMSgt, USAF Chief Administration					
13. ABSTRACT (Maximum 200 words)					
					
14. SUBJECT TERMS			15. NUMBER OF PAGES		
			181		
16. PRICE CODE					
17. SECURITY CLASSIFICATION OF REPORT		18. SECURITY CLASSIFICATION OF THIS PAGE		19. SECURITY CLASSIFICATION OF ABSTRACT	
20. LIMITATION OF ABSTRACT					

19941207 070

PHOTO QUALITY ENPHOTOZED 1

15. NUMBER OF PAGES

181

16. PRICE CODE

17. SECURITY CLASSIFICATION OF REPORT

18. SECURITY CLASSIFICATION OF THIS PAGE

19. SECURITY CLASSIFICATION OF ABSTRACT

20. LIMITATION OF ABSTRACT

94-138

A STUDY OF MAGNETIC ACTIVITY EFFECTS ON THE THERMOSPHERIC
WINDS IN THE LOW LATITUDE IONOSPHERE

by

Ricardo Cruz Davila

A thesis submitted in partial fulfillment
of the requirements for the degree

of

MASTERS OF SCIENCE

in

Physics
(Upper Atmospheric Option)

Approved:

B Fejer
Bela G. Fejer
Major Professor

W Farrell Edwards
W. Farrell Edwards
Committee Member

Kent L. Miller
Kent L. Miller
Committee Member

James P. Shaver
James P. Shaver
Dean of Graduate Studies

UTAH STATE UNIVERSITY
Logan, Utah

1994

Academic Year	1993-1994	<input checked="" type="checkbox"/>
Grad. Class	Graduate	<input type="checkbox"/>
Degree	Master's	<input type="checkbox"/>
Major	Geosciences	<input type="checkbox"/>
Minors	Geology	<input type="checkbox"/>
Thesis/Project	Thesis	<input type="checkbox"/>
Supervisors	Fejer, Edwards, Shaver	
Committee Members	Miller	
Other Committee Members		
Comments	Approved by the Graduate Committee	

A-1

ACKNOWLEDGMENTS

I would like to thank the Air Force Institute of Technology (AFIT) for sponsoring my studies at Utah State University and giving me the chance to further my education. I also thank my fellow AFIT and physics graduate students for their help and support.

I have gained an appreciation of the space science field from my teacher and advisor, Dr. Bela Fejer. I will always be grateful for his guidance and support. I also appreciate the help provided by the rest of my committee: Dr. Kent Miller and Dr. Farrell Edwards. I also thank the following professors for their encouragement and support: Dr. Manfred Biondi, Dr. John Meriwether, Dr. Cassandra Fesen, and Dr. Patrick Espy. A special “Thank you, Don” to Dr. Donald Thompson for creating a powerful plotting routine (PLOTL) and taking the time to show me how to use it. I thank Ludger Scherliess and Todd Pederson for the programming help and space science discussions. A special thanks to Donna, Shawna, Barbara, and Marylin for the “morning coffee ritual.”

Outside of the physics community, I thank Sheldon and Jaci Cooper. We don’t go through life looking for good friends, so it’s neat when it happens. I enjoyed our time together ... thanks for being such good friends.

Last, my deepest love and appreciation to my wife and best friend, Sonia “Sweets” Davila. She has always provided me the support, encouragement, and patience in all that I do. I love you very much.

Ricardo Davila

CONTENTS

	Page
ACKNOWLEDGMENTS	ii
LIST OF TABLES	vii
LIST OF FIGURES	viii
ABSTRACT	xiv
 CHAPTER	
1. INTRODUCTION	1
2. THE LOW LATITUDE IONOSPHERE THERMOSPHERIC WINDS	9
2.1. INTRODUCTION	9
2.2. LOW LATITUDE IONOSPHERE	9
2.3. UPPER ATMOSPHERIC WINDS	12
2.3.1. Stratosphere and Mesosphere Winds	12
2.3.2. Thermospheric Winds	15
2.3.3. Equatorial Thermospheric Winds	19
2.4. PREVIOUS WIND STUDIES	24
3. MODELING TECHNIQUES	31
3.1. INTRODUCTION	31
3.2. UPPER ATMOSPHERIC MODELING	31
3.2.1. History of Atmospheric Modeling	31
3.2.2. Upper Atmospheric Models	33
3.2.2.1. Mass Spectrometer and Incoherent Scatter (MSISE90) Model	33
3.2.2.2. Horizontal Wind Model (HWM93)	34
3.2.2.3. Vector Spherical Harmonic (VSH) Wind Model	35
3.2.2.4. Thermosphere/Ionosphere General Circulation Model (TIGCM93)	36

3.3. THERMOSPHERE/IONOSPHERE GENERAL CIRCULATION MODEL (TIGCM)	36
3.3.1. TIGCM History	36
3.3.2. TIGCM Description	38
3.3.3. TIGCM Model Equations	40
3.3.3.1. Thermodynamic Equation	40
3.3.3.2. Momentum Equations	41
3.3.3.3. Continuity Equation	42
3.3.3.4. Hydrostatic Equation	42
3.3.4. TIGCM Diagnostic Processor	43
3.4. TIGCM PREDICTIONS	44
4. MEASUREMENT TECHNIQUES AND DATA	49
4.1. INTRODUCTION	49
4.2. AIRGLOW EMISSIONS	49
4.2.1. Hydroxyl (OH)	50
4.2.2. Monatomic Oxygen, O(¹ S), 557.7 nm	50
4.2.3. Monatomic Oxygen , O(¹ D), 630.0 nm	51
4.3. FABRY-PEROT INTERFEROMETER	51
4.3.1. Historical Perspective	51
4.3.2. Interferometry	52
4.3.3. Two-beam and Multiple-beam Interference	53
4.3.4. Basic Optical Principles for the FPI	54
4.3.4.1. The Meaning of Finesse	58
4.3.4.2. Throughput and Etendue	59
4.3.4.3. Etalon	60
4.3.5. FPI Equipment Description	60
4.3.5.1. Arequipa FPI	61
4.3.5.2. Arecibo FPI	62
4.3.6. FPI Measured Winds	63
4.3.6.1. Arequipa	63

4.3.6.2. Arecibo	65
4.3.7. FPI Data Analysis	65
4.4. ISR NEUTRAL WIND MEASUREMENTS	74
4.4.1. ISR Neutral Winds	74
4.4.2. ISR Measured Data	76
4.5. ELECTRON DENSITY DATA	76
4.5.1. Airglow Emissions and Heights	81
4.5.2. Calculating the Volume Emission Rate	81
4.5.3. F-Layer Height and Airglow Emission Height	84
4.5.3.1. Arecibo F-Layer and Airglow Emission Heights ..	84
4.5.3.2. Jicamarca F-Layer and Airglow Emission Heights ..	86
4.6. SPLINES	91
5. QUIET TIME LOW LATITUDE THERMOSPHERIC WINDS	96
5.1. INTRODUCTION	96
5.2. SEASONAL AND SOLAR CYCLE EFFECTS	96
5.2.1. Arequipa	96
5.2.1.1. Seasonal Effects	97
5.2.1.2. Solar Cycle Effects	100
5.2.1.3. TIGCM93 Solar Cycle Activity Model Results ..	104
5.2.1.4. HWM93 Solar Cycle Activity Model Predictions ..	107
5.2.2. Arecibo	108
5.2.2.1. Seasonal Effects	108
5.2.2.2. Solar Cycle Effects (FPI Measurements)	114
5.2.2.3. Solar Cycle Effects (ISR Measurements)	117
5.2.2.4. TIGCM93 Solar Cycle Activity Model Results ..	117
5.2.2.5. HWM93 Solar Cycle Activity Model Results	122
5.3. DATA AND MODEL COMPARISONS	122

6. MAGNETIC ACTIVITY EFFECTS ON THE LOW LATITUDE THERMOSPHERIC WINDS	131
6.1. INTRODUCTION	131
6.2. MAGNETIC ACTIVITY EFFECTS	131
6.2.1. Arequipa	131
6.2.2. Arecibo	133
6.3. SHORT-TERM AND EXTENDED MAGNETIC ACTIVITY	139
6.4. NEUTRAL WIND RESPONSE TO MAGNETIC ACTIVITY	140
6.4.1. Arequipa and Arecibo Northward Wind	140
6.4.2. Arequipa and Arecibo Eastward Wind	143
6.5. MAGNETIC ACTIVITY CUBIC SPLINE AND MODEL PREDICTIONS	146
6.5.1. Arequipa	146
6.5.1.1. Cubic Spline Predictions	146
6.5.1.2. TIGCM93 Predictions	150
6.5.1.3. HWM93 Predictions	151
6.5.2. Arecibo	156
6.5.2.1. Cubic Spline Predictions	156
6.5.2.2. TIGCM93 Predictions	159
6.5.2.3. HWM93 Predictions	159
7. CONCLUSIONS	164
7.1. CONCLUSIONS	164
7.1.1. Airglow Emission Heights	164
7.1.2. Solar Activity Effects	165
7.1.3. Magnetic Activity Effects	166
7.2. FUTURE WORK	167
REFERENCES	170
APPENDIX. PERMISSION LETTERS	176

LIST OF TABLES

Table		Page
1	Ionospheric Regions by Altitude, Major Ion, and Day/Night Electron Density	3
2	Chronological Development of the TGCM	37
3	Empirical Models Used in the TIGCM	39
4	Solar Flux Histogram of 1988-1990 Arequipa Neutral Wind Data	64
5	Magnetic Activity Histogram of 1988-1990 Arequipa Neutral Wind Data	64
6	Solar Flux Histogram of 1981-1989 Arecibo Neutral Wind Data	67
7	Magnetic Activity Histogram of 1981-1989 Arecibo Neutral Wind Data	67
8	95% Confidence Intervals for the May-August Eastward Winds over Arequipa, Peru	73
9	Solar Flux Histogram of 1983-1987 ISR Neutral Wind Data	77
10	Magnetic Activity Histogram of 1983-1987 ISR Neutral Wind Data	77
11	Solar Flux Histogram of 1966-1969, 1984, 1988, and 1991 Jicamarca Electron Density	79
12	Magnetic Activity Histogram of Jicamarca Electron Density	79
13	Solar Flux Histogram of 1981-1989 Arecibo Electron Density	80
14	Magnetic Activity Histogram of Arecibo Electron Density Data	80
15	Volume Emission Rate Parameters	82
16	Magnetic Activity Classification	139

LIST OF FIGURES

Figure		Page
1	Typical middle latitude daytime and nighttime electron density profiles and ionospheric regions up to 600 km for moderate solar flux conditions and quiet geomagnetic conditions	2
2	Typical temperature gradient profile and heights for the atmospheric temperature regimes	4
3	General magnitude of middle latitude zonal winds from the surface to 120 km for December at 0000 LT	13
4	Latitude vs. altitude cross-sections of the average zonal wind	14
5	The temperatures and winds at 250 km for December, March, and June	17
6	Graphs of neutral acceleration time constants and F for midday at sunspot minimum	18
7	Illustration of how the thermospheric winds affect the ionosphere	19
8	Calculated vertical ion drift velocities for several driving wind components	21
9	Measured vertical plasma drifts in the equatorial F-region for various seasons and solar conditions	22
10	Contours of the zonal neutral wind at 250 km, calculated from the thermospheric model by Anderson and Roble (1974)	23
11	Dynamics Explorer 2 data of electron density, zonal winds, and temperature near 300 km at low latitudes	25
12	Arequipa equinox month average meridional and zonal winds from 1983 to 1990	27
13	Arequipa June solstice average meridional and zonal winds from 1983 to 1990	28
14	The annual variation of the average northward meridional and eastward zonal Fabry-Perot winds over Arecibo	29

15	Zonal neutral wind velocities measured by the Fabry-Perot interferometer on four consecutive nights in January 1988	30
16	Meridional winds from the TIGCM93 model for Solar Minimum Conditions	45
17	Zonal winds from the TIGCM93 model for Solar Minimum Conditions	45
18	Meridional winds from the TIGCM93 model for Solar Minimum Conditions	46
19	Zonal winds from the TIGCM93 model for Solar Minimum Conditions	46
20	Paths of light rays in multiple reflection between two parallel mirrors	55
21	Diagram showing the path difference between two successive rays	56
22	Basic Fabry-Perot arrangement	56
23	Frequency distribution of Arequipa data collection	66
24	Frequency distribution of Arecibo data collection	68
25	May-August eastward average of the thermospheric wind over Arequipa	70
26	November-February northward average of the thermospheric wind over Arecibo	71
27	May-August frequency distribution bar graphs of the deviation of the wind values in each bin from their mean for Arequipa	72
28	November-February northward average of the ISR calculated neutral wind over Arecibo	78
29	May-August calculated 630.0 nm volume emission rate over Arecibo	83
30	Arecibo seasonal F-layer and airglow emission height averages for low and high solar activity during quiet magnetic activity	85
31	Arecibo seasonal F-layer and airglow emission height averages for quiet and disturbed magnetic activity	87

32	Jicamarca seasonal F-layer and airglow emission height averages for low and moderate solar activity during quiet magnetic activity	89
33	Jicamarca seasonal F-layer and airglow emission height averages for quiet and disturbed magnetic activity	90
34	Spline fit for the May-August eastward wind over Arequipa	93
35	Spline fit for the November-February northward wind over Arecibo	94
36	Spline fit for the November-February Arecibo ISR calculated neutral wind along the magnetic meridian	95
37	Measured FPI eastward averages over Arequipa, Peru, for equinox and near June solstice for all solar activity and quiet geomagnetic activity conditions	98
38	Measured FPI northward wind averages over Arequipa, Peru for equinox and near June solstice for all solar activity and quiet geomagnetic activity conditions	99
39	Measured eastward wind averages over Arequipa, Peru, for various seasons for moderate and high solar activity	102
40	Measured northward wind averages over Arequipa, Peru, for various seasons for moderate and high solar activity	103
41	TIGCM93 eastward wind predictions over Arequipa, Peru, for various seasons for high, moderate, and low solar activity conditions and for quiet magnetic activity	105
42	TIGCM93 northward wind predictions over Arequipa, Peru, for various seasons for high, moderate, and low solar activity conditions and for quiet magnetic activity	106
43	HWM93 eastward wind predictions over Arequipa, Peru, for various seasons for high, moderate, and low solar activity conditions and for quiet magnetic activity	109
44	HWM93 northward wind predictions over Arequipa, Peru, for various seasons for high, moderate, and low solar activity conditions and for quiet magnetic activity	110

45	Measured eastward averages over Arecibo, Puerto Rico, for various seasons for all solar activity and quiet magnetic activity conditions	112
46	Measured northward wind averages over Arecibo, Puerto Rico, for various seasons for all solar activity and quiet magnetic activity conditions	113
47	Measured eastward wind averages over Arecibo, Puerto Rico, for various seasons for low and high solar activity	115
48	Measured northward wind averages over Arecibo, Puerto Rico, for various seasons for low and high solar activity	116
49	ISR neutral winds for Arecibo, Puerto Rico, for various seasons for low and moderate solar activity	118
50	TIGCM93 eastward wind predictions over Arecibo, Puerto Rico, for various seasons for high, moderate, and low solar activity conditions and for quiet magnetic activity	120
51	TIGCM93 northward wind predictions over Arecibo, Puerto Rico, for various seasons for high, moderate, and low solar activity conditions and for quiet magnetic activity	121
52	HWM93 eastward wind predictions over Arecibo, Puerto Rico, for various seasons for high, moderate, and low solar activity conditions and for quiet magnetic activity	123
53	HWM93 northward wind predictions over Arecibo, Puerto Rico, for various seasons for high, moderate, and low solar activity conditions and for quiet magnetic activity	124
54	Model and observed eastward wind comparison for Arequipa, Peru	126
55	Model and observed northward wind comparison for Arequipa, Peru	127
56	Model and observed eastward wind comparison for various seasons for Arecibo, Puerto Rico	128
57	Model and observed northward wind comparison for various seasons for Arecibo, Puerto Rico	129
58	Measured eastward wind averages over Arequipa, Peru, for the equinox and June solstice periods for quiet ($K_p \leq 3$) and disturbed ($K_p \geq 3$) conditions	132

59	Measured northward wind averages over Arequipa, Peru, for the equinox and June solstice periods for quiet ($K_p \leq 3$) and disturbed ($K_p \geq 3$) conditions	134
60	Measured eastward wind averages over Arecibo, Puerto Rico, for various seasons for quiet ($K_p \leq 3$) and disturbed ($K_p \geq 3$) conditions	135
61	Measured northward wind averages over Arecibo, Puerto Rico, for various seasons for quiet ($K_p \leq 3$) and disturbed ($K_p \geq 3$) conditions	137
62	Measured ISR neutral winds over Arecibo, Puerto Rico, for various seasons for quiet ($K_p \leq 3$) and disturbed ($K_p \geq 3$) conditions	138
63	June solstice extended quiet ($\Sigma Q, Q$) and extended disturbed ($\Sigma D, D$) northward wind comparisons for Arequipa and Arecibo	141
64	Equinox extended quiet ($\Sigma Q, Q$) and extended disturbed ($\Sigma D, D$) northward wind comparisons for Arequipa and Arecibo	142
65	June solstice extended quiet ($\Sigma Q, Q$) and extended disturbed ($\Sigma D, D$) eastward wind comparisons for Arequipa and Arecibo	144
66	Equinox extended quiet ($\Sigma Q, Q$) and extended disturbed ($\Sigma D, D$) eastward wind comparisons for Arequipa and Arecibo	145
67	June solstice extended quiet ($\Sigma Q, Q$) and short term disturbed ($\Sigma Q, D$) eastward wind comparisons for Arequipa and Arecibo	147
68	Cubic spline predictions for the northward winds over Arequipa for equinox (day = 90) and June solstice (day = 180) for moderate solar flux ($\Phi = 150$) conditions	148
69	Cubic spline predictions for the eastward winds over Arequipa for equinox (day = 90) and June solstice (day = 180) for moderate solar flux ($\Phi = 150$) conditions	150
70	TIGCM93 quiet ($K_p = 1$) and disturbed ($K_p = 6$) eastward wind predictions over Arequipa for all seasons	152
71	TIGCM93 quiet ($K_p = 1$) and disturbed ($K_p = 6$) northward wind predictions over Arequipa for all seasons	153

72	HWM93 quiet ($K_p = 2$) and disturbed ($K_p = 5$) eastward wind predictions over Arequipa for all seasons	154
73	HWM93 quiet ($K_p = 2$) and disturbed ($K_p = 5$) northward wind predictions over Arequipa for all seasons	155
74	Cubic spline predictions for the northward winds over Arecibo for all seasons and moderate solar flux ($\Phi = 150$) conditions	157
75	Cubic spline predictions for the eastward winds over Arecibo for all seasons and moderate solar flux ($\Phi = 150$) conditions	158
76	TIGCM93 quiet ($K_p = 1$) and disturbed ($K_p = 6$) eastward wind predictions over Arecibo for all seasons	160
77	TIGCM93 quiet ($K_p = 1$) and disturbed ($K_p = 6$) northward wind predictions over Arecibo for all seasons	161
78	HWM93 quiet ($K_p = 2$) and disturbed ($K_p = 5$) eastward wind predictions over Arecibo for all seasons	162
79	HWM93 quiet ($K_p = 2$) and disturbed ($K_p = 5$) northward wind predictions over Arecibo for all seasons	163

ABSTRACT

A Study of Magnetic Activity Effects on the Thermospheric
Winds in the Low Latitude Ionosphere

by

Ricardo Cruz Davila, Master of Science

Utah State University, 1994

Major Professor: Dr. Bela G. Fejer
Department: Physics

The purpose of this thesis is to examine the effects of magnetic activity on the low latitude F-region thermospheric winds. The F-region (120-1600 km) is a partially ionized medium where O⁺ and O are the major ion and neutral species, respectively. The thermospheric winds at these altitudes are driven primarily by pressure gradient forces resulting from the solar heating during the day and cooling at night. For this study, we use measured Fabry-Perot Interferometer (FPI) winds at Arequipa (16.5°S, 71.5°W) and measured FPI and Incoherent Scatter Radar (ISR) winds at Arecibo (18.6°N, 66.8°W).

Previous wind studies at Arequipa and Arecibo concentrated on the climatological wind patterns highlighting solar cycle effects and seasonal variations; however, these studies did not address the effects of magnetically disturbed conditions on the seasonal averaged winds. To properly investigate storm time effects on the neutral winds, we must first investigate solar cycle effects on the seasonal averages during magnetically quiet ($K_p < 3$) conditions. This study will include a detailed analysis

of solar cycle effects on the seasonally averaged winds for Arequipa and Arecibo. In addition to the wind averages, we used cubic splines to fit the average wind profiles and to provide better comparisons with modeled results. We also performed a study on the airglow emission heights using both Jicamarca and Arecibo electron density profiles. This established the height which we will use to compare our experimental data with the model winds.

To investigate magnetic activity effects on the FPI and ISR winds, we used three magnetic activity cases which cover all storm time scenarios. These magnetic activity cases are the extended quiet, short-term disturbed, and extended disturbed conditions. The first case, the extended quiet, is the condition where the previous and short term magnetic activity is quiet (12 hour $K_p \leq 3$ and the $K_p \leq 3$). The short-term disturbed case is defined for the condition where the previous magnetic activity is quiet (12 hour $K_p \leq 3$) and then becomes disturbed ($K_p \geq 3$). Last, we considered the case where previous and short-term magnetic activity are disturbed (12 hour $K_p \geq 3$ and the $K_p \geq 3$).

Our last objective is to use our data to validate the predictions from the Thermosphere/Ionosphere General Circulation model (TIGCM93) and the Horizontal Wind Model (HWM93). This study should further our understanding of the physical processes which produce the low latitude quiet and disturbed winds. The TIGCM93 is a first principal model and the HWM93 is an empirical model based on ground-based and satellite measurements. The main advantage of using the TIGCM93 is the ease of studying the dynamics of ionospheric phenomena by simply changing various model inputs, while the HWM93 allows us a comparison between our experimental wind data sets with the established climatology of the winds over Arequipa and Arecibo.

(195 pages)

CHAPTER 1

INTRODUCTION

The ionosphere is defined as the tenuous gas of electrons and ions that envelop the earth from 60 km to about 600 - 800 km. Early radio experiments conducted in the 1930s indicated the ionosphere could be subdivided into regions based on the electron and ion densities. Today, the standard designations for these regions of the ionosphere are the D, E, F₁, F₂, and topside ionosphere. Typically the F₁- and F₂-regions are referred to as simply the F-region. The D-region (60 - 90 km) is present only during the day and is the one region that contains negative ions. The E-region (90 - 140 km) and F₁-region (140 - 200 km) consist of molecular ions, while the F₂-region (200 - 400 km) consists of atomic ions with O⁺ being the dominant ion species. In addition to ion composition, the E- and F-regions exhibit significant electrodynamic effects. Tidal oscillations generate electric fields and currents in the E-region while neutral wind dynamics drive the electrodynamics in the F-region. The topside ionosphere is the name given to the ionosphere above ~ 400 km. This region is generally characterized by an exponential decrease in the electron density and a gradual transition from the O⁺ ions to the H⁺ ions above ~ 800 km. Figure 1 shows the typical altitude profile of the ionospheric regions with respect to the electron density. The approximate breakdown of these regions by altitude, daytime electron density, and ion composition is shown in TABLE 1. A more detailed description of the ionosphere's regions and dynamics can be found in a number of textbooks [e.g., *Chamberlain*, 1987; *Hargreaves*, 1992; *Kelley*, 1989; *Tohmatsu*, 1990].

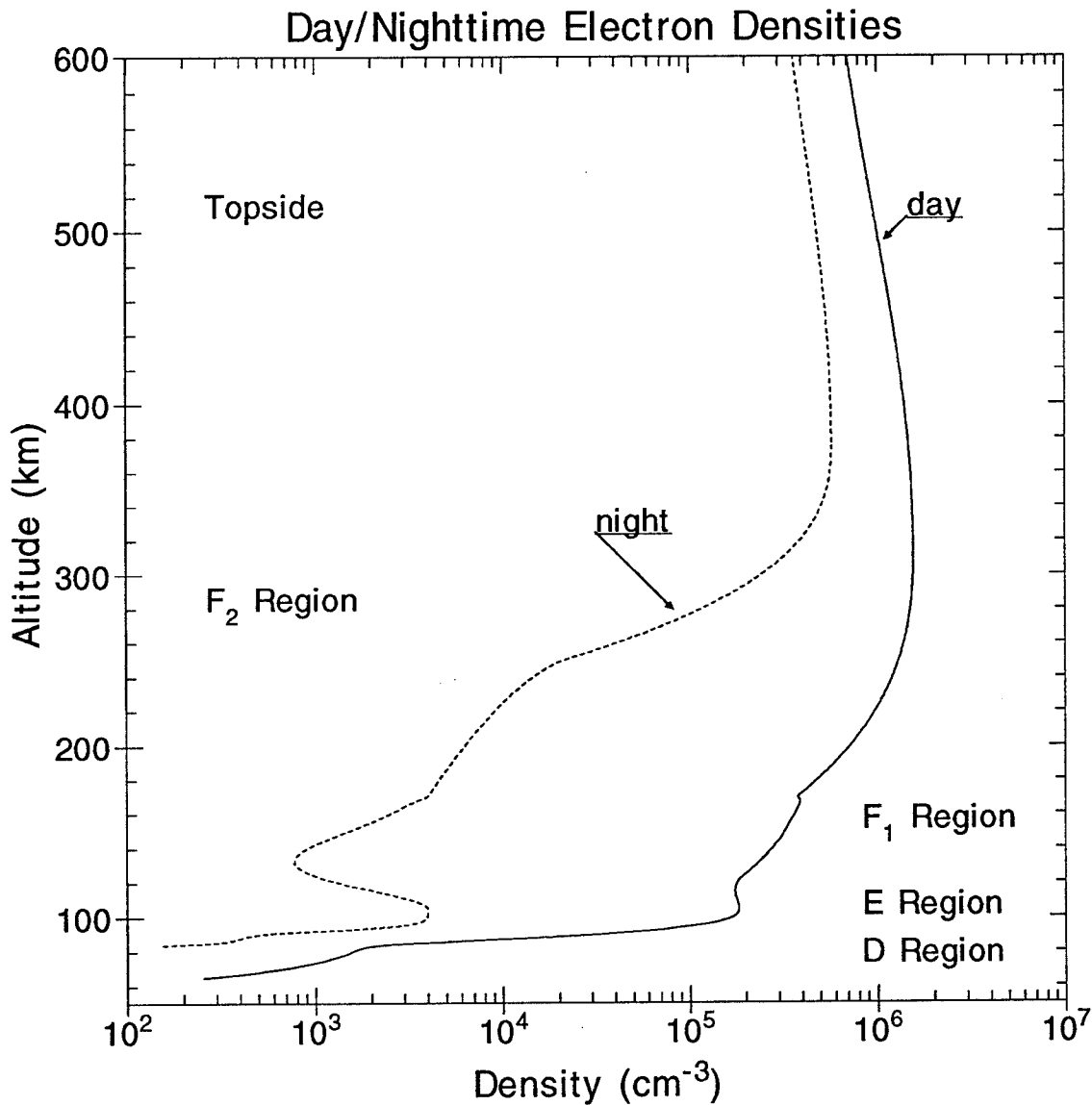


Figure 1. Typical middle latitude daytime (solid line) and nighttime (dashed line) electron density profiles and ionospheric regions up to 600 km for moderate solar flux ($\Phi = 150$) conditions and quiet geomagnetic ($A_p = 4$) conditions. The electron density profiles were generated using the International Reference Ionosphere model [Bilitza, 1989].

TABLE 1. Ionospheric Regions by Altitude, Major Ion, and Day/Night Electron Density.

Region	Altitude Range (km)	Major Ion Components	Typical Electron Densities (cm ⁻³)
D	60 - 90	NO ⁺ , O ₂ ⁺	1.5×10^4 (day) absent at night
E	90 - 140	O ₂ ⁺ , NO ⁺	1.5×10^5 (day) $< 1.0 \times 10^4$ (night)
F ₁	140 - 200	O ⁺ , NO ⁺	2.5×10^5 (day) absent at night
F ₂	200 - 400	O ⁺ , N ⁺	1.0×10^6 (day) 1.0×10^5 (night)

Besides the electron density profile, the atmosphere can also be classified by the temperature gradient (see Figure 2). The troposphere (0 - 12 km) is the region where the temperature gradient decreases by approximately 7 K/km. The boundary between the troposphere and the next region, the stratosphere, is called the tropopause (~ 12 km). In the stratosphere (12 - 55 km), the temperature increases with height because ozone absorbs virtually all the incoming solar extreme ultraviolet (EUV) radiation. The stratopause separates the stratosphere from the next region, the mesosphere. The mesosphere (55 km - 90 km) is characterized by a decreasing temperature with height and contains the coldest temperature (~ 180 K) at its upper boundary, the mesopause. The mesopause is the lower boundary of the final temperature region, the thermosphere (> 90 km). The thermosphere's temperature increases with height since atomic oxygen, O, absorbs solar EUV radiation. The temperatures in the thermosphere can reach as high as 1300 K above 300 km.

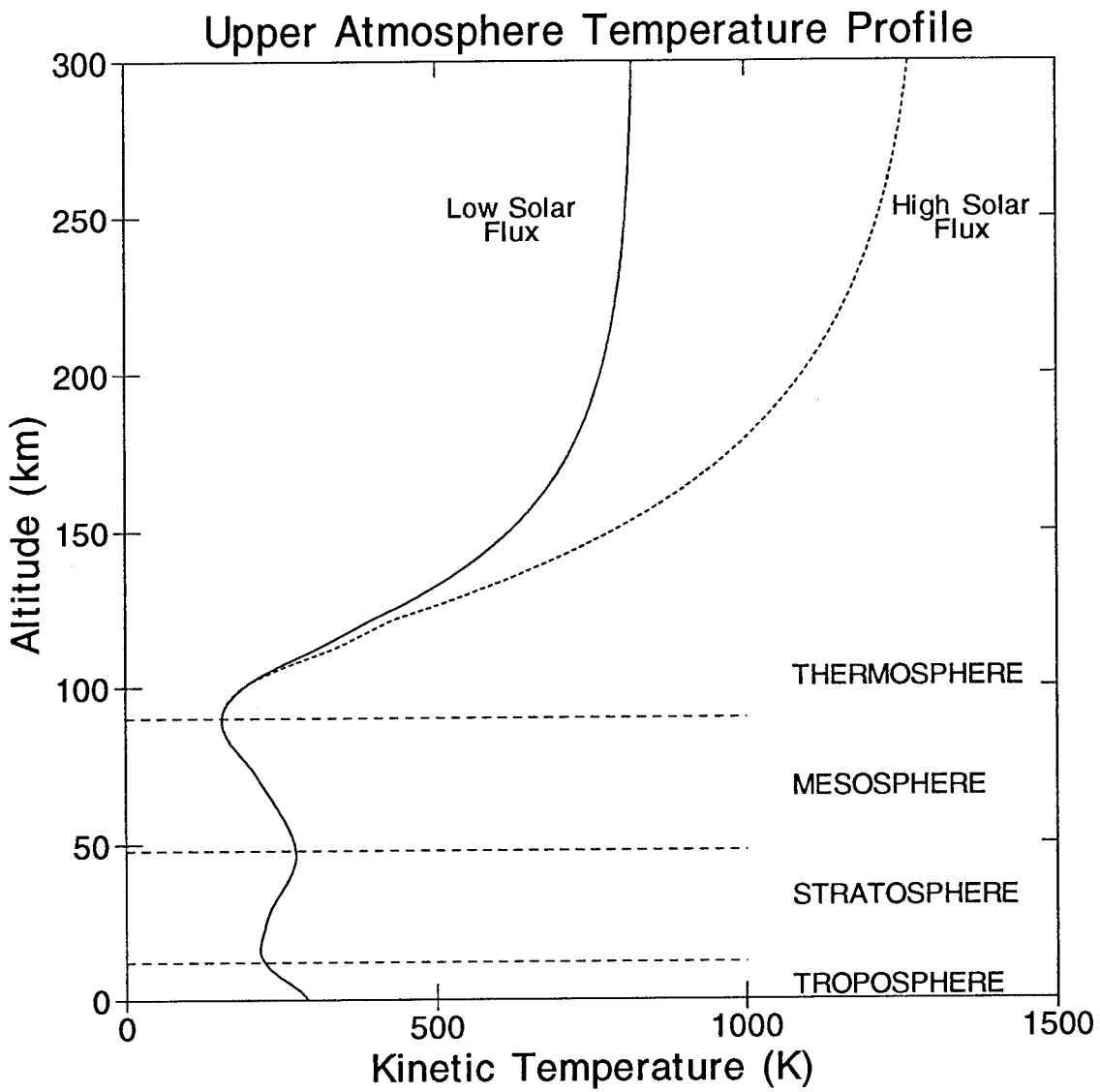


Figure 2. Typical temperature gradient profile and heights for the atmospheric temperature regimes. The temperature profiles, provided by the MSISE90 model [Hedin, 1991], for low solar flux ($\Phi = 75$) and high solar flux ($\Phi = 200$) conditions.

There are significant latitudinal effects on the ionosphere density distribution and dynamics. At high latitudes the magnetosphere-ionosphere coupling is the dominant force driving the neutral and electromagnetic dynamics. The precipitation of particles in the auroral oval directly affects the electron density distribution and can be the major source of ionization. At middle latitudes, the height of the F-region electron density peak is primarily affected by the neutral wind, diffusion, recombination, and downward flow of plasma from the ionospheric heights above 1200 km. The middle latitude maximum electron density concentration occurs at the height where the downward diffusion and electron loss by recombination are comparable. The primary source of ionization in this region is by the solar EUV. At low latitudes, the magnetic field is nearly horizontal, which results in unique transport effects associated with vertical $\vec{E} \times \vec{B}$ drifts. In addition to the vertical drifts, the electron density is influenced by interhemispheric flows caused by the neutral winds.

The focus of this thesis will be the low latitude F-region, a complex and dynamic region of the ionosphere where a variety of processes affect the plasma concentration. In this region, the predominant neutral constituent is atomic oxygen, which is ionized by solar radiation of wavelengths less than 911 Å. However, as altitude increases in the F-region, the plasma density distribution is determined more by transport processes such as ambipolar diffusion, neutral wind drag, and electrodynamics rather than local ionization. Plasma is transported along the magnetic field lines by diffusion and the neutral wind effects and across the magnetic field by electrodynamic forces.

For this work, we study the dynamics of the low latitude neutral winds. Below 120 km, the lower boundary of the thermosphere, the zonal winds are weakest at the tropopause (~ 12 km) and the mesopause (~ 85 km). The strongest winds below 120 km occurs near the stratopause (~ 55 km). The winds in the stratosphere and mesosphere result from the balance between the pressure gradient and Coriolis forces. Above 120 km, the wind speeds gradually increase and the pressure gradient force becomes the primary forcing term. The pressure gradient force results from the in situ heating of the upper atmosphere by the absorption of EUV by atomic oxygen. Besides pressure gradients, the thermospheric winds can be influenced by geomagnetic disturbances generated at the high latitudes.

The effects of geomagnetic disturbances (or storm time effects) on the thermospheric winds have been observed at all latitudes and modeled using sophisticated theoretical circulation models [e.g., *Richmond and Matsushita*, 1975; *Richmond*, 1979; *Blanc and Richmond*, 1980; *Burnside et al.*, 1991; *Forbes et al.*, 1993; *Buonsanto and Foster*, 1993]. Several cases of high latitude disturbance effects on the thermospheric dynamics at low latitudes have also been documented [e.g., *Burnside et al.*, 1991; *Fejer*, 1993; *Buonsanto and Foster*, 1993]. One such physical disturbance described in the literature is the generation of large-amplitude gravity waves that propagate towards low latitudes during storm time conditions. These waves have been shown to be instrumental in affecting both the neutral atmosphere and low latitude electrodynamics [*Burnside et al.*, 1991; *Fejer*, 1993].

Global numerical models are a necessary and valuable tool for enhancing our understanding of storm time processes. We use the National Center for Atmospheric Research (NCAR) thermosphere-ionosphere general circulation model (TIGCM93) [Roble *et al.*, 1988; Fesen *et al.*, 1993] and the empirical horizontal wind model (HWM93) [Hedin *et al.*, 1991] to assess the current ability to model these high latitude disturbances on the low latitude neutral winds. The NCAR TIGCM93 solves the full nonlinear primitive equations for eastward and northward momentum, thermodynamics, continuity, and hydrostatics for 24 constant pressure levels from 97 to 500 km [Fesen *et al.*, 1993] while the HWM93 uses wind data measured by satellite and ground-based incoherent scatter radar and Fabry-Perot optical interferometers. The TIGCM93 provides insight into what factors influence low latitude ionosphere for quiet and disturbed conditions while the HWM93 describes the average wind behavior for a selected altitude, solar flux , and geomagnetic condition.

The primary focus of this thesis research is to examine the F-region neutral wind response to storm time events. The data used for this study are winds measured by Fabry-Perot Interferometers (FPI) at Arecibo and Arequipa, derived neutral winds from Incoherent Scatter Radar (ISR) at Arecibo, and electron density profiles collected at Jicamarca, Peru and Arecibo, Puerto Rico. Solar activity is determined by the 10.7-cm solar flux index (Φ) for the day of the FPI neutral wind measurement, ISR derived neutral wind, and measured electron density. Magnetic activity is determined by the K_p index for the given observation. Quiet and disturbed magnetic activity conditions are given by $K_p \leq 3$ and $K_p \geq 3$, respectively.

Chapters 2 and 3 provide a brief introduction to the morphology of the low latitude ionosphere, upper atmospheric wind system, and current atmospheric models for investigating the wind climatology and physics. Chapter 4 describes in detail the wind measuring techniques and the data analysis used for averaging the quiet and disturbed neutral winds. Chapters 5 and 6 provide the results of the response of the neutral wind to quiet and disturbed conditions, respectively. These chapters also provide comparisons of the measured winds to the TIGCM93 and HWM93 predicted results. These comparisons help determine the ability to model the low latitude wind response to quiet and disturbed conditions. Finally, chapter 7 contains the conclusions and suggestions for future neutral wind studies.

CHAPTER 2

THE LOW LATITUDE IONOSPHERE THERMOSPHERIC WINDS

2.1. INTRODUCTION

The focus of this thesis is the low latitude thermospheric neutral winds. Before investigating the neutral wind response to magnetically quiet and disturbed geomagnetic conditions, we must first establish the morphology of the low latitude ionosphere. This chapter describes the unique characteristics of the low latitude ionosphere, provides the physical description of the upper atmospheric winds, and summarizes the low latitude thermospheric wind studies.

2.2. LOW LATITUDE IONOSPHERE

For this study, we use measured and modeled data from the American sector (~70°W geographic) low latitude ionosphere. The American sector low latitude ionosphere includes the ionospheric regions over Arequipa, Peru (16.5°S, 71.5°W, 3.2°S dip latitude) and Arecibo, Puerto Rico (18.6°N, 66.8°W, 30.0°N dip latitude). The dip latitude is the north-south component of the geomagnetic coordinate system. For example, the magnetic dip latitude is 90°N and 90°S at the magnetic north and south poles, respectively. The dip latitude at the magnetic equator is 0 degrees. The low latitude ionosphere incorporates the unique neutral and electrodynamic properties of the equatorial region as well as the dynamics found in the transition region between the low and middle latitudes.

The fundamental equation governing the amount of ionization at any point in the ionosphere is the continuity equation:

$$\frac{\partial N}{\partial t} + \vec{\nabla} \cdot (N \vec{V}) = P - L \quad (1)$$

Here N is the electron density, $\vec{\nabla} \cdot (N \vec{V})$ is the transport term, P is the production rate, and L is the loss rate.

In the low latitude ionosphere, the E-region ionization is produced mainly from O_2 molecules by photoionization:



The E-region ion production is balanced by the loss of ionization, principally by the dissociative recombination reactions:

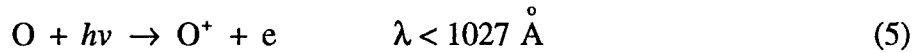


and

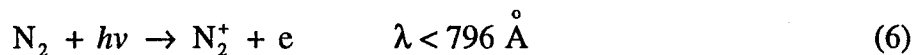


The recombination time constant for the reactions (3) and (4) is 3×10^{-7} cm³sec⁻¹ [Tascione, 1988]. The rate of change of the E-region electron density is simply the difference between the ion production and the ion loss processes.

In the F-region the principal ion is O^+ formed by



and to a lesser extent



The loss process for the F-region combines atom-ion interchange and dissociative recombination reactions. First, the following atom-ion interchange reactions occur:



and



Second, the ions are lost by the same dissociated recombination processes outlined in reactions (3) and (4).

The low latitudes exhibit unique transport effects due to electromagnetic dynamics generated by the thermospheric winds. To a first-order approximation the F-region neutral winds are driven by pressure gradients forces that arise from solar EUV heating at F-region altitudes. These pressure gradients cause the wind to blow from the subsolar point to the night side. Over Arecibo, these winds and ambipolar diffusion contribute to the transport of ionization by moving the electrons and ions along the magnetic field lines. During the day, the pressure gradients force the winds in the poleward direction, causing the ions to flow down the magnetic field lines. At night, the winds blow towards the equator forcing the ions to flow up the field lines. These nighttime equatorward winds lift the level of ionization into a region of lower loss rate making it possible to maintain the electron density in the absence of solar production [Walker, 1988].

At equatorial latitudes, the vertical $\vec{E} \times \vec{B}$ drift is the primary transport process that affects the electron and ion density distribution. Data obtained by the incoherent

scatter radar at Jicamarca, Peru [e.g., *Fejer*, 1991, 1981; *Fejer et al.*, 1991; *Kelley*, 1989; *Meriwether et al.*, 1986] have provided some insight into the effects of the vertical drifts on the equatorial neutral winds and the electron density profile. The effects of the vertical drifts on the winds over the magnetic equator will be covered in a later section.

2.3. UPPER ATMOSPHERIC WINDS

2.3.1. Stratosphere and Mesosphere Winds

Figures 3 and 4 show the average zonal wind profile obtained from the HWM93 [*Hedin et al.*, 1993] for the upper atmosphere. These wind profiles are for altitudes from the surface to 120 km. Generally the winds are weakest at the tropopause (~ 12 km) and the mesopause (~ 85 - 90 km), and strongest at the stratopause (~ 55 - 60 km).

The general equation governing the atmospheric wind motion is an extension of Newton's second law of motion [*Hargreaves*, 1992]:

$$\frac{\partial \vec{U}}{\partial t} + 2(\vec{\Omega} \times \vec{U}) = -\frac{1}{\rho} \vec{\nabla} p + \vec{g} + \vec{F} \quad (9)$$

The terms starting from the left side are the rate of change of velocity, the Coriolis term, the pressure gradient, acceleration due to gravity, and an acceleration term due to any other force that acts on the medium [*Hargreaves*, 1992]. To a first approximation, the stratospheric and mesospheric winds result from the balance between the Coriolis force and the pressure gradient force. This balance between the Coriolis force and the pressure gradient force is called the *geostrophic balance*. The average result for these

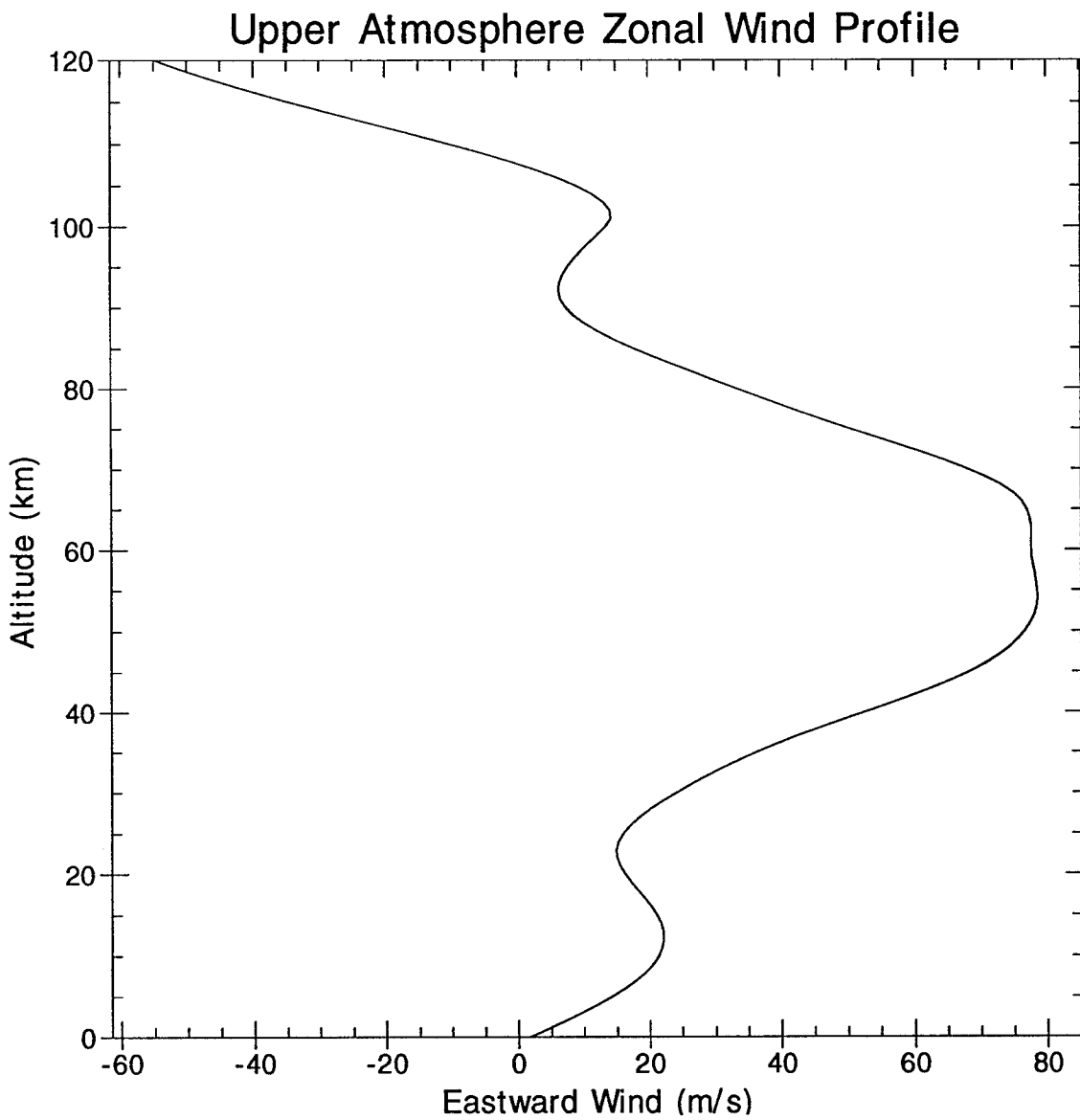


Figure 3. General magnitude of middle latitude zonal winds from the surface to 120 km for December at 0000 LT. The zonal wind data were provided by the HWM93 empirical model [Hedin *et al.*, 1993] for low solar flux ($\Phi = 75$) quiet geomagnetic activity ($A_p = 4$).

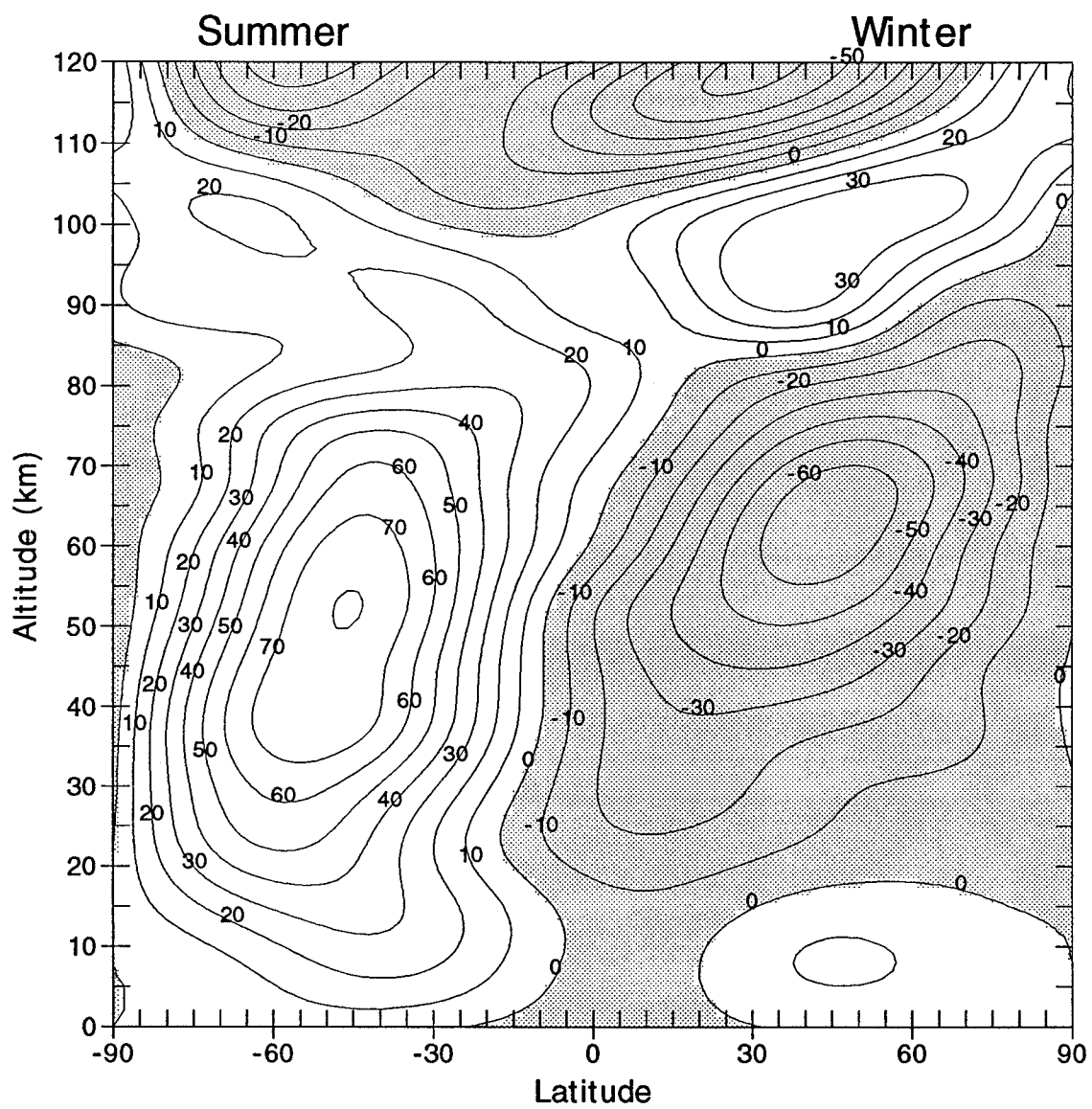


Figure 4. Latitude vs. altitude cross-sections of the average zonal wind at 0000 LT. The zonal wind data were provided by the HWM93 empirical model for low solar flux ($\Phi = 75$) and quiet geomagnetic activity ($A_p = 4$). The positive contours represent the eastward winds and the shaded area or negative contours identify the westward winds.

regions is a zonal wind -- eastward in the summer, westward in the winter [Hargreaves, 1992]. In the stratosphere and mesosphere, the pressure gradient is related to the temperature gradient; hence, the winds are sometimes called the *thermal winds*.

Semi-diurnal and diurnal tides influence upper mesospheric winds. Solar EUV heating of the ozone layer in the stratosphere results in tidal motions in both the upper stratosphere and mesosphere. These tides then propagate up through the atmosphere, influencing both the upper mesospheric and thermospheric winds.

2.3.2. Thermospheric Winds

Why are the thermospheric winds important in earth's atmosphere? The thermospheric winds affect the height of the F layer and also provide a source of energy that generates the electric fields [Kelley, 1989]. For this thesis, only the thermospheric winds above 200 km are studied. Early measurements of winds above 200 km revealed a wind system generated by pressure gradients set up by atmospheric heating. This heating was created by absorption of solar EUV by the abundant species at ~ 250 km, atomic oxygen. The thermal expansion of the atmosphere forms the "diurnal bulge" that follows the subsolar point by $\sim 1 - 2$ hours [Rishbeth, 1972]. It is the atmospheric expansion that gives rise to horizontal pressure gradients that can drive the horizontal wind system; hence, the primary forcing term for thermospheric wind patterns is the pressure gradient term. Although the pressure term is the primary force, equation (9) indicates other forcing terms that sometimes cannot be neglected.

As stated earlier, the primary forcing term for upper atmospheric winds is the pressure gradient associated with the diurnal bulge that results from solar EUV heating.

The diurnal bulge is located at low latitudes and is coincident with the subsolar point. Figure 5 provides a first order approximation to the thermospheric winds at December, March, and June at 250 km for moderate solar flux and quiet geomagnetic conditions. Overall, the average wind is poleward during the day, eastward after sunset, and equatorward after midnight.

A more detailed equation of motion is:

$$\rho \frac{d\vec{U}}{dt} = -\vec{\nabla}p + \rho\vec{g} + \eta\nabla^2\vec{U} - \vec{\nabla}\cdot\vec{\pi}_w - 2\rho\vec{\Omega}\times\vec{U} - \rho v_{ni}(\vec{U} - \vec{V}_i) \quad (10)$$

where ρ - neutral density, p - pressure, \vec{g} - acceleration due to gravity, $\vec{\pi}_w$ - momentum flux density tensor, $\vec{\Omega}$ - angular velocity, v_{ni} - neutral/ion collision frequency, \vec{U} - neutral velocity, and \vec{V}_i - ion velocity. The terms starting from the left side are the total force on the neutral particles, the pressure gradient force, acceleration due to gravity, the viscous force, advective time derivative of the momentum, the Coriolis force, and the ion drag force. For thermospheric winds, neglecting the Coriolis force, the primary limitation on the wind speed comes from the various drag terms [Kelley, 1989]. Figure 6 is a graph showing the relative daytime magnitudes of a few terms in equation 10.

Besides the pressure gradient force, the ion drag also affects the upper thermospheric winds. The ion drag becomes important when the ion collision frequencies are much smaller than the ion gyrofrequencies. Examples of typical F-region thermospheric daytime ion collision frequencies (v_i) are 20 s^{-1} and ion gyrofrequencies (ω_i) are typically 210 rad/s . When the ion gyrofrequency is greater than the ion collision frequency, the ions gyrate along the magnetic field lines; thus, the ions

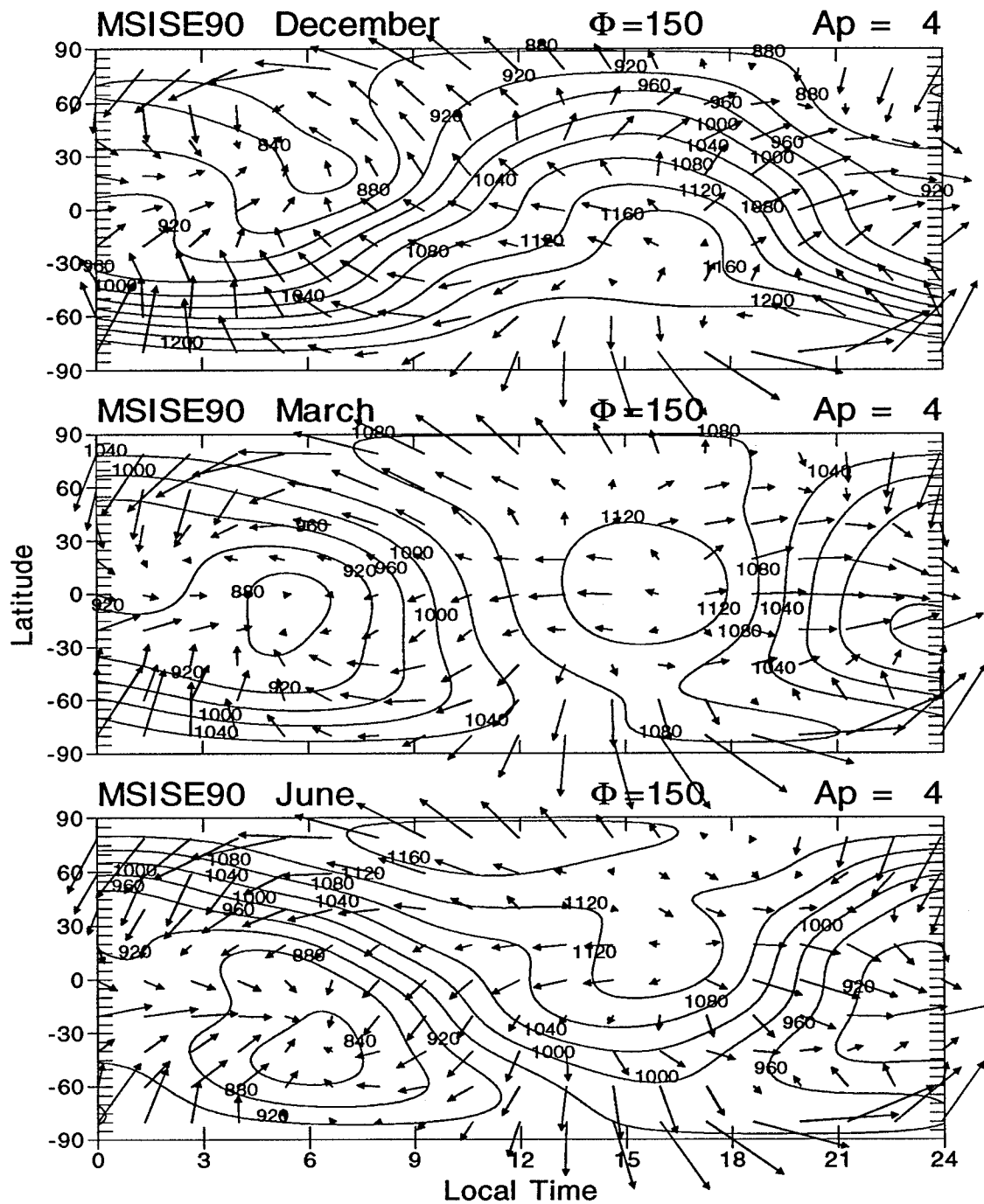


Figure 5. The temperatures (solid curves) and winds (arrows) at 250 km for December, March, and June. These data were obtained using the HWM93 for low flux ($\Phi = 75$) and quiet geomagnetic activity ($A_p = 4$)

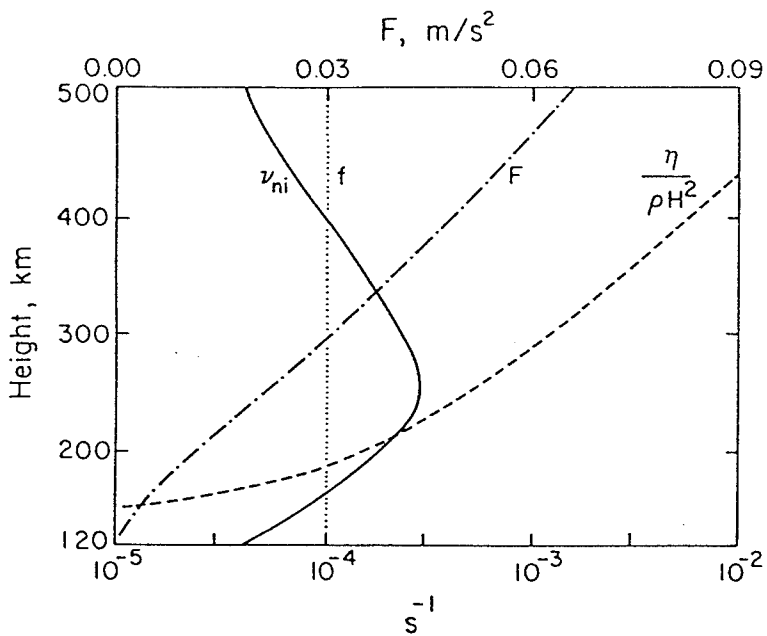


Figure 6. Graphs of neutral acceleration time constants and F for midday at sunspot minimum. The upper scale applies to the acceleration due to the pressure gradient F . The lower scale refers to the ion drag parameter ν_{ni} ; the Coriolis parameter for latitude of 45° , f , and the normalized kinematic viscosity parameter $\eta/\rho H^2$ [After Rishbeth, 1972. Reproduced with permission of Pergamon Press.]

cannot flow across the magnetic field lines like the neutral winds. In the F -region, the effect of the ions being confined to the magnetic field line is a slowing of the neutral winds. This “slowing down” force is called the ion drag.

A poleward wind forces the ions to gyrate down the magnetic field lines while an equatorward wind causes the ions to gyrate up the magnetic field lines. If the magnetic field line is horizontal to the earth's surface (dip angle ~ 0), the winds will not have any effect on raising or lowering the plasma. This is the situation at equatorial latitudes.

If the plasma is lifted up the field lines, the ion density is reduced, allowing for the possibility of strong zonal winds. Similarly, if the plasma is forced down the field

lines, the ion density increases and the neutral wind speed decreases. Figure 7 shows the effects of raising (lowering) the plasma due to equatorward (poleward) winds.

At equatorial latitudes the meridional winds do not raise or lower the plasma; hence, the vertical ion motion is not affected by meridional winds at Arequipa. The next section addresses the wind dynamics at the equatorial latitudes.

2.3.3. Equatorial Thermospheric Winds

The last section examined the effect of the steady drag on the neutral wind for the case where the ion gyrofrequency is greater than the ion collision frequency. At equatorial latitudes the meridional effect on raising and lowering the ions along the field

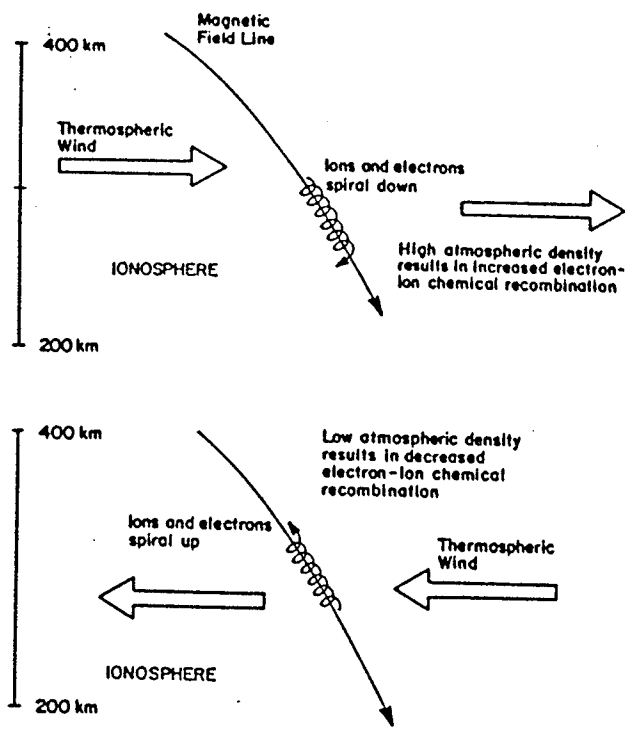


Figure 7. Illustration of how the thermospheric winds affect the ionosphere.

lines is negligible since the magnetic field is nearly parallel to the earth's surface (dip angle ≈ 0). Before exploring further the wind dynamics of the equatorial latitude region, a short discussion is presented on the theoretical wind speed calculations at this region.

At equatorial latitudes the Coriolis force is neglected but the drag force is still important. Thus, for steady-state conditions, the equation of motion (10) reduces to [Kelley, 1989]:

$$\frac{d\bar{U}}{dt} = \bar{F} - v_{ni}\bar{U} = 0 \quad (11)$$

where \bar{F} is the pressure gradient force and $v_{ni}\bar{U}$ is the drag force. Equation (11) indicates that the equation of motion reduces to a balance between the pressure gradient and the drag force. Solving for the velocity, the neutral velocity becomes:

$$\bar{U} = -\frac{\bar{F}}{v_{ni}} \quad (12)$$

By using the values in Figure 6, the pressure gradient and viscosity coefficient can be obtained as a function of altitude. For example, at 300 km, the velocity of the neutral wind is calculated to approximately 130 m/s. This result is well below early calculations of the neutral wind by Lindzen [Kelley, 1989]. Because Lindzen did not include the drag force, his calculated wind speed was 550 m/s compared to the more realistic 130 m/s. Thus the ion drag is the crucial factor that provides correct results for typical upper thermospheric wind speeds.

What causes the strong eastward zonal winds near the magnetic equator during the hours of 2000-2400 LT? Without the effect of meridional winds on raising or

lowering the ions, some other mechanism is necessary to explain the upper thermospheric wind pattern during the postsunset hours. The prereversal enhancement of the zonal electric field is indirectly responsible for the strong easterly winds [Kelley, 1989]. The effect of the prereversal enhancement is to introduce a strong vertical $\vec{E} \times \vec{B}$ that lifts the ions during 1700-2000 UT (see Figures 8 and 9). Figure 9 shows the upward vertical drift is most pronounced during the equinox and June solstice periods and has large day-to-day and solar cycle vertical drift shortly before midnight, which increases the ion drag and reduces the variations [Fejer *et al.*, 1991]. With the ions out of the way, the ion drag is greatly reduced, thus nearly doubling the thermospheric wind speeds (see Figure 10). This effect is clearly shown in the zonal

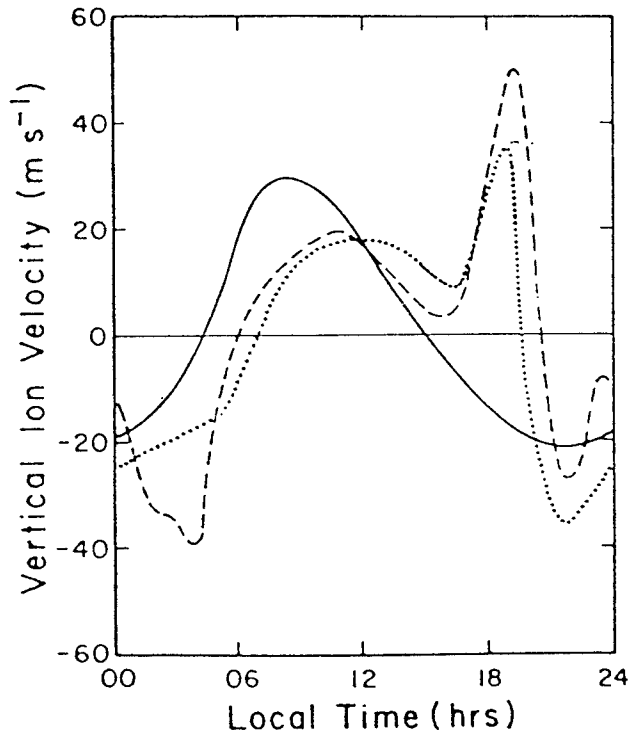


Figure 8. Calculated vertical ion drift velocities for several driving wind components. The solid line includes only the tidal-driven E-region dynamo, while the dashed line includes the F-region dynamo as well. Typical vertical plasma drifts are indicated by the dotted line [After Heelis *et al.*, 1974. Reproduced with permission of Pergamon Press.]

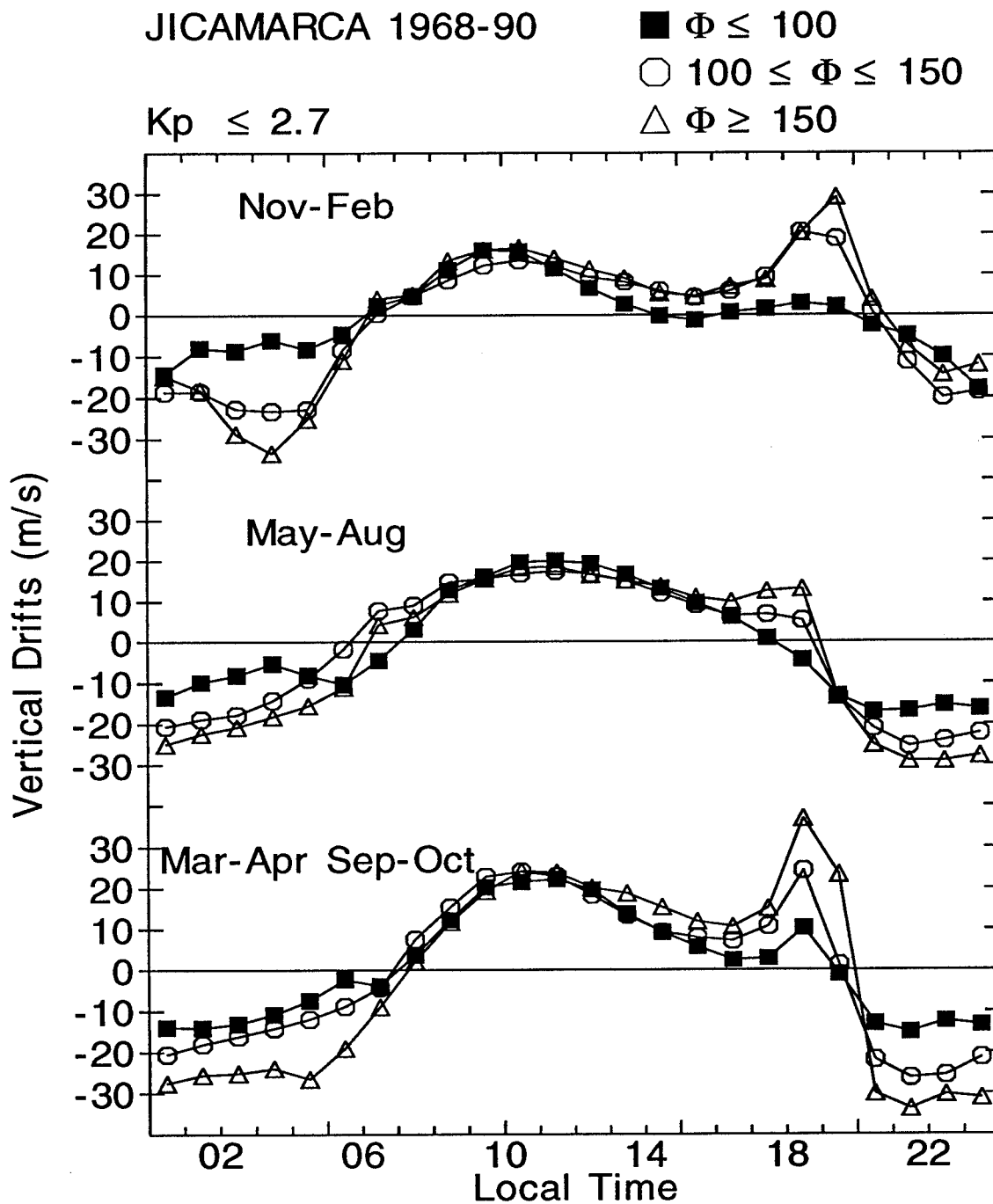


Figure 9. Measured vertical (positive for upward motions) plasma drifts in the equatorial F-region for various seasons and solar cycle conditions.

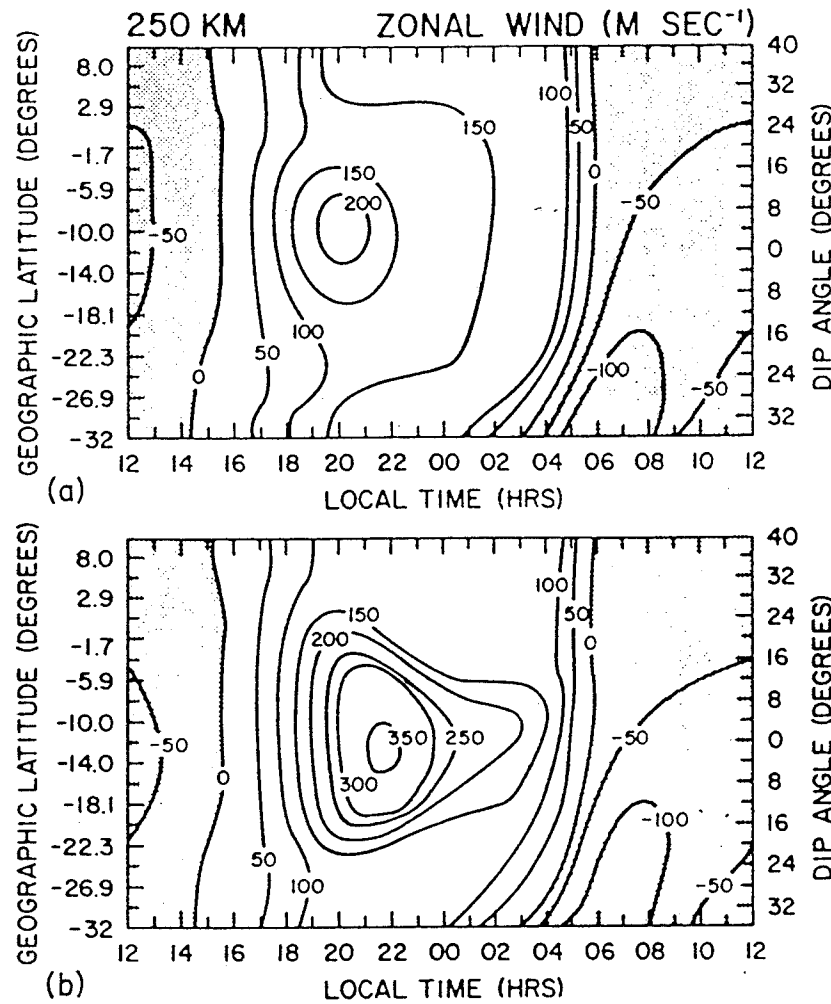


Figure 10. Contours of the zonal neutral wind at 250 km, calculated from the thermospheric model by Anderson and Roble (1974) as a function of latitude and local time: (a) without the postsunset enhancement of the $\vec{E} \times \vec{B}$ drift velocity and (b) including the postsunset enhancement [After Anderson and Roble, 1974. Reproduced with permission of the American Geophysical Union].

wind measurements made by the Dynamics Explorer 2 satellite (see Figure 11).

The previous two sections provided only a glimpse of how the upper thermospheric winds are generated and effected by ion drag and $\vec{E} \times \vec{B}$ vertical drifts. Other ionospheric effects such as gravity waves, tides, and geomagnetic storms also play a significant role in the dynamics of the upper thermosphere. While this work does not highlight the effects of gravity waves and tides, it is important to realize that the vertical drifts and ion drag are not the only mechanisms affecting the thermospheric neutral winds. Chapter 6 will discuss the effects of geomagnetic storms, also known as disturbed conditions, on the low latitude neutral winds.

2.4. PREVIOUS WIND STUDIES

Several climatological studies of the thermospheric winds have been conducted at Arequipa and Arecibo. Although significant longitudinal variations of the neutral winds were noted in the Dynamic Explorer 2 satellite measurements [Raghavarao *et al.*, 1991], the measured neutral winds over Arequipa and Arecibo were shown to be consistent with other low latitude sites at different longitudes [Biondi *et al.*, 1991, 1990; Meriwether *et al.*, 1986; Sahai *et al.*, 1992]. This section briefly presents the most significant results of these studies. We will also highlight the magnetic activity studies since this work focus on the neutral wind response to storm time events.

For Arequipa, results by Biondi *et al.* [1990, 1991] and Meriwether *et al.* [1986] showed the thermospheric winds exhibited both solar cycle effects and seasonal variations, with the seasonal variations being more pronounced (see Figures 12

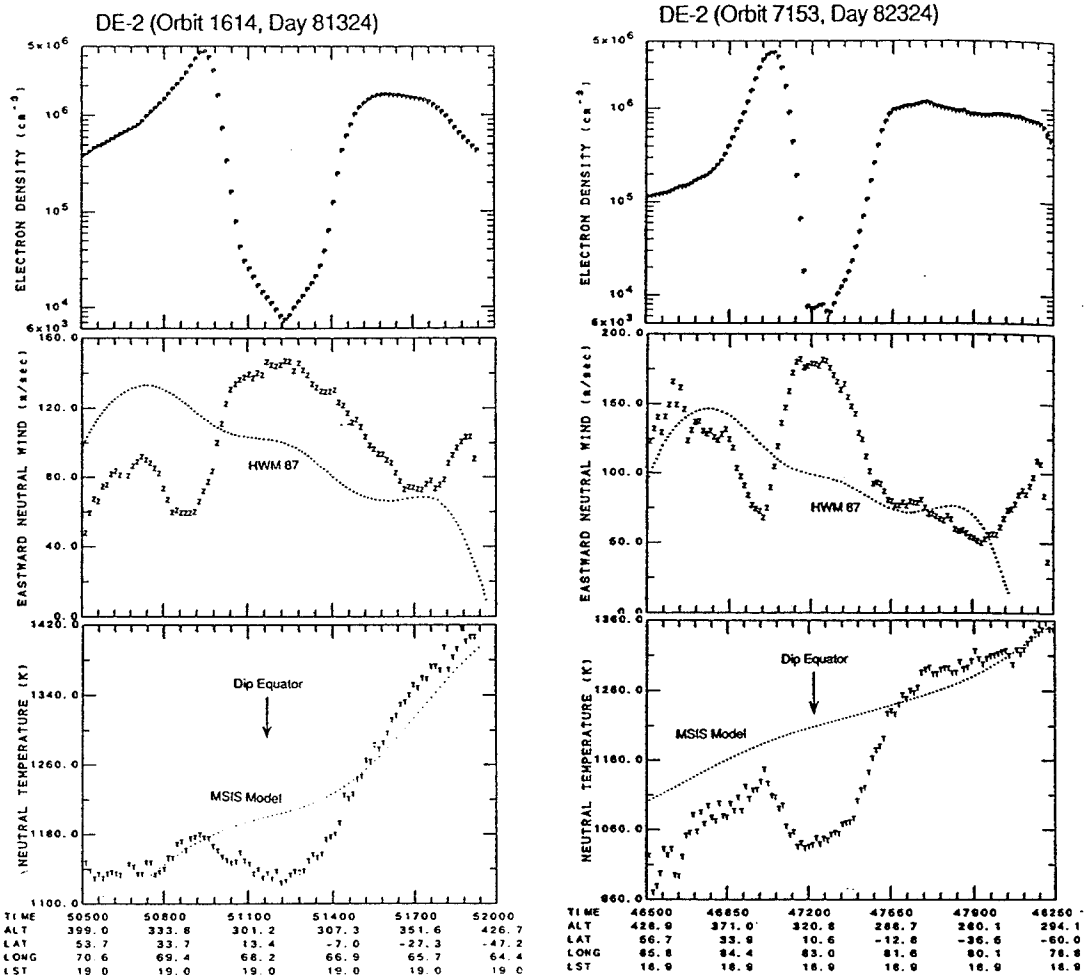


Figure 11. Dynamics Explorer 2 data of electron density (upper panel), zonal winds (middle panel), and temperature (lower panel) near 300 km at low latitudes. The measurements were taken on November 20, 1981 at 1900 hrs LST (left graph) and November 20, 1982 at 18.9 hrs LST (right graph). These graphs show an inverse relationship between the magnitudes of the wind velocities ('Z') and the electron density ('P') profiles. Note at the Dip Equator, the measurements support the increased zonal winds at the time of the sharp increase of the upward velocity in the dusk sector. [After Raghavarao *et al.*, 1991. Reproduced with permission of the American Geophysical Union.]

and 13). These studies did not address magnetic activity effects.

Thermospheric wind studies over Arecibo by *Burnside and Tepley* [1989] and *Burnside et al.* [1981, 1983, 1987, 1991] showed the neutral winds are not affected by changes in the solar cycle activity, although there exist pronounced seasonal variations. This study did not provide a detailed analysis of the solar cycle effects on the seasonal averages (see Figure 14). As for storm time effects, these studies concentrated on a few disturbed days and did not address the issue of the repeatability of the neutral wind response. During a geomagnetic disturbance on the night of 14 January 1988 ($K_p > 7$), *Burnside et al.* [1991] showed measured FPI winds over Arecibo (see Figure 15). The results in Figure 15 show mainly westward neutral winds and near zero meridional winds during the night. These results also show a return to average eastward zonal and poleward meridional wind during the night of 15 January where the three hourly K_p returned to moderate to quiet geomagnetic conditions ($K_p < 3$).

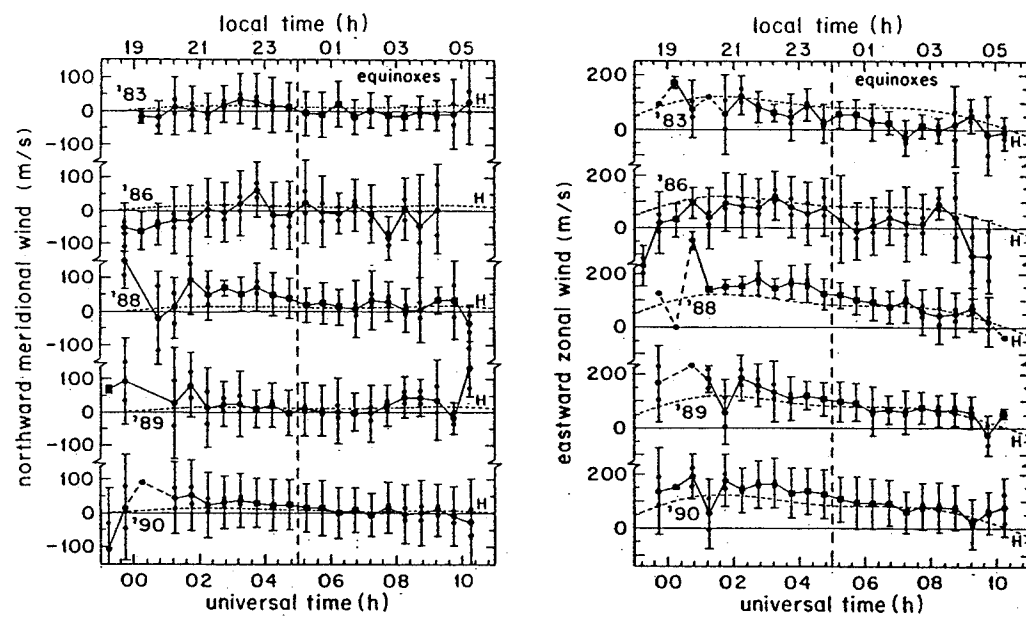


Figure 12. Arequipa equinox month average meridional and zonal winds from 1983 to 1990. The short-dash curves labeled H represent predictions of the HWM-87 by *Hedin et al.* [1988]. [After *Biondi et al.*, 1991, Reproduced with permission from the American Geophysical Union].

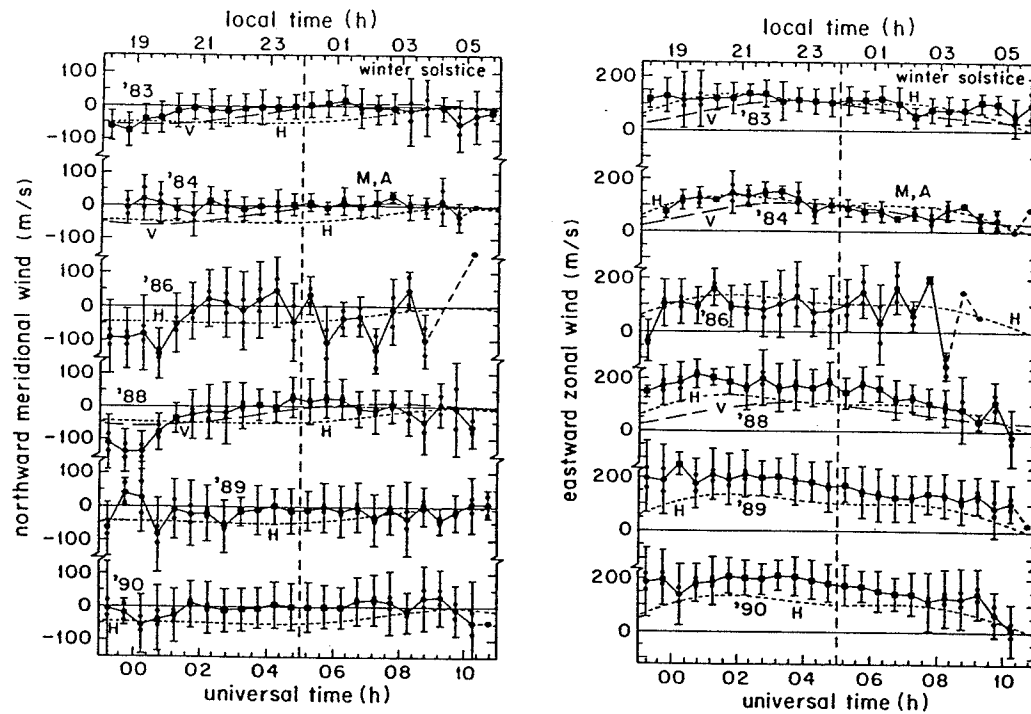


Figure 13. Arequipa June solstice average meridional and zonal winds from 1983 to 1990. The months included in each year's average are June and July, except for 1984, where May and August are used, as indicated by the M and A symbols. The short-dash curves labeled H represent predictions of the HWM-87 by *Hedin et al.* [1988]. The long-dash curves labeled V are the VSH TGCM predictions by *Killeen et al.* [1987]. [After *Biondi et al.*, 1991, Reproduced with permission from the American Geophysical Union].

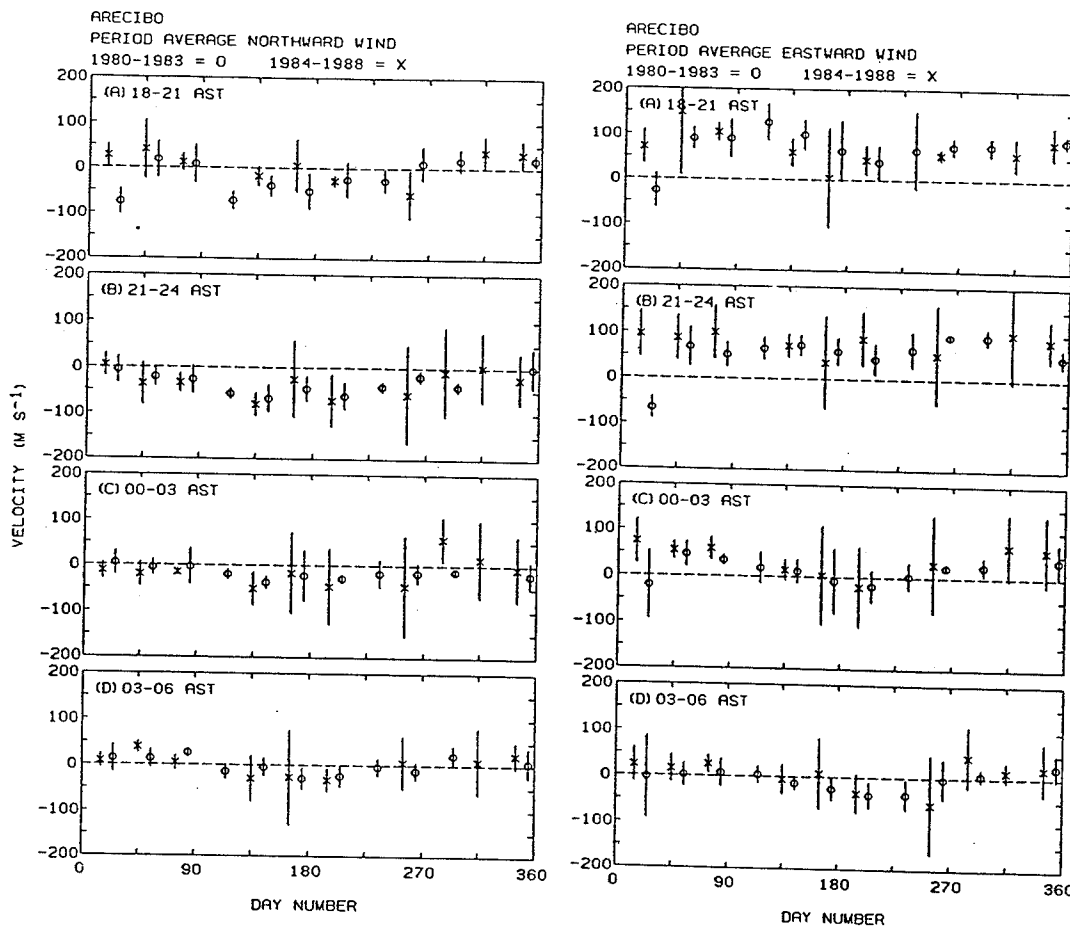


Figure 14. The annual variation of the average northward meridional and eastward zonal Fabry-Perot winds over Arecibo. The open circles represent the results obtained by sorting the measurements from 1980 to 1983 into 30-day periods. The crosses show the results for the measurements from 1984 to 1988. [After Burnside and Tepley, 1989. Reproduced with permission by the American Geophysical Union].

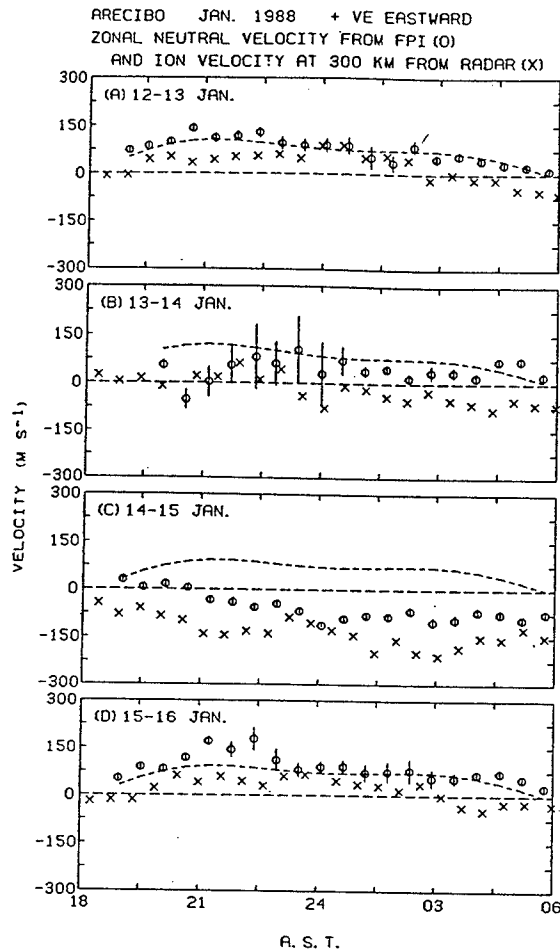


Figure 15. Zonal neutral wind velocities measured by the Fabry-Perot interferometer (circles) on four consecutive nights in January 1988. Cross show the ion velocity at 300 km measured by the incoherent scatter radar. The dashed lines are the zonal winds given by the HWM-87 empirical model. [After Burnside *et al.*, 1991. Reproduced with permission by the American Geophysical Union].

CHAPTER 3

MODELING TECHNIQUES

3.1. INTRODUCTION

The long-term average and the day-to-day variability of the ionosphere can be analyzed using upper atmospheric models. These models further our understanding of the physical mechanisms that contribute to the long-term and daily variability of the ionosphere. This thesis has already presented several model predictions from the empirical models HWM93 [*Hedin et al.*, 1993] and MSISE90 [*Hedin*, 1991], and the first principal model TIGCM93 [*Fesen et al.*, 1993]. This chapter provides the historical aspects of upper atmospheric modeling and outlines several models used for this study. The chapter concludes with a more detailed description of the TIGCM93 physical equations and low latitude neutral wind predictions.

3.2. UPPER ATMOSPHERIC MODELING

3.2.1. History of Atmospheric Modeling

The development of upper atmospheric models (above 20 km altitude) is based on tropospheric forecast models such as the Limited Fine Mesh (LFM) and the Nested Grid Model (NGM). The National Weather Service uses the LFM and NGM for daily weather prediction. Because of the similarities in atmospheric dynamics in both the upper and lower atmosphere, upper atmospheric scientists borrowed many ideas from the lower atmospheric forecast models and incorporated them into upper atmospheric

models. This section provides a brief history of lower atmospheric modeling because of its importance to the thermospheric modeling efforts.

The British scientist L.F. Richardson was the first to attempt to predict weather numerically [*Holton*, 1992]. His work is considered the cornerstone of weather prediction and is based on finite difference calculations. Unfortunately, Richardson was hampered by two major problems. Since his work was done in the 1920s, he did not have the luxury of computers to perform the numerous arithmetic operations. Richardson estimated that 64,000 people would be required to keep up with these global forecasts [*Holton*, 1992].

Richardson's second problem concerned his initial attempt to predict weather between two grid points. This first weather prediction failed so miserably that people doubted that weather prediction would become a feasible operation. It was not until after World War II that researchers realized the problem associated with Richardson's first forecast attempt. When Richardson set up the differential equations for his forecast, he included terms for high speed sound and gravity wave solutions. As the numerical prediction was marched forward in time, the sound and gravity wave solutions amplified so much that they obliterated the correct numerical predictions!

After 1950, meteorologists made significant progress in weather prediction and modeling. It was not until 20 years later, however, that upper atmospheric scientists began exploring the possibility of applying these lower atmospheric equations to the regions above the troposphere.

In 1979, the Thermospheric General Circulation Model (TGCM) was created to better understand the processes affecting the upper atmospheric weather. The TGCM, based on similar equations used to predict tropospheric weather, has undergone several model revisions. These changes will be highlighted later in this paper.

3.2.2. Upper Atmospheric Models

Several models used to study the upper atmosphere include the Mass Spectrometer and Incoherent Scatter Extended (MSISE90) Model, the Horizontal Wind Model (HWM93), the Vector Spherical Harmonic (VSH) model, and the TIGCM. Before describing these models, the distinction should be made between empirical, semi-empirical, and first principle models. An empirical model is a model whose calculations are based on collected data and are statistical by nature. Examples of an empirical model are the MSISE90 and the HWM93 since their calculations are based on data collected from satellite mass spectrometer, incoherent scatter radar measurements and satellite measurements. A physical model is a model whose calculations are based on physical principles. The TIGCM is an example of a physical model. A semi-empirical model is a model whose calculations are based on collected data and physical principles. The VSH model is an example of a semi-empirical model.

3.2.2.1. Mass Spectrometer and Incoherent Scatter

(MSISE90) Model

The MSISE90 is an empirical model based on in situ and Incoherent Scatter Radar measurements. The MSISE90 version provides modeled data from the surface

to approximately 3000 km altitude. The model calculates profiles of number densities, total mass density, and neutral temperature for N, N₂, O₂, O, He, Ar, and H [Hedin, 1991]. These predictions are based on data collected from several satellites, rocket probes (in situ), and five incoherent scatter radars [Hedin, 1991]. The MSISE90 model predictions are functions of several geophysical values such as 10.7-cm solar flux, Ap index, latitude and longitude, and universal time.

3.2.2.2. Horizontal Wind Model (HWM93)

After discussing the MSISE90 model, it is only natural to wonder if a similar type of empirical model is used to estimate upper atmospheric winds. The HWM93 is the MSISE90 equivalent for upper atmospheric winds. The HWM93 is based on thermospheric wind data obtained from the Atmosphere Explorer E (AE-E) and Dynamics Explorer-2 (DE-2) satellites, and ground-based data from several incoherent scatter radars and Fabry-Perot optical interferometers [Hedin *et al.*, 1991].

The HWM93 model requires the user to input the day of year, time of day (UT), altitude, geographic latitude and longitude, local solar time, 3-month average and previous day value of the 10.7-cm solar flux index, and either the daily Ap magnetic index or prescribed history of 3-hour Ap indices [Hedin *et al.*, 1991]. Once the user enters these data, HWM93 gives the estimated zonal and meridional winds from 100 km to 500 km.

Like the MSISE90 model, the HWM93 uses two different fitting routines above and below 200 km. Above 200 km, where viscosity limits neutral wind latitudinal

gradients, these altitude variations are each represented by an extension of the Bates formula. This is the same formula used for thermospheric temperature profiles [Hedin *et al.*, 1991]. Below 200 km the wind profiles are represented by a cubic spline. This cubic spline is defined by cubic polynomials between specified nodes with first and second derivatives continuous across the interior nodes [Hedin *et al.*, 1991]. These nodes are located between 250 km and 300 km because of the limited data in this altitude range.

3.2.2.3. Vector Spherical Harmonic (VSH) Wind Model

The VSH model is a computer subroutine that provides a description of the composition and dynamics of the thermosphere [Killeen *et al.*, 1987]. Given the time, location, the Ap index, and the 10.7-cm solar flux, the VSH routine returns a variety of parameters. First, the VSH routine returns densities for O, O₂, N₂, H, O⁺, electron, and total mass. Second, the routine returns the mixing ratios for O, N₂, and O₂. The dynamic parameters returned are the neutral zonal winds, meridional winds, vertical winds, neutral and ion temperatures, and pressure. These data are provided for altitudes ranging from 130 km to 600 km [Killeen *et al.*, 1987].

Two types of data are used to drive the VSH model: coefficient library and real-time data [Killeen *et al.*, 1987]. The coefficient library consists of TIGCM data output. The real-time data are made up of solar flux and magnetic activity indices, as well as any compositions, density, and/or wind information as obtained by satellite measurement [Killeen *et al.*, 1987]. The VSH model is a semi-empirical model because of the

dependence on collected data and the TIGCM calculated data. Because the upper limit of the TIGCM is 500 km, the VSH model uses the MSIS-86 model results above 500 km altitude.

Two reasons make the VSH model an appealing option. First, the model makes temperature results available for comparison with other empirical models [*Killeen et al., 1987*]. Second, the VSH model uses more coefficients in its analysis. This provides more accurate results than other empirical models such as MSIS [*Killeen et al., 1987*]. The main drawback is that this model does not improve on the TIGCM results.

3.2.2.4. Thermosphere/Ionosphere General Circulation

Model (TIGCM93)

This following section describes NCAR's TIGCM93. To develop an appreciation for this model, the next section will focus on the history, description, calculated results, primitive equations, and model output of the TIGCM93. For the remainder of this chapter, we shall refer to this model as the TIGCM rather than the TIGCM93. The "93" refers to the version number of the most current TIGCM

3.3. THERMOSPHERE/IONOSPHERE GENERAL CIRCULATION

MODEL (TIGCM)

3.3.1. TIGCM History

The first NCAR General Circulation Model was operational in 1979. Dr. Raymond Roble is considered the father of the thermospheric general circulation models

since he was the first to adjust Holton's primitive equations and apply the revised equations to thermospheric physics. TABLE 2 lists a chronological development of the thermospheric general circulation models.

The first thermospheric general circulation model, released in 1979, was called the Thermosphere General Circulation Model (TGCM). This model used the revised primitive equations, described in a following section, to predict the general circulation of the thermosphere. Besides the primitive equations, the TGCM relied on several empirical models to supplement its calculations. The empirical models (see TABLE 2) provided input for the dynamo processes for both E- and F-regions, neutral gas

TABLE 2. Chronological Development of the TGCM.

Year	Empirical Model	General Circulation Model
1979	Ionospheric Dynamo MSIS Aurora Solar Tides	TGCM (100 - 500 km)
1989	Dynamo Aurora Solar Tides	TIGCM (95 - 500 km)
1991	Aurora Solar Tides	TIE-GCM (95 - 500 km)
1992	Aurora Solar	TIME-GCM (30 - 500 km)

concentration (MSIS), ionospheric coupling interactions, and external forcing mechanisms (aurora, solar, and tidal motions).

The TIGCM was released in 1989. The differences between the TIGCM and the TGCM were the inclusion of coupling mechanisms in the ionosphere and prediction of neutral concentrations. Since the TIGCM predicted the ionospheric coupling and neutral gas concentrations, the requirement for the Ionospheric and MSIS empirical models was dropped. In addition, the lower boundary of the model was dropped to 95 km. However, this model has not been fully tested.

3.3.2. TIGCM Description

The TIGCM model treats all three spatial dimensions (x , y , and z), including time, by finite differences, allowing more flexibility than thermospheric models prior to the TGCM [Dickinson *et al.*, 1981]. The TIGCM solves the primitive equations of dynamic meteorology but adapts to the physics appropriate to thermospheric heights.

The TIGCM contains most of the physics to model a coupled ionosphere and thermosphere atmosphere. Besides the primitive equations (thermodynamic, east and west momentum, continuity, and hydrostatic equations), the model includes most of the basic chemical reactions that occur in the thermosphere. The most apparent limitation of this model is that it does not contain the F-region dynamo and as a result cannot be considered a true physical model.

The TIGCM calculates global distributions of the neutral gas temperatures; zonal, meridional, and vertical winds; the major neutral gas constituents number

densities of O₂, O, and N₂; and the minor neutral gas constituent number densities of N(²D), N(⁴S), and NO [Roble, 1992]. The interactive model of the ionosphere solves for global distributions of the ion species O⁺, O₂⁺, N₂⁺, NO⁺, N⁺ and the electron density. Additional predictions for the interactive ionosphere model include electron and ion temperatures. The model has an effective 5 x 5 latitude by longitude horizontal grid with 25 constant pressure surfaces extending approximately between 95 and 500 km in altitude with a vertical resolution of two grid points per scale height [Roble, 1992]. The model time step is 5 minutes and it takes about 20 minutes for the NCAR CRAY CPU to simulate 1 day [Roble, 1992].

The TIGCM, like the TGCM, uses several empirical models for its calculations. These empirical models are listed in TABLE 3. If no name is specified for the empirical model, the author's name is used (italics); otherwise the name of the model is listed. TABLE 3 indicates that the TIGCM model is dependent on empirical models to

TABLE 3. Empirical Models Used in the TIGCM

Empirical Model	Model Calculations
Richmond	low and middle latitude electric fields [Richmond et al., 1980]
Heelis	high latitude electric fields [Heelis et al., 1982]
Fuller-Rowell and Evans	auroral particle inputs [Fuller-Rowell and Evans, 1987]
Hinteregger	solar EUV inputs [Hinteregger, 1981]
Forbes and Vial	amplitudes and phases of the upward propagating semidiurnal tides [Forbes and Vial, 1989, 1991]

successfully predict upper atmospheric properties.

3.3.3. TIGCM Model Equations

The equations used by the TIGCM are based on the pressure coordinate primitive equations of lower-atmospheric dynamic meteorology [Dickinson *et al.*, 1981]. The primitive equations are the thermodynamic, eastward and northward momentum, continuity, and hydrostatic equations.

3.3.3.1. Thermodynamic Equation

The thermodynamic equation in spherical coordinates is

$$\frac{\partial T}{\partial t} = \frac{g e^z}{p_o c_p} \frac{\partial}{\partial z} \left(\frac{K_T}{H} \frac{\partial T}{\partial z} \right) - aT - \vec{V} \cdot \vec{\nabla} T - w \left(S + \frac{\partial T}{\partial z} + \frac{RT}{c_p m} \right) + \frac{Q'}{c_p} \quad (13)$$

where T - temperature, z - $\log_e(p_0/p)$, g - acceleration of gravity, p_o - reference pressure 50 μ Pa, c_p - specific heat per unit mass, K_T - thermal conductivity coefficient, H - mean scale height, a - radiative damping coefficient, $\vec{V} \cdot \vec{\nabla}$ - horizontal advective operator, w - vertical motion, S - static stability, m - specified mean molar mass, and Q' - heating term. The terms from left to right in the equation are the total heating rate, downward heat conduction, radiative cooling, heat advection, the adiabatic heating and cooling due to expansion and contraction of the gases in the thermosphere, and the heating term. The heating term includes solar EUV and UV heating, Joule heating, and

heating due to auroral particle precipitation. Mathematically, this Q' term is:

$$\frac{Q'}{c_p} = \frac{1}{c_p} (Q_s + Q'_J + Q_p) \quad (14)$$

where Q_s - rate of solar heating per unit mass, Q'_J - rate of Joule heating per unit mass, and Q_p - rate of auroral particle precipitation heating per unit mass

3.3.3.2. Momentum Equations

The TIGCM uses the eastward and northward momentum equations in spherical coordinates are:

Eastward Momentum Equation

$$\begin{aligned} \frac{\partial u}{\partial t} = & \frac{ge^z}{p_o} \frac{\partial}{\partial z} \left(\frac{\mu}{H} \frac{\partial u}{\partial z} \right) + fv + \left\{ \lambda_{xx}(u_I - u) + \lambda_{xy}(v_I - v) \right\} \\ & + \left\{ -\vec{V} \cdot \vec{\nabla} u - \frac{uv}{r} \tan \phi \right\} - \frac{1}{r \cos \phi} \frac{\partial \Phi'}{\partial \lambda} - w \frac{\partial u}{\partial z} \end{aligned} \quad (15)$$

Northward Momentum Equation

$$\begin{aligned} \frac{\partial v}{\partial t} = & \frac{ge^z}{p_o} \frac{\partial}{\partial z} \left(\frac{\mu}{H} \frac{\partial u}{\partial z} \right) - fu + \left\{ \lambda_{yy}(v_I - v) + \lambda_{yx}(u - u_I) \right\} \\ & + \left\{ -\vec{V} \cdot \vec{\nabla} v - \frac{u^2}{r} \tan \phi \right\} - \frac{1}{r} \frac{\partial \Phi'}{\partial \phi} - w \frac{\partial v}{\partial z} \end{aligned} \quad (16)$$

where u - eastward neutral velocity, $z = \log_e(p_0/p)$, v - northward neutral velocity, μ - coefficient of viscosity, g - acceleration of gravity, p_o - reference pressure $50\mu\text{Pa}$, u_I - zonal ion-drift velocity, $\lambda_{xx}, \lambda_{xy}, \lambda_{yx}, \lambda_{yy}$ - ion drag tensor, H - mean scale height, v_I -

meridional ion-drift velocity, $\vec{V} \cdot \vec{\nabla}$ - horizontal advective operator, w - vertical motion,

Φ - geopotential, f - Coriolis parameter, and ϕ - latitude.

The terms from left to right (for both momentum equations) are the total net force per unit mass, force per unit mass due to vertical viscosity, Coriolis force per unit mass, ion-drag force per unit mass, nonlinear momentum advection force per unit mass, and the pressure force per unit mass.

3.3.3.3. Continuity Equation

The continuity equation in spherical coordinates is

$$\frac{1}{r \cos \phi} \frac{\partial}{\partial \phi} (v \cos \phi) + \frac{1}{r \cos \phi} \frac{\partial u}{\partial \lambda} + e^z \frac{\partial}{\partial z} (e^{-z} w) = 0 \quad (17)$$

where ϕ - latitude, r - radial distance from the earth, v - northward velocity, u - eastward velocity, w - dz/dt ('vertical motion'), z - $\log_e \frac{P_o}{P}$ vertical height in pressure coordinates, and λ - longitude.

The continuity equation expresses the conservation of mass for a fluid.

3.3.3.4. Hydrostatic Equation

The hydrostatic equation is:

$$\frac{\partial \Phi'}{\partial z} = R(T_o + T) / m \quad (18)$$

where Φ' - geopotential, R - universal gas constant, T_o - global mean temperature, T - temperature, and m - mass.

The ideal gas law and the hydrostatic balance combine to form the hydrostatic equation. The ideal gas law for the atmosphere describes the thermodynamic state of the atmosphere at any point and is determined by the values of pressure, temperature, and density at a specified point [Holton, 1992]:

$$p = \rho RT \quad (19)$$

where p - pressure, ρ - atmospheric density, R - gas constant, and T - temperature.

The hydrostatic balance condition is a good approximation for the vertical dependence of the pressure field in the real atmosphere. The hydrostatic balance condition defines the relationship between pressure and height.

There is a difference between geopotential and geopotential height. The gradient of a potential function Φ , the geopotential, is equal to the acceleration due to gravity [Holton, 1992]:

$$\bar{\nabla} \Phi = -\bar{g} \quad (20)$$

By setting the geopotential to zero at mean sea level, the geopotential at height z becomes the work required to raise a unit mass to height z from mean sea level (Holton, 1992):

$$\Phi = \int_0^z g dz \quad (21)$$

For most atmospheric calculations, the geopotential height is used instead of the geopotential Φ . The geopotential height is mathematically defined as $Z = \frac{\Phi(z)}{g_o}$.

3.3.4. TIGCM Diagnostic Processor

One of the outputs of the NCAR TIGCM is a history file containing the

calculated wind, temperature, and composition fields at all model grid points for each hour [*Killeen and Roble, 1984*]. The TIGCM diagnostic processor is run after the TIGCM completes its calculations. The processor reads the history file, ion drag tensors, ion drift velocities, specific heats, coefficients of viscosity, and coefficients of thermal conductivity, and then applies horizontal and vertical finite differencing to obtain the individual forcing terms appearing in the momentum equations at a given altitude for a given time [*Killeen and Roble, 1984*]. The processor provides these terms both for the global TIGCM grid at the given universal time and for selected grid points for each hour of local time [*Killeen and Roble, 1984*].

3.4. TIGCM PREDICTIONS

Figures 16 and 17 show the TIGCM predictions for the neutral winds over Jicamarca, Peru (17.5°S , 71.0°W , dip latitude $\sim 1.3^{\circ}\text{S}$). Because the magnetic field lines are horizontal over Jicamarca, the effects of the meridional winds on the motion of the ions are negligible. Section 2.3.2 explained how the prereversal enhancement or the vertical $\vec{E} \times \vec{B}$ drift drives the plasma upward thereby reducing the ion drag. We note that the TIGCM predicted winds are consistent with this theory since we find the maximum winds occur during 2000 LT - 2300 LT.

Figures 18 and 19 show the output for the TIGCM93 meridional and zonal winds for Arecibo, Puerto Rico (18°N , 71°W). The figures show the December and June solstice winds at 300 km for solar minimum conditions ($\Phi = 75$). The most noticeable effect is the north-to-south wind shift between the December and June

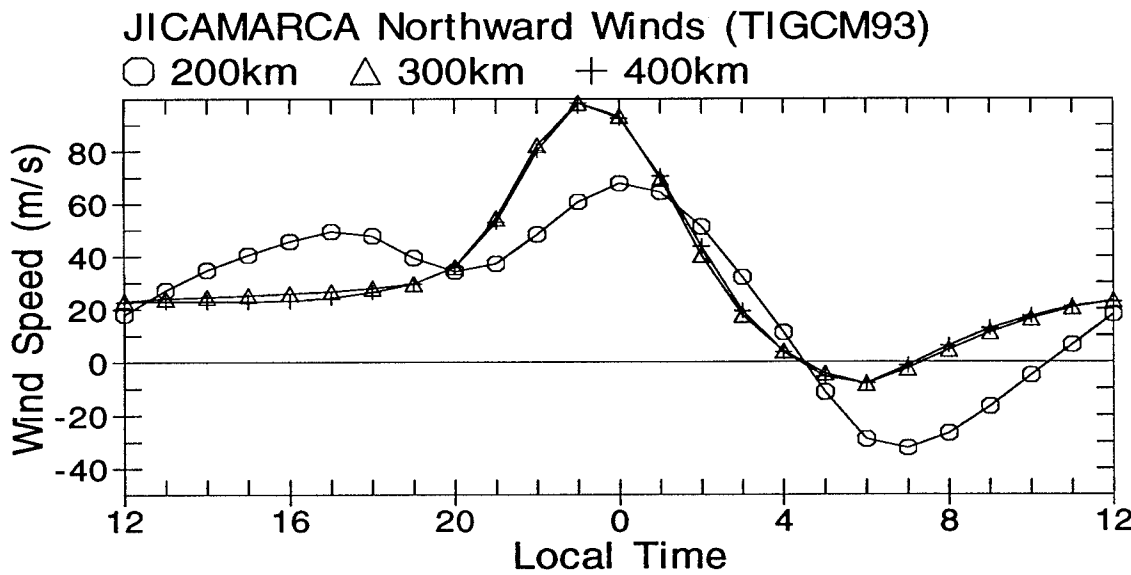


Figure 16. Meridional winds from TIGCM93 model for Solar Minimum Conditions. F10.7 = 75, Northward is positive, and local time is centered about 2400 LT. Model results for grid point near Jicamarca (17.5° S, 70.0° W) for December Solstice.

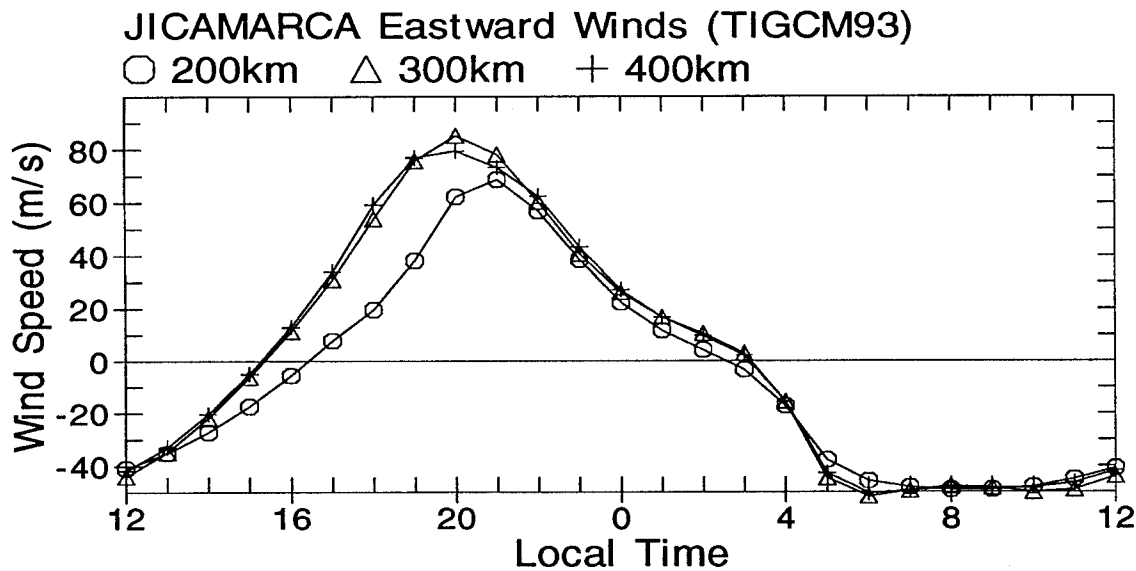


Figure 17. Zonal winds from TIGCM93 model for Solar Minimum Conditions. F10.7 = 75, Eastward is positive, and local time is centered about 2400 LT. Model results for grid point near Jicamarca (17.5° S, 70.0° E) for December Solstice.

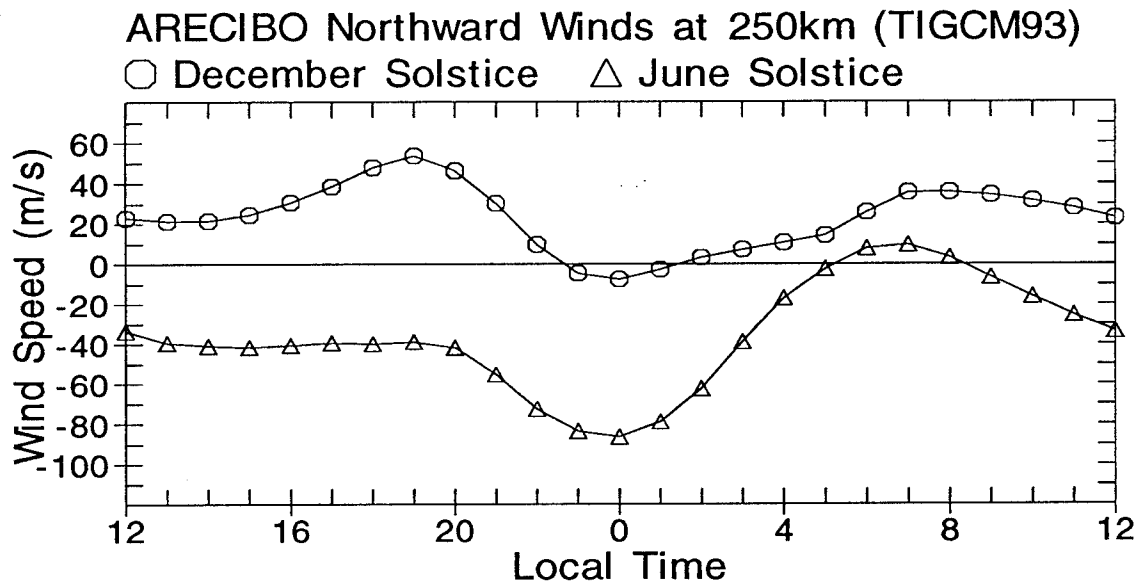


Figure 18. Meridional winds from TIGCM93 model for Solar Minimum Conditions. F10.7 = 75, Northward is positive, and local time is centered about 2400 LT. Model results for grid point near Arecibo (17.5°N, 65.0°W) for both December and June Solstice.

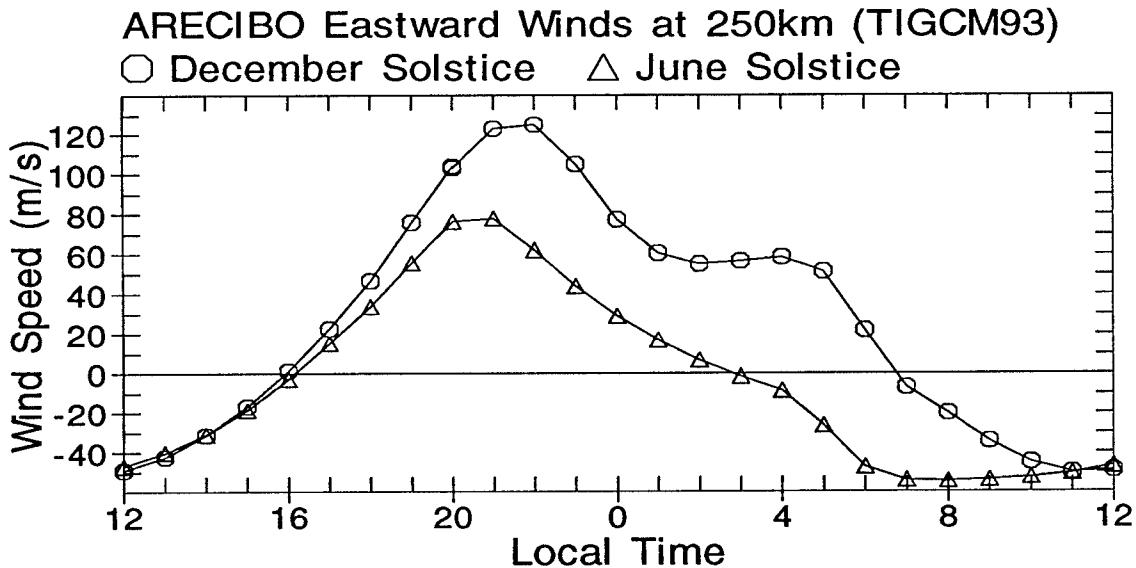


Figure 19. Zonal winds from TIGCM93 model for Solar Minimum Conditions. F10.7 = 75, Eastward is positive, and local time is centered about 2400 LT. Model results for grid point near Arecibo (17.5°N, 65.0°W) for both December and June Solstice.

solstices. This wind change is a result of the sun's apparent path across the earth's surface. For the December solstice, the sun's position crosses south of Arecibo while during the June solstice the sun's position crosses north of Arecibo. The pressure gradients over Arecibo are effected by the sun's apparent path; hence, these pressure gradients are directed in such a way as to cause predominate wind situations for the December and June solstice plots. The main differences between the modeled zonal winds are the smaller eastward wind speeds during the night for the June solstice conditions and earlier morning reversal time during the summer.

Considering only the ion drag and viscosity forces, a poleward wind forces the plasma to move down the field lines while the equatorward wind forces the plasma to move up the field lines. If the ion drag and viscosity were the only forcing mechanisms involved, strong zonal winds should prevail once the plasma is lifted along the field lines. Likewise, if the plasma is forced down the field lines, the zonal winds should be reduced because of the increase of the plasma density. Further review of Figures 18 and 19 reveals an inconsistency in the December solstice meridional and zonal winds. Before midnight, the meridional winds are in a northerly direction that should result in forcing the plasma down the field lines, but the zonal winds are increasing during this time. Figures 18 and 19 are not consistent with the theory outlined above, but the meridional wind effect on increasing or decreasing the ion drag is an oversimplification of the physics in this region. This theory neglects tidal, gravity wave, and electrodynamic effects. This raises a major weakness with the TIGCM93 model, i.e., the lack of modeling the electrodynamic effects. During the December solstice, a

vertical $\vec{E} \times \vec{B}$ drift may contribute to raising the plasma and indirectly cause the strong eastward winds. This lack of electric field predictions prompted the creation of an enhanced global circulation model, TIE-GCM, that includes the electric field calculations [Richmond *et al.*, 1992]. We do not use TIE-GCM predictions since this model is still in the process of model validation.

CHAPTER 4

MEASUREMENT TECHNIQUES AND DATA

4.1. INTRODUCTION

Our study uses measured Fabry-Perot Interferometer (FPI) and Incoherent Scatter Radar (ISR) winds. In addition to the wind data, we use ISR measured electron density data for calculating the airglow volume emission rate and emission layer height. This chapter provides a brief outline of airglow emissions, FPI equipment and operation, FPI data analysis, ISR neutral wind derivation, ISR electron density measurements, volume emission rate calculations, and spline fits.

4.2. AIRGLOW EMISSIONS

Because the FPI is essentially a spectroscopic device, this instrument detects and measures spectral lines. Earth's atmosphere contains many naturally emitting sources at altitudes ranging from 70 km to 800 km. These emitting sources are called airglow. The Earth's airglow results from the re-emission of energy from atmospheric particles following daytime excitation by solar radiation [Bone, 1991]. During the day, the airglow intensity is much smaller than the intensity of the sunlight, hence making it almost impossible to detect. At night, the airglow intensity is too low to monitor with the unaided eye, but this low intensity presents no problem for a spectroscopic instrument such as the FPI. The next three sections highlight the most commonly used airglow emissions in the upper atmosphere.

4.2.1. Hydroxyl (OH)

The OH airglow emission occurs over a relatively narrow region of the mesosphere. The peak emission occurs around 85 km and the thickness of this emitting layer is approximately 10 km. The following chemical reaction is responsible for the OH emission:



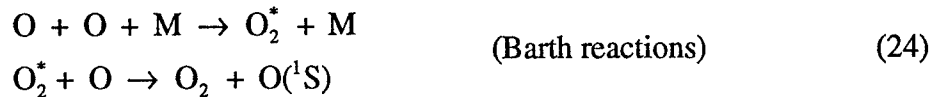
The * indicates that the OH molecule is in the excited state which subsequently emits a photon as it transitions to the ground state. Although OH airglow bands cover a wide range of the electromagnetic spectrum, the infrared OH bands are the strongest emitters. The OH emission intensity ranges from values greater than 100 R at night to approximately 10^5 R during the day (where 1 R = 10^6 photons $\text{cm}^{-2}\text{sec}^{-1}$). The OH emission layer is important since it characterizes the dynamics in the mesosphere.

4.2.2. Monatomic Oxygen, O^{1S} , 557.7 nm

At night, airglow O^{1S} is produced in both the lower E (97 km) and F (230 km) ionospheric regions. The dominant processes that create the O^{1S} emissions are:



and



The * identifies molecules in the excited state and M stands for any third body.

Typical night intensities for the O(¹S) airglow range from 100 R to 200 R. This airglow has a radiative lifetime of 0.7 sec [Jacka, 1984]. The O(¹S) emission line provides a method to study the E and F ionospheric region dynamics.

4.2.3. Monatomic Oxygen , O(¹D), 630.0 nm

Although the O(¹S) airglow emission occurs at altitudes near 250 km, a more commonly used emission for this altitude is the O(¹D) 630.0 nm airglow emission. The dissociative recombination of O₂⁺ and electrons produce the O(¹D) airglow emission. This recombination occurs near 250 km and is described chemically as:



The O(¹D)'s radiative lifetime of 110 sec is much longer than the 0.7 sec radiative lifetime for the O(¹S) emission. The long radiative lifetime and long collision time between F-region particles (0.3 sec) make the O(¹D) emission a suitable choice for wind and kinetic temperature measurements for the upper thermosphere. For the remainder of this thesis, the O(¹D) emission line will be referred to as the 630.0 nm airglow emission.

4.3. FABRY-PEROT INTERFEROMETER

4.3.1. Historical Perspective

The first FPI was developed in 1897 by Charles Fabry and Alfred Perot, although the physical principles behind the FPI were actually developed more than a century prior by Sir Isaac Newton [Hernandez, 1986]. The original intent, as outlined

by Fabry and Perot, was to use the FPI to provide accurate measurements of the standard meter. It was not long, however, before interested parties realized the spectroscopic capabilities of this instrument.

Astronomers were the first scientific group to take advantage of the FPI's high spectral resolution. High spectral resolution is necessary to determine the composition of distant stars. Solar physicists used the instrument to characterize the sun's spectrum and discovered other elements existed in the solar atmosphere in addition to hydrogen and helium.

In 1912, scientists used the FPI to test the kinetic theory of gases. Such tests were instrumental in explaining the Doppler broadening and shift effects [Hernandez, 1986]. Doppler broadening is the temperature broadening of a spectral line emission from a gas compound and Doppler shift is the wavelength shift as a result of the bulk motion of the emitters. Both Doppler broadening and doppler shift are essential when describing the upper atmosphere. Additional uses of the FPI include measurements of viscosity effects in air, the Zeeman effect, the index of refraction of gases, and the isotropic and fine structure investigations [Hernandez, 1986].

The first upper atmospheric wind and temperature FPI measurements were conducted in 1960. Since then, the FPI has routinely been used to measure the winds and temperatures of the mesosphere and thermosphere.

4.3.2. Interferometry

This section outlines the basic principles of interferometry. Optics textbooks

by *Hecht and Zajac* [1979] and *Fowles* [1975] present a more complete description of this subject.

4.3.3. Two-beam and Multiple-beam Interference

All interferometric instruments, including the FPI, are based on the principle of optical interference. A thorough description of optical interference requires quantum mechanical explanations, an endeavor beyond the scope of this study. Fortunately, the theory behind the FPI requires only basic optical principles.

To understand interference, it is helpful to picture a light wave as a sinusoidal wave. Each light wave has a unique amplitude (intensity), wavelength, and relative phase angle. For simplicity, we consider light of only one wavelength (monochromatic light).

If two light waves are directed at the same point in space but travel along different paths, the waves will affect each other's amplitude either constructively or destructively. Because we imposed a monochromatic condition on these light waves, the resultant amplitude from the interference of these two beams is a function of the relative phase angle difference between the two light waves. This type of interference is called two-beam interference.

Two-beam interference occurs for coherent and incoherent light. Incoherent light consists of light waves with different amplitudes and relative phase angles. An example of incoherent light is the scattered light from the earth's atmosphere. This light undergoes a near continuous interference process but it is impossible to observe due to

the different phase angles and the high frequencies (10^{15} Hz). Any light interference in earth's atmosphere occurs too quickly to be detected by human eyes. Coherent light is light whose waves have a constant phase difference. It is easy to observe interference with coherent light because it is possible to find a distance where light interferes and the resultant wave amplitude remains constant. It is coherent light that produces the bright (constructive) and dark (destructive) fringes seen in most interference patterns.

Multiple-beam interference differs from two-beam interference in the number of light waves (or light beams) that interfere. The beams in multiple-beam interference are made up of more than two light waves with constant phase differences and identical wave amplitudes. This type of interference occurs for the transmitted beams from two parallel, semireflective mirrors. These transmitted beams are parallel to each other and theoretically interfere at infinity. To observe this interference, a positive lens is placed in the path of the parallel beams, thus causing the light beams to constructively or destructively interfere at the lens's focal length. It is multiple-beam interference that forms the optical foundation for the FPI.

4.3.4. Basic Optical Principles for the FPI

The most common method of producing a larger number of mutually coherent beams is by division of wave amplitude [Fowles, 1975]. Two parallel, semitransparent mirrors are all that is needed to produce this effect. A light beam with amplitude E_0 incident on the outside mirror surface will be reflected between the two mirrors plates (see Figure 20). Figure 20 shows the resulting parallel transmitted waves (E_{ot}^2 , $E_{ot}^2r^2$,

etc., where t and r are the transmission and reflection coefficients, respectively).

The phase difference between two successive transmitted waves is given by:

$$\delta = \frac{4\pi}{\lambda_0} nd \cos\theta \quad (26)$$

where δ is the phase difference between the two rays, λ_0 is the wavelength of the incident radiation, n is the index of refraction of the medium, d is the mirror separation, and θ is the angle of incidence. Figure 21 shows a detailed look at the successive waves and the geometric factors used in the phase difference calculation. From Figure 21, the path difference between two successive transmitted waves, t , is:

$$t = 2nd \cos\theta \quad (27)$$

The light waves in that emerge from the second mirror are parallel to each other. This situation is similar to the transmitted beams discussed in the previous section. If a

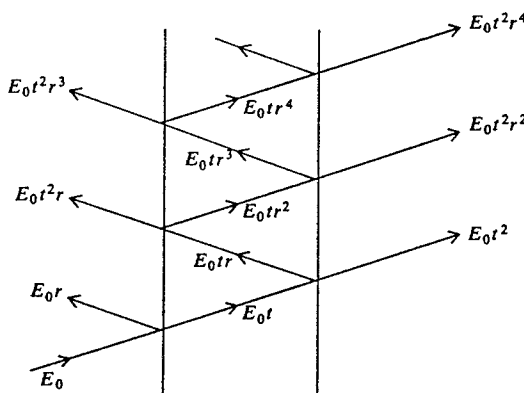


Figure 20. Paths of light rays in multiple reflection between two parallel mirrors [After G. Fowles, 1975, pg. 86. Reproduced with permission of Dover Publications]

positive lens is placed beyond the second mirror, the rays will be brought together at the focal plane of the lens. At this point, enough information has been provided to understand the most basic FPI arrangement (see Figure 22). Figure 22 shows how the focusing lens brings the rays together at a specific point. The etalon in the diagram is identical to the two parallel mirror setup discussed earlier in this study.

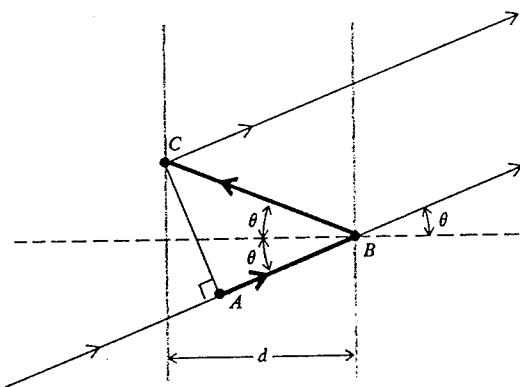


Figure 21. Diagram showing the path difference between two successive rays [After G. Fowles, 1975, pg. 87. Reproduced with permission of Dover Publications]

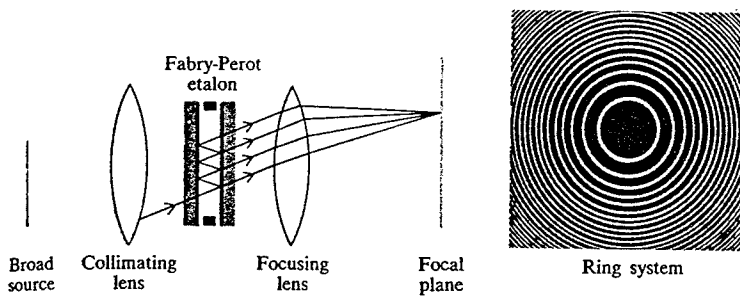


Figure 22. Basic Fabry-Perot arrangement [After G. Fowles, 1975, pg. 91. Reproduced with permission of Dover Publications]

The ring system in Figure 22 is produced when a broad source of light enters the FPI. Since airglow is a broad light source, the incident light enters the FPI over a wide range of angles [Vadnais, 1992]. After the light is transmitted by the etalon, the focusing lens focuses the light at the focal plane where the ring system is formed. Each ring in the ring system represents a different order of interference. The bright rings are created by constructive interference and the dark rings by destructive interference.

At the angle ϕ where a bright ring or fringe is located, the relationship between the wavelength and the mirror (etalon) spacing d is:

$$m\lambda = 2nd \cos\phi \quad (28)$$

where m is an integer identifying the order of interference [Gornall, 1983]. If the light rays interfere on the optical axis ($\phi = 0$), equation (28) reduces to:

$$m\lambda = 2nd \quad (29)$$

An FPI satisfying equation (29) may be tuned to transmit any wavelength by varying the index of refraction n or the mirror spacing d . The index of refraction may be changed by varying the gas pressure between the mirrors. This pressure scanning method was used to collect the Arequipa and Arecibo FPI data used for this study. Today, most FPIs scan by changing the mirror spacing d . The most versatile technique for changing the mirror spacing is using piezoelectric elements. These elements keep the mirrors parallel to one another as the spacing changes [Gornall, 1983].

The intensity of the transmitted waves is an important quantity for FPI measurements. The equation for the intensity of the transmitted rays is:

$$I_t = I_o \left[\left[1 - \frac{A}{1-R} \right]^2 \frac{1}{1 + F \sin^2 \frac{\delta}{2}} \right] \quad (30)$$

where A is the absorptance, R the reflectivity, δ the phase difference, and F the finesse.

The term

$$1 + F \sin^2 \frac{\delta}{2} \quad (31)$$

is known as the Airy function. The finesse F is discussed in the next section.

4.3.4.1. The Meaning of Finesse

Finesse is a measure of the interferometer's ability to resolve closely spaced lines; the higher the finesse the better [Gornall, 1983]. A more conceptual definition of finesse is the number of interfering monochromatic light beams involved in forming the interference fringes. Many factors such as the reflectivity, mirror flatness, and pinhole diameter affect the total instrument finesse value.

The *reflectivity finesse* for a plane mirror interferometer is a function of the mirror reflectivities [Gornall, 1983]. The equation for reflectivity finesse is:

$$F_R = \frac{\pi\sqrt{R}}{1-R} \quad (32)$$

where R is the reflectivity.

No mirror is perfectly flat. A non-flat mirror used in an FPI becomes important when viewing small spectral resolution. The equation for this *flatness finesse* is:

$$F_F = \frac{M}{2} \quad (33)$$

where M is defined as the fractional wavelength deviation from true flatness or parallelism across the mirror aperture [Gornall, 1983].

The net finesse due to flatness and reflectivity is called the *instrumental finesse* and is mathematically defined as:

$$\frac{1}{F_i^2} = \frac{1}{F_R^2} + \frac{1}{F_F^2} \quad (34)$$

When the FPI is used as a spectrometer, the pinhole size determines the degree of collimation of light passing and reaching the detector [Gornall, 1983]. If the pinhole size is too large, many light rays pass through the system. The effect of too many rays entering the FPI detector is to broaden the instrumental line width. This *pinhole finesse* is defined as:

$$F_p = \frac{4\lambda f^2}{D^2 d} \quad (35)$$

where f is the focal length of the second lens and D is the pinhole diameter.

The total *instrumental finesse* for a FPI spectrometer is a function of the reflectivity, flatness, and pinhole finesse. Mathematically the total finesse for the FPI spectrometer is defined as:

$$\frac{1}{F_i^2} = \frac{1}{F_R^2} + \frac{1}{F_F^2} + \frac{1}{F_p^2} \quad (36)$$

4.3.4.2. Throughput and Etendue

The strength of the FPI over other interferometers is its "etendue" or light

gathering power [Gornall, 1983]. For the ideal case of small aperture and flat parallel mirrors, the transmission on the peak of a fringe is:

$$T_{\max} = \left(1 - \frac{A}{1-R}\right)^2 \quad (37)$$

where A is the absorption due to the mirrors. This maximum transmission results when the phase difference, δ , is a multiple of 2π . The etendue for the FPI is mathematically defined as:

$$U = \Omega \cdot A_m = \frac{\pi D^2 \lambda}{4dF_i} \quad (38)$$

where λ is the incident wavelength, Ω is the solid angle subtended at a mirror aperture A_m , D is the pinhole diameter, d is the distance between the mirrors, and F_i is the instrument finesse.

4.3.4.3. Etalon

A glass plate with optically flat and parallel surfaces separated by a fixed distance is the simplest form of Fabry-Perot and is called an etalon [Higgins, 1987]. A light ray incident to the first parallel surface will undergo many reflections between the two parallel mirror surfaces. If the light is coherent, constructive and destructive interference will occur between the reflected and transmitted portions of the beam [Higgins, 1987].

4.3.5. FPI Equipment Description

This section provides a basic understanding of the Arequipa and Arecibo FPIs.

We do not intend to provide a detailed description of the FPI equipment and operation, but we want to provide enough information to understand how the FPI measures the upper atmospheric winds.

High-resolution determinations of the center frequency of the oxygen line emission of 630.0 nm with reference to the center frequency in zenith observations (averaged over a night of vertical measurements) give a direct indication of the component of thermospheric flow in the observing direction [*Meriwether et al.*, 1986].

4.3.5.1. Arequipa FPI

A detailed description of the Arequipa FPI is provided in *Biondi et al.* [1990 and 1991] and *Meriwether et al.* [1986]. The Arequipa measurements were made at the Arequipa Automated Airglow Observatory (16.5°S , 71.5°W , 3.2°S dip latitude) in Peru. The Arequipa observatory is located ~ 450 km south of Jicamarca, Peru.

A refractive-index-tuned, field-widened FPI of 94-mm clear aperture and 2×10^{-3} nm resolution is used to determine the Doppler shifts in the nightglow line emissions over Arequipa. The complete FPI system consists of the optical instrument and a companion tilting filter photometer.

The wind measurements are taken along the cardinal azimuths at 30° elevation and in the zenith, with the average 630.0 nm line position looking vertically used to define the zero velocity reference for the eastward and northward wind component determination. Measurements of the 632.8 nm line from a stabilized He-Ne laser are used to determine the free spectral range and overall finesse of the FPI, as well as any

instrument drifts [Biondi *et al.*, 1990]. The spectral profile of the source emission was scanned by changing the index of refraction of the medium (argon gas) between the plates by compressing or expanding the argon with a computer-controlled piston housed in a sealed cylinder [Meriwether *et al.*, 1986].

The observations and calculations indicate that the typical airglow emission is broad (> 50 km between the half-intensity points) and that the altitude of peak emission varies between ~ 250 km and ~ 325 km, depending of the time of night, season, and part of the solar cycle. It is assumed that the 630.0 nm winds do not change appreciably in magnitude and direction over this altitude range.

4.3.5.2. Arecibo FPI

The Arecibo FPI is a pressure-scanned FPI with a 15-cm diameter etalon situated near the town of Arecibo, Puerto Rico (18°N , 67°W , 50° dip latitude). The pressure of the argon gas in the system is controlled by a piston that is stepped to various positions under computer control. The field of view of the FPI is $1/2^{\circ}$. The aperture size is 6.3 mm, a size which reduces the overall instrument finesse to about 10. A 50-mm diameter interference filter with a bandwidth of .5 nm was used to restrict transmission to some 25 orders near 630.0 nm. The etalon spacing was 10 mm, minimizing the contamination of OH emissions.

At Arecibo, FPI measurements are made at eight equally spaced azimuth positions with a constant zenith angle of 60° . In analyzing the data, it is assumed that the spatial variation of the neutral wind velocity is linear across the region that is

observed. The eight independent measurements allow calculations of the deformation of the flow, the mean velocity, and the divergence.

Because the mean overhead neutral wind velocity is determined by observing the airglow from eight emitting regions, each located some 500 km from the station, systematic errors are possible unless a number of conditions hold. These conditions are the horizontal gradient in wind velocity is constant across the observing region, the height of the emitting layer is the same everywhere, and the neutral wind does not vary with altitude.

4.3.6. FPI Measured Winds

The next two sections present the Arequipa and Arecibo data measurements.

4.3.6.1. Arequipa

TABLES 4 and 5 show a breakdown of the Arequipa eastward measured FPI data in terms of 10.7-cm solar flux (Φ) and magnetic activity (given by the K_p index). The total data points and the percentage of the total are given for each 25-unit solar flux increment. TABLE 4 shows that the 1988-1989 data are characterized by moderate to high solar activity. Although the northward data are not shown, these data show similar total and percentage of the total values.

TABLE 5 shows the total eastward measured FPI data points for a given K_p interval and a given 3-hour period. This table shows the majority of data were collected during quiet and moderate magnetic activity ($K_p < 3^+$).

Figure 23 shows the 15-day (1/2 month) distribution for the measured Arequipa

TABLE 4. Solar Flux Histogram of 1988-1989 Arequipa Neutral Wind Data
 Total Number of Wind Profiles: 474

Part (a)

Solar Flux	< 100	$100 \leq \Phi < 125$	$125 \leq \Phi < 150$
Total	0	50	68
Percentage of	0.0	10.5	14.3
Total (%)			

Part (b)

Solar Flux	$150 \leq \Phi < 175$	$175 \leq \Phi < 200$	$\Phi \geq 200$
Total	106	120	130
Percentage of	22.4	25.3	27.4
Total (%)			

TABLE 5. Magnetic Activity (K_p) Histogram of 1988-1989 Arequipa Neutral Wind Data

Part(a)

Hour (LT)	$0 \leq K_p < 1$	$1 \leq K_p < 2$	$2 \leq K_p < 3$	$3 \leq K_p < 4$
< 21	68	201	181	91
21-00	153	497	619	310
00-03	165	452	688	264
03-06	65	226	241	76

Part(b)

Hour (LT)	$4 \leq K_p < 5$	$5 \leq K_p < 6$	$6 \leq K_p < 7$	$K_p \geq 7$
< 21	63	11	0	13
21-00	145	36	28	3
00-03	155	52	13	4
03-06	49	16	0	3

data. This graph shows the majority of Arequipa data were collected during the May-August months; hence, the winter solstice is well represented. The least amount of data was collected during the November-February months (summer solstice). The northward 15-day distribution is not shown but is similar to the results shown in Figure 23.

4.3.6.2. Arecibo

TABLES 6 and 7 show a breakdown of the Arecibo eastward measured FPI data in terms of 10.7-cm solar flux and magnetic activity. TABLE 6 shows the Arecibo data are represented for low, moderate, and high solar flux activity. TABLE 7 shows the majority of the data were collected for quiet magnetic activity ($K_p < 3$).

The 15-day distribution for the measured Arecibo data is presented in Figure 24. This graph shows the majority of Arecibo data were collected during May-August. Unlike the Arequipa data, the Arecibo data show a wide monthly distribution allowing a more complete seasonal average study. The northward 15-day Arecibo distribution is not shown but is similar to the results shown in Figure 24.

4.3.7. FPI Data Analysis

Seasonal averages of the nightly variations in the eastward and northward winds have been obtained from the measurements by taking all the data points for a given season for a selected 10.7-cm solar flux and magnetic activity intervals, sorting them into 30-minute bins, and averaging the number of data points, n , in each bin to obtain the sample mean value, $v_{mean} = (\sum v_i) / n$. The variability in the measurements

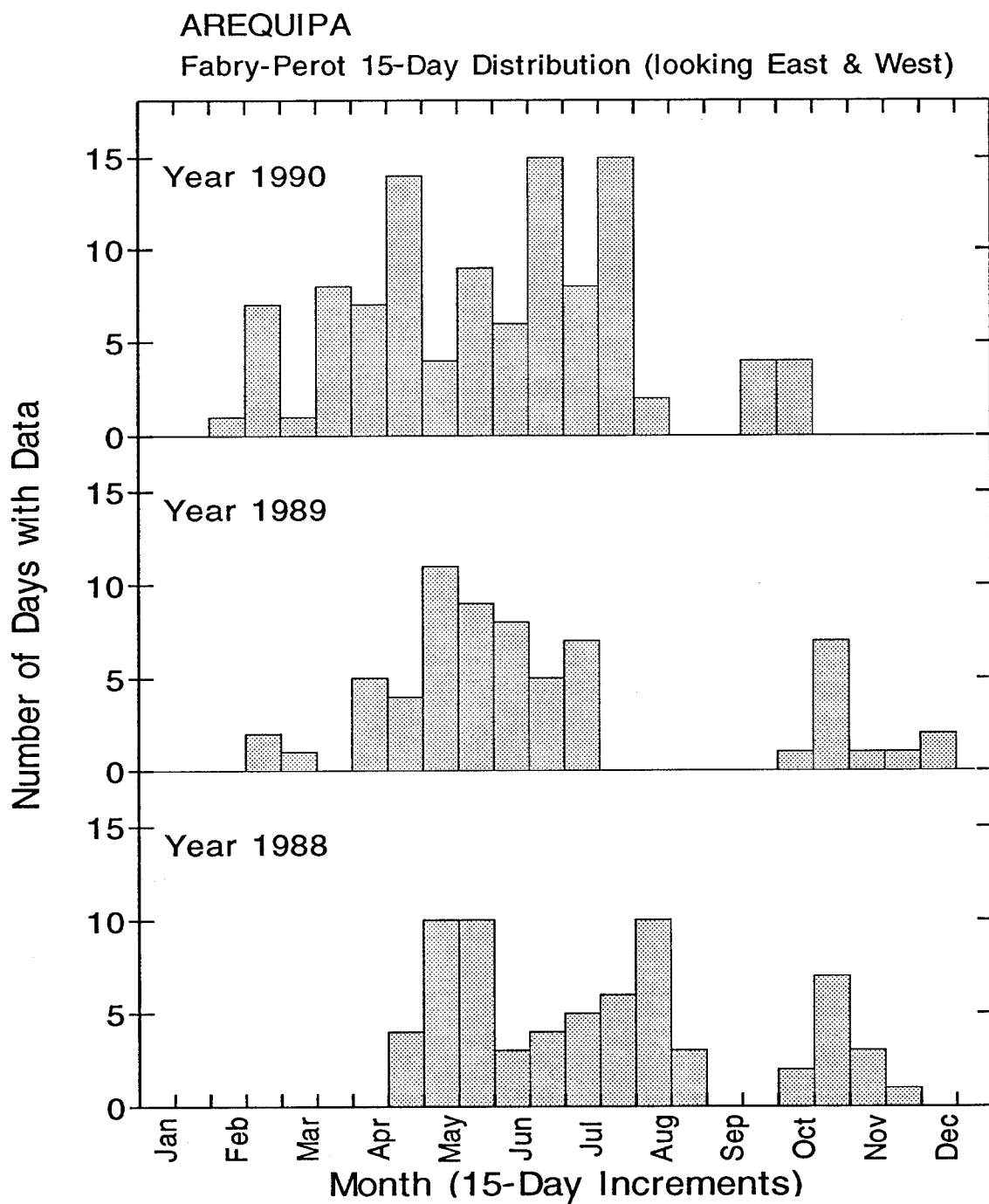


Figure 23. Frequency distribution of Arequipa data collection. The time interval is 15-day (1/2 month) increments.

TABLE 6. Solar Flux Histogram of 1981-1989 Arecibo Neutral Wind Data
Total Number of Wind Profiles: 202

Part (a)

Solar Flux	< 100	$100 \leq \Phi < 125$	$125 \leq \Phi < 150$
Total	64	17	29
Percentage of	31.7	8.4	14.4
Total (%)			

Part (b)

Solar Flux	$150 \leq \Phi < 175$	$175 \leq \Phi < 200$	$\Phi \geq 200$
Total	33	32	27
Percentage of	16.3	15.8	13.4
Total (%)			

TABLE 7. Magnetic Activity (K_p) Histogram of 1981-1989 Arecibo Neutral Wind Data

Part (a)

Hour (LT)	$0 \leq K_p < 1$	$1 \leq K_p < 2$	$2 \leq K_p < 3$	$3 \leq K_p < 4$
< 21	50	104	148	71
21-00	139	250	365	195
00-03	146	368	327	159
03-06	137	284	259	70

Part (b)

Hour (LT)	$4 \leq K_p < 5$	$5 \leq K_p < 6$	$6 \leq K_p < 7$	$K_p \geq 7$
< 21	32	7	3	2
21-00	72	17	6	7
00-03	92	17	9	8
03-06	55	34	4	0

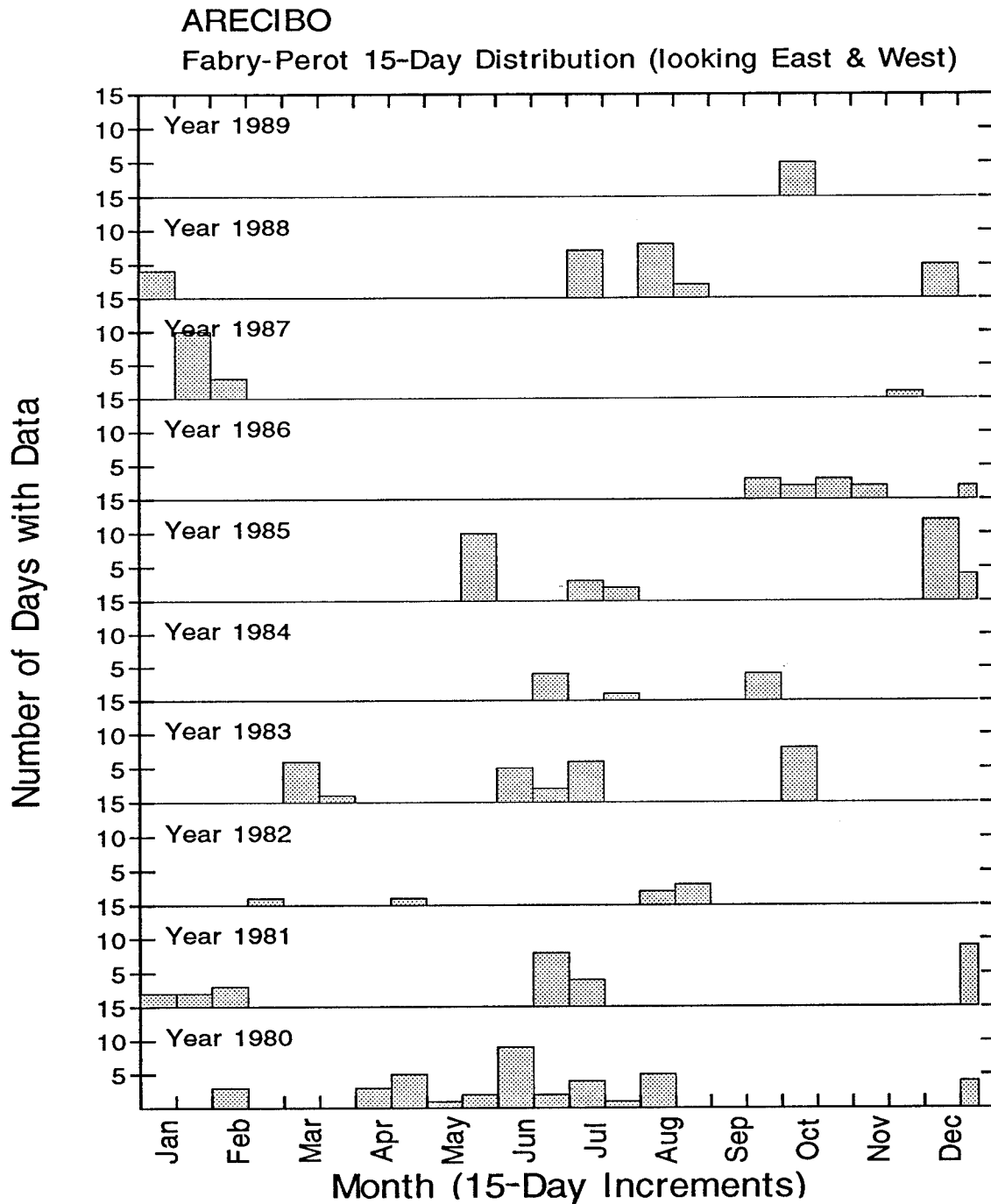


Figure 24. Frequency distribution of Arecibo data collection. The time interval is 15-day (1/2 month) increments.

for each 30-minute bin is determined by the sample mean standard deviation, s , of the data from its mean. The quantity s is given by

$$s = \left[\left(\sum (v_i - v_{mean})^2 \right) / n \right]^{1/2} \quad (39)$$

For our study, we analyze eastward and northward wind using graphs like those in Figures 25 and 26. These plots are separated into three parts: the bottom plot shows the scatter profiles of each night's wind observations, the top histogram indicates the number of points in each 30-minute time bin, and the middle are the sample mean wind component values at 30-minute intervals (open circles) and the ± 1 standard deviations from the means (error bars). The middle plot also shows the 10.7-cm solar flux and the magnetic activity intervals, the representative day for the season, and the mean solar flux ($\overline{\Phi}$) and magnetic activity ($\overline{K_p}$) values.

Figure 25, the May-August eastward wind over Arequipa, shows large standard deviations ($\sim \pm 75$ m/s - 100 m/s). We use a statistical analysis technique outlined in *Biondi et al. [1991]* to show that we can apply a reasonable confidence limits in spite of the large nightly wind variation. Figure 27 shows the northward and eastward data for the given time, solar flux, and magnetic activity conditions follow the form of a normal distribution. Because the data follow a normal distribution, we can apply the usual confidence limit analysis to provide us a more quantitative assessment in the average wind profile. TABLE 8 shows the results of applying the 95% confidence limits to the data in Figure 25. TABLE 8 shows the small lower and upper boundaries of the confidence interval, which provides us more confidence in the average wind profile for Arequipa.

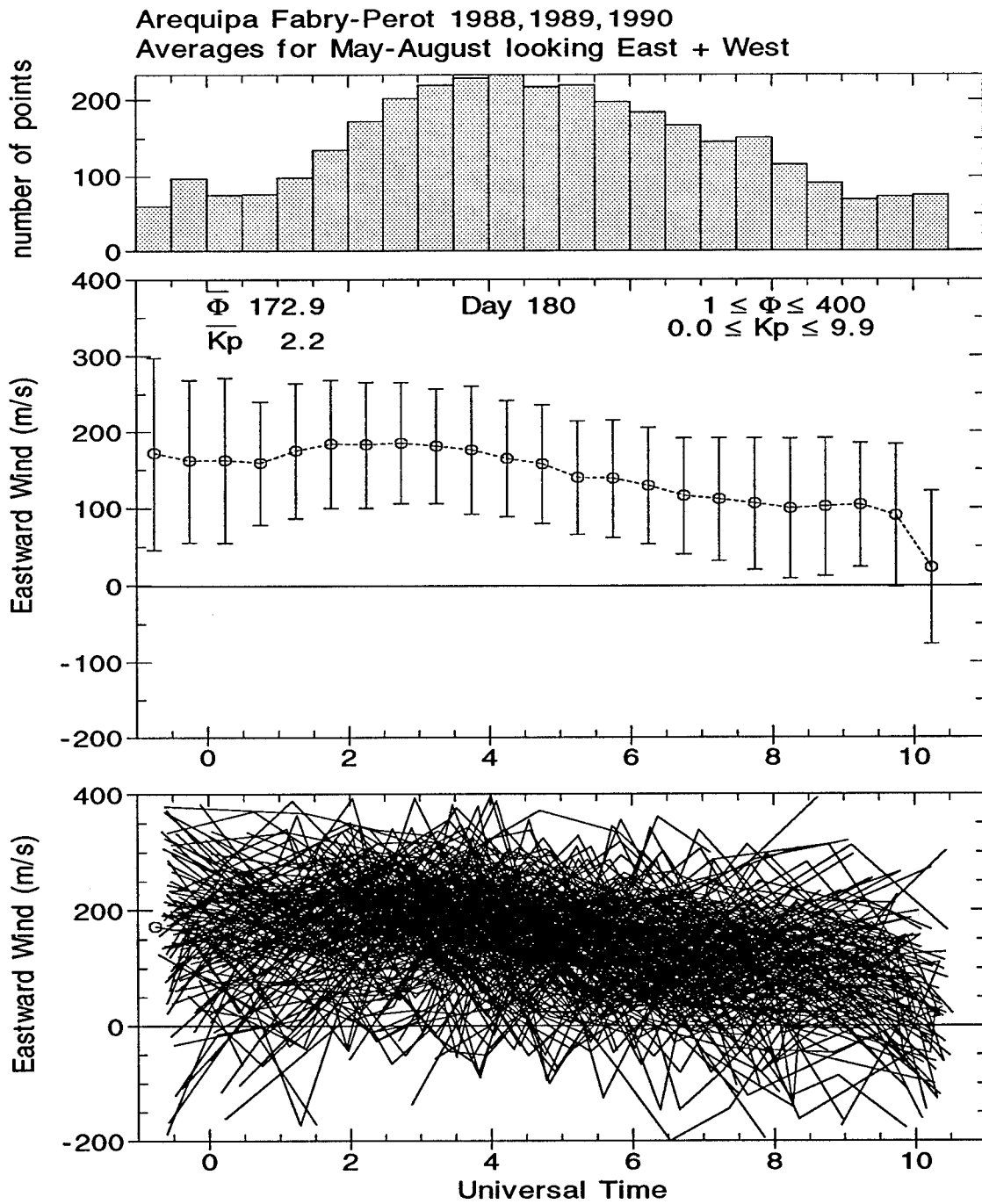


Figure 25. May-August eastward average of the thermospheric wind over Arequipa. The top plot is the number of data points in each 30 min interval, the middle plot is the mean values of the wind component (points) and the ± 1 standard deviation (vertical bars), and the bottom is the scatter plots of the eastward wind for the given solar flux and magnetic activity intervals.

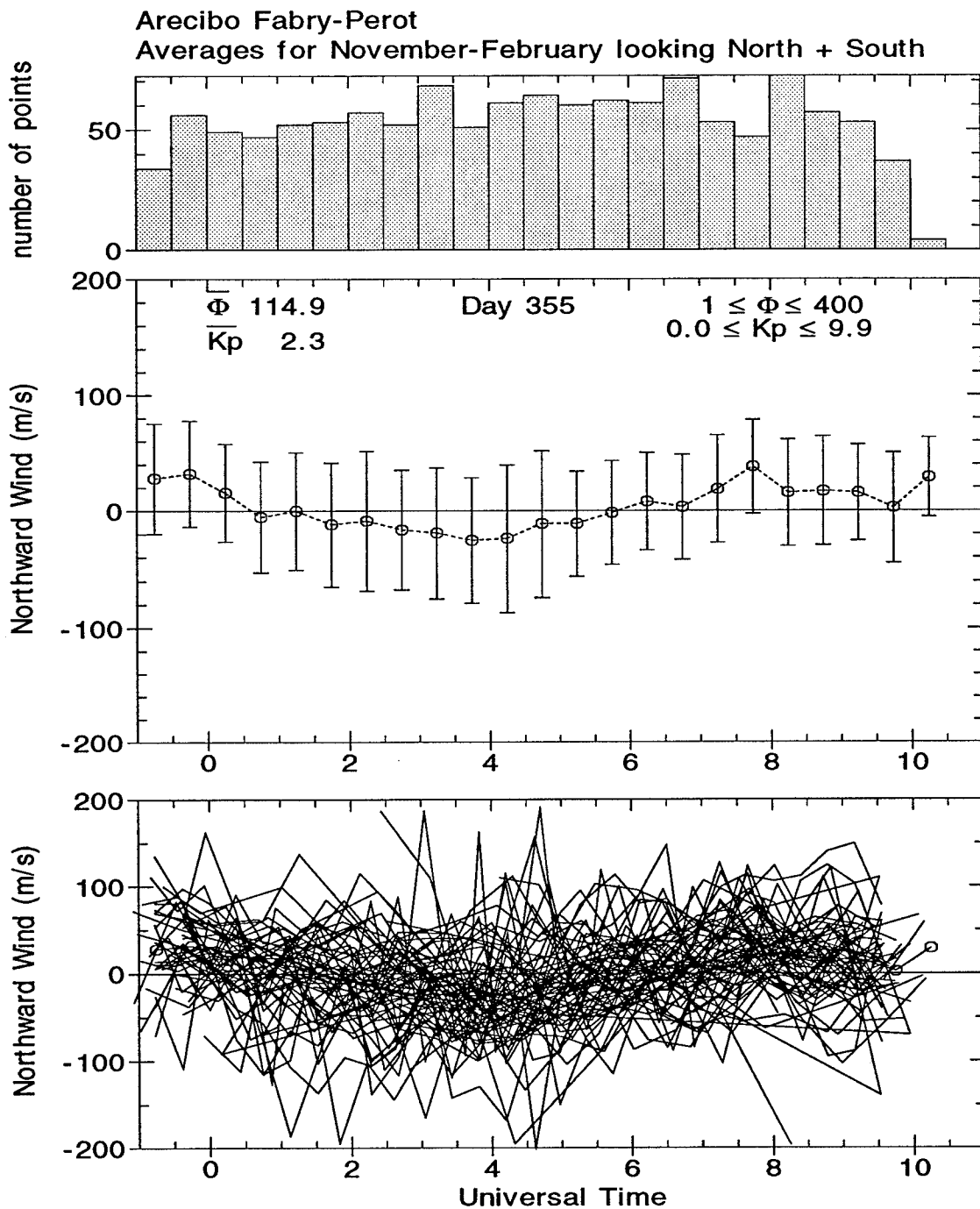


Figure 26. November-February northward average of the thermospheric wind over Arecibo. The top plot is the number of data points in each 30 min interval, the middle plot is the mean values of the wind component (points) and the ± 1 standard deviation (vertical bars), and the bottom is the scatter plots of the eastward wind for the given solar flux and magnetic activity intervals.

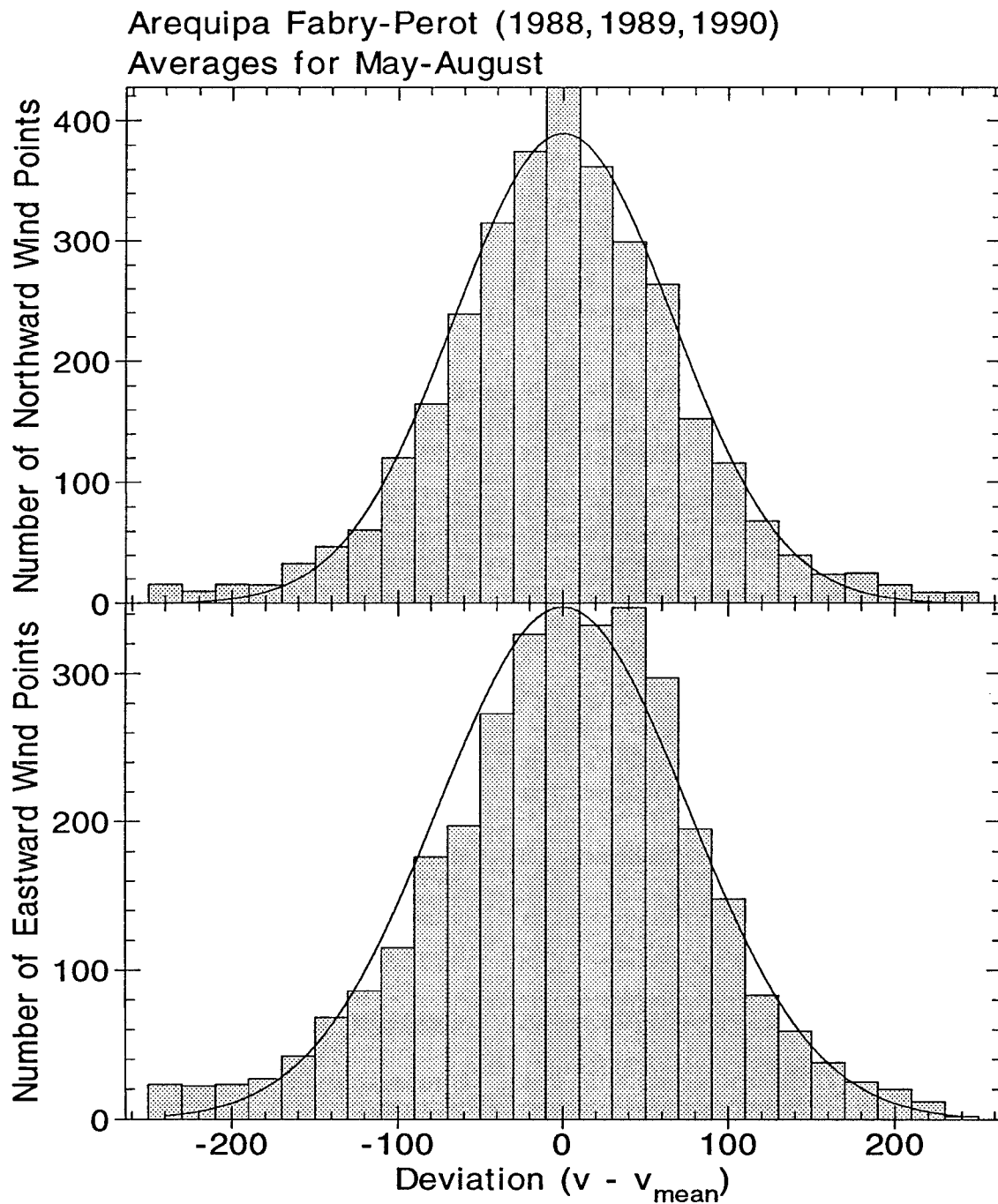


Figure 27. May-August frequency distribution bar graphs of the deviation of the wind values in each bin from their mean ($v - v_{\text{mean}}$), for Arequipa. The smooth curves are the least-squares fits to the data of normal distributions centered at $(v - v_{\text{mean}}) = 0$.

TABLE 8. 95% Confidence Intervals for the May-August Eastward Winds over Arequipa, Peru.

Time (UT)	v_{mean} (m/s)	Standard Deviation (m/s)	Number of Points	95% confidence lower boundary (m/s)	95% confidence upper boundary (m/s)
-0.75	172.1	125.8	60	140.2	203.9
-0.25	162.1	106.7	97	140.8	183.3
0.25	162.8	108.3	75	138.3	187.3
0.75	159.1	80.7	76	141.0	177.3
1.25	175.5	88.7	98	157.9	193.0
1.75	184.4	84.3	135	170.2	198.6
2.25	183.1	82.7	172	170.8	195.5
2.75	185.4	79.7	202	174.4	196.4
3.25	181.4	75.5	219	171.4	191.4
3.75	176.1	84.1	228	165.2	187.1
4.25	164.8	76.2	232	155.0	174.6
4.75	157.8	77.6	217	147.5	168.1
5.25	139.9	74.1	219	130.1	149.7
5.75	138.6	76.9	197	127.8	149.3
6.25	129.5	76.5	184	118.4	140.5
6.75	116.2	75.8	167	104.7	127.7
7.25	111.8	80.1	145	98.7	124.8
7.75	106.2	85.7	151	92.6	119.9
8.25	99.8	90.9	115	83.2	116.4
8.75	102.0	89.7	91	83.6	120.4
9.25	104.7	80.8	69	85.7	123.8
9.75	90.9	93.0	73	69.5	112.2
10.25	23.1	99.2	75	0.6	45.5

We did not conduct a similar analysis for Arecibo since the Arecibo standard deviations about the mean are small compared to those of Arequipa.

4.4. ISR NEUTRAL WIND MEASUREMENTS

In addition to using FPI measured winds, we use neutral winds derived from the ISR at Arecibo. These ISR winds provide us additional data for comparing with the FPI measured meridional winds over Arecibo. We can compare directly the ISR-derived neutral winds to the meridional FPI measured winds since the magnetic declination at Arecibo is less than 10° .

4.4.1. ISR Neutral Winds

The determination of the meridional neutral wind velocity along the geomagnetic meridian from ISR data is a well understood technique [e.g., *Harper, 1973; Salah and Holt, 1974; Burnside et al., 1983, 1991; Wickwar et al., 1984*]. For our study, we use the Arecibo ISR-derived neutral winds from 1983 to 1987. A complete description of the ISR neutral wind derivation at Arecibo is outlined in *Burnside et al. [1983]*. In this section, we present a brief description of the steps used to calculate the neutral wind from the Arecibo ISR data.

Data are obtained by the Arecibo 430 MHz ISR in a continuous beamswinging mode with a fixed zenith angle of 15° . Calculations for the F-layer parameters are obtained every 16 minutes (the time it takes to complete one rotation of the feed). Line-of-sight plasma velocities are derived from the imaginary part of the autocorrelation function. Next, a harmonic analysis is performed on the line-of-sight ion

velocities to get the horizontal components. For these calculations, it is assumed that spatial and temporal gradients in the ion velocity are small enough to be neglected.

In the direction of geomagnetic south, the neutral wind velocity is given by *Burnside et al.* [1983]

$$U_x = (v_{\parallel} - v_d) \sec I \quad (40)$$

where v_{\parallel} is the ion velocity antiparallel to the magnetic field, v_d is the O⁺ diffusion velocity, and I is the magnetic inclination angle ($\sim 50^\circ$). The diffusion velocity of O⁺ in the neutral atmosphere was derived by *Schunk and Walker* [1970] and is given by

$$v_d = -D_a \sin I \left[\frac{1}{H_p} + \frac{1}{N} \frac{dN}{dz} + \frac{1}{T_p} \frac{dT_p}{dz} + \frac{w}{T_r} \frac{dT_r}{dz} \right] \quad (41)$$

where N is the electron density, $H_p = 2kT_p / mg$ is the plasma scale height, $T_p = (T_i + T_e) / 2$, $T_r = (T_i + T_n) / 2$, T_n is the neutral temperature, and w is a thermal diffusion factor with a value of 0.37. The parameter m is the ion mass (16 amu), and g is the acceleration due to gravity. The ambipolar diffusion coefficient, D_a , is given by *Schunk and Walker* [1970]

$$D_a = \frac{3.02 \times 10^{17} T_n^{1/2}}{\alpha [O] + 19.9 [N_2] T_n^{-1/2}} \quad (42)$$

where

$$\alpha = 1.08 - 0.14 \log_{10} T_n + 0.0045 (\log_{10} T_n)^2 \quad (43)$$

The ISR measurements of v_{\parallel} are obtained every 38 km and the determination of v_d require knowledge of the plasma scale height and the vertical gradient in electron density, which is obtained from the 600-m height resolution Barker code measurements

at Arecibo [Burnside *et al.*, 1991]. Except for the ambipolar diffusion coefficient, D_a , each of the five terms in equation (41) for v_d is obtained by ISR measurements. Measurements of atomic oxygen [O] and nitrogen [N₂] are found from the MSIS model. These concentrations are used for calculating D_a in equation (42).

4.4.2. ISR Measured Data

The Arecibo ISR data used in this research were obtained from the National Center for Atmospheric Research (NCAR) Coupling, Energetics, and Dynamics of the Atmospheric Regions (CEDAR) database. The CEDAR database is located at the NCAR facility in Boulder, Colorado. For our study, we use collected data from 1983 to 1987; hence, this data characterize the neutral wind during low solar activity. TABLES 9 and 10 show the breakdown of this ISR data in terms of solar activity and magnetic activity. Figure 28 shows an example of the ISR neutral wind graphs used for our study.

4.5. ELECTRON DENSITY DATA

We use Jicamarca, Peru and Arecibo measured ISR electron density profiles for calculating the airglow emission heights over Arequipa and Arecibo, respectively. Jicamarca is 450 km north of Arequipa; hence the measurements over Jicamarca are also representative of the conditions over Arequipa. The electron density profiles were obtained from the CEDAR database. TABLES 11 and 12 show the breakdown of the solar flux and magnetic activity for Jicamarca and TABLES 13 and 14 show the breakdown for the Arecibo electron density data.

TABLE 9. Solar Flux Histogram of 1983-1987 ISR Neutral Wind Data
 Total Number of Data Points: 100

Part (a)

Solar Flux	> 100	$100 \leq \Phi < 125$	$125 \leq \Phi < 150$
Total	59	22	19
Percentage of Total (%)	59	22	19

Part (b)

Solar Flux	$150 \leq \Phi < 175$	$175 \leq \Phi < 200$	$\Phi \geq 200$
Total	0	0	0
Percentage of Total (%)	0	0	0

TABLE 10. Magnetic Activity (K_p) Histogram of 1983-1987 ISR Neutral Wind Data

Part (a)

Hour (LT)	$0 \leq K_p < 1$	$1 \leq K_p < 2$	$2 \leq K_p < 3$	$3 \leq K_p < 4$
00-04	686	1904	2689	1982
04-08	860	2171	2282	2667
08-12	968	2079	2842	2031
12-16	943	2308	3425	2481
16-20	1650	2181	4740	3437
20-00	945	1652	3113	2387

Part (b)

Hour (LT)	$4 \leq K_p < 5$	$5 \leq K_p < 6$	$6 \leq K_p < 7$	$K_p \geq 7$
00-04	809	566	95	0
04-08	553	92	331	0
08-12	884	379	0	0
12-16	1053	122	0	0
16-20	1392	464	0	149
20-00	1748	442	65	0

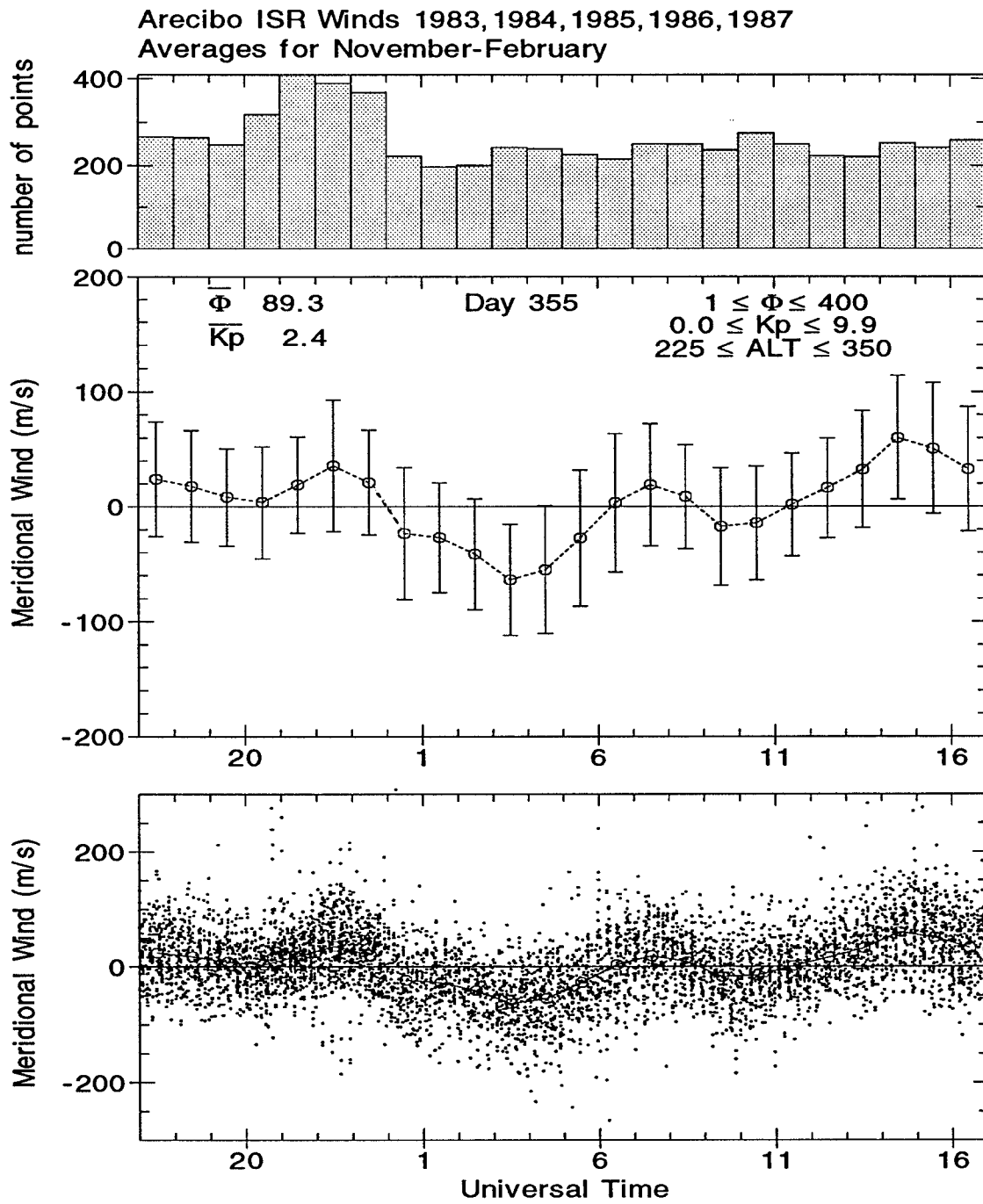


Figure 28. November-February northward average of the ISR calculated neutral wind over Arecibo. The top plot is the number of data points in each 1 hr interval, the middle plot is the mean values of the wind component (points) and the ± 1 standard deviation (vertical bars), and the bottom is the scatter plots of the eastward wind for the given solar flux, magnetic activity, and altitude intervals.

TABLE 11. Solar Flux Histogram of 1966-1969, 1984, 1988, and 1991 Jicamarca Electron Density

Part (a)

Solar Flux	> 100	$100 \leq \Phi < 125$	$125 \leq \Phi < 150$
Percentage of Total (%)	1.5	8.3	52.8

Part (b)

Solar Flux	$150 \leq \Phi < 175$	$175 \leq \Phi < 200$	$\Phi \geq 200$
Percentage of Total (%)	23.1	8.7	5.6

TABLE 12. Magnetic Activity (K_p) Histogram of Jicamarca Electron Density Data Percentage of Total

Part (a)

Hour (LT)	$0 \leq K_p < 1$	$1 \leq K_p < 2$	$2 \leq K_p < 3$	$3 \leq K_p < 4$
00-04	20.3	26.0	23.9	20.1
04-08	18.0	24.0	27.0	18.6
08-12	18.1	28.4	18.8	17.3
12-16	15.6	29.7	25.3	11.1
16-20	15.9	28.5	26.6	12.7
20-00	16.3	24.8	25.4	21.1

Part (b)

Hour (LT)	$4 \leq K_p < 5$	$5 \leq K_p < 6$	$6 \leq K_p < 7$	$K_p \geq 7$
00-04	8.5	1.0	0.2	0.0
04-08	8.4	2.5	1.1	0.4
08-12	8.8	4.9	2.2	1.4
12-16	11.9	2.7	1.6	2.0
16-20	10.0	3.6	1.5	1.2
20-00	8.6	1.9	1.1	0.7

TABLE 13. Solar Flux Histogram of 1981-1989 Arecibo Electron Density

Part (a)

Solar Flux	> 100	$100 \leq \Phi < 125$	$125 \leq \Phi < 150$
Percentage of Total (%)	40.3	12.5	14.7

Part (b)

Solar Flux	$150 \leq \Phi < 175$	$175 \leq \Phi < 200$	$\Phi \geq 200$
Percentage of Total (%)	11.2	6.8	14.4

TABLE 14. Magnetic Activity (K_p) Histogram of Arecibo Electron Density Data
Percentage of Total

Part (a)

Hour (LT)	$0 \leq K_p < 1$	$1 \leq K_p < 2$	$2 \leq K_p < 3$	$3 \leq K_p < 4$
00-04	9.1	27.7	29.2	19.7
04-08	12.1	28.7	26.9	22.2
08-12	12.0	24.6	32.7	19.0
12-16	11.7	25.9	30.5	17.9
16-20	12.3	19.0	31.6	20.4
20-00	10.8	19.0	28.8	23.1

Part (b)

Hour (LT)	$4 \leq K_p < 5$	$5 \leq K_p < 6$	$6 \leq K_p < 7$	$K_p \geq 7$
00-04	9.1	4.3	0.9	0.1
04-08	6.9	1.6	1.6	0.0
08-12	8.7	1.9	0.7	0.4
12-16	10.6	1.7	1.3	0.4
16-20	11.9	2.4	1.8	0.6
20-00	12.4	4.3	1.1	0.6

4.5.1. Airglow Emissions and Heights

The ionosphere-thermosphere is home to several important chemical reactions. For this study, we focus our attention on the dissociative recombination of O_2^+ . This reaction plays a fundamental role in the generation of two of the most important emission lines widely used for FPI studies, that is, the 557.7 nm and 630.0 nm emissions [Sobral *et al.*, 1993]. The dissociative recombination of O_2^+ is the main source of the atomic oxygen excited species $O(^1D)$ and $O(^1S)$ in the nocturnal F-region [Sobral *et al.*, 1993]. The equations and formulas used to calculate the volume emission rates are found in *Link and Cogger* [1988].

4.5.2. Calculating the Volume Emission Rate

TABLE 15 lists the chemical reactions and their associated rate coefficients used in determining the 630.0 nm emission rate. The rate coefficient or rate of reaction is defined as the decrease in concentration of a reactant or the increase in concentration of a product in a unit time. The electron, ion, and neutral temperatures are given by the symbols T_e , T_i , and T_n , respectively. Last, $\tau_e = T_e / 300$ and $\tau_i = T_i / 300$.

The 630.0 nm volume emission rate is given by the following formula:

$$V_{630.0\text{nm}} = \frac{0.76\beta_1 k_1 [O^+] [O_2]}{1 + (k_3[N_2] + k_4[O_2] + k_5[e]) / A_{l_b}} \quad (44)$$

where $\beta_1 = 1.1$ and $A_{l_b} = 7.45 \times 10^{-3} \text{s}^{-1}$.

The Jicamarca and Arecibo electron density profiles have a 38-km height resolution. To compensate for the large 38-km resolution, we used a numerical

TABLE 15. Volume Emission Rate Parameters

Reaction	Rate Coefficient, ($\text{cm}^{-3} \text{s}^{-1}$)	References
$\text{O}^+ + \text{O}_2 \rightarrow \text{O}_2^+ + \text{O}$	$k_1 = 3.23 \times 10^{-12} e^{(3.72/\tau_i - 1.87/\tau_i^2)}$	Chen et al. [1978]
$\text{O}^1\text{D} + \text{N}_2 \rightarrow \text{O}^3\text{P} + \text{N}_2$	$k_3 = 2.0 \times 10^{-11} e^{111.8/T_e}$	Streit et al. [1976]
$\text{O}^1\text{D} + \text{O}_2 \rightarrow \text{O}^3\text{P} + \text{O}_2$	$k_4 = 2.9 \times 10^{-11} e^{67.5/T_e}$	Streit et al. [1976]
$\text{O}^1\text{D} + \text{e} \rightarrow \text{O}^3\text{P} + \text{e}$	$k_5 = 1.6 \times 10^{-12} T_e^{0.91}$	Berrington and Burke [1981]

technique to fit the known electron density data points to a 5th degree polynomial. The numerical method, least-squares fitting of discrete points, is described in detail in *Hornbeck* [1983]. After obtaining the 5th degree polynomial, we impose a minimum altitude boundary of 170 km, a maximum altitude boundary of 530 km, and a 5 km altitude increment. Figure 29 shows the polynomial fit (dashed line) and the average (solid line) electron density profile. Once the electron density profile is determined by the polynomial, we calculate the volume emission rate.

As indicated in equation (44), we must determine the concentration of O^+ , O_2 , and N_2 before calculating the 630.0-nm volume emission rate. We obtain the O^+ from the electron density profile and the neutral concentrations from the MSISE90 model. The details and description of this model are outlined in *Hedin* [1991]. The required inputs for the MSISE90 model are the solar flux and the magnetic activity given by the A_p index. For these inputs, we enter the average solar flux and the A_p index provided of the electron density data for a given solar activity and magnetic activity interval.

The time interval for the data analysis is ± 15 minutes either side of a given hour (e.g., we use the data within ± 15 minutes of 0100 LT to determine the average electron density profile for 0100 LT).

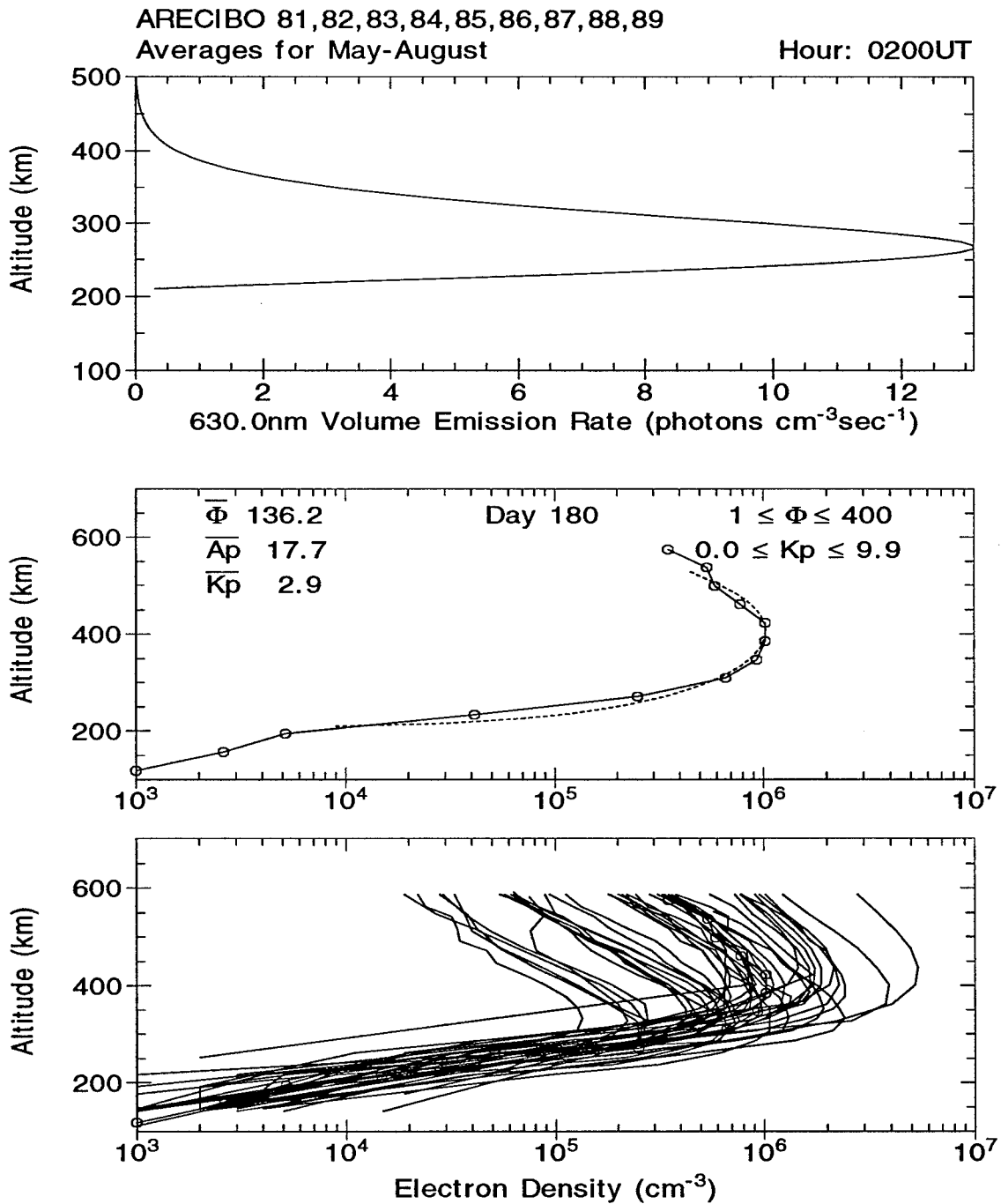


Figure 29. May-August calculated 630.0 nm volume emission rate over Arecibo. The top plot is calculated volume emission rate, the middle plots are the mean electron density profile (solid line) and the modeled electron density profile (dashed line), and the bottom is the scatter plots of the eastward wind for the given solar flux and magnetic activity intervals.

4.5.3 F-Layer Height and Airglow Emission Height

Using the electron density profiles measured at Arecibo and Jicamarca, MSISE90 empirical model predictions, and rate coefficients and formulas defined in *Link and Cogger* [1988 and 1989], we calculate the volume emission rates. These volume emission rates will provide us the airglow emission height or the height at which the FPI measures the thermospheric winds. Since we are interested in establishing the climatological season average, we calculate the airglow emission heights for all seasons, high and low solar activity, and quiet and disturbed magnetic activity.

4.5.3.1. Arecibo F-Layer and Airglow Emission Heights

As described in section 4.5.3, we use the Arecibo electron density profiles collected during January 1981 to November 1989 for our study. This data set covers both high and low solar activity and quiet and disturbed magnetic activity effects. Figures 30 and 26 show the solar cycle and magnetic activity effects on the F-layer peak (H_{MAX}) and airglow emission height ($h_{\eta MAX}$) for all seasons.

The solar activity effects (see Figure 30) were separated for high ($\Phi \geq 120$) and low ($\Phi \leq 120$) conditions for quiet magnetic activity ($K_p \leq 3$) for the winter solstice (November-February), equinox (March-April, September-October), and summer solstice (May-August).

For the winter solstice, we note $h_{\eta MAX}$ is ~ 260 km and 235 km through the night for high and low solar activity, respectively. The H_{MAX} is ~ 75 km and 85 km higher than $h_{\eta MAX}$ for the pre- and postmidnight periods for high flux conditions while

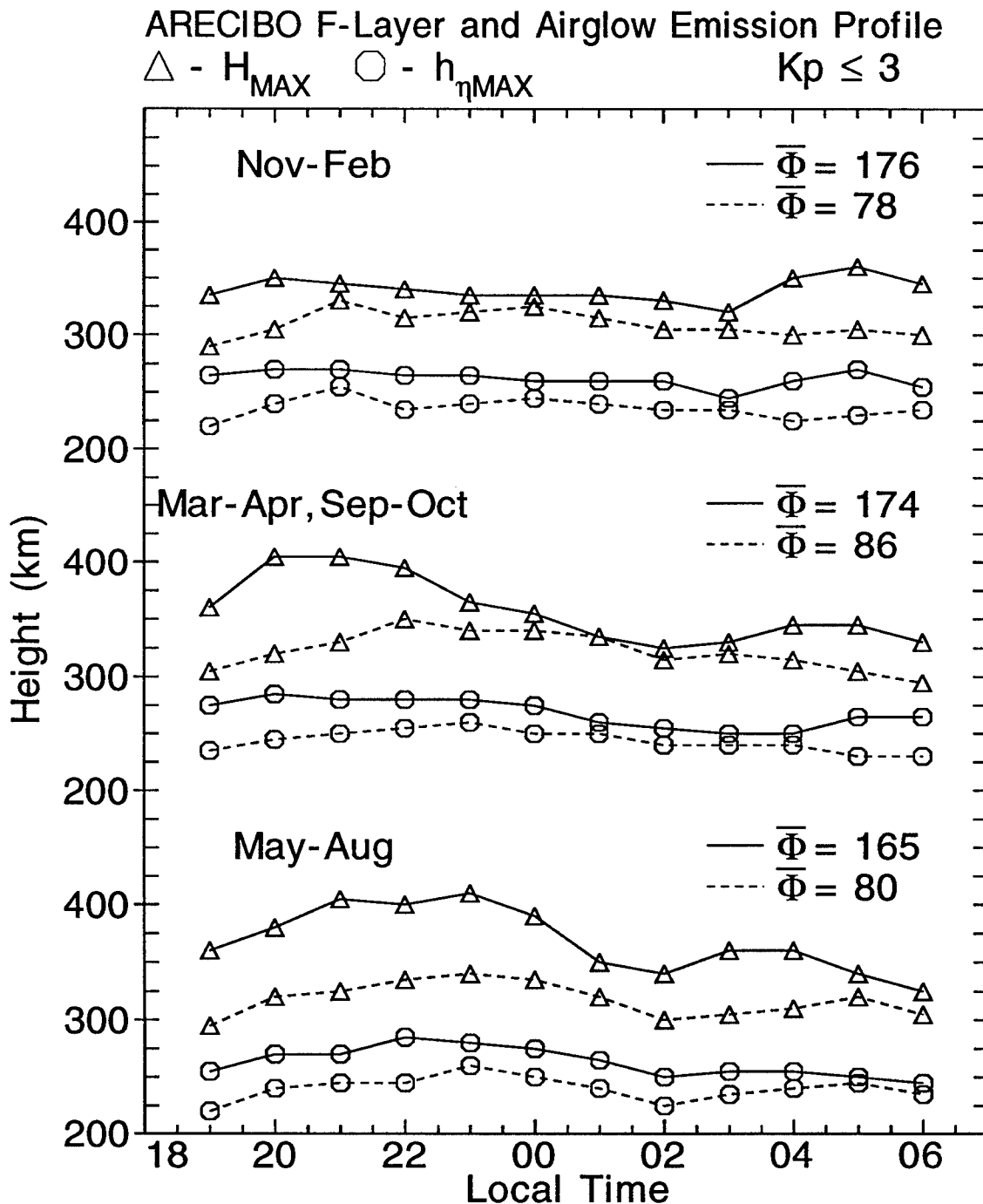


Figure 30. Arecibo seasonal F-layer and airglow emission height averages for low and high solar activity during quiet magnetic activity.

H_{MAX} is ~ 75 km higher than $h_{\eta MAX}$ through the night for low flux conditions.

The equinox months for high solar activity show $h_{\eta MAX}$ at ~ 275 km in the premidnight period lowering to 255 km in the postmidnight period and $h_{\eta MAX}$ is ~ 250 km and 240 km in the pre- and postmidnight periods for low solar activity. The H_{MAX} is ~ 120 km and 100 km higher than $h_{\eta MAX}$ for the pre- and postmidnight periods for high flux conditions and H_{MAX} is ~ 75 km higher than $h_{\eta MAX}$ for low solar activity.

The summer solstice months show $h_{\eta MAX}$ at ~ 280 km in the premidnight period and ~ 260 km in the postmidnight period for high solar activity and ~ 250 km and ~ 240 km in the pre- and postmidnight periods. H_{MAX} is ~ 120 km and 100 km higher than $h_{\eta MAX}$ for the pre- and postmidnight periods during high solar activity while H_{MAX} is ~ 80 km higher than $h_{\eta MAX}$ for the night at low flux conditions.

The magnetic activity effects (see Figure 31) were separated for disturbed ($K_p \geq 3$) and quiet ($K_p \leq 3$) conditions for all solar flux activity. We note no significant difference between the quiet and disturbed $h_{\eta MAX}$ for all seasons. We further note that the average $h_{\eta MAX}$ height is 250 km. H_{MAX} also shows no significant difference between the quiet and disturbed conditions for all seasons. H_{MAX} shows the largest difference in the equinox and winter months (~ 120 km higher than $h_{\eta MAX}$ in the premidnight period) and smallest difference in the winter solstice months (~ 75 km and 100 km higher than $h_{\eta MAX}$ in the pre- and postmidnight periods)

4.5.3.2. Jicamarca F-Layer and Airglow Emission Heights

The Jicamarca electron density data were collected in 1966-1969, 1984, 1988,

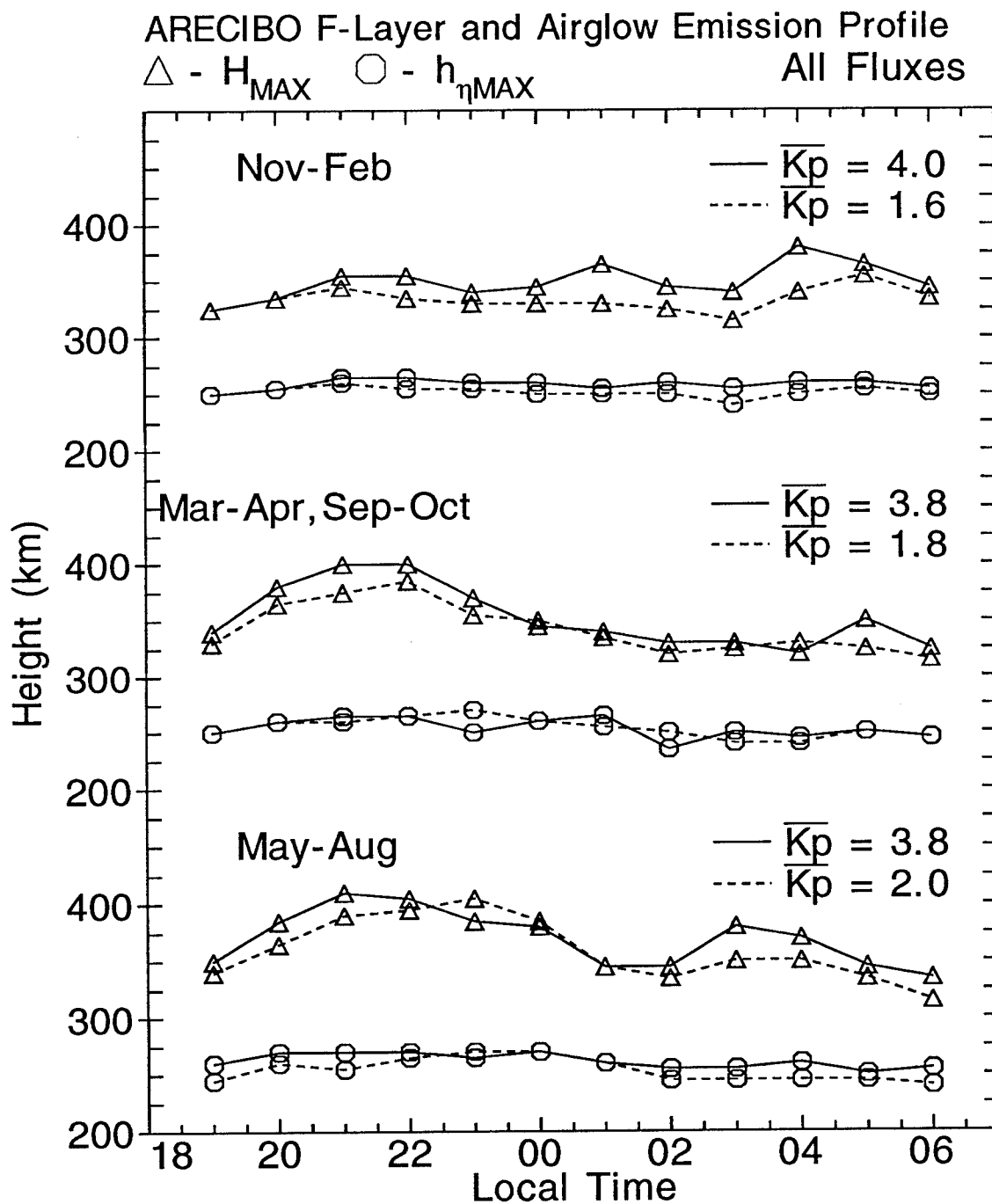


Figure 31. Arecibo seasonal F-layer and airglow emission height averages for quiet and disturbed magnetic activity.

and 1991. These data were characterized by low to moderate solar activity. Figures 32 and 33 show the solar cycle and magnetic activity effects on the H_{MAX} and $h_{\eta MAX}$ for all seasons.

Figure 33 shows the moderate ($\Phi \geq 130$) and low ($\Phi \leq 130$) solar activity effects on H_{MAX} and $h_{\eta MAX}$ for low magnetic activity conditions for the summer solstice (November–February), equinox (March–April, September–October), and winter solstice (May–August). Due to the limited Jicamarca data set, it was necessary to increase the magnetic activity interval to $K_p \leq 4$ to ensure a good statistics for the moderate and low solar activity average.

For the summer solstice, we note $h_{\eta MAX}$ is ~ 230 km and 250 km in the pre- and postmidnight periods for the moderate flux activity while $h_{\eta MAX}$ is ~ 270 km in the premidnight period for low solar activity. The Jicamarca data set lacked sufficient data satisfying the criteria outline above for an H_{MAX} and $h_{\eta MAX}$ in the postmidnight period for low flux activity. The H_{MAX} is ~ 300 km higher than $h_{\eta MAX}$ in the premidnight period and 100 km higher than $h_{\eta MAX}$ in the postmidnight period for moderate flux conditions while H_{MAX} is ~ 150 km higher than $h_{\eta MAX}$ in the premidnight period for low solar activity. The large H_{MAX} values in the premidnight period is a result of the prereversal enhancement of the $\bar{E} \times \bar{B}$ drift after sunset over the magnetic equator [Anderson, 1974].

The equinox months for high solar activity show $h_{\eta MAX}$ at ~ 225 km in the premidnight period lowering to 240 km in the postmidnight period for moderate and low solar activity. The H_{MAX} is ~ 300 km and 90 km higher than $h_{\eta MAX}$ for the pre- and

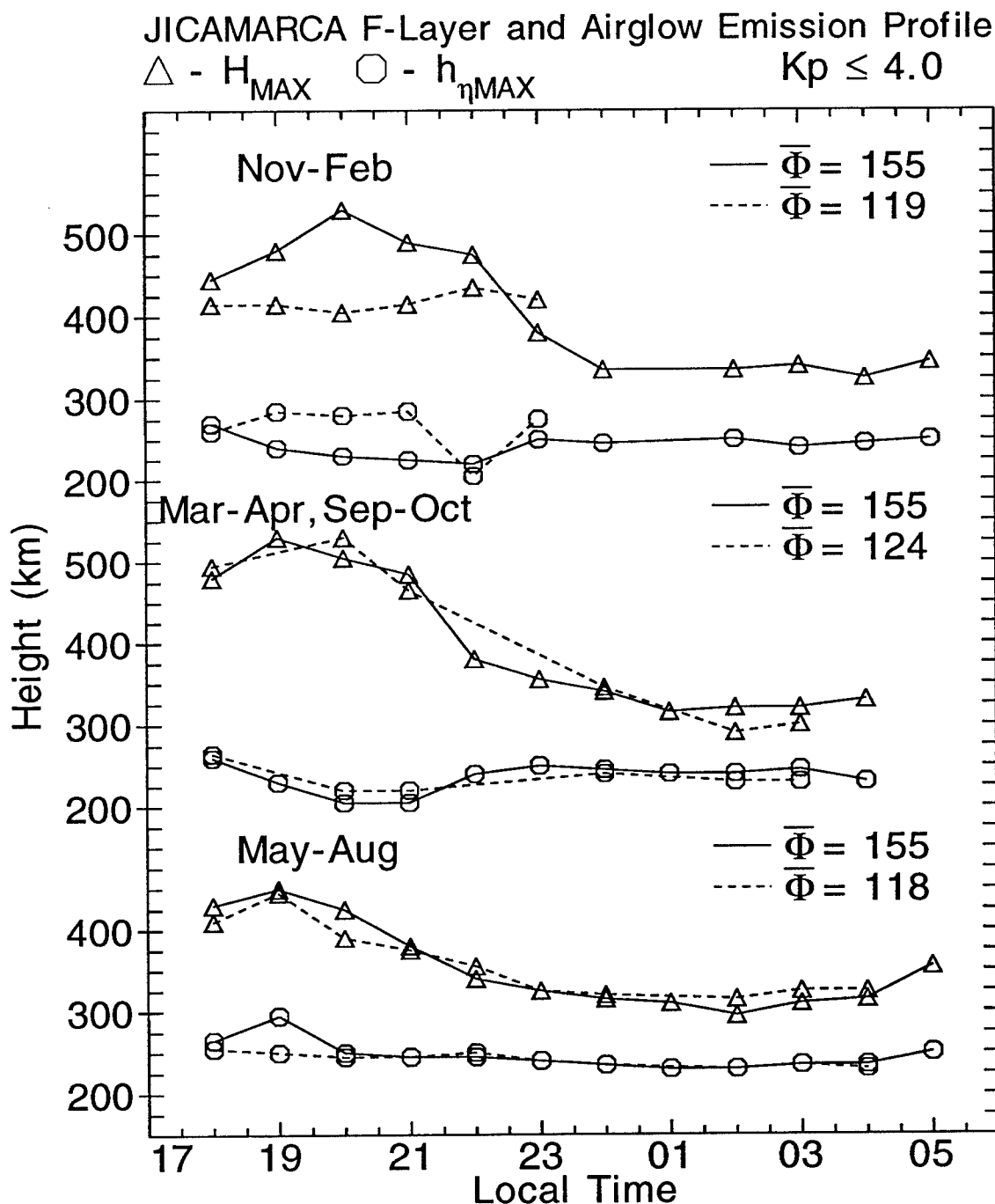


Figure 32. Jicamarca seasonal F-layer and airglow emission height averages for low and moderate solar activity during quiet magnetic activity.

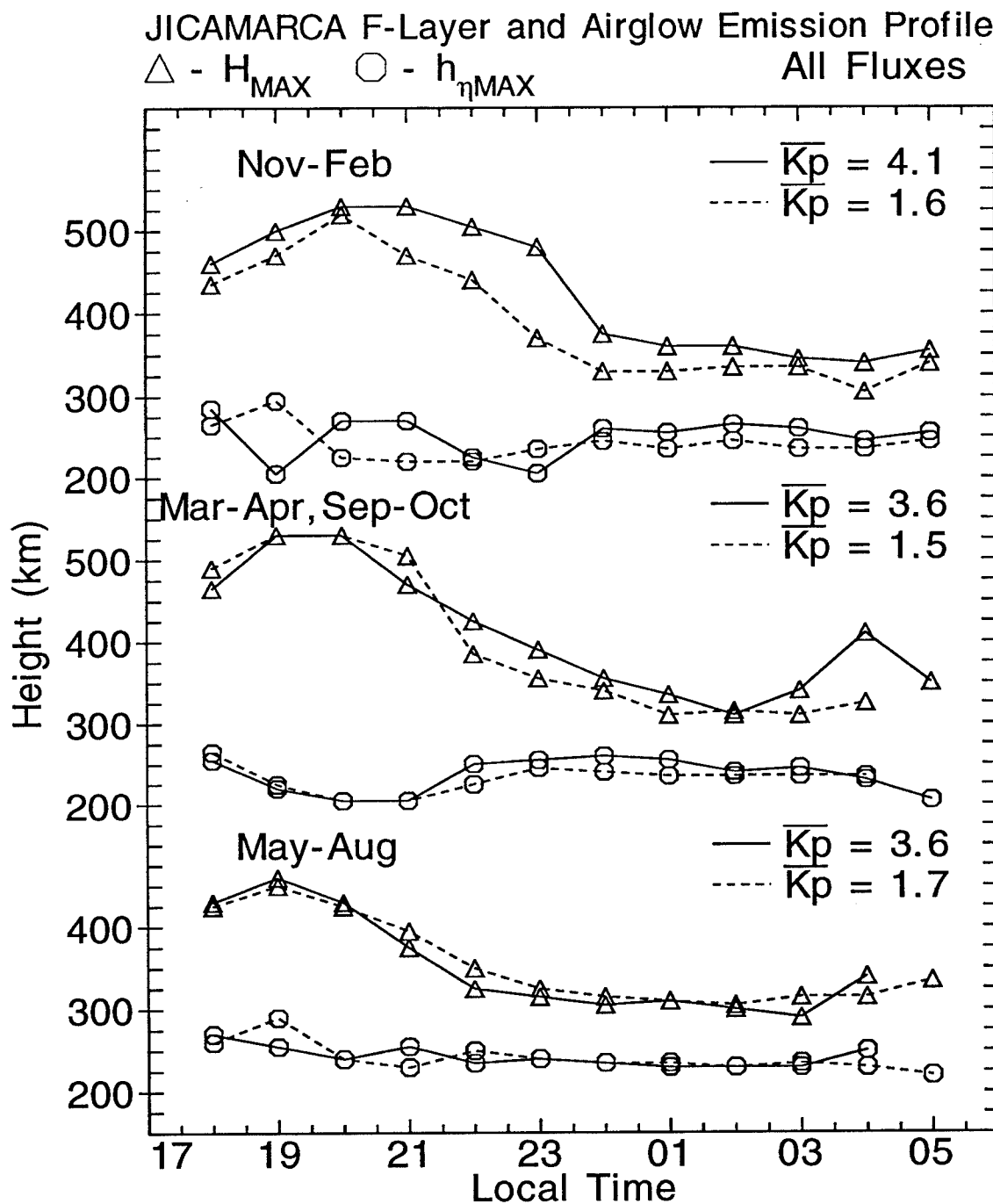


Figure 33. Jicamarca seasonal F-layer and airglow emission height averages for quiet and disturbed magnetic activity.

postmidnight periods for moderate and low solar flux condition.

The winter solstice months show $h_{\eta\text{MAX}}$ at ~ 250 km through the night for moderate and low solar activity. H_{MAX} is ~ 175 km and 75 km higher than $h_{\eta\text{MAX}}$ for the pre- and postmidnight periods during moderate and low solar activity.

The magnetic activity effects (see Figure 33) were separated for disturbed ($K_p \geq 3$) and quiet ($K_p \leq 3$) conditions for all solar flux conditions. Similar to the results for Arecibo, the data show no significant variation between the quiet and disturbed $h_{\eta\text{MAX}}$ for all seasons. For the summer and winter solstice months, we note an average $h_{\eta\text{MAX}}$ of ~ 250 km while the equinox months show an $h_{\eta\text{MAX}}$ of ~ 220 km and ~ 240 km in the pre- and postmidnight periods. H_{MAX} also shows no significant difference between the quiet and disturbed conditions for the equinox and winter solstice months, but we do note a lower H_{MAX} (~ 50 km) for quiet magnetic activity during the summer solstice months. Last, all seasons show a significantly larger H_{MAX} when compared to $h_{\eta\text{MAX}}$ for the premidnight period for the summer and equinox months.

4.6. SPLINES

We use an empirical data modeling technique using spline fits outlined in *Wand* [1981] to model the F-region neutral winds over Arequipa and Arecibo. Splines are bell-shaped functions whose degree of continuity depends on the order of the spline. We use splines of degree four, which means these splines have continuous derivatives up to the second order. We use this spline technique because it provides good

agreement with the average wind profile, thereby making the spline result an excellent choice for comparison with modeled data.

We constructed two separate spline models of the thermospheric wind data, one for the zonal component of the neutral wind and the other for the meridional component. Nodes for these models were set every 1.5 hours for a total of nine nodes. We found this node distribution enhanced the smoothness of the spline fit curves to the measured results.

The zonal and meridional components of the neutral wind models are both defined by the form:

$$\sum_{i=1}^m \left[a_{i,1} + a_{i,2} \sin\left(\frac{2\pi d}{365}\right) + a_{i,3} \cos\left(\frac{2\pi d}{365}\right) \right] N_i(t) + a_{i,4} \text{flux} + a_{i,5} kp + a_{i,6} \text{flux}^2 \quad (45)$$

where m is the number of nodes in the respective model, and a_{ij} are the model coefficients obtained by a least squares fit to the respective data points. Because of the differences between the eastward and northward wind speeds, the final empirical model will be different for the two wind components because the coefficients, a_{ij} , will be different. The model given in equation (45) is a function of the local time (t), the 10.7-cm solar flux (flux), the magnetic activity (K_p), and the day of the year (d). We perform least squares fits to the respective zonal and meridional data sets to obtain the model coefficients. Figures 34 to 36 show examples of the agreement between the spline fits and the average wind profiles.

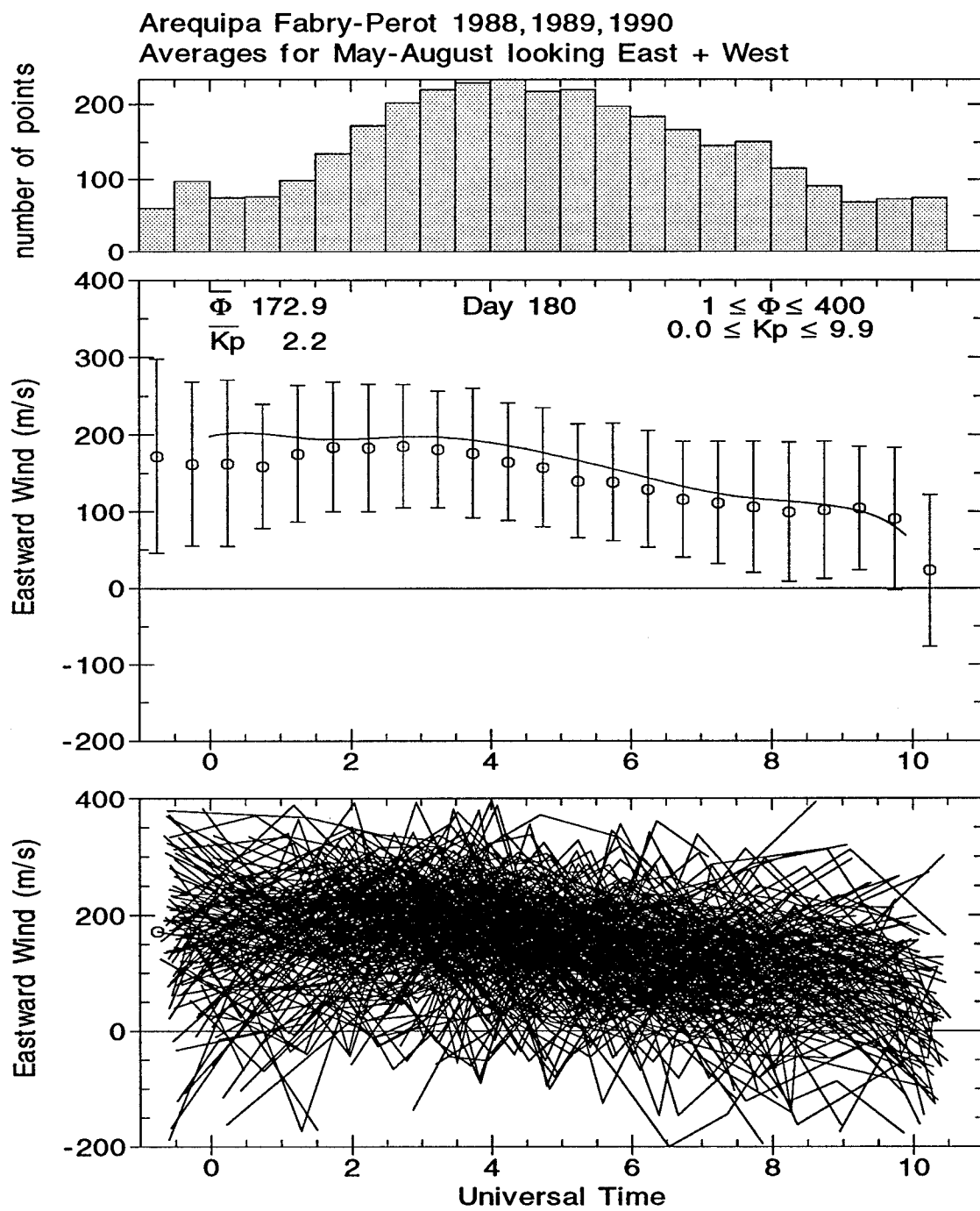


Figure 34. Spline fit for the May-August eastward wind over Arequipa. The solid line in the middle plot is the spline fit for the average solar flux and magnetic activity conditions.

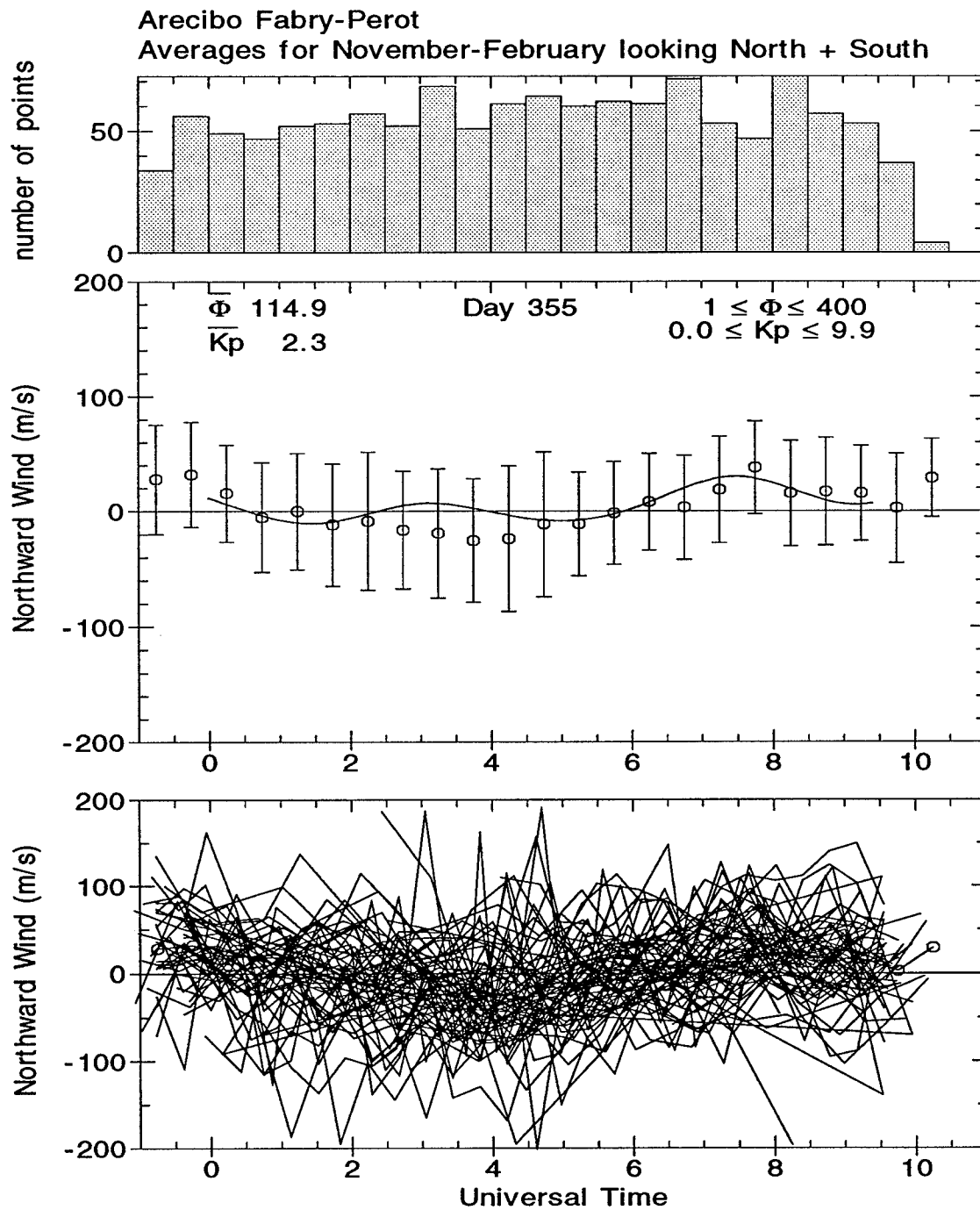


Figure 35. Spline fit for the November-February northward wind over Arecibo. The solid line in the middle plot is the spline fit for the average solar flux and magnetic activity conditions.

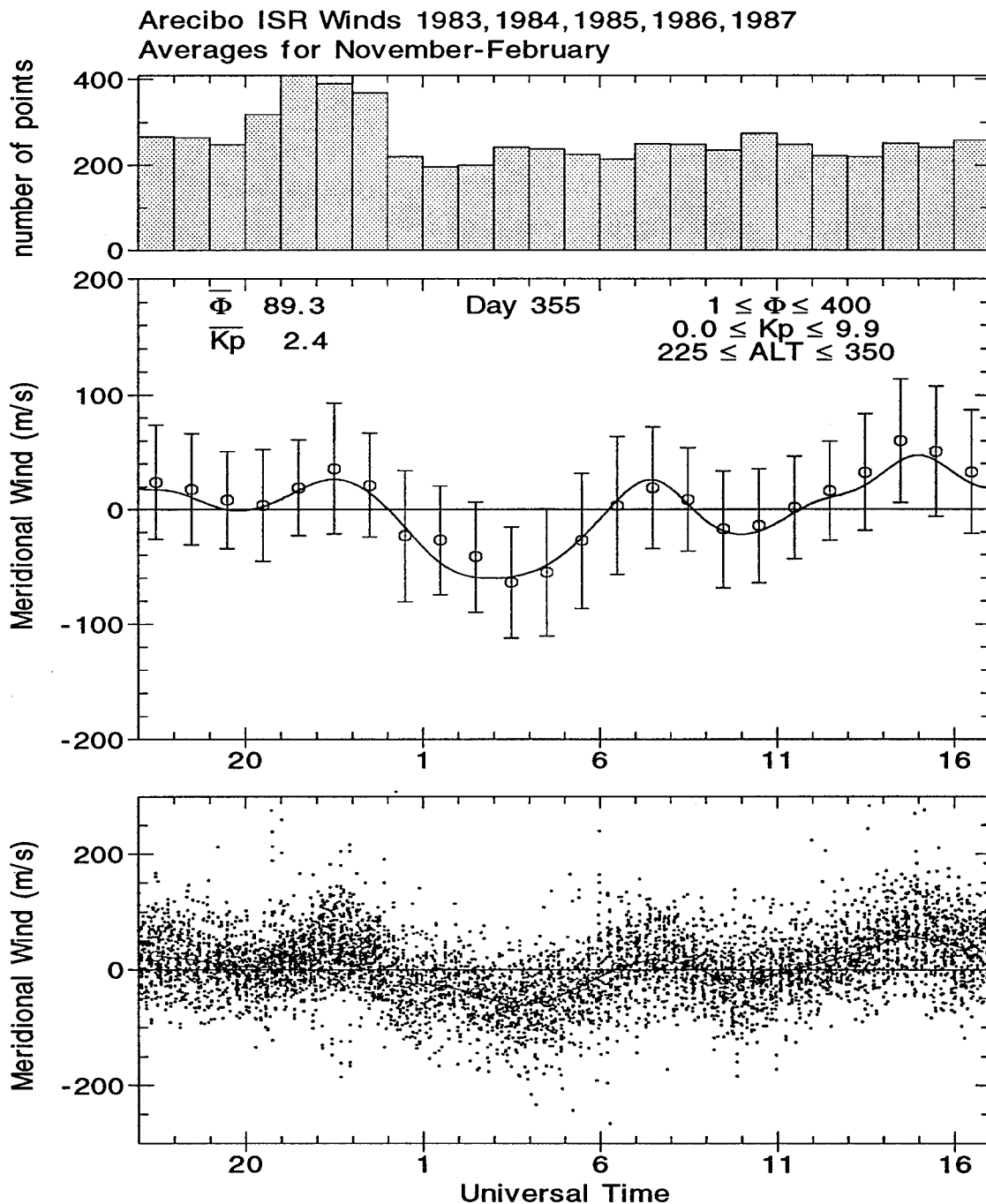


Figure 36. Spline fit for the November-February Arecibo ISR calculated neutral wind along the magnetic meridian. The solid line in the middle plot is the spline fit for the average solar flux and magnetic activity conditions.

CHAPTER 5

QUIET TIME LOW LATITUDE THERMOSPHERIC WINDS

5.1. INTRODUCTION

This chapter presents the geomagnetic quiet measured wind data over Arequipa, Peru and Arecibo, Puerto Rico. We calculated the average winds during quiet time conditions to eliminate magnetic activity effects. In addition to Fabry-Perot wind measurements, we use ISR calculated neutral winds over Arecibo to enhance our study of seasonal and solar cycle effects on the neutral winds. We also investigate the TIGCM93 and HWM93 predicted winds during quiet geomagnetic conditions.

5.2. SEASONAL AND SOLAR CYCLE EFFECTS

This section details the seasonal and solar cycle effects on the thermospheric winds over Arequipa and Arecibo. With the measured data, we also use TIGCM93 and HWM93 results to provide an indication of the success of these models in predicting the quiet time average winds over these low latitude locations.

5.2.1. Arequipa

To analyze both the seasonal and solar cycle effects on the neutral winds, we use 1988-1990 measured FPI data. In all the following Arequipa FPI data analysis, we neglect the December solstice (November-February) measurements due to the limited data collected during this period.

5.2.1.1. Seasonal Effects

Figures 37 and 38 show the averaged eastward and northward F-region quiet time ($K_p \leq 3$) thermospheric neutral winds over Arequipa for all solar flux levels during equinox (March-April, September-October) and June solstice (May-August) periods. These average zonal winds in Figure 37 are generally eastward through most of the night for all seasons except after ~ 0300 LT where the data show an eastward decrease or westward reversal. The strongest winds occur during the June solstice months with average peak winds of 175 to 250 m/s in the premidnight period.

Figure 38 shows the average meridional winds over Arequipa. These average winds consist of small wind speeds (< 50 m/s) after 2100 LT for the equinox and June solstice while the winds before 2100 LT show a significant northward wind speed (> 50 m/s) for the equinox months and a southward wind (> 50 m/s) for the June solstice period.

Despite using a different analysis technique, our results are consistent with previous Arequipa wind studies outlined in *Biondi et al.* [1991]. *Biondi et al.* [1991] investigated the seasonal effects by calculating monthly and seasonal wind averages (equinox and June solstice) for a given year (1988, 1989, etc.). Our averaging method differs from that used in *Biondi et al.* [1991] because we combined the 1988-1990 wind data for a given season. We also used measured FPI winds during quiet geomagnetic conditions to reduce magnetic activity effects, whereas *Biondi et al.* [1991] combined quiet and disturbed winds for the seasonal average calculations. *Biondi et al.* [1991] showed the strongest eastward winds occur during the June solstice period and the

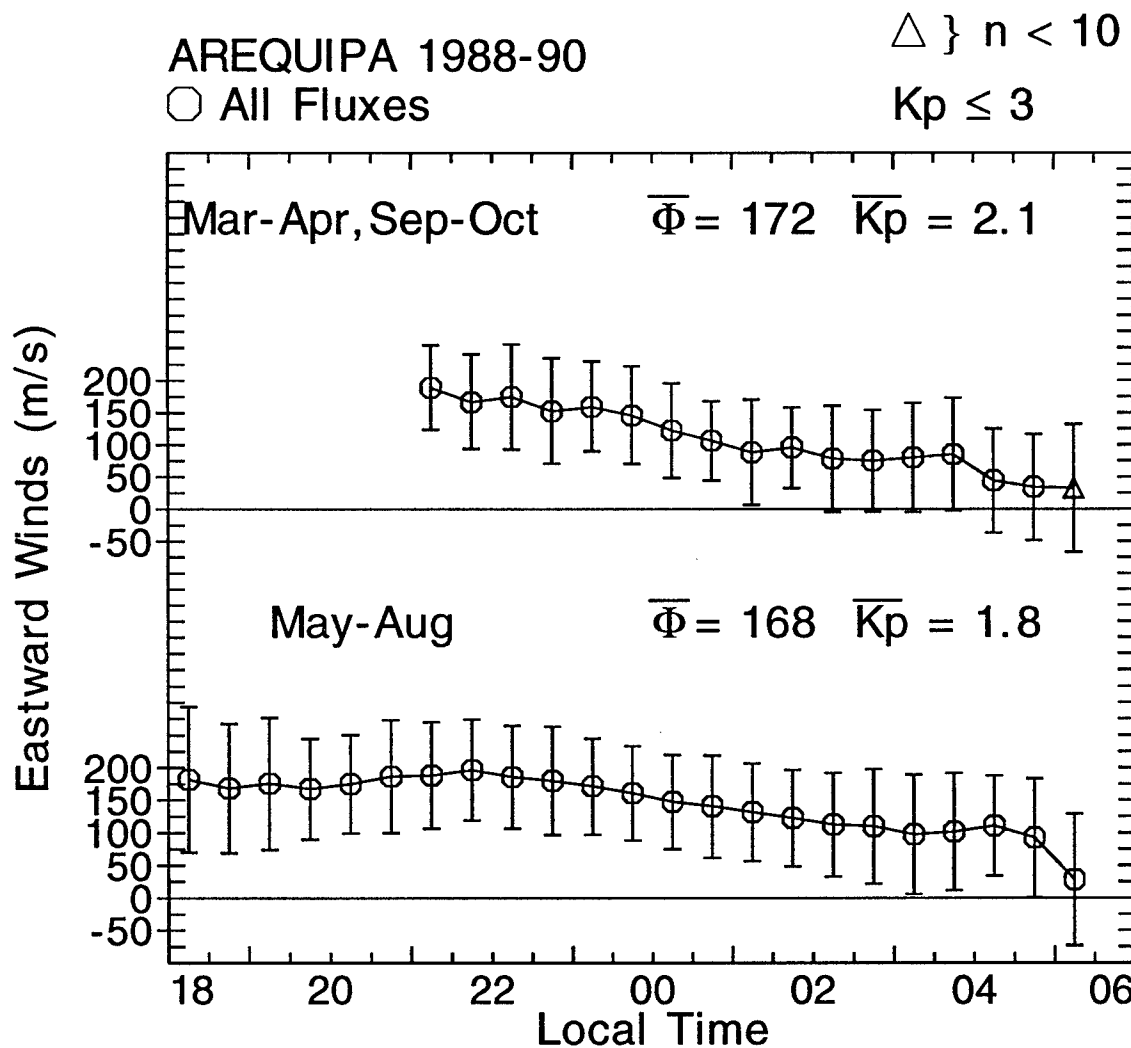


Figure 37. Measured FPI eastward wind averages over Arequipa, Peru, for equinox (March-April, September-October) and near June solstice (May-August) for all solar activity and quiet ($K_p \leq 3$) geomagnetic activity conditions.

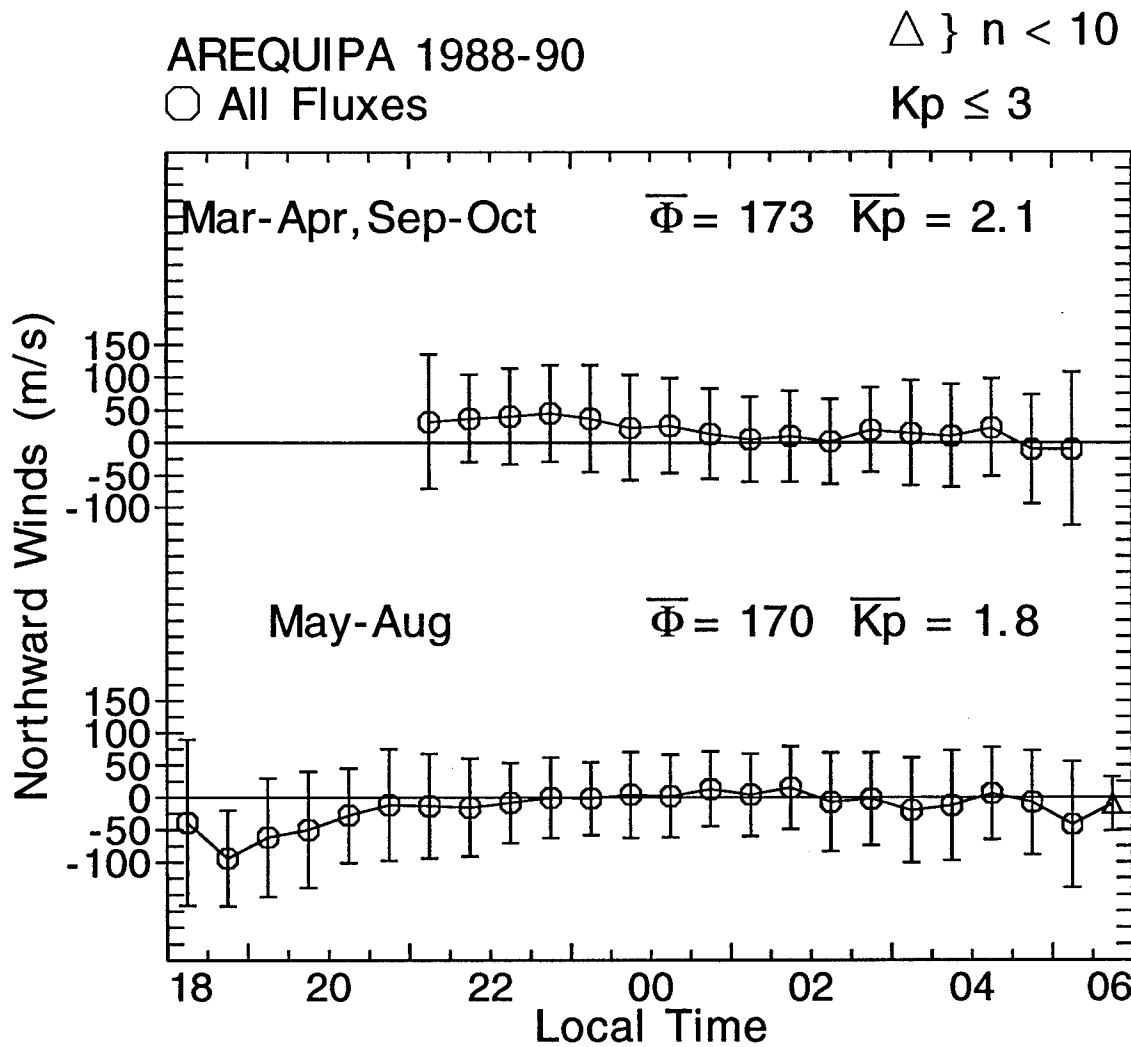


Figure 38. Measured FPI northward wind averages over Arequipa, Peru, for equinox and near June solstice for all solar activity and quiet geomagnetic activity conditions.

northward winds exhibit moderate (< 50 m/s) wind speeds after midnight during the equinox and June solstice periods.

We also compared our equinox meridional wind results to derived neutral winds from the Atmospheric Explorer E (AE-E) satellite. AE-E measurements of the 630.0 nm emission in the nighttime equatorial thermosphere were used to infer the height of the F-region peak, H_{MAX} , during the December solstice and spring equinox (March-April) periods [Burrage *et al.*, 1990]. These airglow measurements were collected during February 1980 through April 1981, a period characterized by moderate to high solar flux activity and low to moderate geomagnetic activity [Burrage *et al.*, 1990]. Using the calculated H_{MAX} values, Burrage *et al.* [1990] obtained magnetic meridional wind components as a function of dip latitude and local time. Our equinox meridional wind average does not agree with the AE-E-derived wind average for the spring equinox period at the lowest latitudes. The AE-E-derived wind near the magnetic equator shows a southward wind reversal beginning near 2100 LT until 0230 LT while our FPI result for equinox shows a northward wind from 2100 LT to 0430 LT. Further review of the AE-E winds shows the derived winds from 15°S to 25°S dip latitudes are consistent with our equinox seasonal average wind. Burrage *et al.* [1990] stated that the derived winds at the lowest latitudes are subject to the greatest uncertainties since the contribution of the meridional neutral wind to the change in H_{MAX} decreases to zero at the equator.

5.2.1.2. Solar Cycle Effects

Figures 39 and 40 show the averaged eastward and northward F-region quiet

time thermospheric neutral winds over Arequipa for two levels of the 10.7-cm solar flux (Φ) index during equinox and June solstice periods. The 1988-1990 Arequipa FPI data are characterized by moderate ($\Phi \leq 160$) to high ($\Phi \geq 160$) solar flux activity. The open symbols represent the mean wind speed for the given solar activity and the error bars represent ± 1 standard deviation about this mean. The error bars for the high solar flux means, the closed symbols, are not shown but they are comparable to those of the moderate solar flux conditions.

Figure 39 shows mainly eastward winds for all seasons over Arequipa. The data show no significant variation due to solar activity during the equinox period; however, the data show a systematic eastward increase in the postmidnight period from moderate to high solar flux conditions during the June solstice months. Figure 40 shows no significant variation of the neutral meridional wind due to solar cycle effects.

Biondi et al. [1990 and 1991] reported that the nighttime zonal wind increases with solar activity. These previous studies showed larger eastwards in the premidnight sector from solar minimum to maximum while our results show the larger eastward winds in the postmidnight period for similar solar activity conditions. One possible explanation of the discrepancy between our results and the previous studies is that *Biondi et al.* [1990 and 1991] used FPI measurements during 1983-1986 and 1988-1990 while we limited our data set to 1988-1990. The 1983-1986 FPI data are characterized by low solar flux conditions. These data also showed lower eastward winds in the premidnight period compared to the 1988-1990 zonal wind data set. We did not use the 1983-1986 wind data set in our analysis because the FPI instrument encountered several

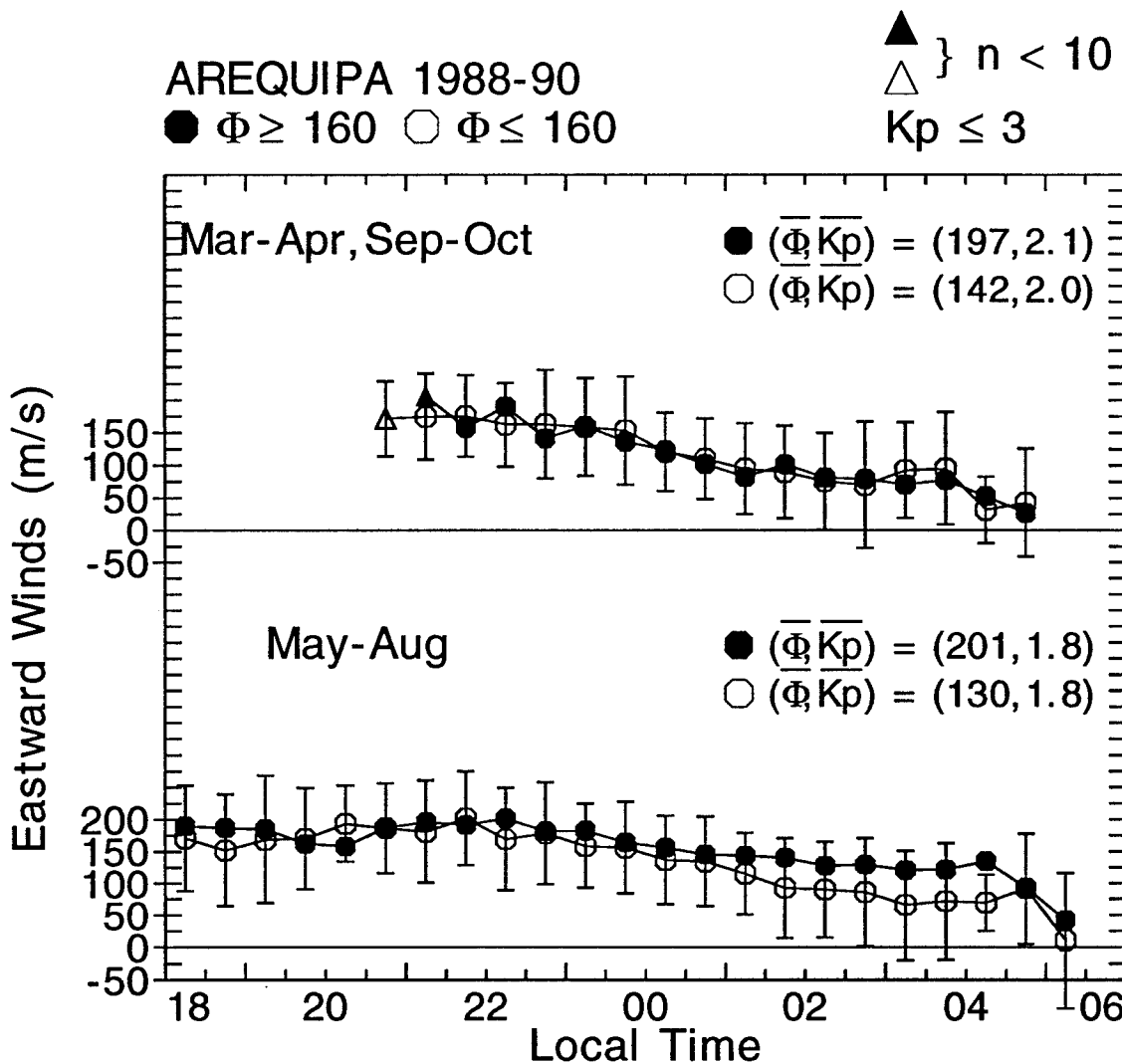


Figure 39. Measured eastward wind averages over Arequipa, Peru, for various seasons for moderate and high solar activity. The average neutral wind velocities are obtained by examining 1/2 hour time bins for the given solar flux interval ($160 \leq \Phi \leq 160$) and quiet geomagnetic conditions. The triangle symbol represents bin averages consisting of less than 10 data points.

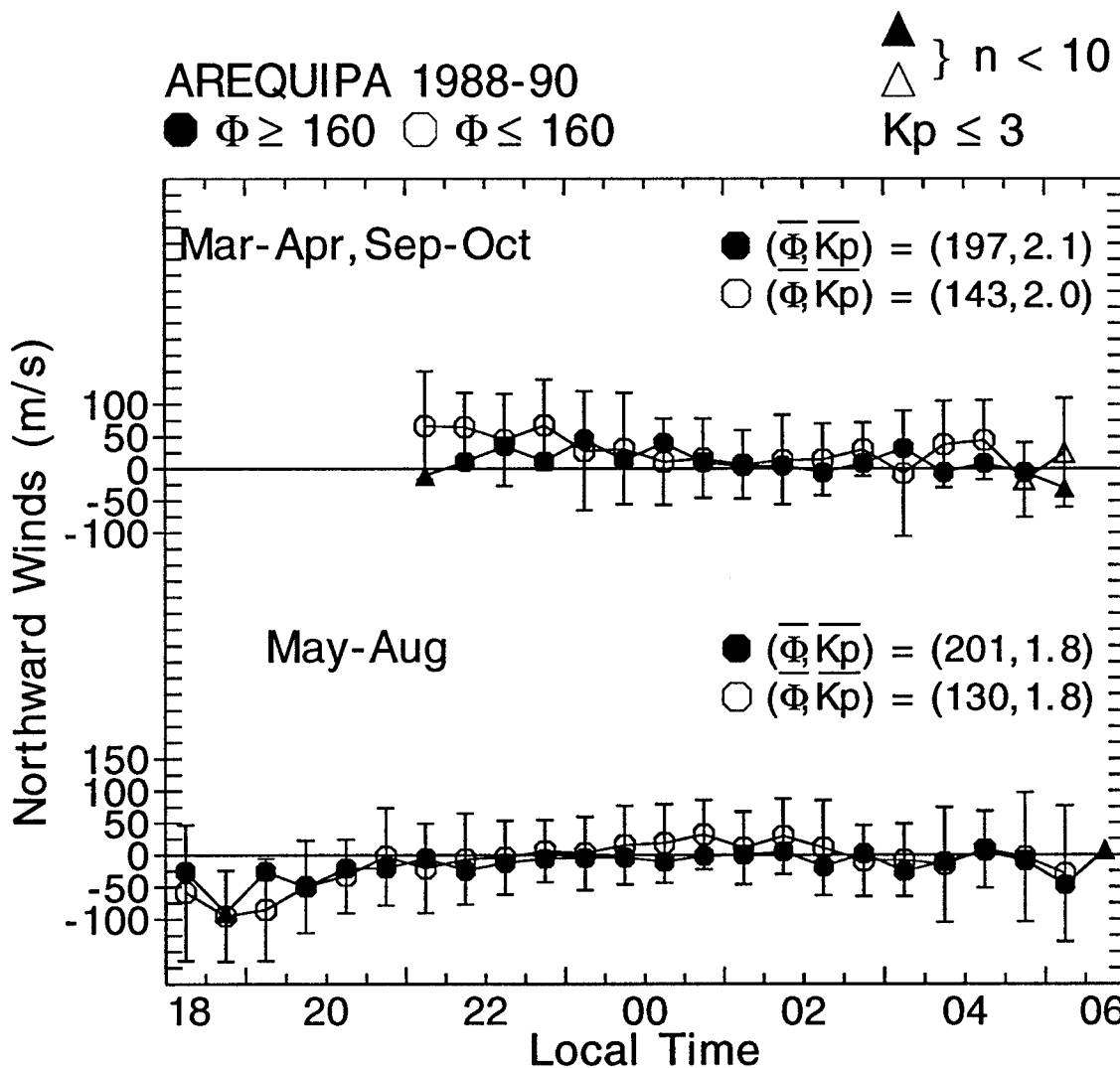


Figure 40. Measured northward wind averages over Arequipa, Peru, for various seasons for moderate and high solar activity. The average neutral wind velocities are obtained by examining 1/2 hour time bins for the given solar flux interval ($160 \leq \Phi \leq 160$) and quiet geomagnetic conditions. The triangle symbol represents bin averages consisting of less than 10 data points.

problems during these years. Our northward wind results agree with the previous meridional wind studies in *Biondi et al.* [1991].

5.2.1.3. TIGCM93 Solar Cycle Activity Model Results

Figures 41 and 42 show the TIGCM93 solar cycle activity predictions for Arequipa for all seasons. To properly investigate the solar cycle effects, we analyze the wind predictions for high ($\Phi = 195$), moderate ($\Phi = 135$), and low ($\Phi = 75$) solar activity conditions. We use the predicted quiet time winds, $K_p = 1$, to reduce magnetic activity effects.

Figure 41 shows the eastward predictions for the December solstice (day = 360), equinox (day = 90), and June solstice (day = 180). Similar to the measured FPI winds in Figure 39, the modeled winds are generally eastward throughout the night for all seasons with a westward reversal occurring after 0430 LT for days 360 and 90. The TIGCM93 peak eastward winds are generally 50 - 75 m/s less than the measured FPI average winds. Exact agreement between the predicted and measured wind does not determine the success of the TIGCM prediction. The relative difference between the predicted low and high solar activity winds compared to the relative difference for the measured winds provides a better measure of how the TIGCM93 predicts the experimental wind results.

We compare only the average zonal winds for the equinox and June solstice periods to the TIGCM predictions. The measured or experimental data set does not contain enough moderate solar flux data during November - February for a valid comparison during the December solstice period. Because the measured Arequipa data

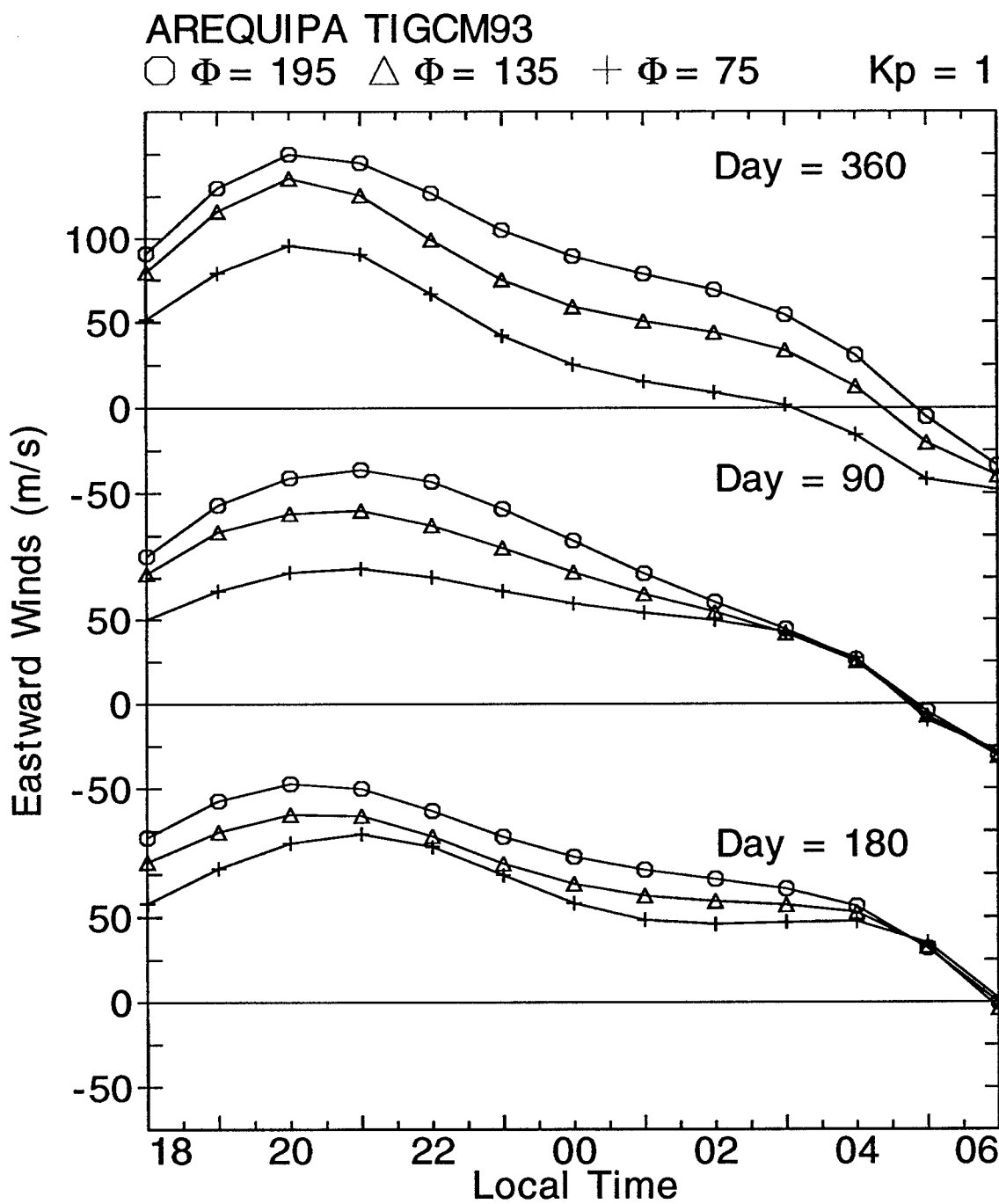


Figure 41. TIGCM93 eastward wind predictions over Arequipa, Peru, for various seasons for high, moderate, and low solar activity conditions and for quiet magnetic activity.

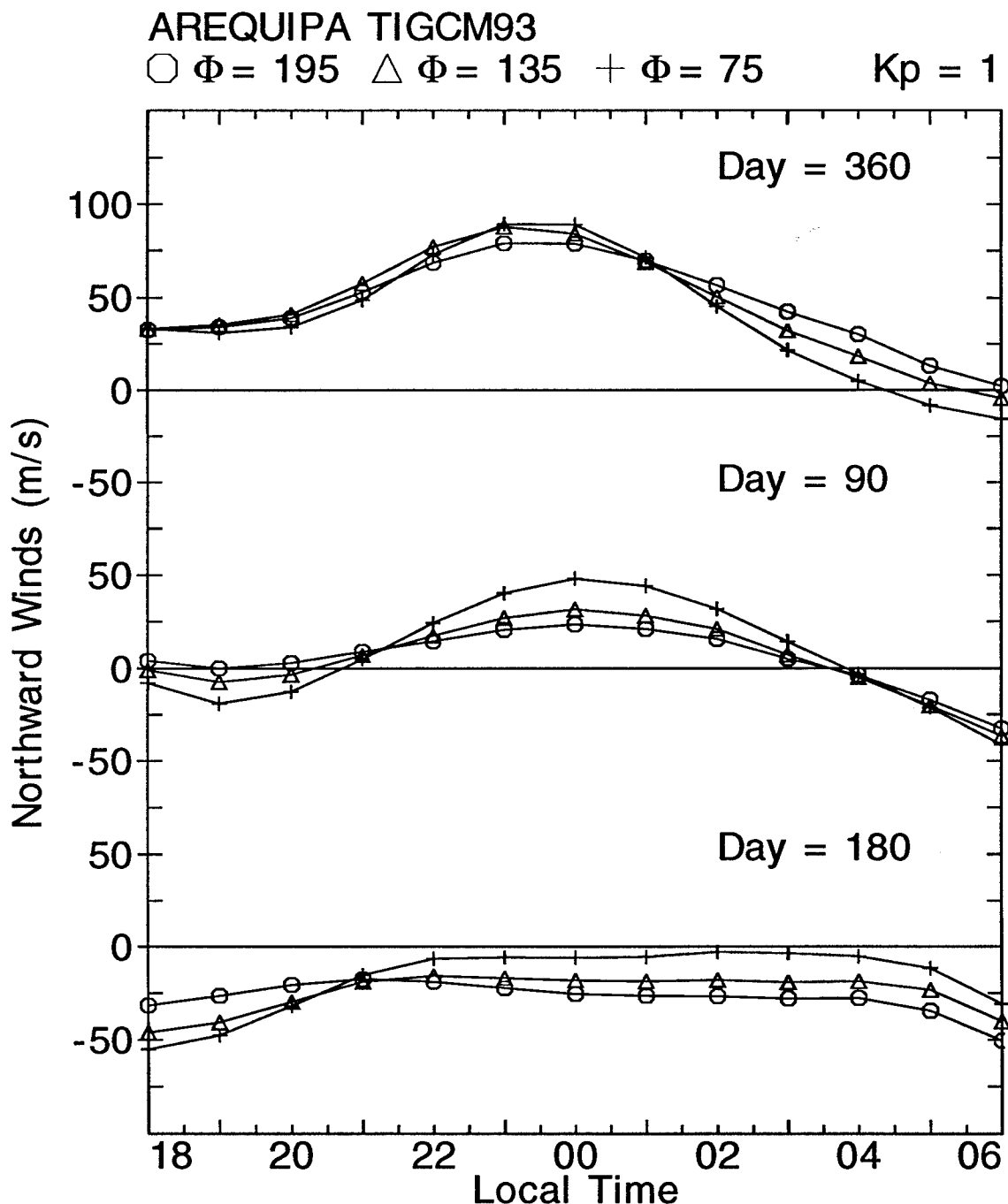


Figure 42. TIGCM93 northward wind predictions over Arequipa, Peru, for various seasons for high, moderate, and low solar activity conditions and for quiet magnetic activity.

are characterized by moderate to high solar activity, we use the predicted high ($\Phi = 195$) and moderate ($\Phi = 135$) relative wind difference to compare to the measured data. For day 90, the TIGCM93 predicts a westward velocity perturbation from high to moderate flux conditions in the premidnight period while the postmidnight shows no significant variation due to solar activity. The relative differences between the predicted wind results for the premidnight period are not consistent with the experimental results while the postmidnight model results show better agreement with the experimental moderate and high flux wind difference. For day 180, the model results show no significant wind variation due to solar activity. The TIGCM93 predictions agree with the experimental wind results in the premidnight period but show less agreement in the postmidnight period. During the postmidnight period, the measured winds show a systematic eastward increase from moderate to high solar activity while the model predicts no significant variation of the winds due to solar activity. Figure 42 shows no significant variation of the meridional averages due to solar activity effects, a result consistent with the measured winds.

5.2.1.4. HWM93 Solar Cycle Activity Model Predictions

Figures 43 and 44 show HWM93 solar cycle activity predictions for Arequipa for all seasons. Similar to the previous section, we analyze the wind predictions for high ($\Phi = 195$), moderate ($\Phi = 135$), and low ($\Phi = 75$) solar activity conditions. We use the HWM93 predicted quiet time winds, $K_p = 2$, to compare to the FPI measured winds. This K_p value agrees with the average K_p index for the measured FPI wind under similar

solar flux and magnetic activity conditions.

Because the HWM93 model uses FPI measured winds for Arequipa, we do not expect to find significant variations between the measured and predicted results. In addition to the FPI data, the HWM93 also contains ISR and satellite data, allowing us to obtain model predictions during times of limited or no FPI wind measurements. Figure 43 shows the Arequipa eastward predictions for the December solstice (Day = 360), equinox (Day = 90), and June solstice (Day = 180). These predicted zonal results for the equinox and June solstices are in complete agreement with our measured data results (see Figure 39). The day 360 predicted results show little variation with solar activity in the premidnight period and a westward perturbation from high to low solar activity in the postmidnight period. Figure 44 shows the model predictions for the Arequipa meridional winds are not affected by solar cycle variations; a result that agrees with our experimental data.

5.2.2. Arecibo

We use 1980-1989 measured FPI data to analyze both the seasonal and solar cycle effects. In addition to the measured FPI data, we use ISR-derived neutral winds to supplement the FPI data analysis. In the following Arequipa FPI solar flux analysis, we neglect the equinox data analysis because of the limited high solar flux ($\Phi \geq 130$) data collected during this period.

5.2.2.1. Seasonal Effects

Figures 45 and 46 show the averaged eastward and northward F-region quiet

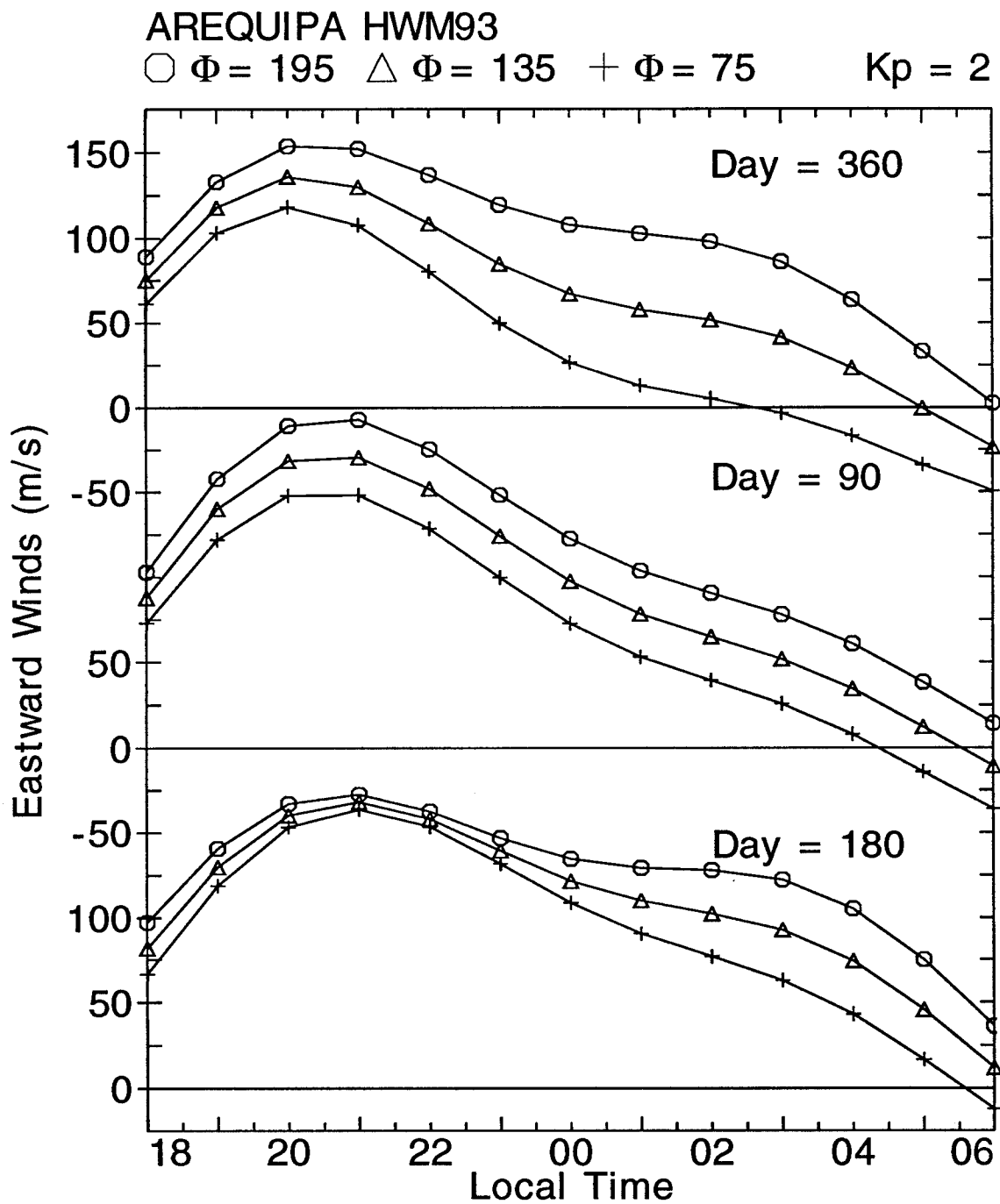


Figure 43. HWM93 eastward wind predictions over Arequipa, Peru, for various seasons for high, moderate, and low solar activity conditions and for quiet magnetic activity.

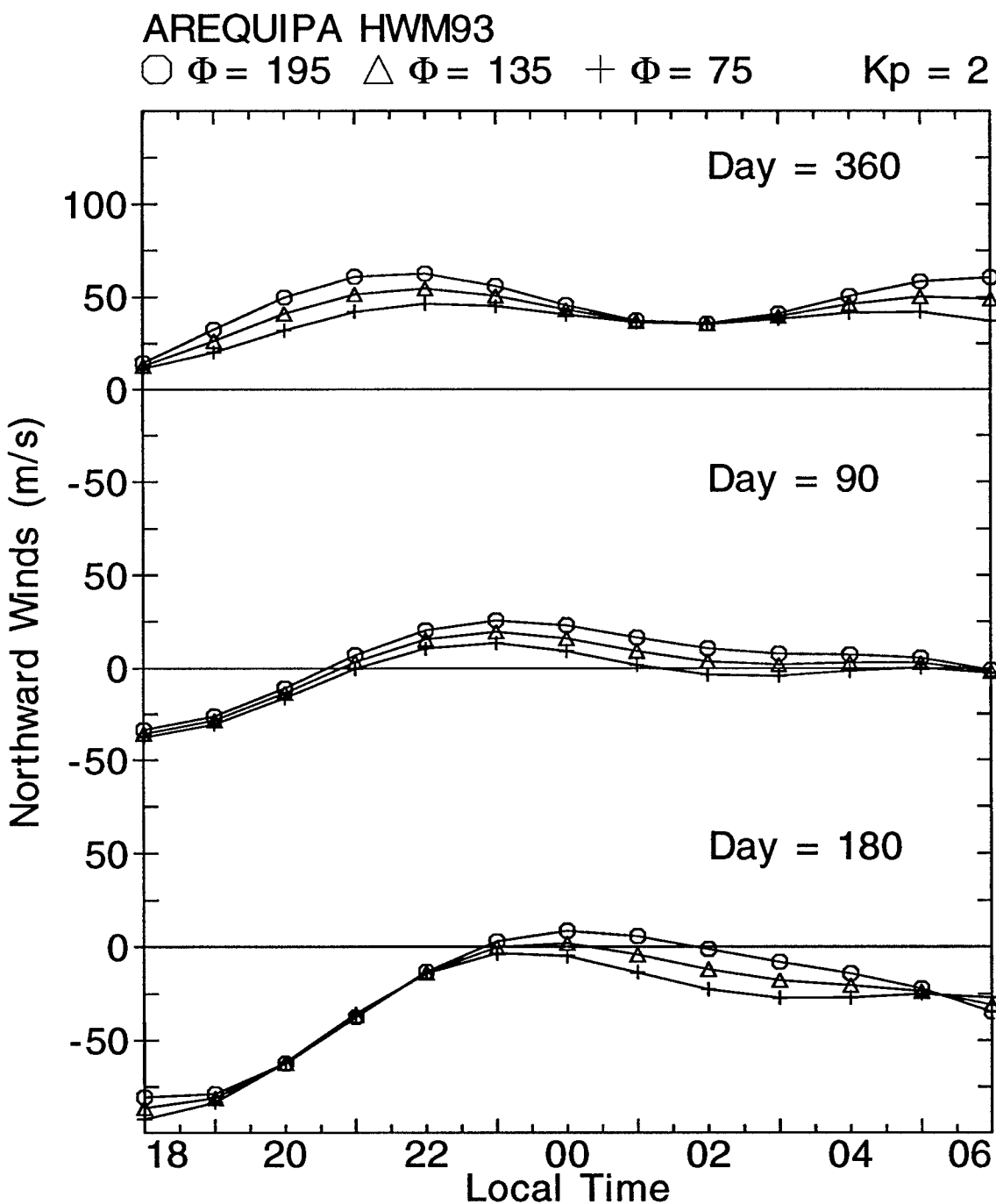


Figure 44. HWM93 northward wind predictions over Arequipa, Peru, for various seasons for high, moderate, and low solar activity conditions and for quiet magnetic activity.

time thermospheric neutral winds over Arecibo for all solar flux levels during December solstice, equinox, and June solstice periods. Figure 45 shows that the averaged FPI winds are generally eastward through the night during the December solstice. The equinox and summer solstice show westward reversals at approximately 0300 LT and 2400 LT, respectively. The maximum eastward winds occur during the December solstice with average peak wind values ranging from 75 to 130 m/s during the premidnight period.

Figure 46 presents the average meridional winds. These winds show a poleward-equatorward-poleward wind flow through the night for all seasons. The maximum meridional winds occur during the June solstice where the data show peak southward winds of 75 to 100 m/s.

Burnside and Tepley [1989] performed similar studies of the seasonal effects of the thermospheric winds over Arecibo. One major difference between this previous study and our work is *Burnside and Tepley [1989]* used measured FPI data from 1980-1987 while our study uses these data and additional FPI measurements during 1988 and 1989. *Burnside and Tepley [1989]* showed that the strongest eastward winds are observed during the December solstice and equinox periods, which agrees with our data set. This previous study also shows the reversal to westward flow in the postmidnight period during the June solstice, which agrees with our eastward wind results. Our meridional wind averages agree with the results outlined in *Burnside and Tepley [1989]*. This previous study showed the meridional winds are weakest during the December solstice and strongest during the June solstice months. *Burnside and Tepley [1989]* also

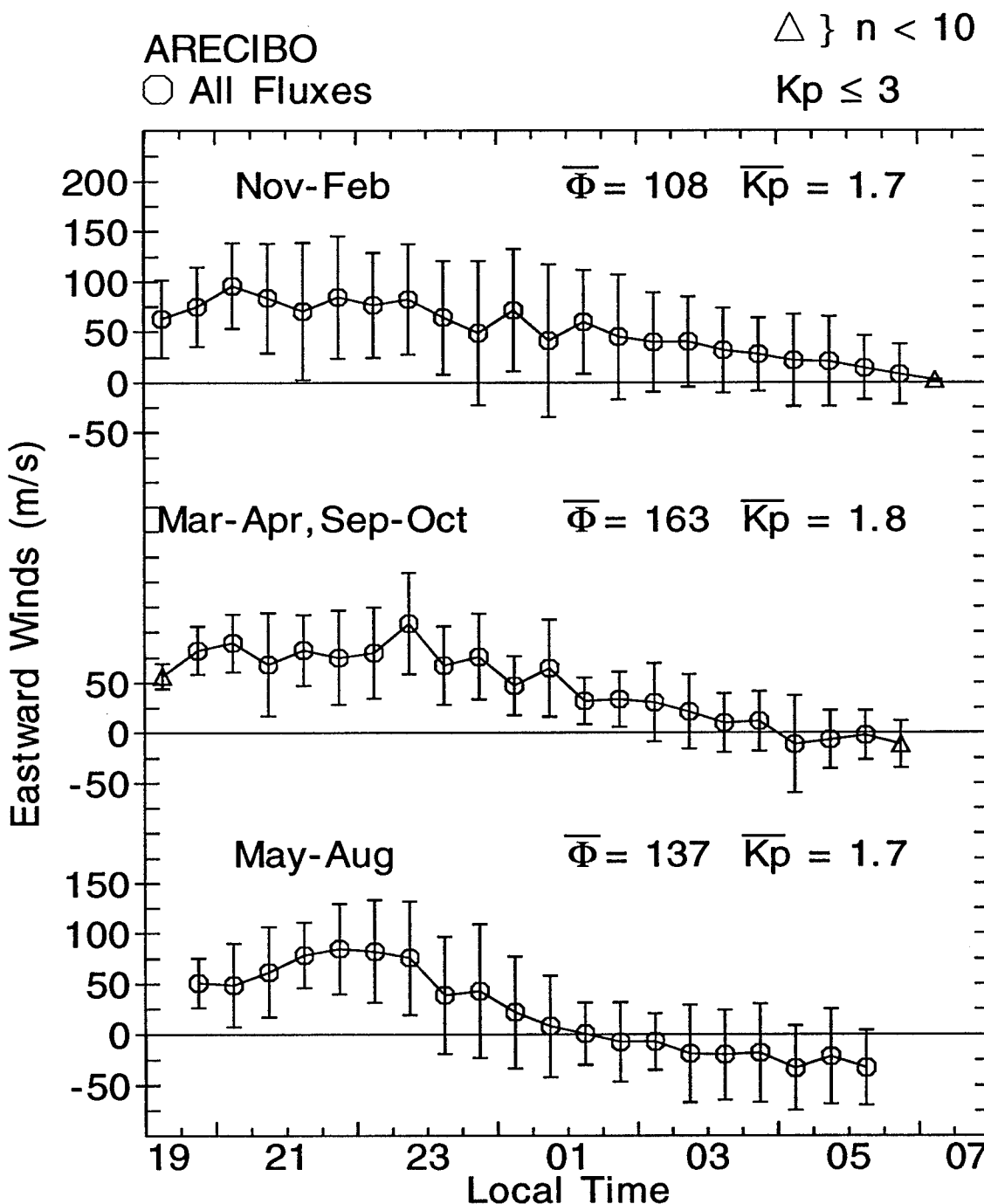


Figure 45. Measured eastward wind averages over Arecibo, Puerto Rico, for various seasons for all solar activity and quiet magnetic activity conditions.

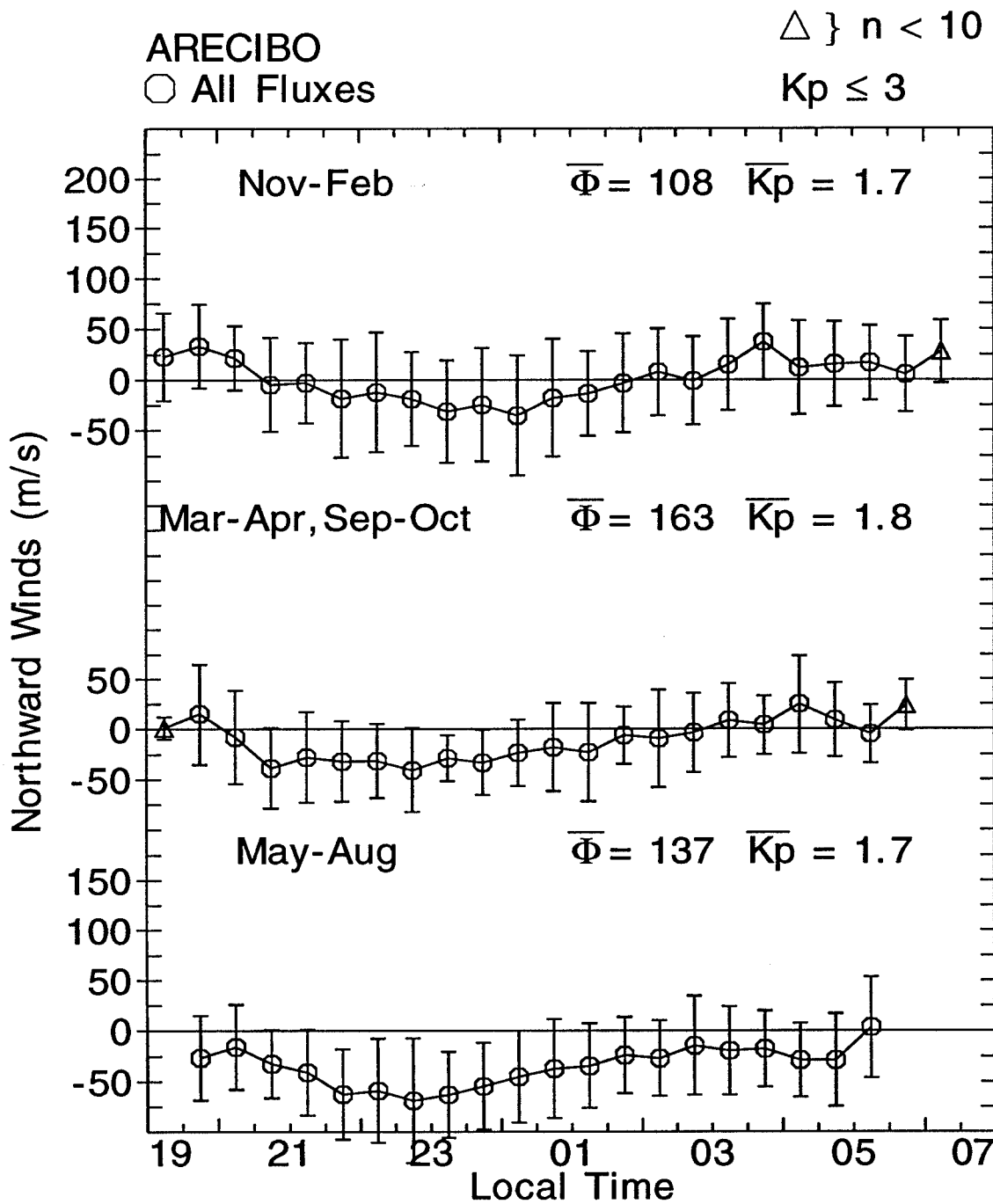


Figure 46. Measured northward wind averages over Arecibo, Puerto Rico, for various seasons for all solar activity and quiet magnetic activity conditions.

showed the strongest and weakest meridional wind speeds are observed during the June and December solstices, respectively. These wind directions and magnitudes are consistent with our meridional results.

5.2.2.2. Solar Cycle Effects (FPI Measurements)

Figures 47 and 48 show the averaged eastward and northward F-region quiet time thermospheric neutral winds over Arecibo for two levels of the 10.7-cm solar flux index for the December solstice and June solstice periods. These data were separated for low solar activity ($\Phi \leq 130$) and high solar activity ($\Phi \geq 130$).

Figure 47 shows generally eastward winds throughout the night for the December solstice. The averaged zonal wind for the June solstice months is eastward in the premidnight sector, reverses before 0100 LT, and becomes westward for the rest of the night. These data show a small westward perturbation for most of the night during the December solstice period from solar minimum to maximum. We note no significant variation between the low and high solar activity averages for the equinox and June solstice periods. Figure 48 shows no significant variation between the low and high solar activity northward averaged winds during the December solstice and June solstice periods; however, the data show perhaps a small southward velocity perturbation for the equinox period from solar minimum to maximum.

Burnside and Tepley [1989] concluded that the thermospheric neutral winds over Arecibo are unaffected by changes in the solar cycle. Our study shows solar cycle effects on the zonal and meridional neutral wind averages. We enhanced the solar cycle analysis study performed in *Burnside and Tepley [1989]* by using a lower time bin

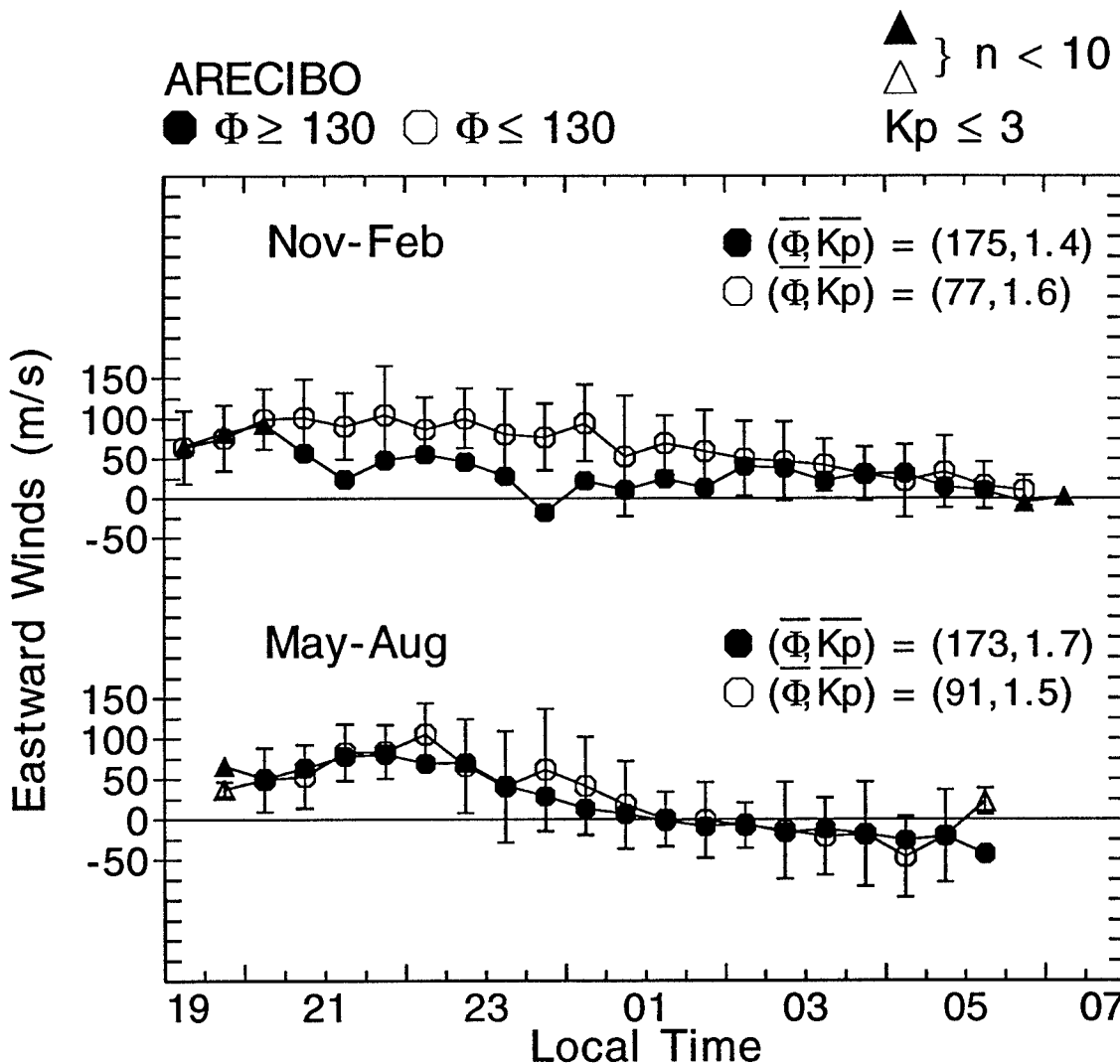


Figure 47. Measured eastward wind averages over Arecibo, Puerto Rico, for various seasons for low and high solar activity. The average neutral wind velocities are obtained by examining 1/2 hour time bins for the given solar flux interval ($130 \leq \Phi \leq 130$) and quiet geomagnetic conditions. The triangle symbol represents bin averages consisting of less than 10 data points.

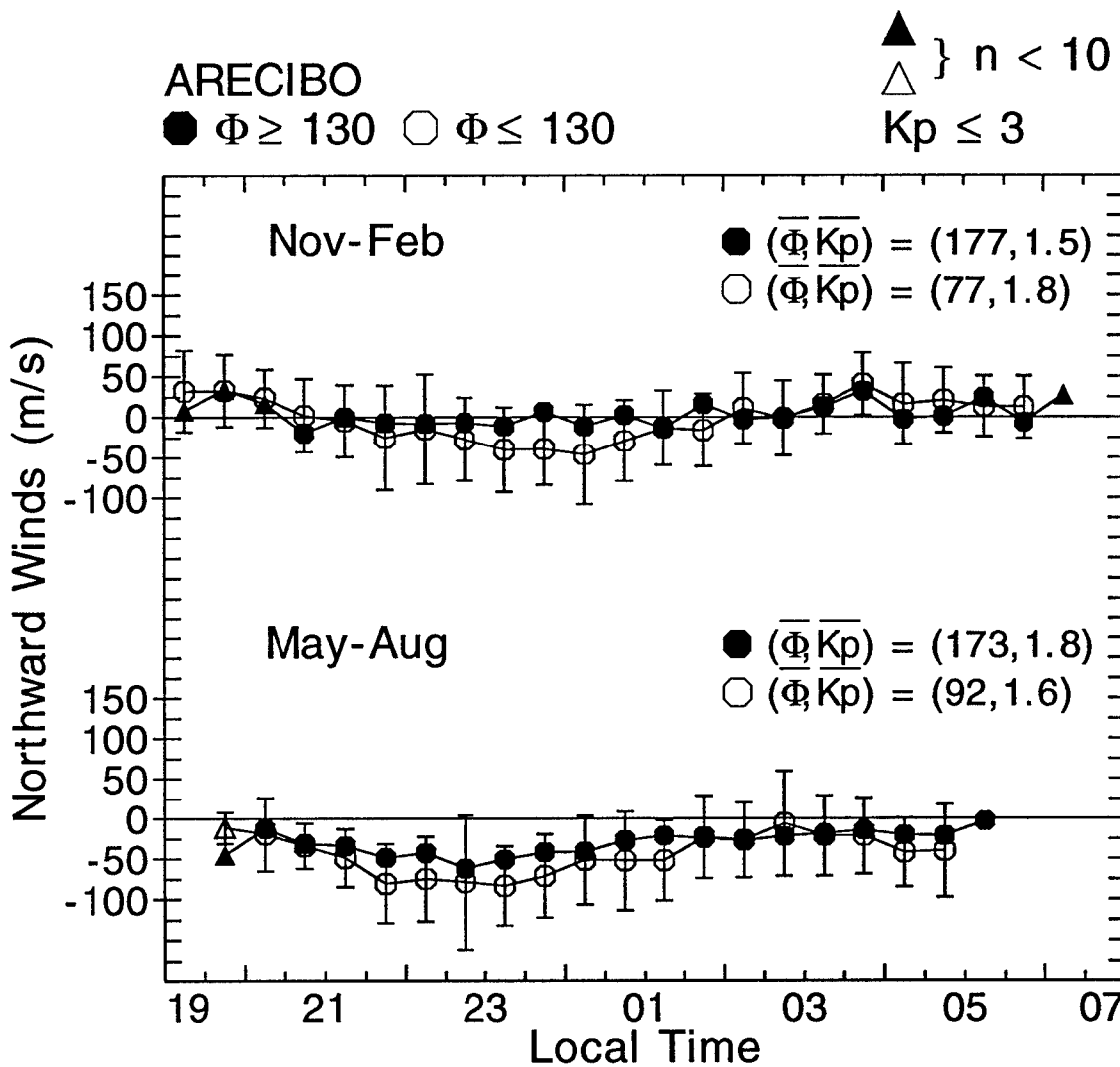


Figure 48. Measured northward wind averages over Arecibo, Puerto Rico, for various seasons for low and high solar activity. The average neutral wind velocities are obtained by examining 1/2 hour time bins for the given solar flux interval ($130 \leq \Phi \leq 130$) and quiet geomagnetic conditions. The triangle symbol represents bin averages consisting of less than 10 data points.

resolution, ensuring we used only quiet time measured winds ($K_p \leq 3$), and incorporating two additional years (1988-1989) of measured FPI data.

5.2.2.3. Solar Cycle Effects (ISR Measurements)

In addition to FPI wind data, we use ISR-derived neutral winds over Arecibo. Although these data are not the primary focus of this study, we nevertheless use the ISR results to supplement the Arecibo FPI data analysis. Although it is possible to derive the ISR neutral winds between altitudes of $\sim 200 - 400$ km, we use the ISR neutral wind measured at the calculated airglow emission height, ~ 250 km, to compare to the FPI measured meridional wind.

The ISR neutral winds were collected during January 1983 to January 1987. Figure 49 shows the average neutral wind response to two levels of solar activity during the equinox and June solstice periods. This data set contained insufficient data in the December solstice to perform a valid comparison of solar activity effects. This data set is characterized by low to moderate solar activity conditions.

Figure 49 shows the average meridional neutral wind for low ($\Phi \leq 100$) and moderate ($\Phi \geq 100$) solar activity during the equinox and June solstice periods for quiet geomagnetic conditions. Unlike the FPI measurements, the ISR is not restricted to nighttime measurements. We note no significant variation between the moderate and low flux conditions for the equinox and June solstice periods.

5.2.2.4. TIGCM93 Solar Cycle Activity Model Results

Figures 50 and 51 show the Arecibo TIGCM93 predicted zonal and meridional

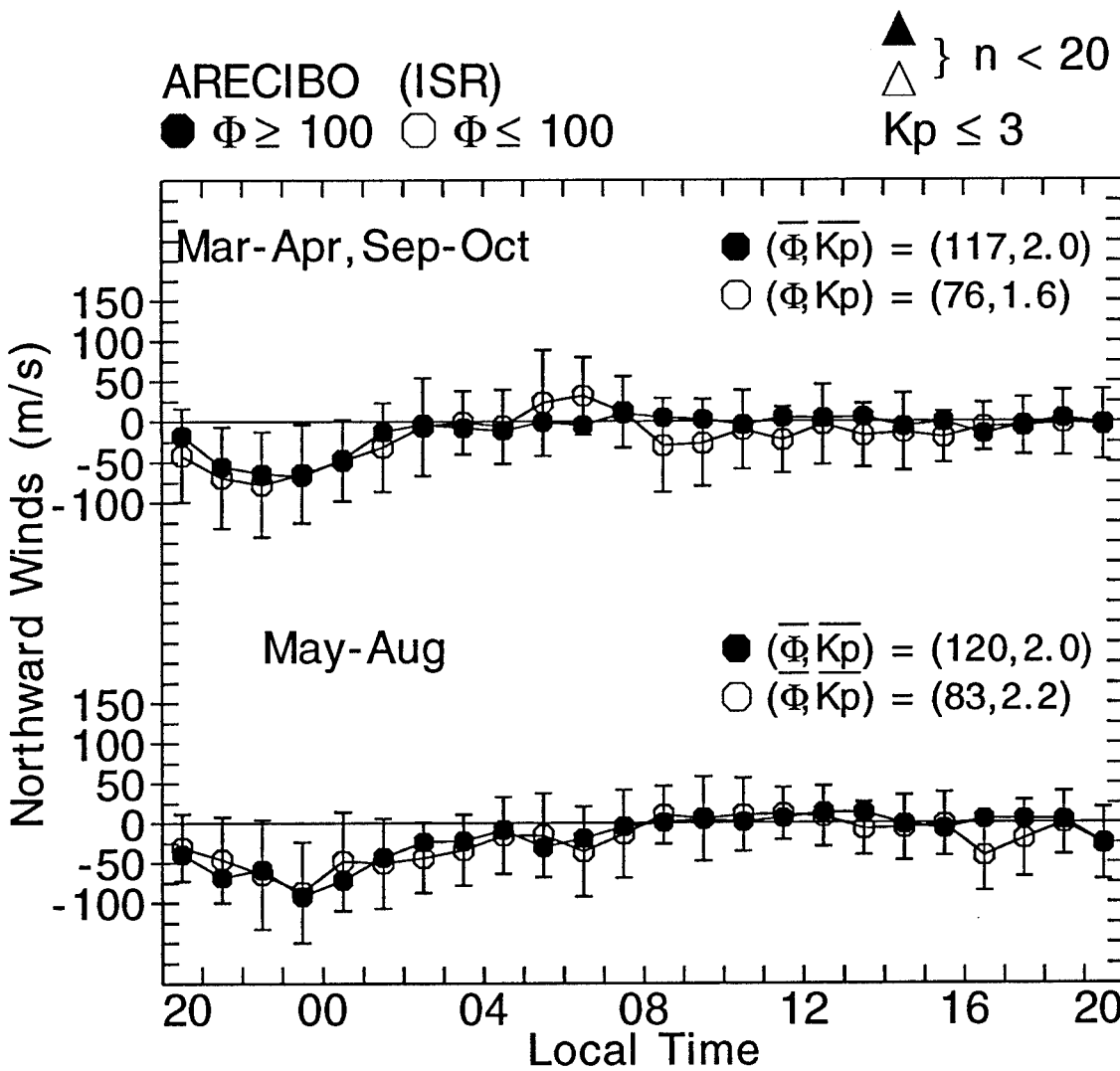


Figure 49. ISR neutral winds for Arecibo, Puerto Rico, for various seasons for low and moderate solar activity. The average neutral wind velocities are obtained by examining 1/2 hour time bins for the given solar flux interval ($100 \leq \Phi \leq 100$) and quiet geomagnetic conditions. The triangle symbol represents bin averages consisting of less than 20 data points.

neutral winds for the high, moderate, and low solar activity conditions. The model provides results for the December solstice (Day = 360), equinox (Day = 90), and June solstice (Day = 180) periods. Unlike Arequipa, the combined measured (FPI) and derived (ISR) wind data for Arecibo contain a sufficient number of data points over the solar cycle to analyze low and high solar flux conditions. We use the relative difference between the predicted high ($\Phi = 195$) and low ($\Phi = 75$) solar flux conditions to compare to the experimental wind results.

For the December solstice, Figure 50 shows no significant variations of the TIGCM zonal wind predictions due to solar activity effects. This result is not consistent with the experimental results since the measured data show a westward perturbation from low to high solar activity. For day 90, the model predictions show no wind variation due to solar activity, a result which agrees with the experimental data. Last, the model results for day 180 show a westward perturbation from high to low solar activity while the experimental data show no significant variation due to solar cycle effects.

Figure 51 shows no significant variation of the meridional TIGCM93 wind predictions to solar activity except for day 180. The December solstice prediction shows a southward wind perturbation from solar minimum to maximum conditions. The experimental data show no significant wind variation due to solar activity for all seasons. Overall, we note good agreement between the measured and TIGCM93 predicted response of the Arecibo winds to solar cycle effects during the equinox and June solstice periods but less agreement during the December solstice period.

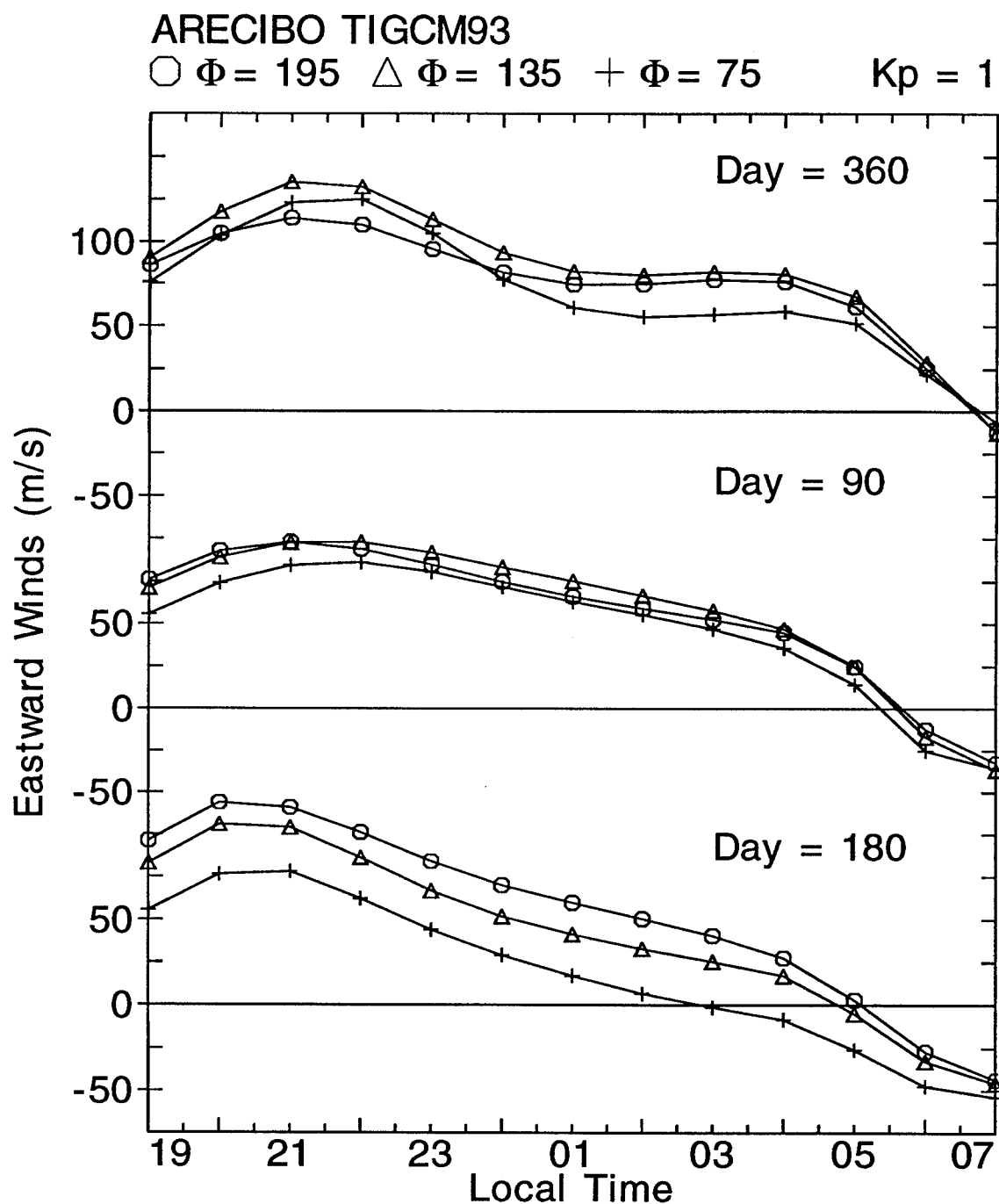


Figure 50. TIGCM93 eastward wind predictions over Arecibo, Puerto Rico, for various seasons for high, moderate, and low solar activity conditions and for quiet magnetic activity.

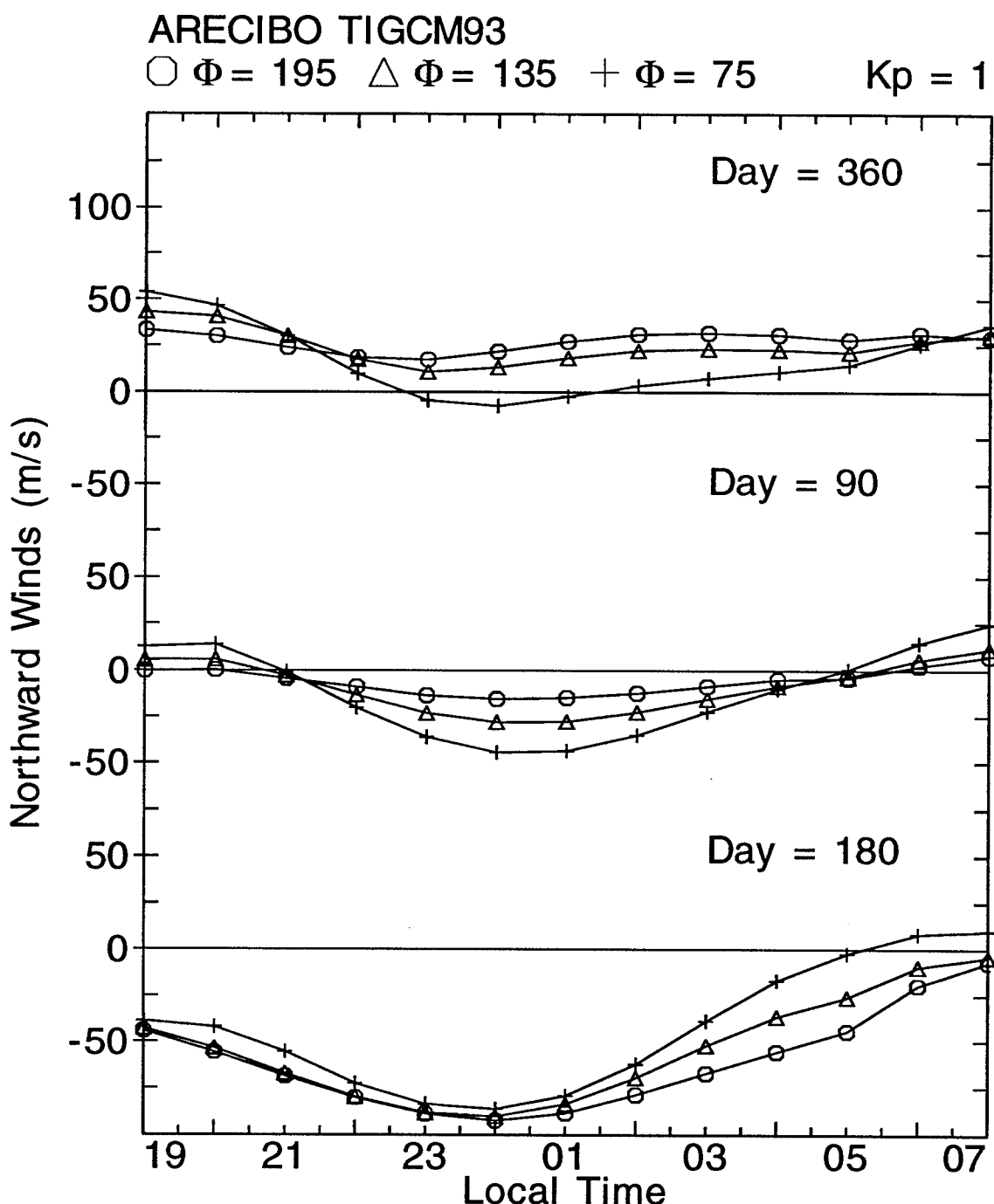


Figure 51. TIGCM93 northward wind predictions over Arecibo, Puerto Rico, for various seasons for high, moderate, and low solar activity conditions and for quiet magnetic activity.

5.2.2.5. HWM93 Solar Cycle Activity Model Results

Figures 52 and 53 show the Arecibo HWM93 modeled zonal and meridional winds for the high, moderate, and low solar activity conditions. These predicted results are for the December solstice, equinox, and June solstice periods. We use the predicted response of the neutral winds during high ($\Phi = 195$) and low ($\Phi = 75$) solar flux conditions to compare to the experimental results. The predicted solar cycle effects on the zonal winds agree with our experimental data except for the postmidnight period for the June solstice period. The HWM93 for day 180 shows a westward velocity perturbation from high to low solar activity, a result not consistent with the measured wind data results. A possible explanation for this discrepancy between the model and observed winds is the HWM93 use of derived ISR winds and satellite measured winds in addition to the FPI wind measurements. Therefore, the HWM93-predicted westward perturbation may come from either the ISR or satellite measurements, or a combination of the ISR and satellite wind measurements. Figure 53 shows the meridional predictions for Arecibo. These data show no significant wind variation due to solar activity. This predicted result agrees with the experimental Arecibo averaged winds.

5.3. DATA AND MODEL COMPARISONS

Figures 54 - 57 show comparisons of the wind results from the TIGCM93, the HWM93, and Arequipa experimental data. We compare these model predictions and experimental average winds using similar solar flux and magnetic activity conditions.

Figure 54 compares the model and experimental average eastward winds over

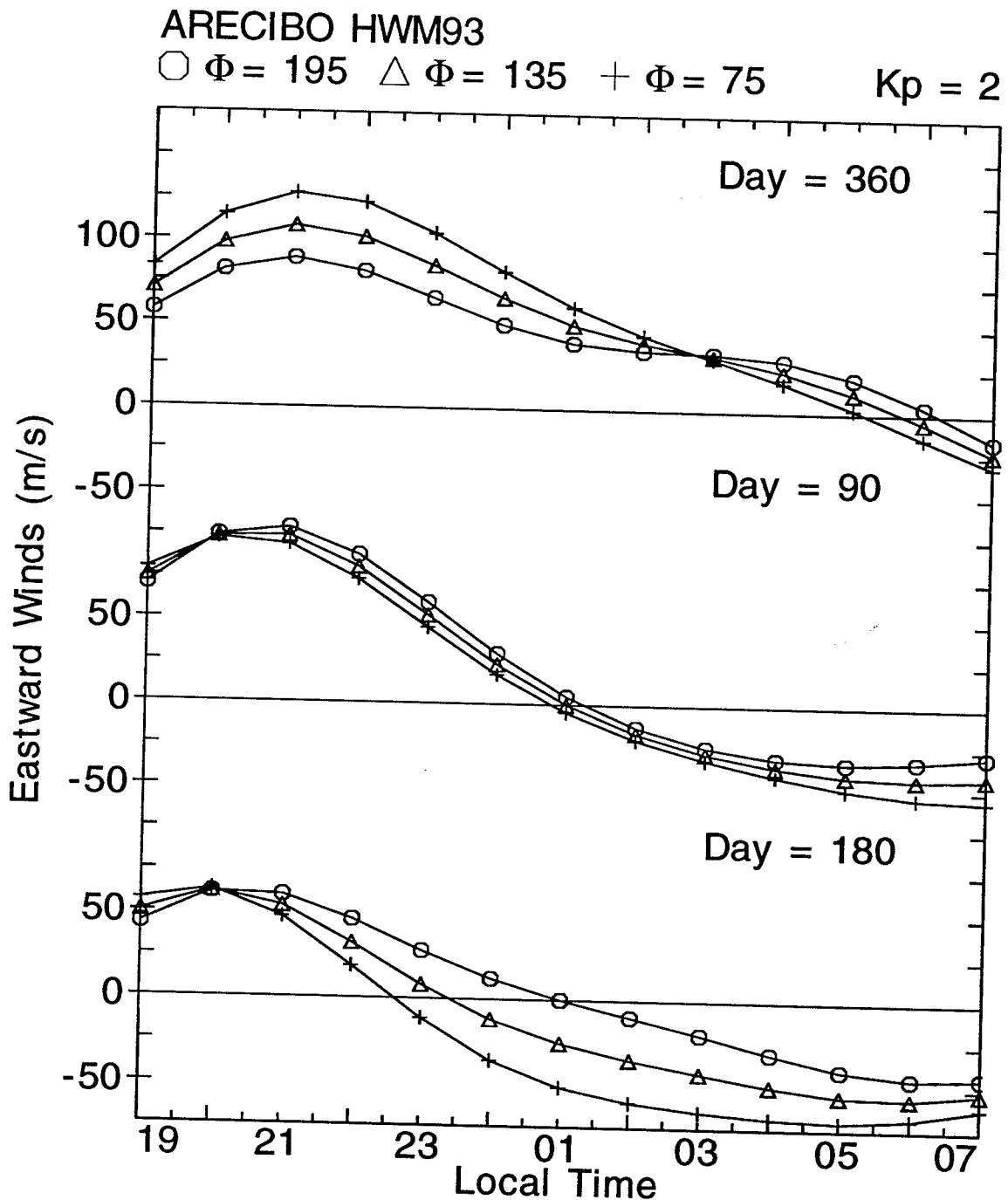


Figure 52. HWM93 eastward wind predictions over Arecibo, Puerto Rico, for various seasons for high, moderate, and low solar activity conditions and for quiet magnetic activity.

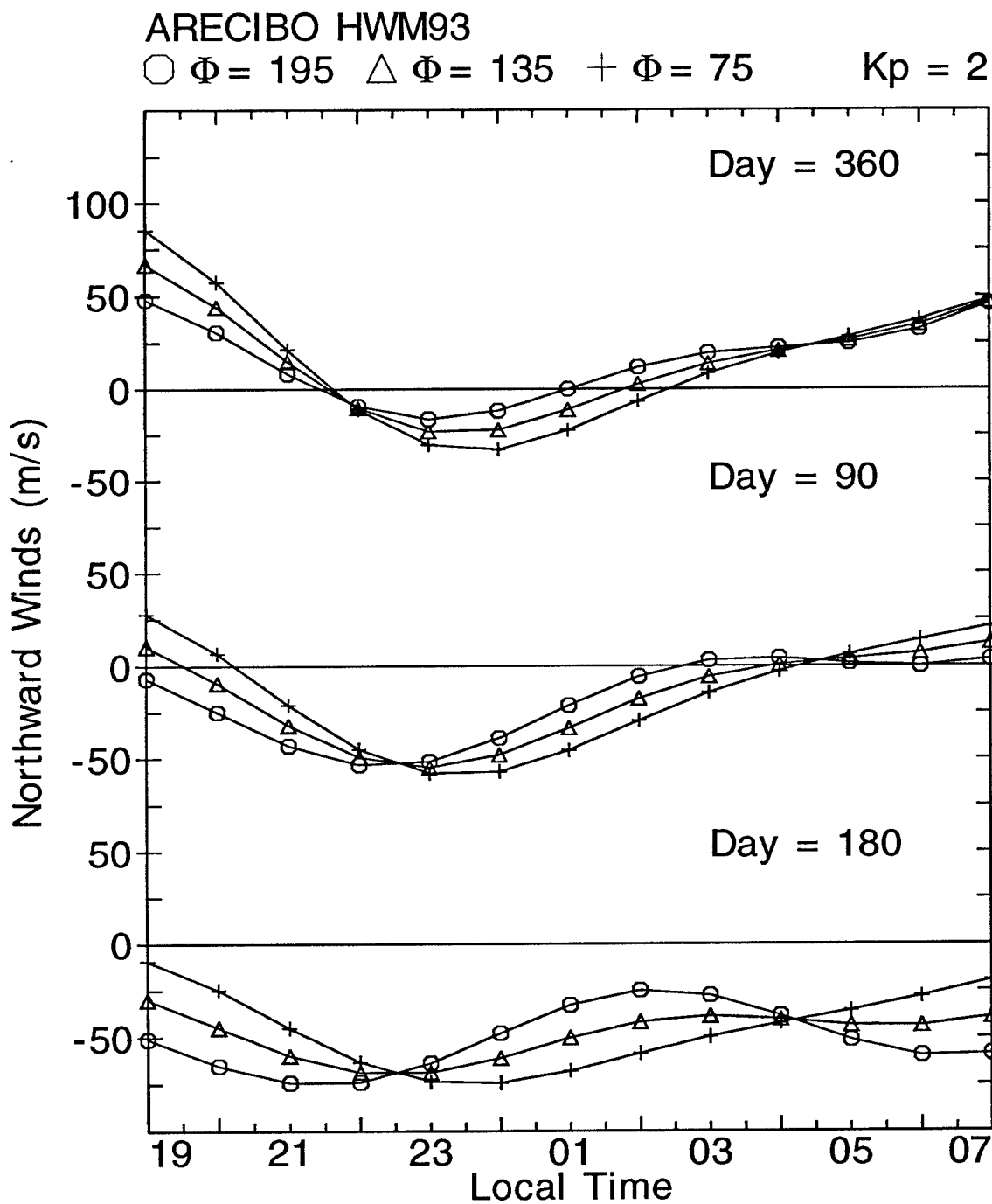


Figure 53. HWM93 northward wind predictions over Arecibo, Puerto Rico, for various seasons for high, moderate, and low solar activity conditions and for quiet magnetic activity.

Arequipa for the December solstice, equinox, and June solstice periods. We use the model winds for quiet magnetic activity conditions, $K_p = 1$ for the TIGCM93 and $K_p = 2$ for the HWM93, and moderate solar activity except during the June solstice. The June solstice experimental wind average consists of wind profiles measured during high solar activity; hence, we use the modeled winds for high solar flux conditions ($\Phi_{TH} = 195$). As expected, the HWM93 wind predictions agree with experimental results for all seasons. The TIGCM93 predictions show excellent agreement with the measured winds in the June solstice and equinox periods. However, the TIGCM93 shows smaller eastward winds throughout the night for the December solstice compared to the experimental winds during the same time period. Figure 55 presents the modeled and measured meridional winds over Arequipa. The model predictions agree with the experimental wind averages during the equinox and December solstice periods, but the TIGCM93 predicts slightly larger northward winds from 2300 LT to 0230 LT compared to the measured data during the June solstice.

Figures 56 and 57 show the model and experimental winds for the eastward and northward averages over Arecibo for the December solstice, equinox, and June solstice periods. Where possible, we used model results with similar solar flux activity to that of the experimental winds. These model solar flux values are different for each season and are provided in parentheses below the average experimental solar flux and magnetic activity values.

Figure 55 compares the TIGCM93 and HWM93 eastward predictions to the experimental winds over Arecibo. The predicted eastward winds agree with the

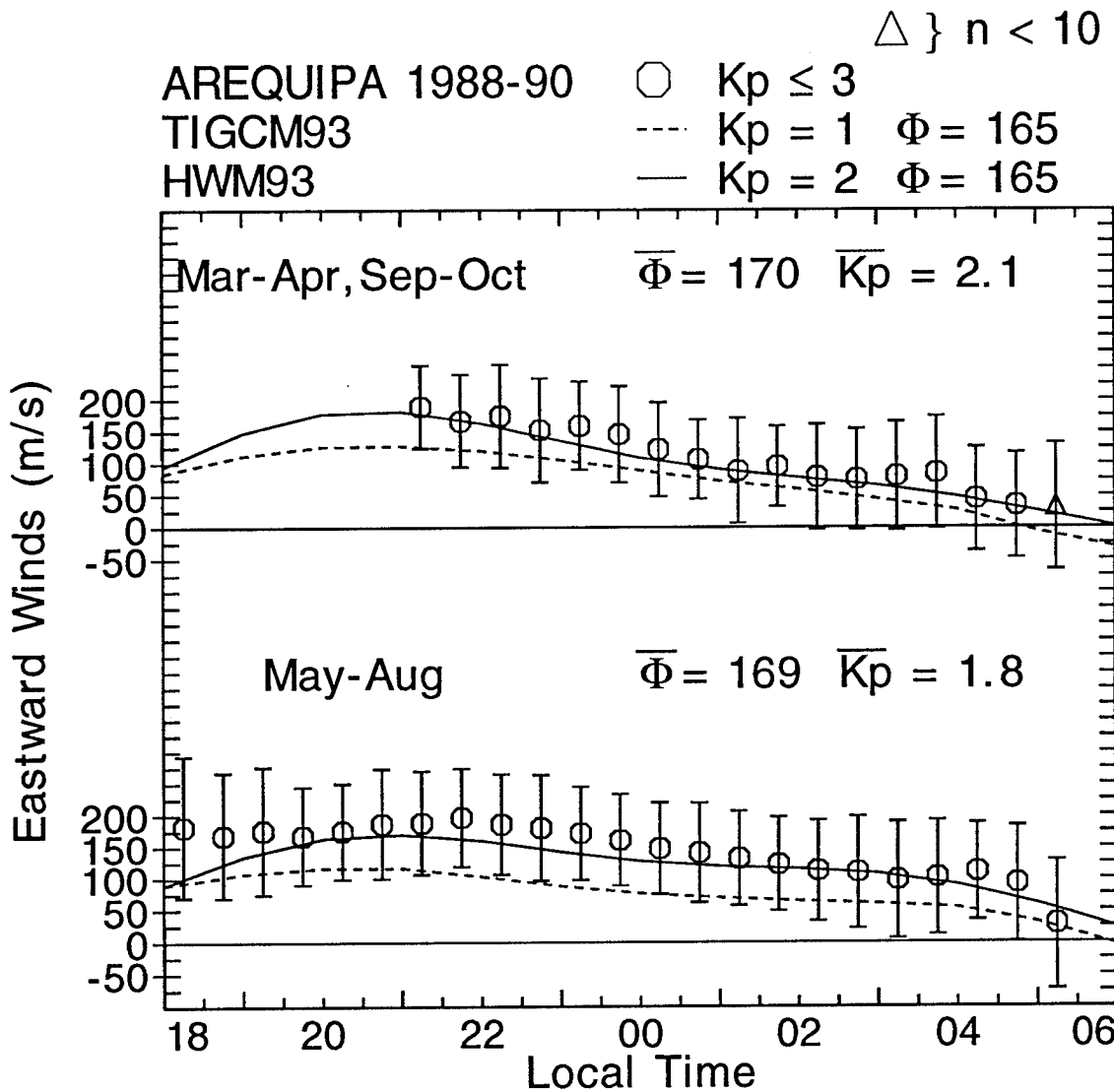


Figure 54. Model and observed eastward wind comparison for Arequipa, Peru. These comparisons are for the equinox and June solstice. The TIGCM93 and HWM93 predictions are given by the dashed and solid line, respectively. The observed wind results, represented by the open circles and error bars (standard deviation), are averaged FPI data for moderate solar flux conditions and quiet magnetic activity.

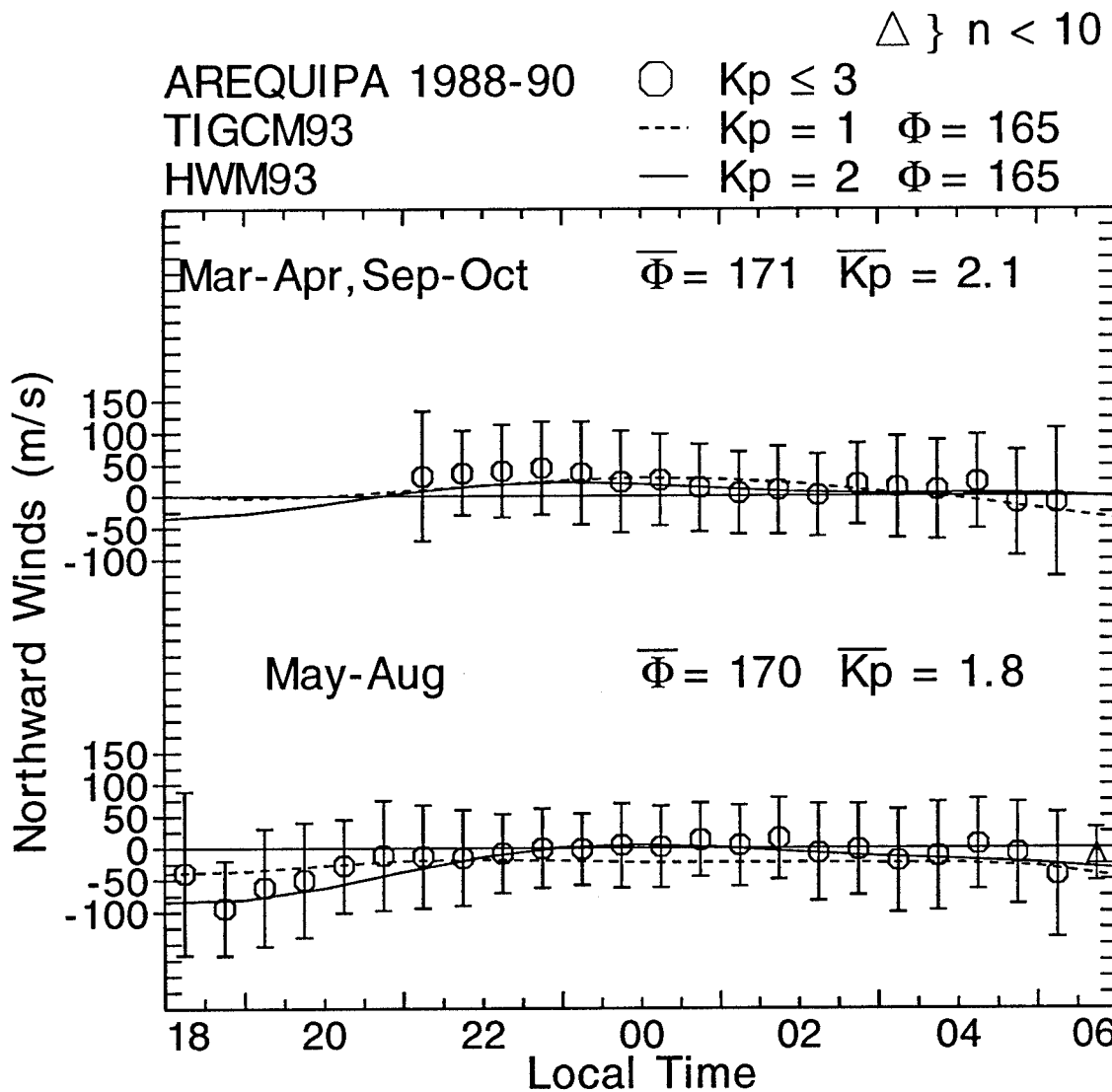


Figure 55. Model and observed northward wind comparison for Arequipa, Peru. These comparisons are for the equinox and June solstice. The TIGCM93 and HWM93 predictions are given by the dashed and solid line, respectively. The observed wind results, represented by the open circles and error bars, are averaged FPI data for moderate solar flux conditions and quiet magnetic activity.

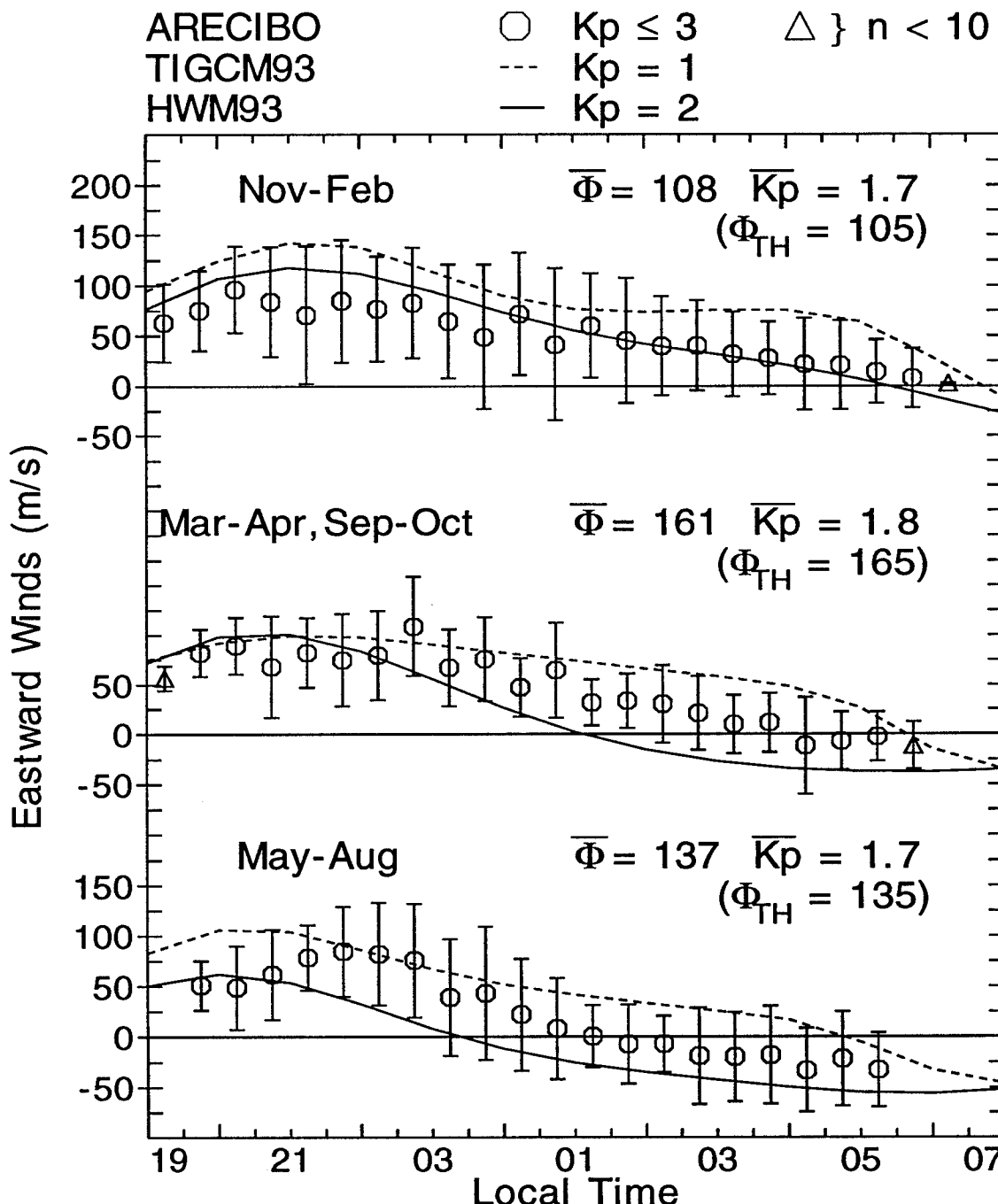


Figure 56. Model and observed eastward wind comparison for various seasons for Arecibo, Puerto Rico. The TIGCM93 and HWM93 predictions are given by the dashed and solid line, respectively. The Φ_{TH} represents the solar flux value used for the model predictions. The average wind results, represented by the open circles and error bars, are averaged FPI data for various solar flux conditions and quiet magnetic activity.

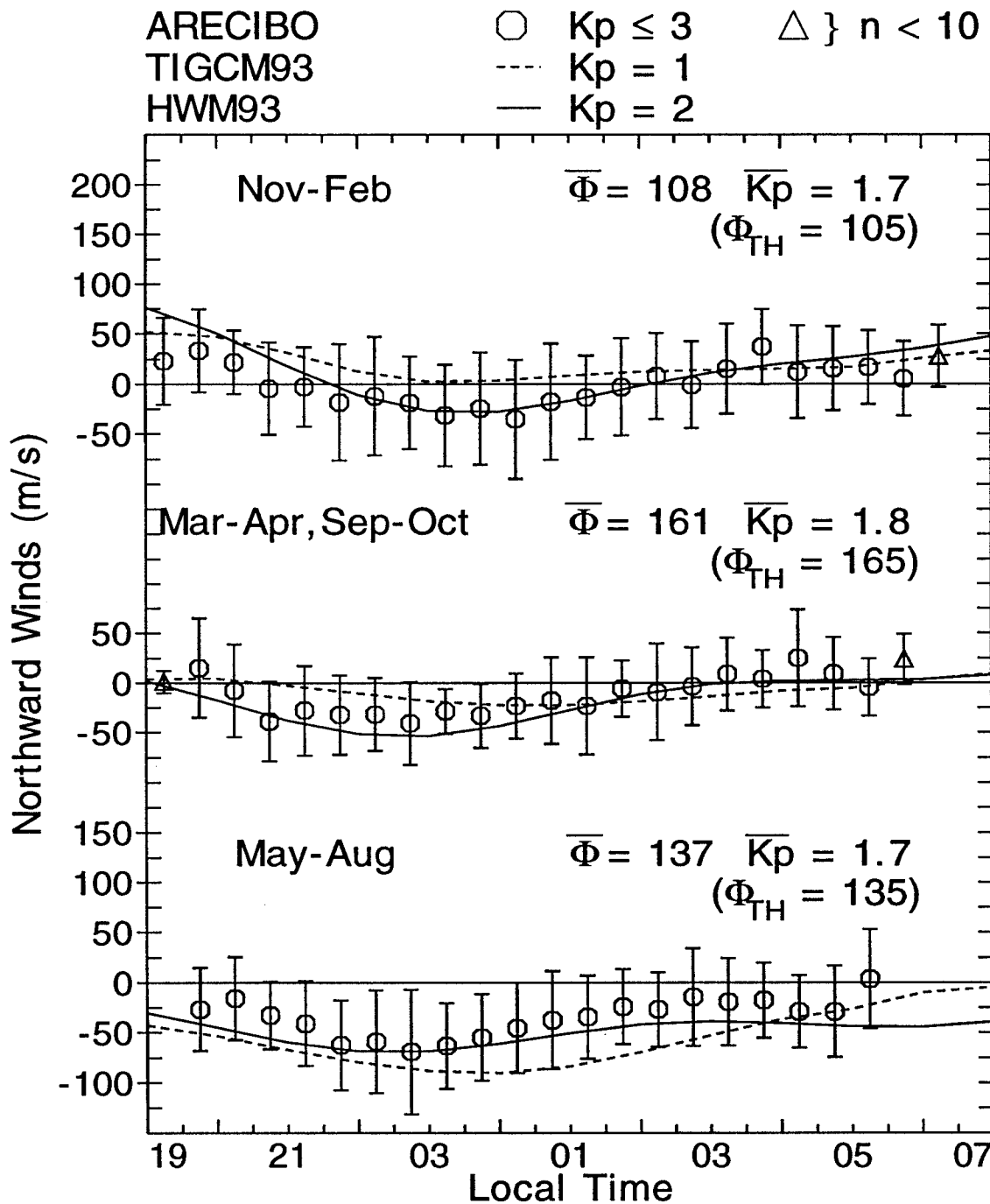


Figure 57. Model and observed northward wind comparison for various seasons for Arecibo, Puerto Rico. The TIGCM93 and HWM93 predictions are given by the dashed and solid line, respectively. The Φ_{TH} represents the solar flux value used for the model predictions. The average wind results, represented by the open circles and error bars, are averaged FPI data for various solar flux conditions and quiet magnetic activity.

measured winds during the premidnight period except for the June solstice where we note poor agreement between the predicted and experimental winds throughout the night. We also note that the TIGCM93 tends to predict larger eastward winds for all seasons, while the HWM93 shows the westward reversal occurring at an earlier time for the experimental average winds during the equinox and June solstice periods. Figure 57 shows good agreement between the Arecibo model northward wind predictions and experimental wind averages.

CHAPTER 6

MAGNETIC ACTIVITY EFFECTS ON THE LOW LATITUDE THERMOSPHERIC WINDS

6.1. INTRODUCTION

In this chapter we use Fabry-Perot measurements at Arequipa (1988-1990) and Arecibo (1980-1989) to determine the magnetic activity effects on the low latitude F-region thermospheric winds. We also compare the magnetic activity response of the measured winds to TIGCM93 and HWM93 predictions.

6.2. MAGNETIC ACTIVITY EFFECTS

6.2.1. Arequipa

Figures 58 and 59 present the averaged eastward and northward neutral winds over Arequipa during magnetically quiet ($K_p \leq 3$) and disturbed ($K_p \geq 3$) conditions for all levels of solar activity during the equinox and June solstice periods. The Arequipa database does not contain enough disturbed wind data for the December solstice to adequately determine the magnetic activity effects on the neutral winds during this period. The error bars represent ± 1 standard deviation about the magnetically quiet mean. The error bars for the disturbed winds are not shown but are comparable to those of the quiet wind. The results in Figure 58 show a westward perturbation when the magnetic activity becomes disturbed for the equinox and June solstice periods. The largest decrease in eastward winds (~ 25 - 50 m/s) during active conditions occurs in the

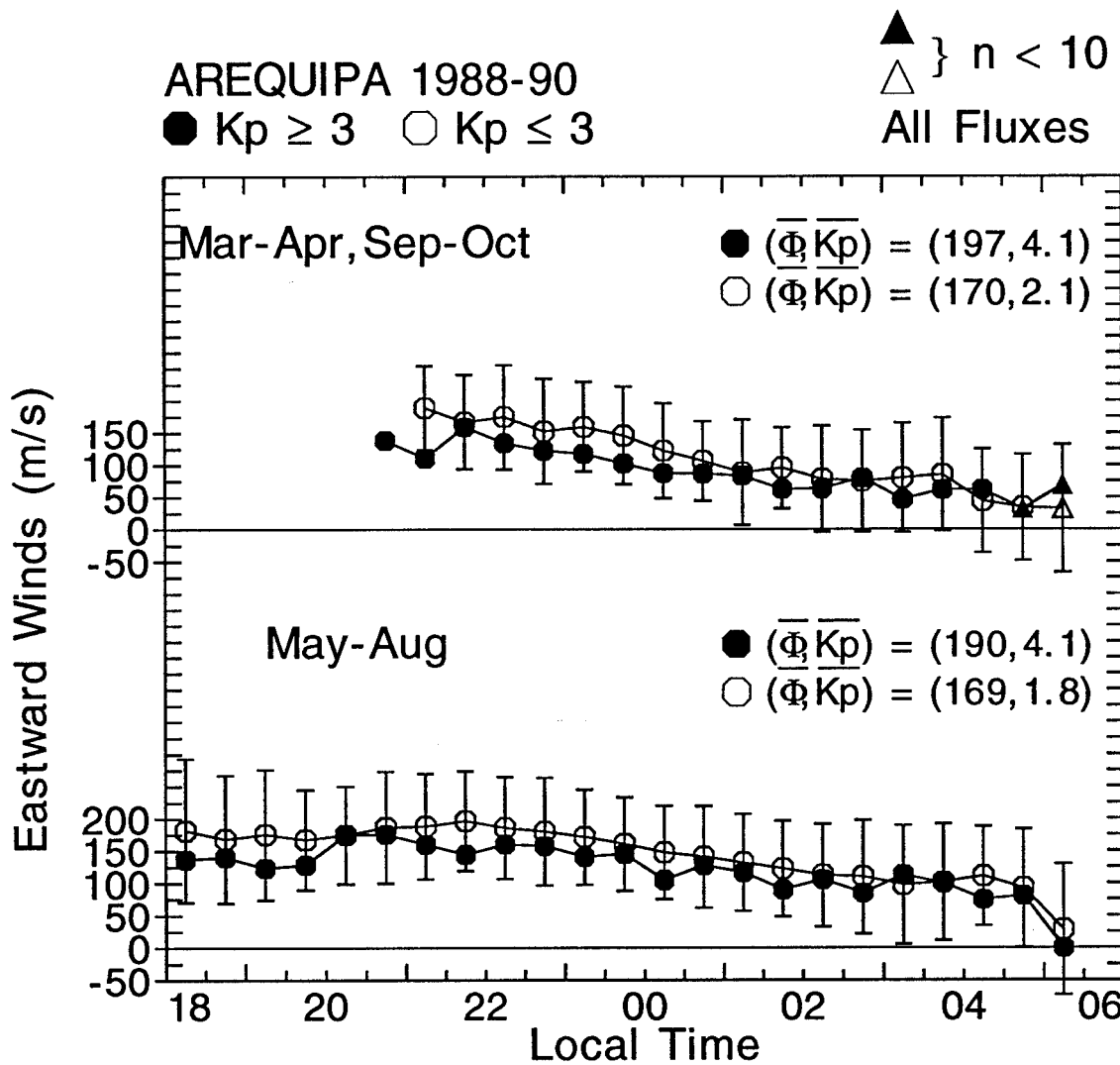


Figure 58. Measured eastward wind averages over Arequipa, Peru, for the equinox (March-April, September-October) and June solstice (May-August) periods for quiet ($K_p \leq 3$) and disturbed ($K_p \geq 3$) conditions. The solid and open triangles represent averages based on less than 10 data points.

premidnight period for both equinox and June solstice seasons. Figure 59 shows the nighttime average neutral meridional winds over Arequipa are relatively unchanged for quiet and active magnetic periods during the represented seasons. This study reports for the first time the effects of geomagnetic activity on the ground-based FPI wind measurements at Arequipa, Peru.

Our quiet and disturbed zonal wind results are consistent with magnetic activity studies in *Wu et al.* [1994] using Dynamics Explorer 2 (DE 2) neutral wind data. The DE 2 satellite uses data collected within the 200 - 400 km altitude range during 1981 - 1983 for day- and nighttime conditions. Although most DE 2 data were collected during the December solstice, some DE 2 data were collected during September - October. This data set allows us to compare DE 2 results with our FPI equinox winds. The DE 2 data were subdivided into geomagnetically active ($K_p > 3$) and quiet ($K_p < 3$) periods to analyze the response of the neutral wind to magnetic activity effects [*Wu et al.*, 1994]. *Wu et al.* [1994] showed a westward perturbation when the magnetic activity became disturbed, a result that agrees with our FPI disturbed observations. The DE 2 data contained too few nighttime disturbed meridional wind data points to properly investigate magnetic activity effects on the northward winds.

6.2.2. Arecibo

We have also averaged the eastward and northward neutral winds for quiet and disturbed conditions over Arecibo for each season. Figure 60 shows the averaged eastward winds for all levels of solar activity during the December solstice, equinox, and

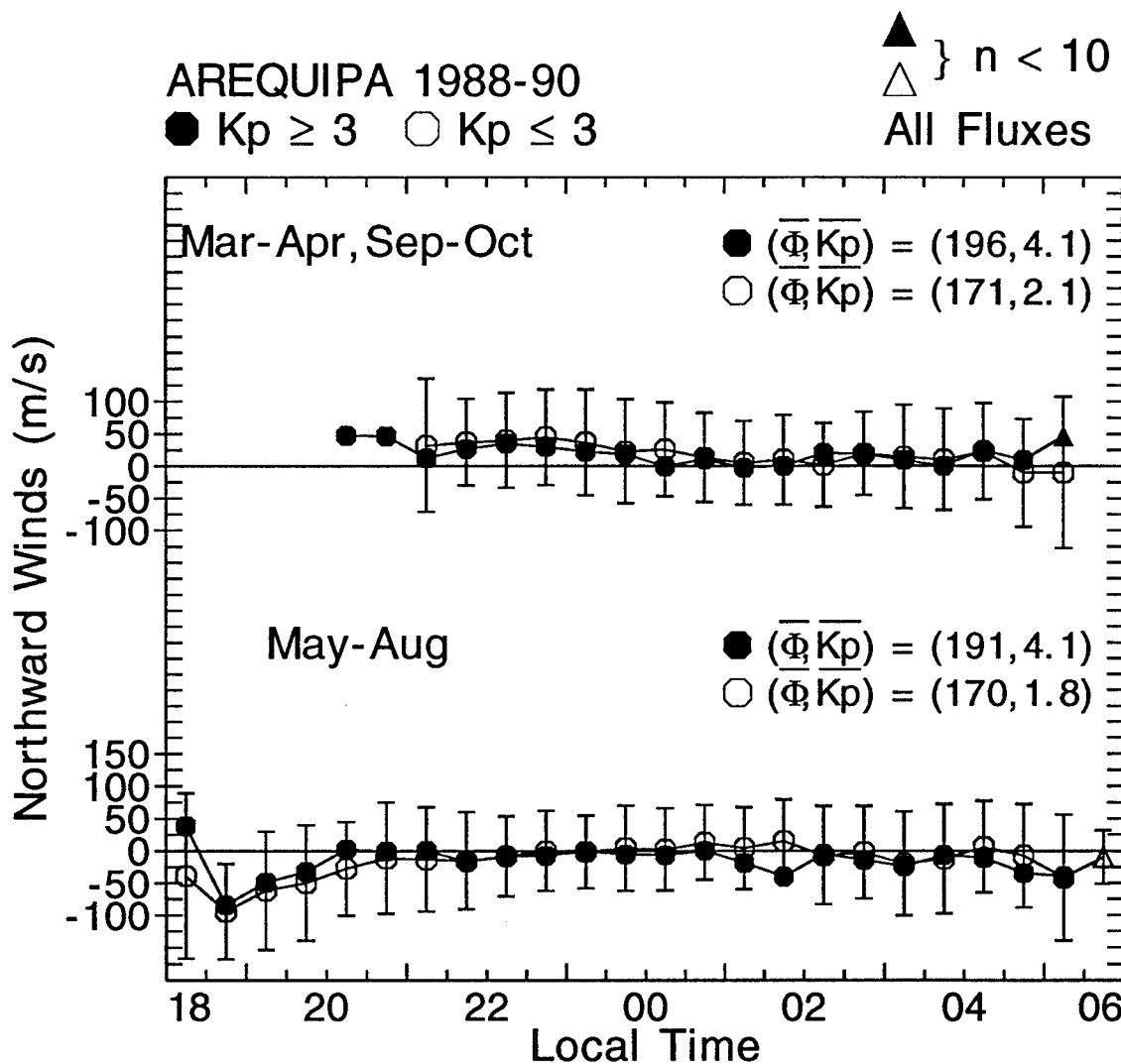


Figure 59. Measured northward wind averages over Arequipa, Peru, for the equinox (March-April, September-October) and June solstice (May-August) periods for quiet ($K_p \leq 3$) and disturbed ($K_p \geq 3$) conditions. The solid and open triangles represent averages based on less than 10 data points.

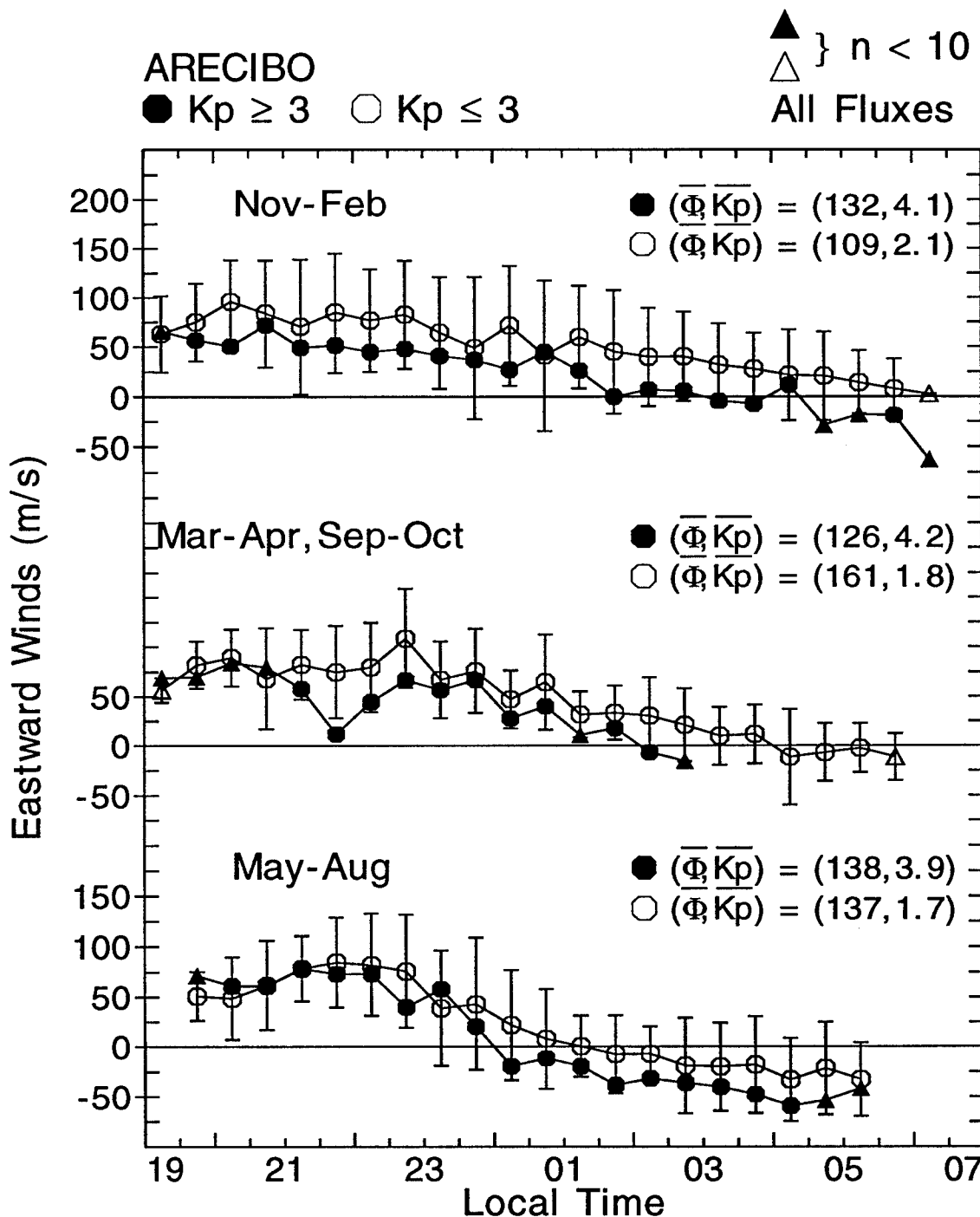


Figure 60. Measured eastward wind averages over Arecibo, Puerto Rico, for various seasons for quiet ($K_p \leq 3$) and disturbed ($K_p \geq 3$) conditions. The solid and open triangles represent averages based on less than 10 data points.

June solstice periods. As the magnetic activity becomes disturbed, the data show a westward perturbation during all nighttime hours for the December solstice and equinox periods while we note a westward perturbations in the postmidnight period during the June solstice. Figure 61 shows no significant variation between the quiet and disturbed northward winds.

Burnside et al. [1991] showed westward perturbations over Arecibo during storm-time conditions. This previous study agrees with our measured wind results. However, these studies concentrated on a few disturbed days and did not provide any indication of the average neutral wind response to magnetic activity effects at Arecibo.

Buonsanto and Foster [1993] and *Burnside et al.* [1991] analyzed the meridional wind response to disturbed conditions over Arecibo. Although these studies showed that the low latitude meridional wind responds to storm time effects, they showed both northward and southward perturbations disturbed conditions. Even though these studies concentrated on a few disturbed days, they are consistent with our results. These northward and southward wind perturbations would tend to cancel each other over a long-term average. This is consistent with our results over Arecibo because we found no significant variation in the average meridional wind response to magnetic activity effects.

In addition to FPI wind data, we use ISR-derived neutral winds over Arecibo. The ISR neutral winds were collected during January 1983 to January 1987. Figure 62 shows the quiet and disturbed wind averages for the December solstice, equinox, and June solstice. We note no significant variation between the December solstice disturbed

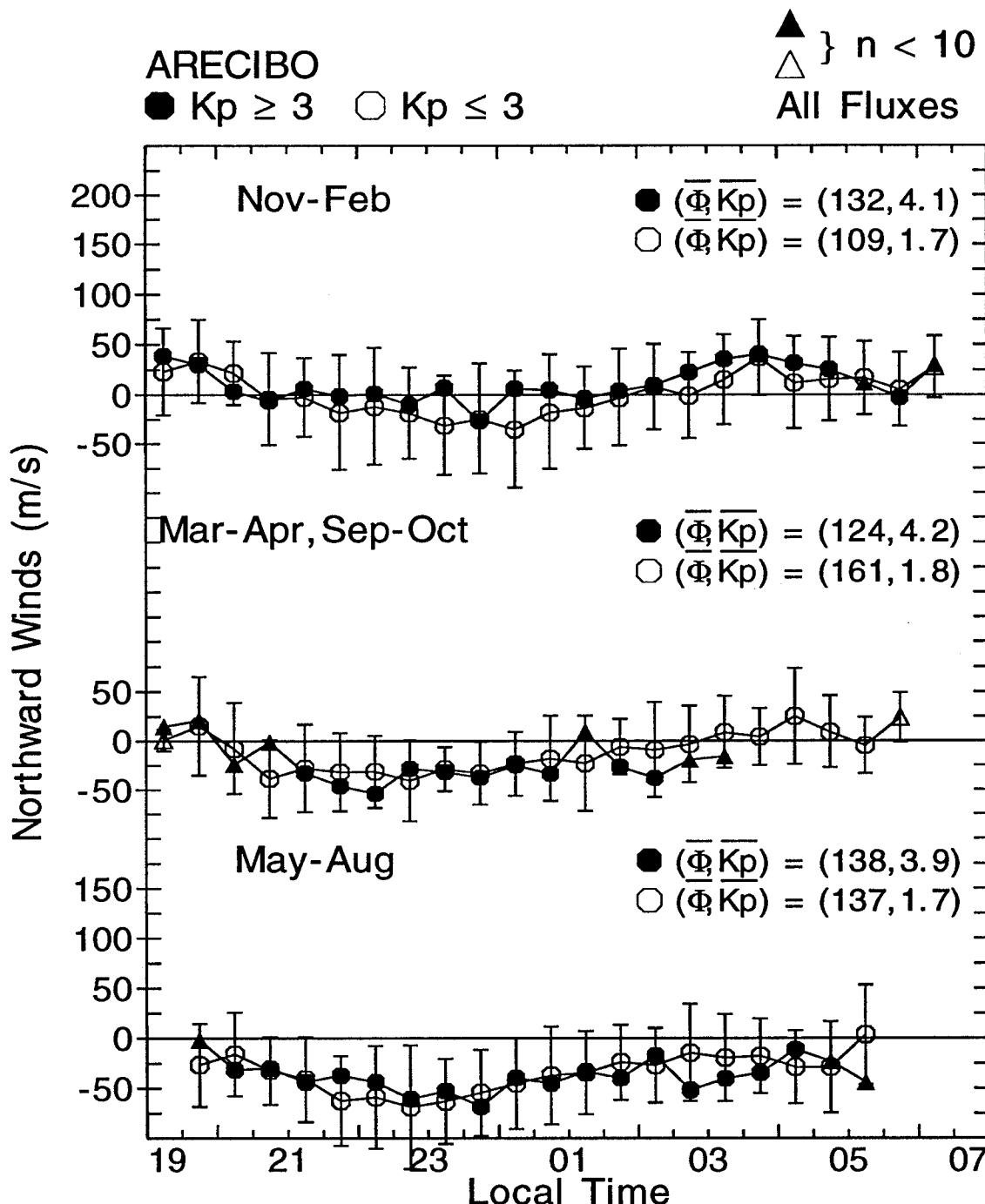


Figure 61. Measured northward wind averages over Arecibo, Puerto Rico, for various seasons for quiet ($K_p \leq 3$) and disturbed ($K_p \geq 3$) conditions. The solid and open triangles represent averages based on less than 10 data points.

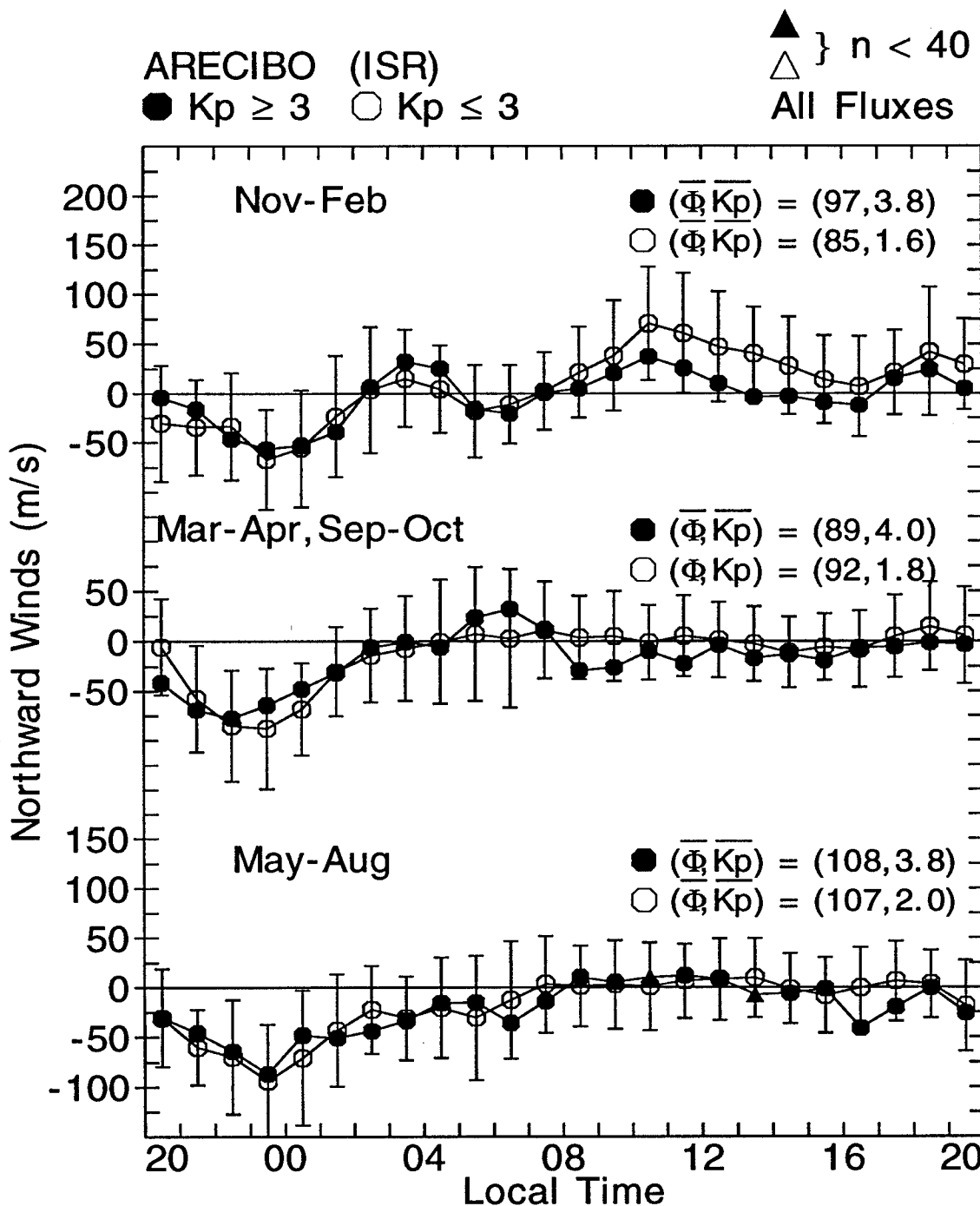


Figure 62. Measured ISR neutral winds over Arecibo, Puerto Rico, for various seasons for quiet ($K_p \leq 3$) and disturbed ($K_p \geq 3$) conditions. The solid and open triangles represent averages based on less than 40 data points.

and quiet winds from 1600 LT to 0900 LT, but the data show a southward perturbation from quiet to disturbed magnetic activity from 1000 LT to 1500 LT. The data also show no significant magnetic activity effects during the equinox and June periods. The ISR and FPI results indicate the response of the average meridional winds is not affected by magnetic activity.

6.3. SHORT-TERM AND EXTENDED MAGNETIC ACTIVITY

We analyze the short-term (3 hour) and extended time (12 hour) magnetic activity to fully investigate the neutral wind response to storm-time events. We define three magnetic activity cases, which cover all storm-time scenarios. These magnetic activity classifications are listed in TABLE 16.

The first magnetic activity classification is the extended quiet condition. This

TABLE 16. Magnetic Activity Classification

Classification Name	K _p Index	Magnetic Activity Name
ΣQ,Q	12 hr K _p ≤ 3 K _p ≤ 3	extended quiet
ΣQ,D	12 hr K _p ≤ 3 K _p ≥ 3	short-term disturbed
ΣD,D	12 hr K _p ≥ 3 K _p ≥ 3	extended disturbed

case is defined by a magnetically quiet 12-hour K_p and 3-hour K_p . The 12-hour K_p is the average of the three consecutive K_p values preceding the K_p value at the time of the wind measurement. The 3-hour K_p is the magnetic activity defined at the time of wind measurement. The second classification highlights short-term disturbed effects. This case is defined by the previous magnetic activity, which is quiet (12-hour $K_p \leq 3$) and then becomes disturbed ($K_p \geq 3$). The last case defines the condition where the previous and short-term magnetic activity are disturbed. This is the first time this type of magnetic activity classification has been applied to investigate the response of the thermospheric neutral winds to magnetic activity effects.

The extended quiet and disturbed classifications define the extreme range of the magnetic activity conditions. If no wind variation is noted between the extended quiet and disturbed cases, we conclude there will be no short-term disturbed effects since this case is included in the disturbed baseline.

6.4. NEUTRAL WIND RESPONSE TO MAGNETIC ACTIVITY

6.4.1. Arequipa and Arecibo Northward Wind

Figures 63 and 64 present the extended quiet and disturbed northward winds over Arequipa and Arecibo for all levels of solar activity. Figure 63 shows the results for the June solstice and Figure 64 shows the results for the equinox period. Our data set does not contain enough statistically reliable averages during the December solstice to conduct a proper analysis of magnetic activity effects for both Arequipa and Arecibo. These graphs show the average wind profile and spline fits for the average solar flux

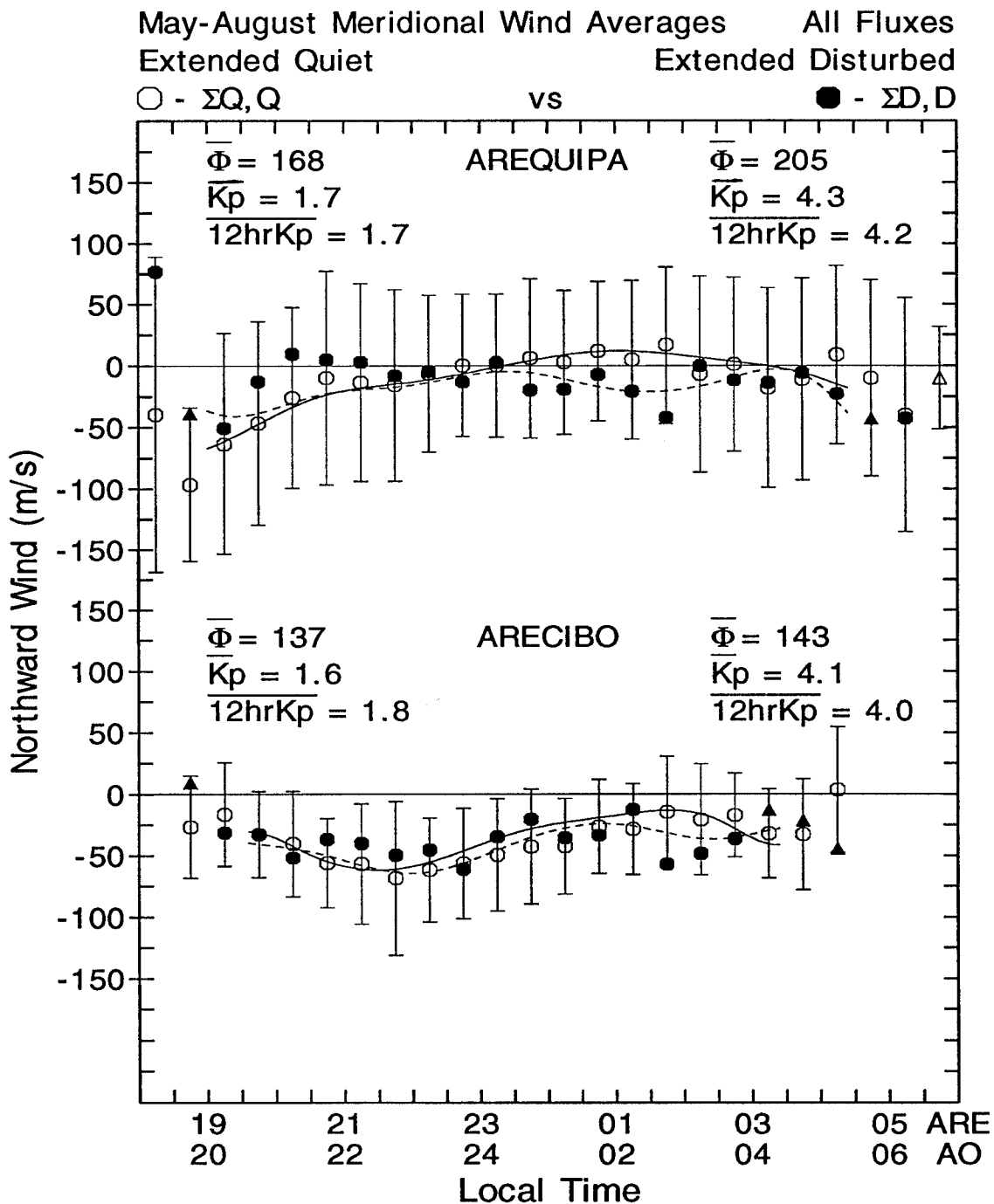


Figure 63. June solstice extended quiet ($\Sigma Q, Q$) and extended disturbed ($\Sigma D, D$) northward wind comparisons for Arequipa and Arecibo. The solid line is the spline fit for the $\Sigma Q, Q$ case and the dashed line is the spline fit for the $\Sigma D, D$ case. The open and solid triangles represent averages consisting of less than 10 wind data points.

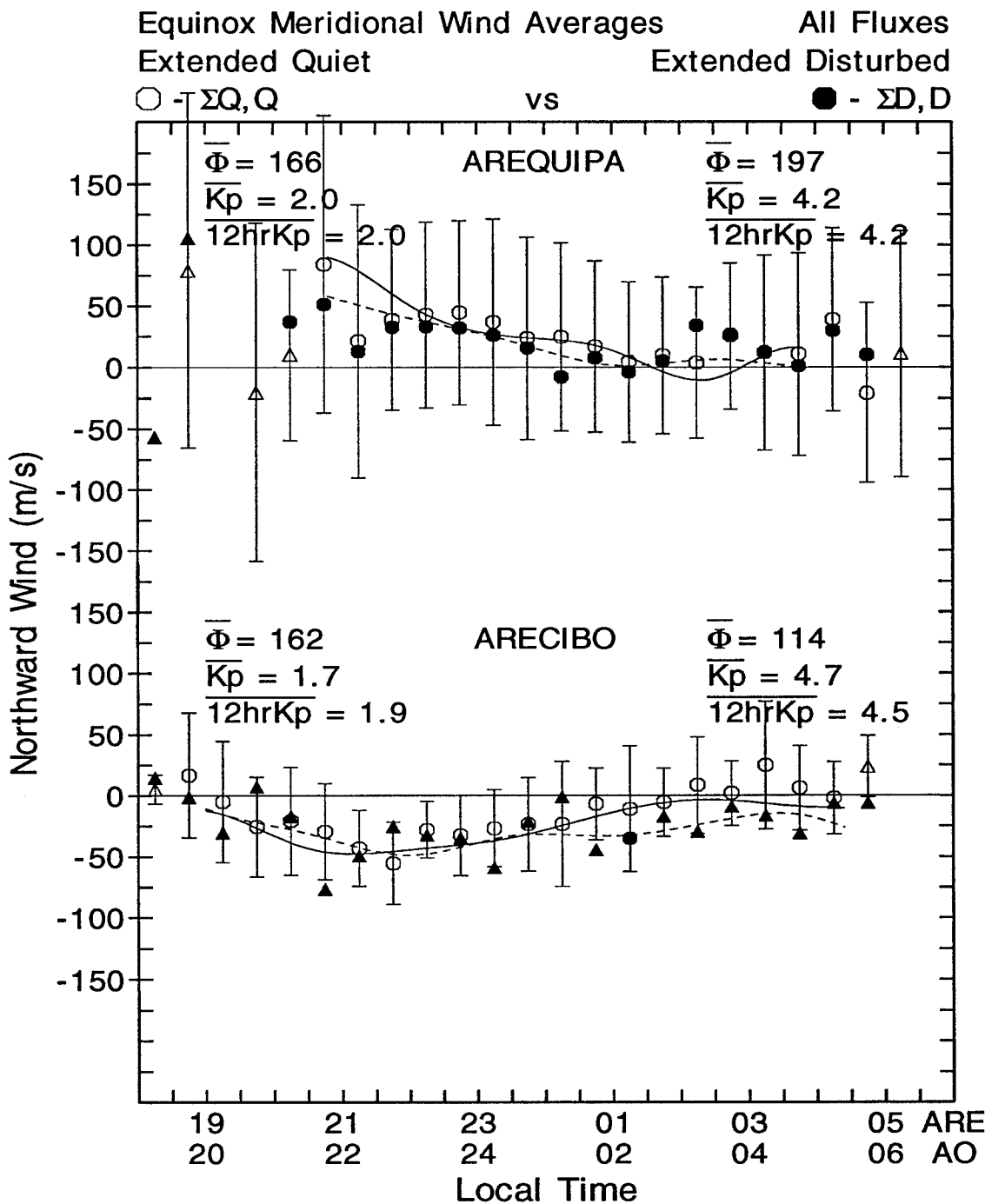


Figure 64. Equinox extended quiet ($\Sigma Q, Q$) and extended disturbed ($\Sigma D, D$) northward wind comparisons for Arequipa and Arecibo. The solid line is the spline fit for the $\Sigma Q, Q$ case and the dashed line is the spline fit for the $\Sigma D, D$ case. The open and solid triangles represent averages consisting of less than 10 wind data points.

($\overline{\Phi}$), average short-term magnetic activity ($\overline{K_p}$), and average extended magnetic activity ($\overline{12hrK_p}$) conditions for Arequipa and Arecibo. The open symbols represent the extended quiet average wind profile, and the filled symbols represent the extended disturbed average wind profile. The solid line is the spline fit for the quiet average profile, and the dashed line is the spline fit for the disturbed average profile. The open and filled triangle symbols represent average wind values consisting of less than ten data points.

Figures 63 and 64 show no significant variation between the extended quiet and disturbed northward averages. Because these comparisons were made using the extreme magnetic activity cases, we conclude that the average northward wind response for Arequipa and Arecibo is not affected by magnetic activity.

6.4.2. Arequipa and Arecibo Eastward Wind

Figures 65 and 66 present the extended quiet and disturbed eastward winds over Arequipa and Arecibo. We use the same graph setups described in the previous section but applied to the eastward quiet and disturbed wind averages. The solid and the dashed lines are the spline fits for the quiet and disturbed average winds, respectively.

The near-June solstice and equinox periods show a significant westward velocity perturbation for the disturbed condition for Arequipa and Arecibo. We compared the extended quiet to the short-term disturbed condition for the June solstice periods in Figure 67 to further isolate the magnetic activity effects on the averaged eastward

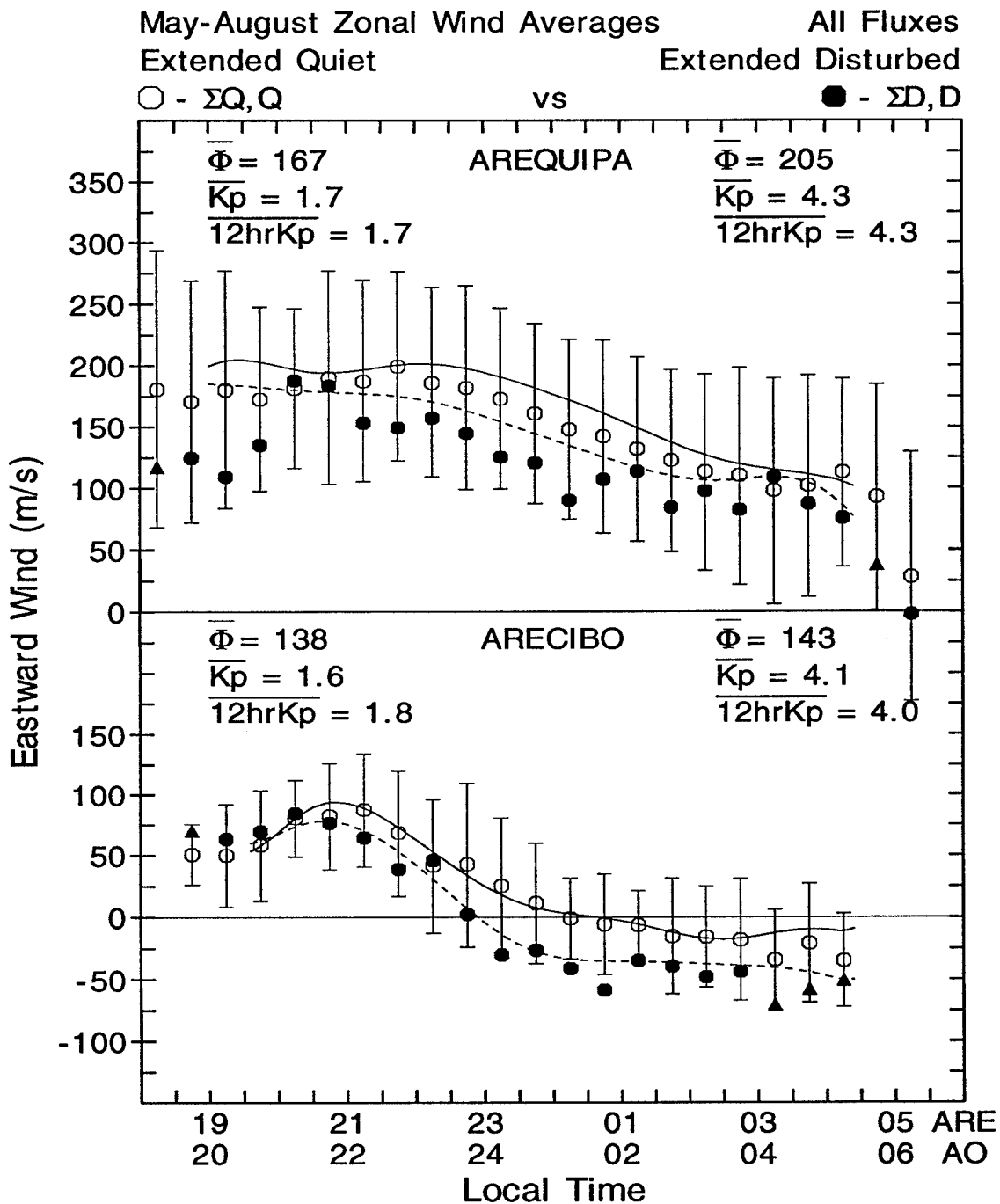


Figure 65. June solstice extended quiet ($\Sigma Q, Q$) and extended disturbed ($\Sigma D, D$) eastward wind comparisons for Arequipa and Arecibo. The solid line is the spline fit for the $\Sigma Q, Q$ case and the dashed line is the spline fit for the $\Sigma D, D$ case. The open and solid triangles represent averages consisting of less than 10 wind data points.

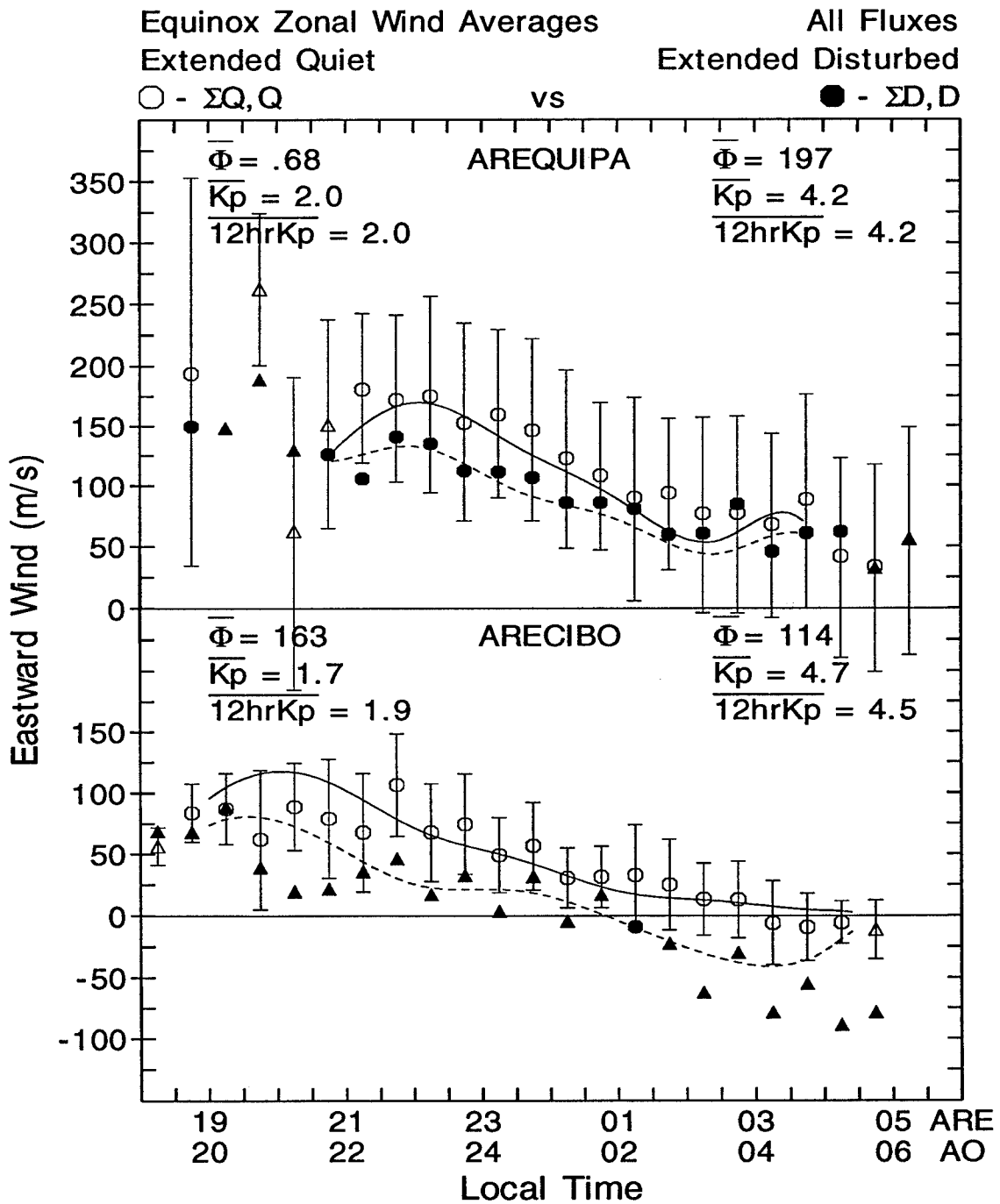


Figure 66. Equinox extended quiet ($\Sigma Q, Q$) and extended disturbed ($\Sigma D, D$) eastward wind comparisons for Arequipa and Arecibo. The solid line is the spline fit for the $\Sigma Q, Q$ case and the dashed line is the spline fit for the $\Sigma D, D$ case. The open and solid triangles represent averages consisting of less than 10 wind data points.

winds. The wind databases for Arequipa and Arecibo do not contain enough short-term disturbed wind data to perform a valid comparison of magnetic activity effects on the winds for the equinox period.

Figure 67 shows no significant variation between the extended quiet and short-term disturbed eastward winds over Arequipa. For Arecibo, we note a small westward velocity perturbation as the short-term becomes disturbed in the postmidnight period during the June solstice.

6.5 MAGNETIC ACTIVITY CUBIC SPLINE AND MODEL PREDICTIONS

6.5.1. Arequipa

6.5.1.1. Cubic Spine Predictions

We now investigate these same magnetic activity conditions using the cubic spline fits. Figures 68 and 69 show the spline fits for the northward and eastward winds over Arequipa for the extended quiet ($\Sigma Q, Q$), short-term disturbed ($\Sigma Q, D$), and extended disturbed ($\Sigma D, D$) magnetic activity cases. The solar flux is set to moderate flux conditions, $\Phi = 150$, to eliminate variations due to solar activity.

Figure 68 shows the cubic spline predictions for the northward winds during the equinox (day 90) and December solstice (day 180) periods. The June solstice (day 360) prediction is not shown due to the limited number of wind data points for this season. These spline predictions show no significant variations in the neutral wind response due to magnetic activity for days 90 and 180.

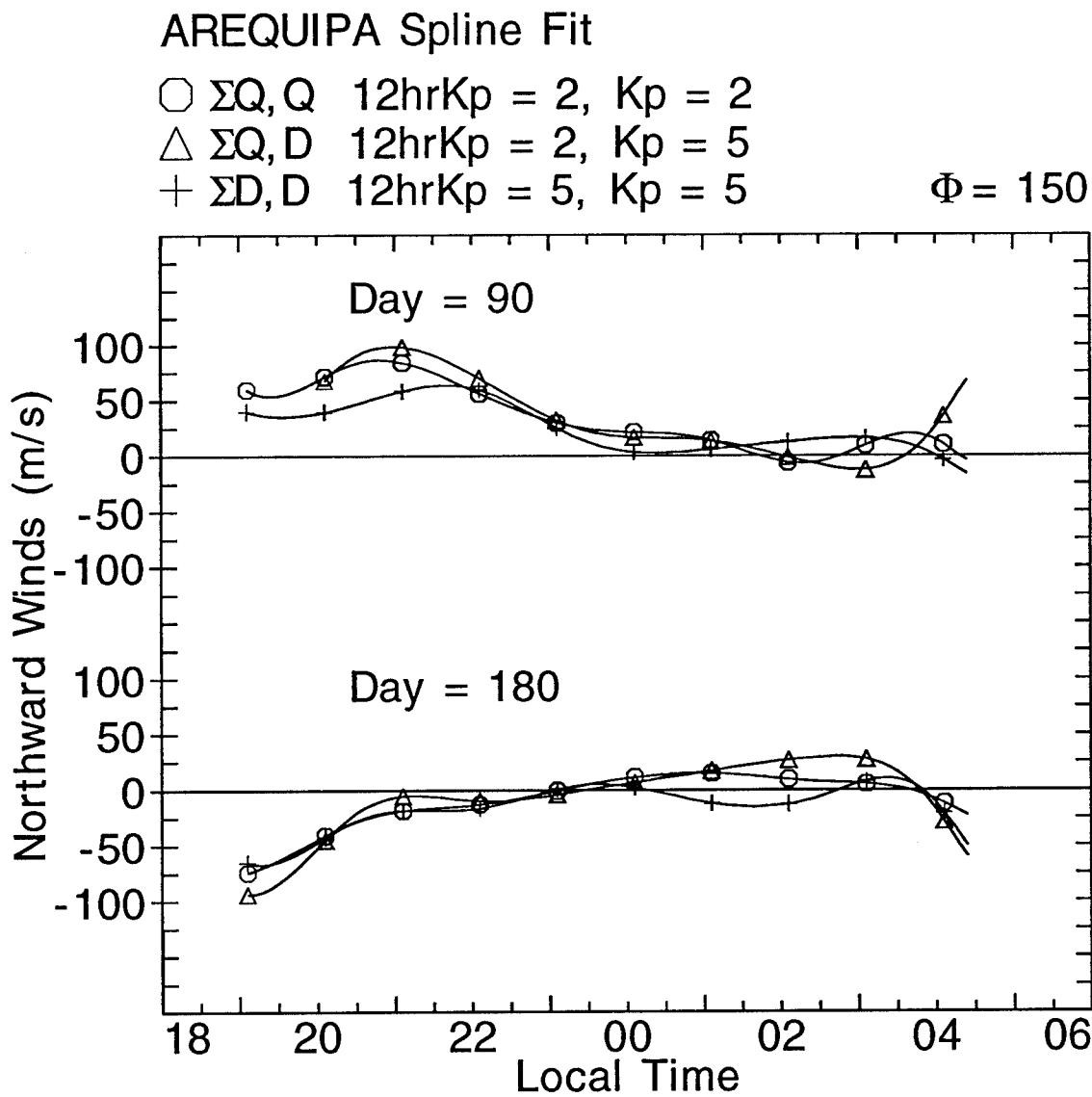


Figure 67. June solstice extended quiet ($\Sigma Q, Q$) and short-term disturbed ($\Sigma Q, D$) eastward wind comparisons for Arequipa and Arecibo. The solid line is the spline fit for the $\Sigma Q, Q$ case and the dashed line is the spline fit for the $\Sigma Q, D$ case. The open and solid triangles represent averages consisting of less than 10 wind data points.

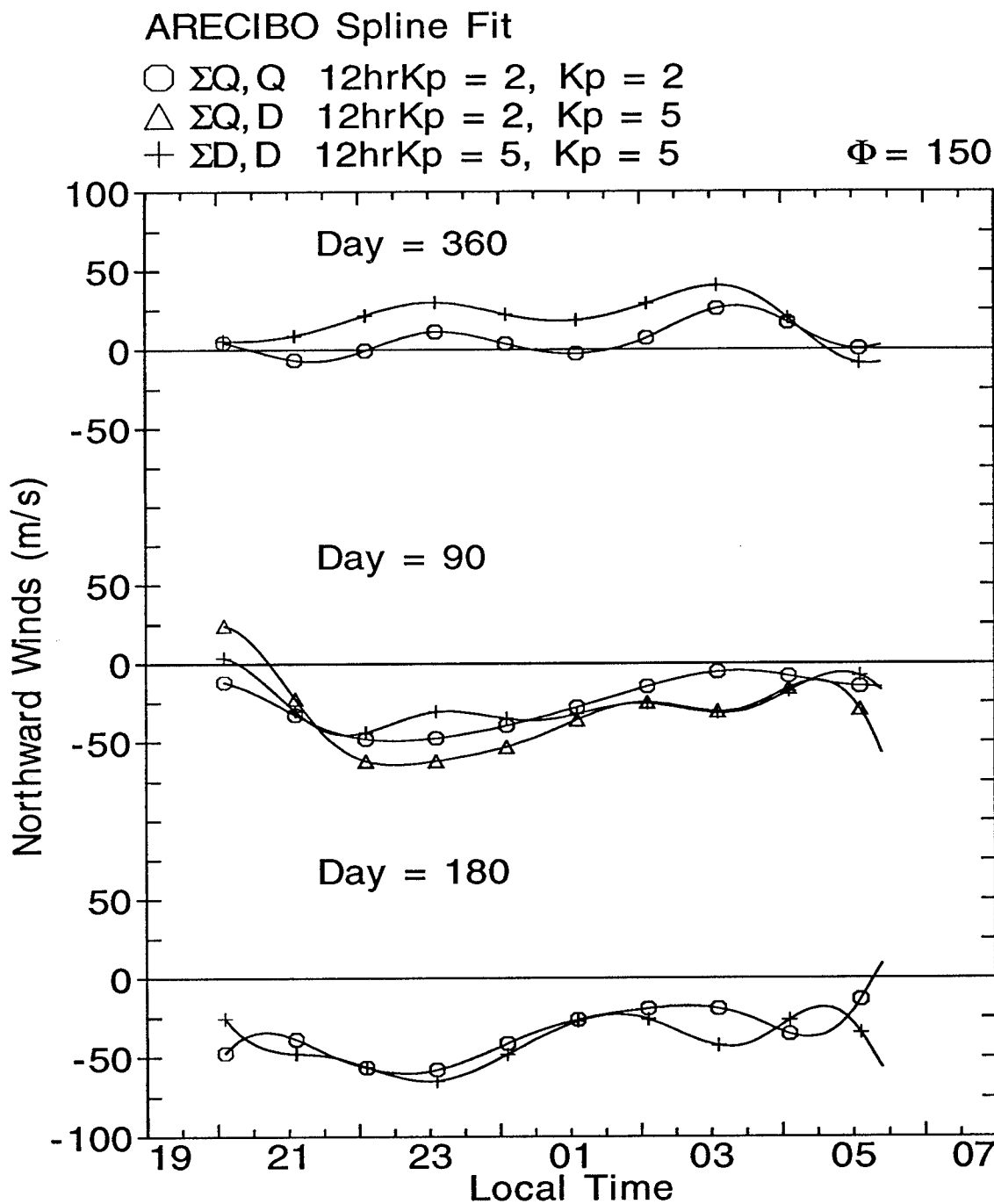


Figure 68. Cubic spline predictions for the northward winds over Arequipa for equinox (day = 90) and June solstice (day = 180) for moderate solar flux ($\Phi = 150$) conditions. The spline fit results are for the extended quiet ($\Sigma Q, Q$), short-term disturbed ($\Sigma Q, D$), and the extended disturbed case ($\Sigma D, D$).

Figure 69 shows the cubic spline predictions for the eastward wind over Arequipa. We calculated spline fits for days 90 and 180. Day 360 results are not shown due to the limited number of wind data points collected during this period. For days 90 and 180, the data show no significant variation between the extended quiet and the short-term disturbed cases; however, the spline prediction shows a westward perturbation through the night when the extended magnetic activity becomes disturbed.

6.5.1.2. TIGCM93 Predictions

Figures 70 and 71 present the seasonal Arequipa TIGCM93 eastward and northward predictions for magnetically quiet and disturbed conditions defined by $K_p = 1$ and $K_p = 6$, respectively. We use the predicted results for high solar activity ($\Phi = 195$). For each TIGCM93 simulation, the model is run to diurnally reproducible solutions or steady-state conditions. The steady-state condition means that the value of a modeled field (e.g., temperature, neutral wind, electron density, etc.) at a given TIGCM93 grid point at a given universal time falls within a few percent of the value calculated on the previous day. Since these model runs were produced using steady-state conditions, the TIGCM93-modeled quiet and disturbed winds are most like the extended quiet and disturbed magnetic activity outline in TABLE 16. In chapter 4 we found the average airglow emission height to be near 250 km through the night; therefore, we use the predicted winds at 250 km.

Similar to the approach used for the experimental wind, we analyze the predicted wind response to magnetic activity effects during the equinox and June

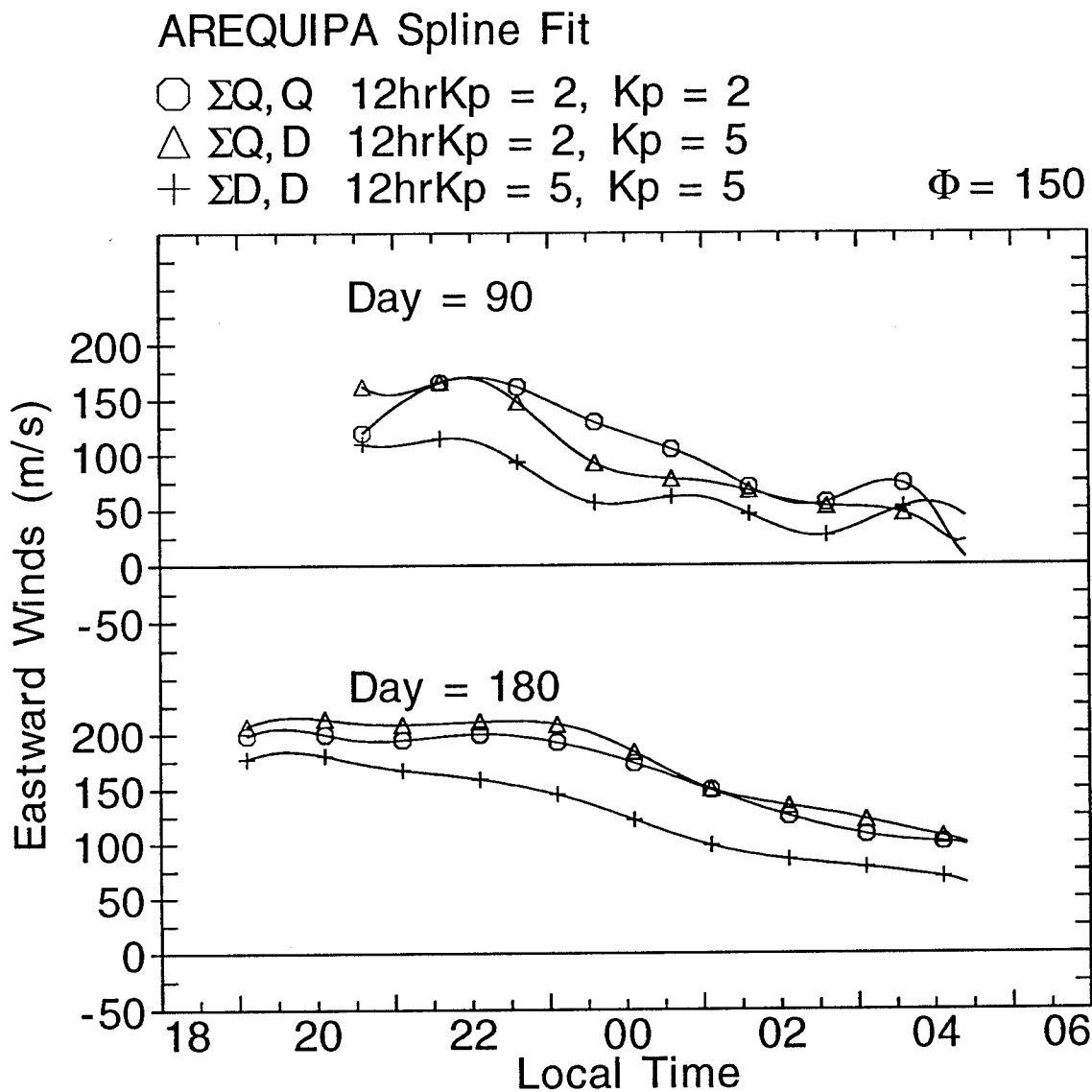


Figure 69. Cubic spline predictions for the eastward winds over Arequipa for equinox (day = 90) and June solstice (day = 180) for moderate solar flux ($\Phi = 150$) conditions. The spline fit results are for the extended quiet ($\Sigma Q, Q$), short-term disturbed ($\Sigma Q, D$), and the extended disturbed case ($\Sigma D, D$).

solstice period. We focus on the nighttime TIGCM93 wind predictions because we want to compare the model results to the FPI wind measurements.

Figure 70 presents the eastward wind predictions. We note a westward velocity perturbation for most of the night for the disturbed wind during all seasons. We see no significant variation between the quiet and disturbed wind from 0300 LT to the early morning hours. For the northward wind prediction in Figure 71, we note no significant variation between the quiet and disturbed wind for days 90 and 180, but we do note a southward velocity perturbation as the magnetic activity becomes disturbed in the postmidnight period for day 360.

6.5.1.3 HWM93 Predictions

Figures 72 and 73 present the seasonal HWM93 model predictions for magnetically quiet and disturbed conditions defined by $K_p = 2$ and $K_p = 5$, respectively. We use predicted results for moderate solar activity ($\Phi = 150$). The HWM93 uses the daily A_p magnetic activity index; therefore, this model emphasizes the long-term magnetic activity effects.

The eastward predictions in Figure 72 show no significant variations between the quiet and disturbed winds in the premidnight period for all seasons; however, the model winds show a small westward velocity perturbation as the magnetic activity becomes disturbed in the postmidnight period for all seasons. The Arequipa northward predictions in Figure 73 show no significant variation between the quiet and disturbed wind throughout the night for all seasons.

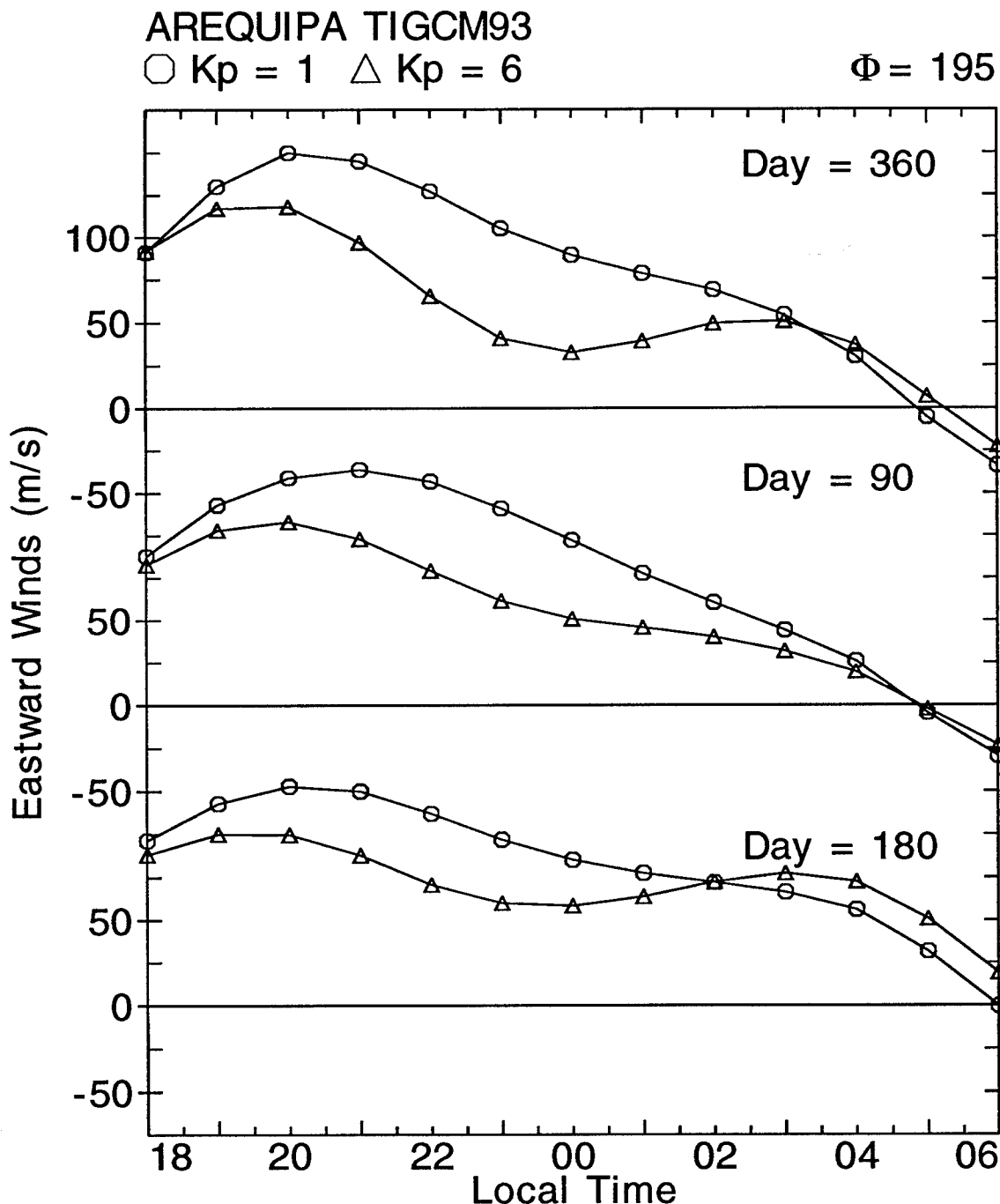


Figure 70. TIGCM93 quiet ($K_p = 1$) and disturbed ($K_p = 6$) eastward wind predictions over Arequipa for all seasons. These predictions are for high solar flux ($\Phi = 195$) conditions.

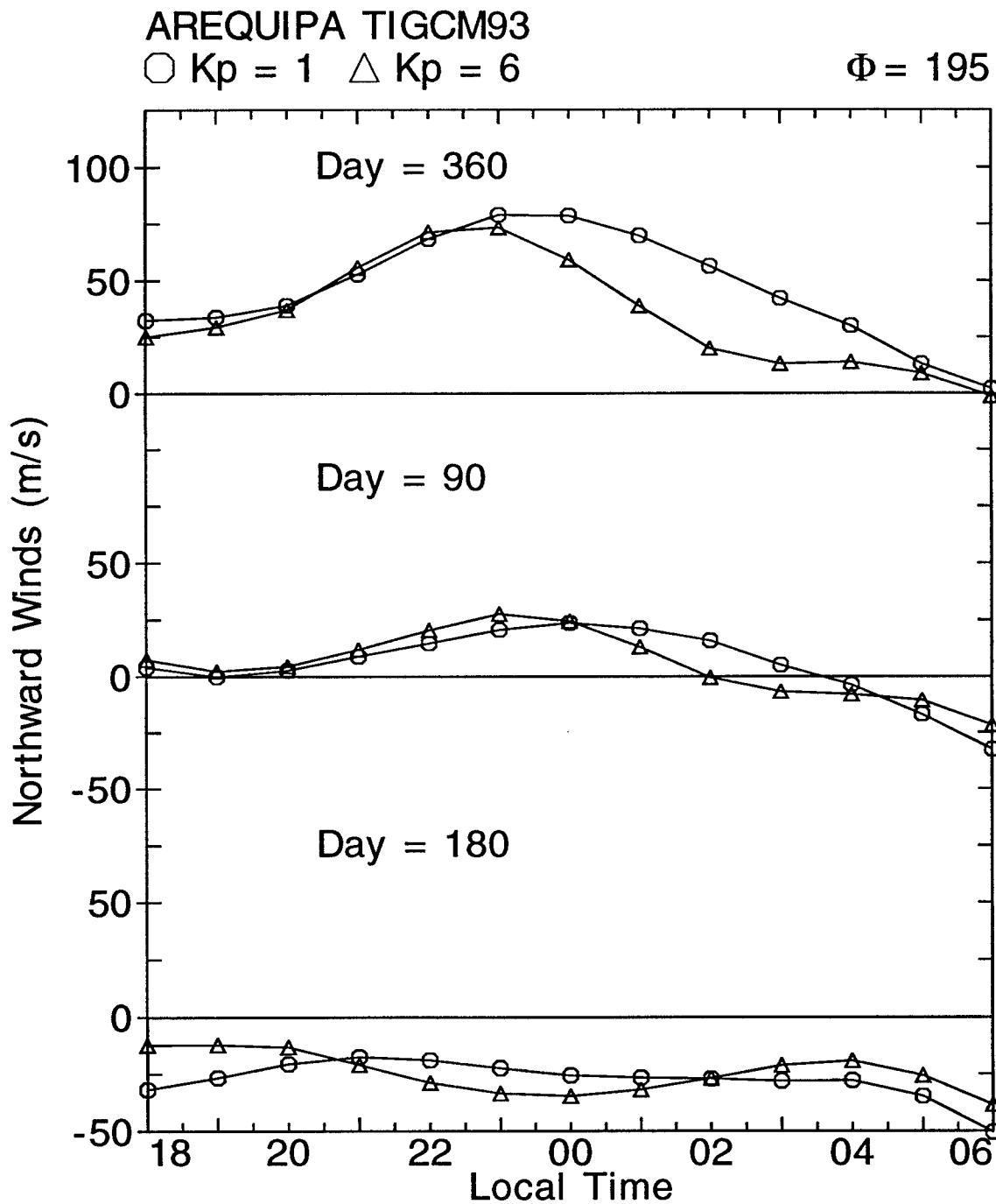


Figure 71. TIGCM93 quiet ($K_p = 1$) and disturbed ($K_p = 6$) northward wind predictions over Arequipa for all seasons. These predictions are for high solar flux ($\Phi = 195$) conditions.

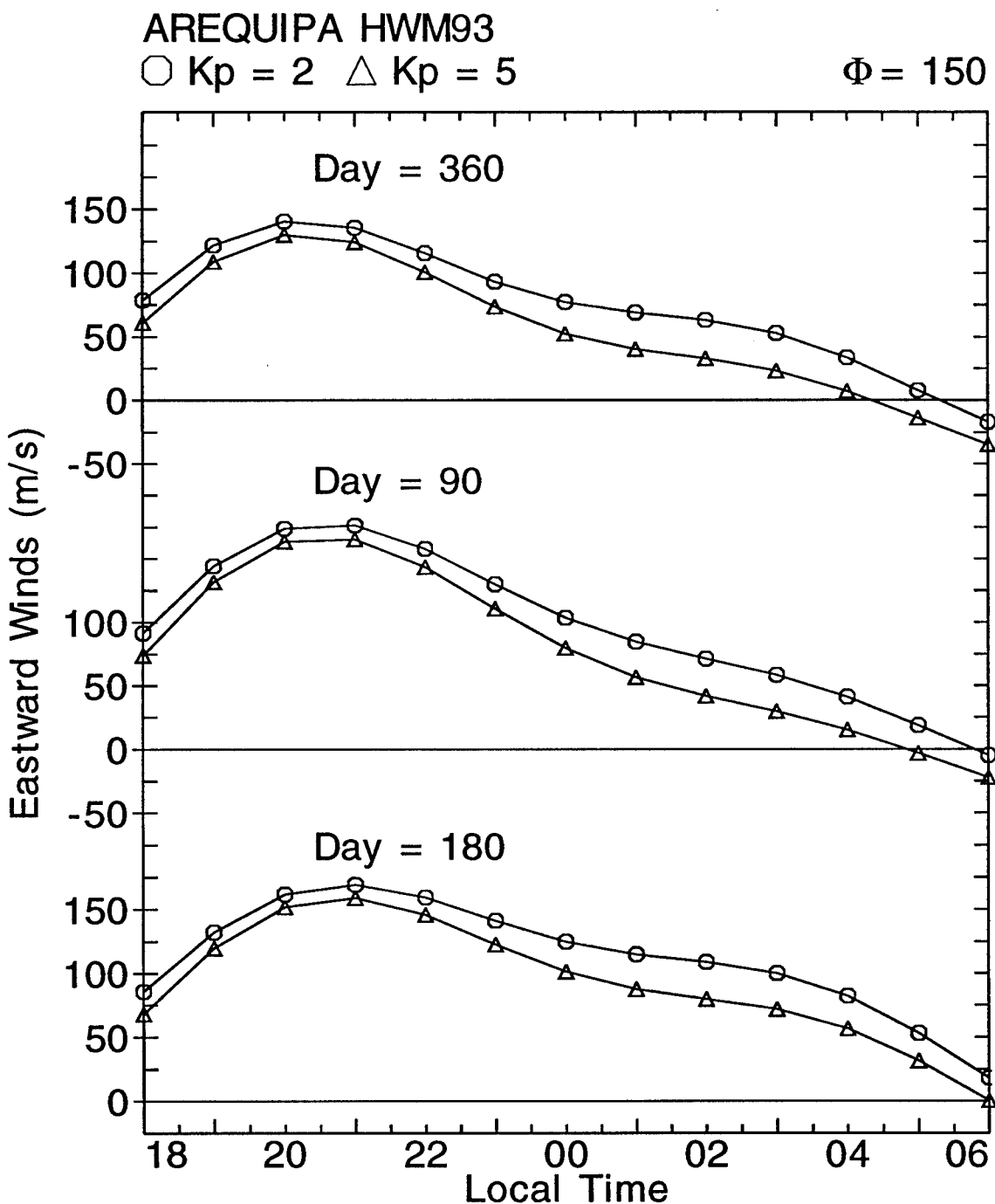


Figure 72. HWM93 quiet ($K_p = 2$) and disturbed ($K_p = 5$) eastward wind predictions over Arequipa for all seasons. These predictions are for moderate solar flux ($\Phi = 150$) conditions.

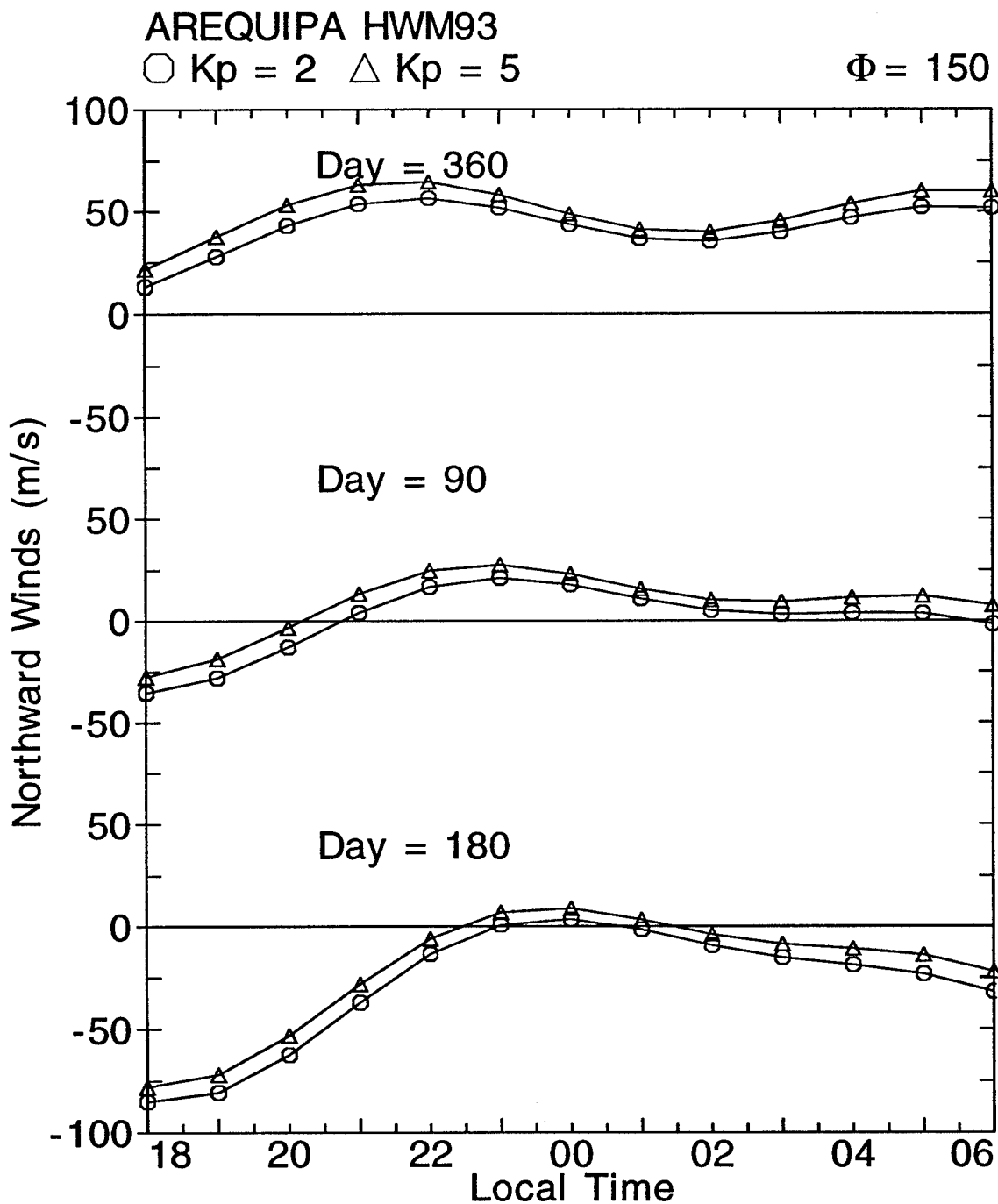


Figure 73. HWM93 quiet ($K_p = 2$) and disturbed ($K_p = 5$) northward wind predictions over Arequipa for all seasons. These predictions are for moderate solar flux ($\Phi = 150$) conditions.

6.5.2. Arecibo

6.5.2.1. Cubic Spine Predictions

Figure 74 shows the spline fits for northward wind over Arecibo during the December solstice (day 360), equinox (day 90), and June solstice (day 180). We do not show the short-term disturbed ($\Sigma Q, D$) effects for days 360 and 180 due to the limited short-term disturbed wind data for the December and June solstices. These spline fits do not show noticeable magnetic activity effects on the northward component for any season. The cubic spline fits for the northward wind agree with the experimental results under similar magnetic activity conditions.

Figure 75 shows the cubic spline fits for the zonal winds for the December solstice, equinox, and June solstice. In contrast to Arequipa, the Arecibo spline results in Figure 75 show a westward velocity perturbation when the short-term magnetic activity becomes disturbed for days 90 and 180. This westward perturbation continues with extended disturbed magnetic activity conditions. For day 360, we note no significant variation in the spline result due to magnetic activity effects.

This westward perturbation is consistent with theoretical results by *Blanc and Richmond* [1980]. Using a first principal theoretical model, they showed the thermospheric winds above 120 km produced by auroral heating during magnetic storms are driven equatorward. The transport of angular momentum by these winds produces a westward motion with respect to the earth. Hence, magnetic activity effects reach Arecibo earlier than Arequipa.

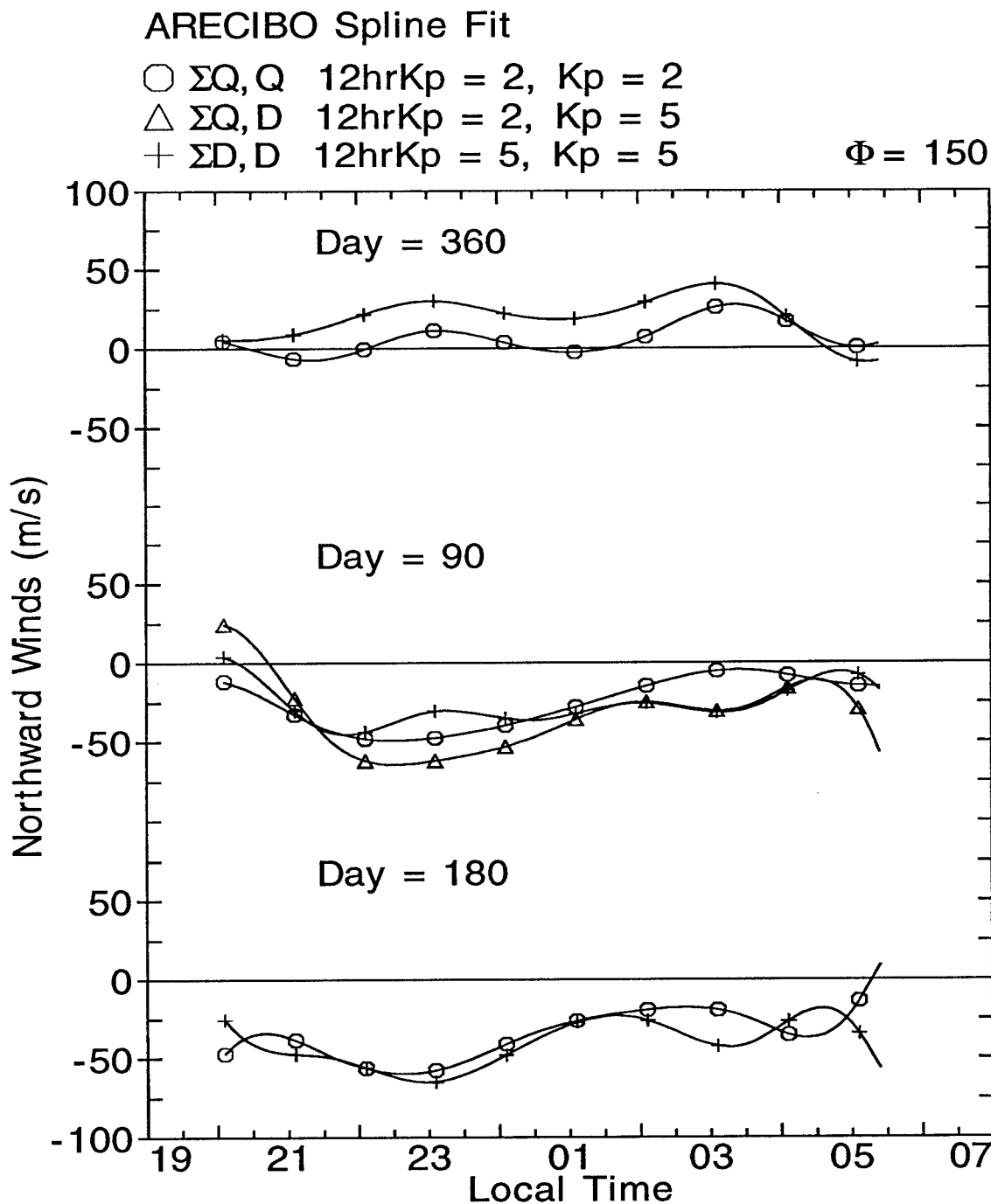


Figure 74. Cubic spline predictions for the northward winds over Arecibo for all seasons and moderate solar flux ($\Phi = 150$) conditions. The spline fit results are for the extended quiet ($\Sigma Q, Q$), short-term disturbed ($\Sigma Q, D$), and the extended disturbed ($\Sigma D, D$) cases.

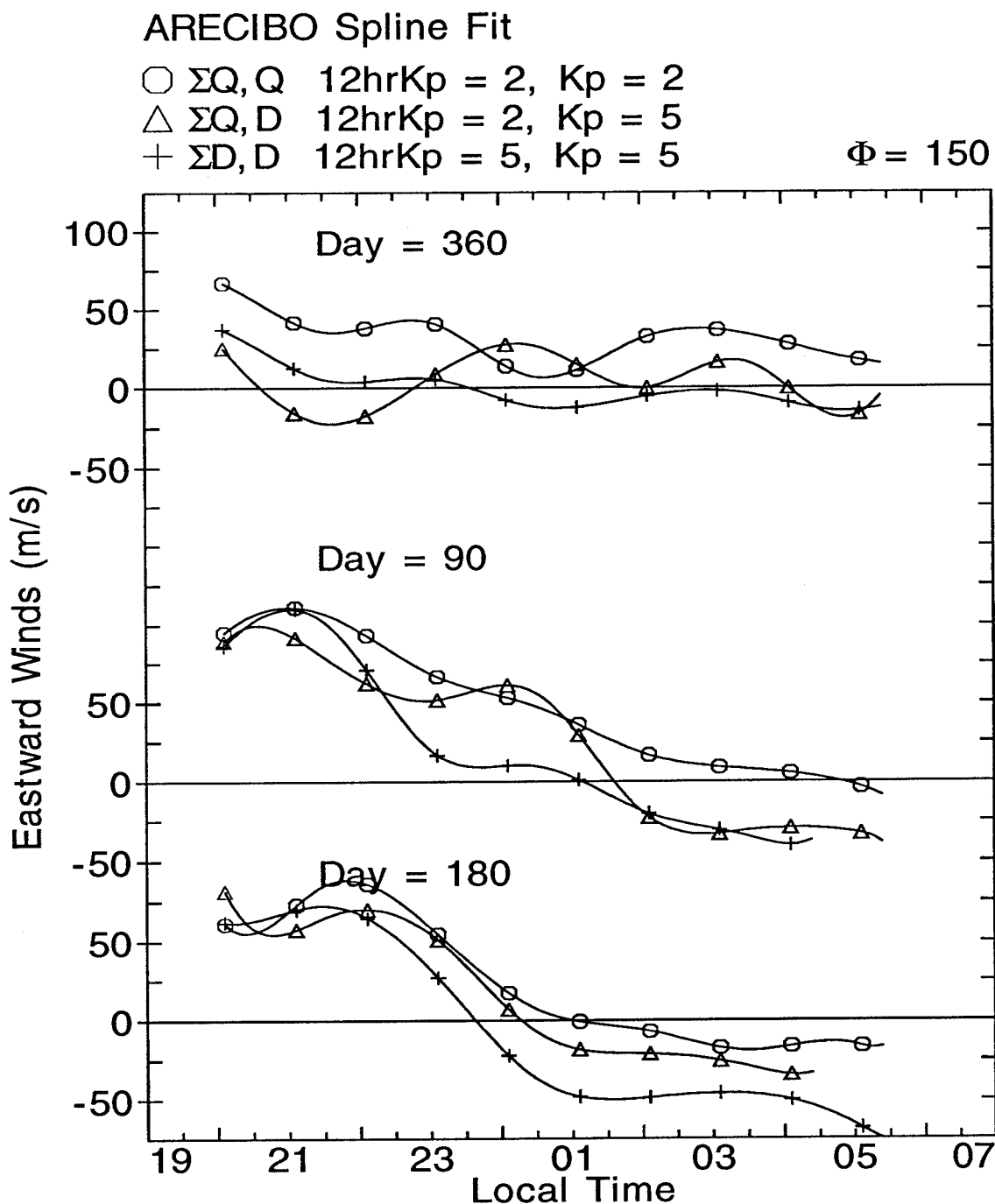


Figure 75. Cubic spline predictions for the eastward winds over Arecibo for all seasons and moderate solar flux ($\Phi = 150$) conditions. The spline fit results are for the extended quiet ($\Sigma Q, Q$), short-term disturbed ($\Sigma Q, D$), and the extended disturbed case ($\Sigma D, D$).

6.5.2.2. TIGCM93 Predictions

Figures 76 and 77 show the Arecibo eastward and northward TIGCM93 predicted winds for quiet and disturbed magnetic activity and low solar activity. The Arecibo eastward winds in Figure 76 show a significant westward velocity perturbation for the disturbed wind for most of the night. We note no significant variation between the quiet and disturbed winds from 0400 LT to early morning. The northward wind predictions in Figure 77 show a southward velocity perturbation through the night for days 360 and 90, while we note a southward velocity perturbation until 0500 LT for day 180.

6.5.2.3. HWM93 Predictions

Figures 78 and 79 show the HWM93 predictions for the eastward and northward winds over Arecibo. Figure 78 presents the predicted eastward results for quiet and disturbed winds for moderate solar activity conditions. We note a small westward velocity perturbation for most of the night during all seasons. The relative velocity difference between the quiet and disturbed eastward winds is ~ 25 m/s for all seasons. The Arecibo northward predictions in Figure 79 show no significant variation between the quiet and disturbed wind throughout the night for any season.

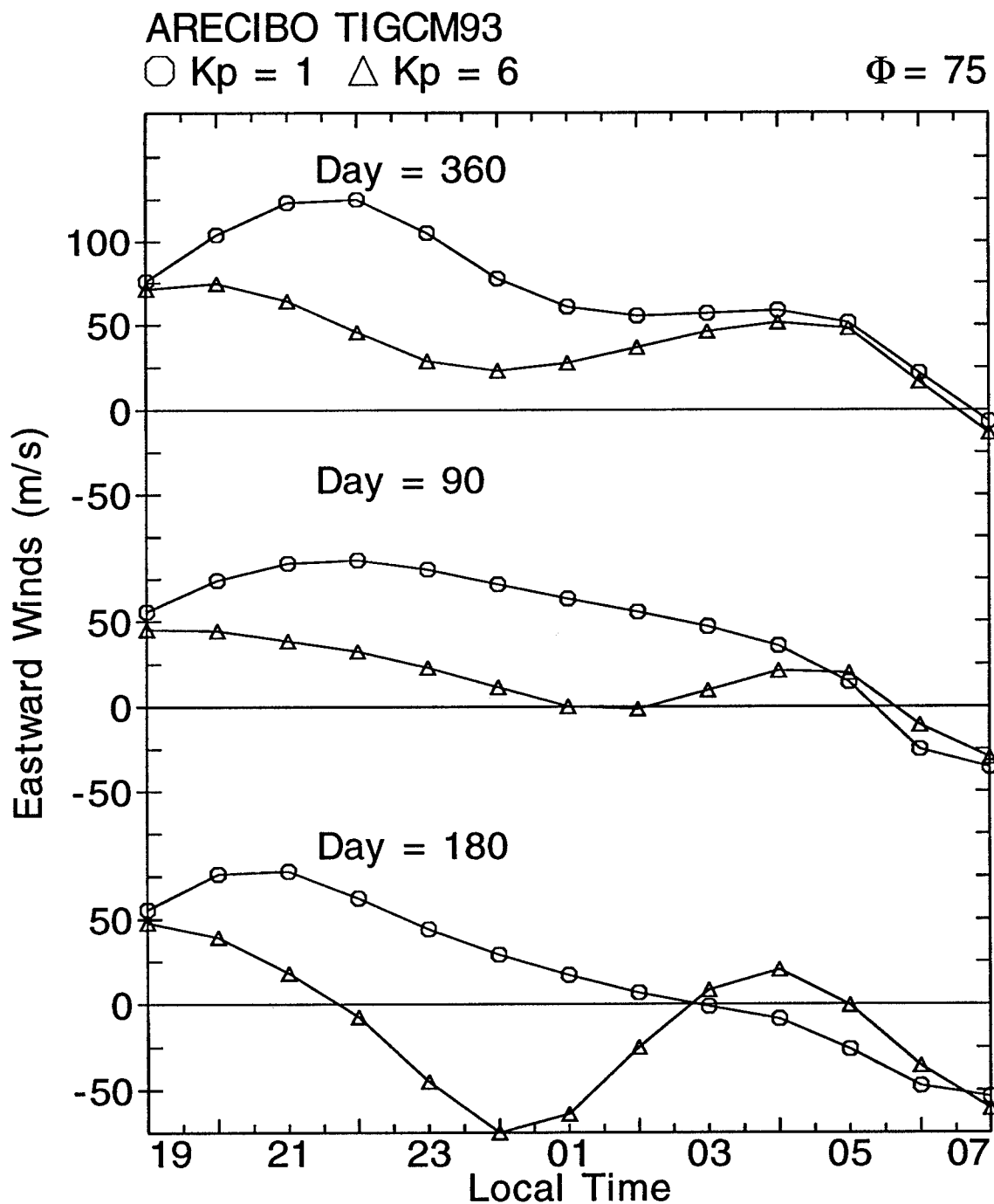


Figure 76. TIGCM93 quiet ($K_p = 1$) and disturbed ($K_p = 6$) eastward wind predictions over Arecibo for all seasons. These predictions are for low solar flux ($\Phi = 75$) conditions.

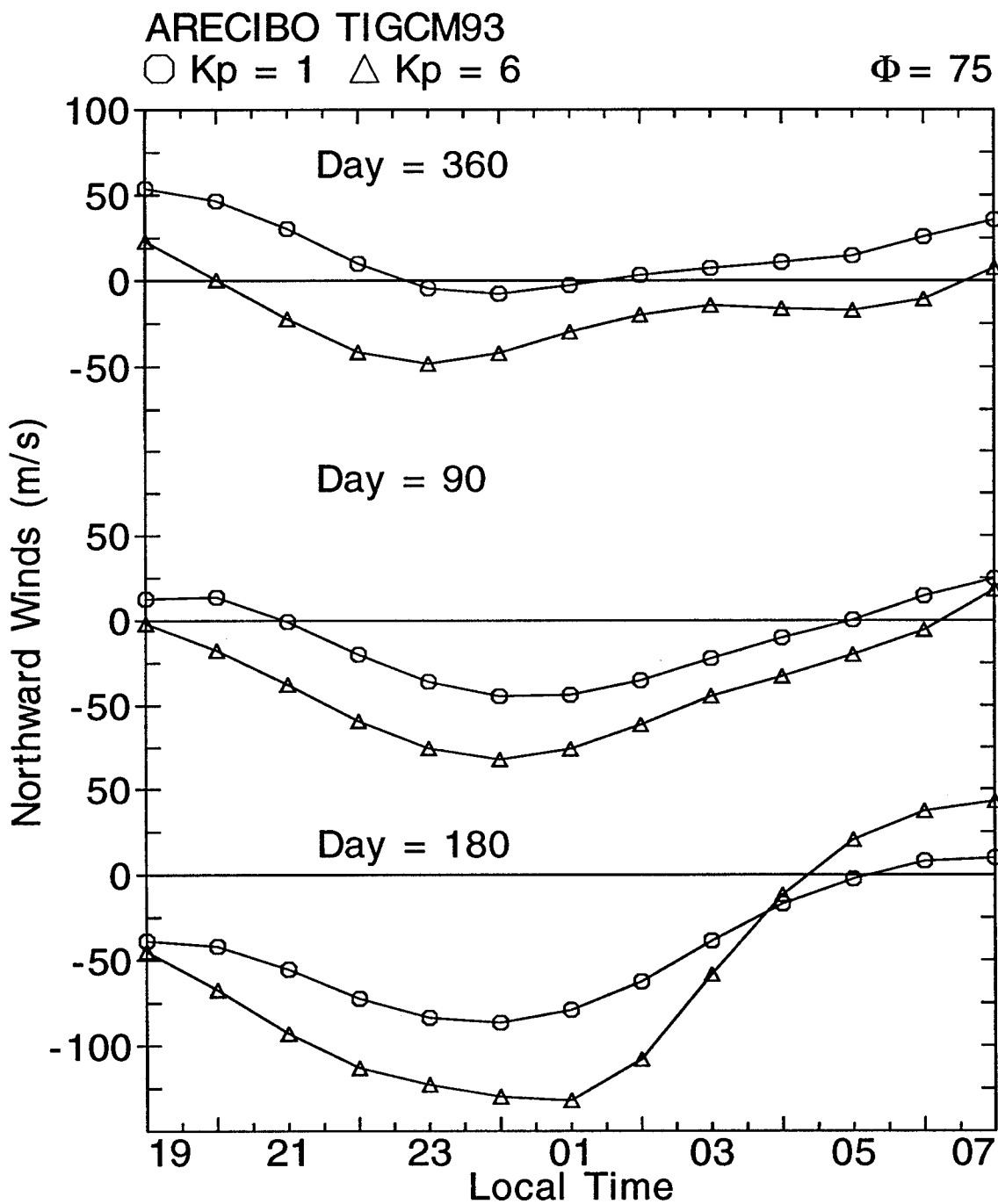


Figure 77. TIGCM93 quiet ($K_p = 1$) and disturbed ($K_p = 6$) northward wind predictions over Arecibo for all seasons. These predictions are for low solar flux ($\Phi = 75$) conditions.

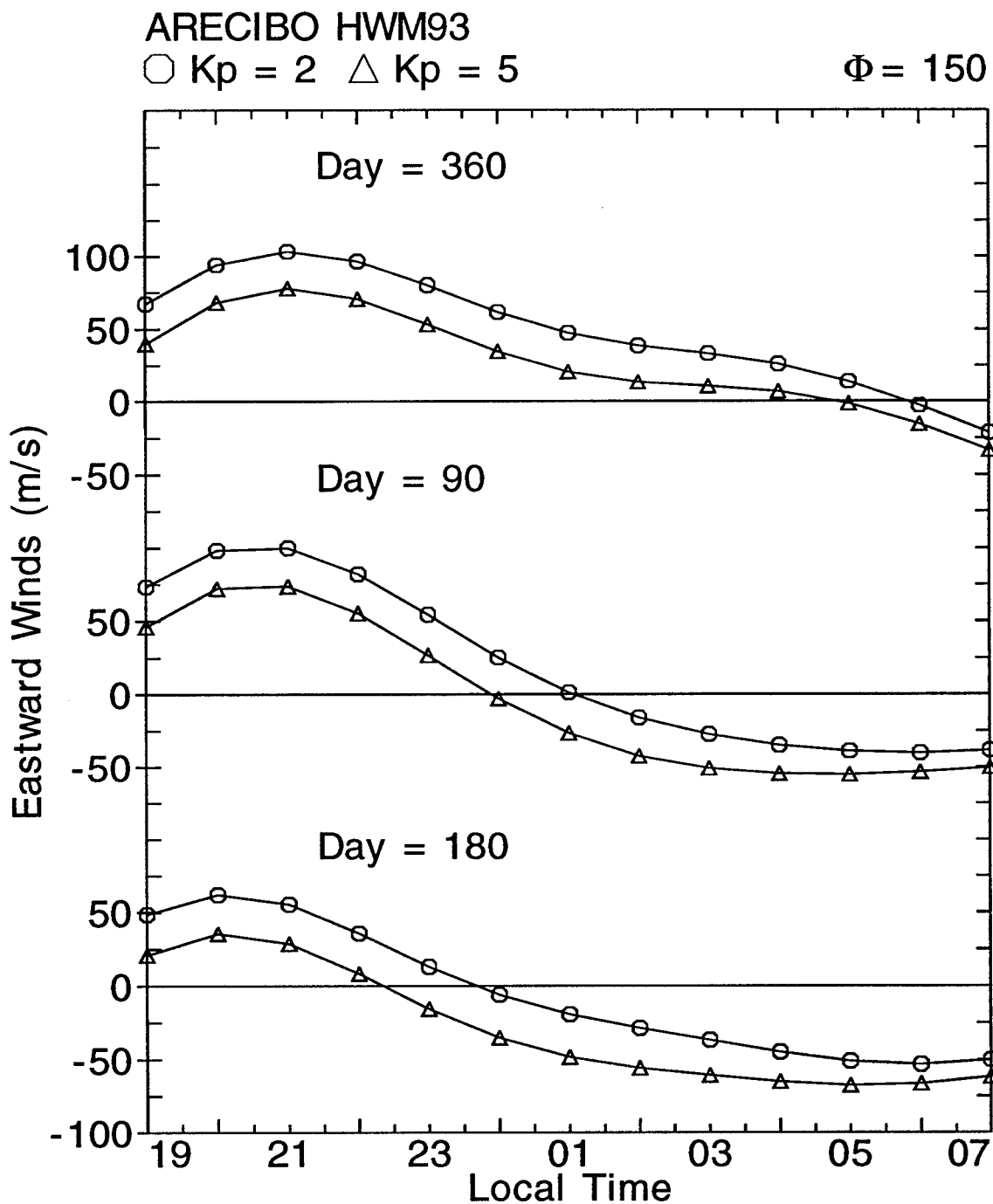


Figure 78. HWM93 quiet ($K_p = 2$) and disturbed ($K_p = 5$) eastward wind predictions over Arecibo for all seasons. These predictions are for moderate solar flux ($\Phi = 150$) conditions.

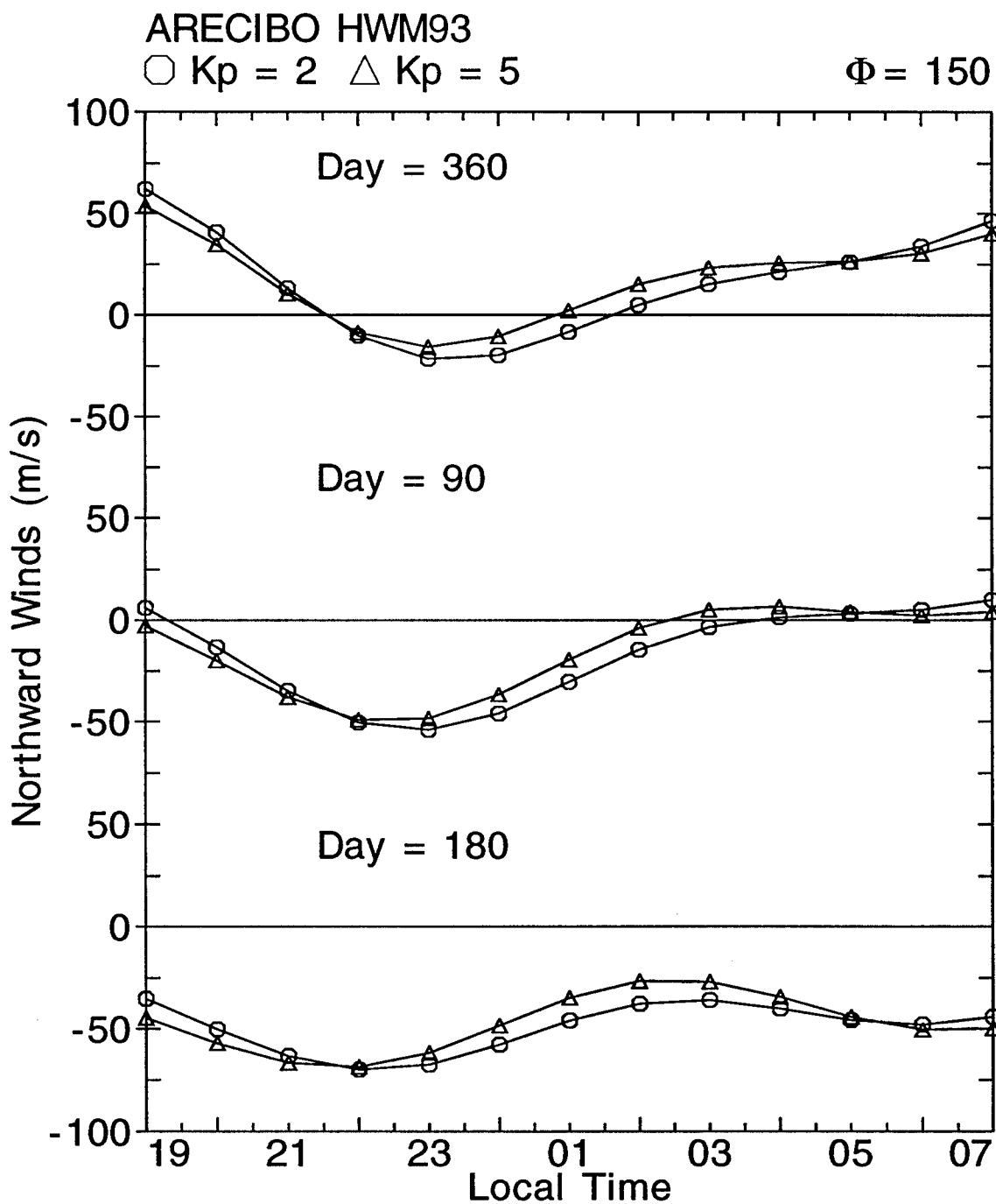


Figure 79. HWM93 quiet ($K_p = 2$) and disturbed ($K_p = 5$) northward wind predictions over Arecibo for all seasons. These predictions are for moderate solar flux ($\Phi = 150$) conditions.

CHAPTER 7

CONCLUSIONS

7.1. CONCLUSIONS

The primary purpose of this thesis is to investigate magnetic activity effects on the low latitude thermospheric neutral winds. To properly investigate storm-time effects on the neutral winds, we first calculated the average airglow emission height for different solar cycle and magnetic activity conditions. Next, we analyzed the solar cycle effects on the seasonal averages. The following paragraphs outline our conclusions on the airglow emission heights, solar cycle effects, and magnetic activity analysis.

7.1.1. Airglow Emission Heights

We used electron density measurements at Arecibo, Puerto Rico, and Jicamarca, Peru, MSISE90 model predictions, and algorithms developed by *Link and Cogger* [1988] to calculate the average airglow emission height over the low latitude ionosphere. This calculated emission height provides us the average altitude of the thermospheric wind measurement and the reference height for modeled and measured wind comparisons. Our study shows the average airglow emission height does not vary with magnetic activity. The airglow height above Arequipa does not change with solar activity; however, we note lower average heights from solar maximum to minimum over Arecibo. Overall, the average airglow emission height is ~ 250 km. Our airglow emission height calculations are consistent with observations by *Burrage et al.* [1990] in

which he calculated the December solstice airglow emission peak to be ~ 270 km at 0100 LT.

7.1.2. Solar Activity Effects

The averaged meridional wind is not affected by solar cycle effects at either Arequipa or Arecibo. The June solstice at Arequipa shows an eastward wind increase of ~ 50 m/s during the postmidnight period from moderate to high solar flux conditions. The Arecibo December solstice period shows an eastward decrease of ~ 50 m/s during the premidnight period from solar minimum to maximum conditions.

Predicted TIGCM93 meridional wind response to solar activity agrees with the experimental results at Arequipa and Arecibo. However, the TIGCM93 predicts higher eastward winds in the premidnight period from low to high solar flux conditions at Arequipa, and the modeled eastward wind response to solar cycle effects over Arecibo does not agree with our experimental results.

Predicted HWM93 meridional wind response to solar activity agrees with the experimental results at Arequipa and Arecibo. However, the model predicts increased eastward winds (~ 25 m/s) in the postmidnight period from low to high solar flux condition at Arequipa during the equinox and June solstice periods. These predictions do not agree with the experimental results for the equinox period. The model results for the December solstice show a smaller wind response (~ 25 m/s) between the moderate to high solar activity average winds than that shown in our experimental analysis (~ 50 m/s). Over Arecibo, the zonal wind predictions agree with the December solstice

measured winds but not with the June solstice period. The Arecibo HWM93 June predictions show an eastward increase of ~ 50 m/s in the postmidnight period from low to high solar flux conditions while our June solstice experimental FPI data show no variation due to solar cycle effects.

Our results of the response of the meridional neutral winds over Arequipa and Arecibo to solar cycle effects are consistent with previous wind studies conducted at these locations [Biondi *et al.*, 1991; Burnside and Tepley, 1989]. Our FPI-measured data showed solar cycle effects on the zonal winds at Arequipa and Arecibo. Previous studies outlined in Biondi *et al.* [1991] showed larger eastward winds from solar minimum to maximum conditions, a result consistent with our solar cycle analysis. For Arecibo, Burnside and Tepley [1989] showed the average zonal wind is not affected by solar cycle effects, a result that does not agree with our study. We enhanced the solar cycle study performed in Burnside and Tepley [1989] by using only quiet-time ($K_p \leq 3$) wind data, incorporating two additional years (1988 and 1989) of FPI wind data, and implementing a finer time resolution (1/2-hour time bins).

7.1.3. Magnetic Activity Effects

The averaged meridional wind is not affected by magnetic activity at either Arequipa or Arecibo based on the K_p index. We note that a westward perturbation or eastward decrease of the average zonal wind due to magnetic activity occurs on a short time scale at Arecibo but not at Arequipa. We conclude that magnetic activity effects reach Arecibo before Arequipa. Both locations show large westward perturbations for

long-term disturbed effects. This westward wind response to disturbed magnetic activity conditions has been shown in previous experimental studies [*Burnside et al.*, 1991; *Wu et al.*, 1994] and theoretical simulations [*Blanc and Richmond*, 1980].

The predicted TIGCM93 zonal wind response to magnetic activity agrees with experimental results in the premidnight period at both locations. The modeled meridional response to magnetic activity agrees with the experimental results at Arequipa but not at Arecibo. The Arecibo TIGCM93 meridional predictions show a northward decrease of ~ 40 - 50 m/s between the quiet and disturbed winds in the premidnight period for all seasons.

The predicted HWM93 zonal wind response to magnetic activity agrees with experimental results in the postmidnight period for Arequipa and all nighttime hours at Arecibo; however, the model underestimates the disturbed wind response. The predicted meridional wind response agrees with the experimental results.

7.2. FUTURE WORK

Clearly, more neutral wind data from FPIs, ISRs, and satellites are needed to fully investigate the solar cycle and magnetic activity effects. A few ideas for future research are presented below.

This thesis presented the climatological averages of the neutral wind response to disturbed magnetic activity conditions. We compared these averages to the HWM93 and TIGCM93 model predictions to find out how well these models could reproduce the experimental results. One possible research opportunity would be to vary the inputs

(tides, solar flux, geomagnetic activity, etc.) to the first principal model, the TIGCM93, to fully investigate the thermospheric physics and coupling mechanisms. This investigation may provide further clues as to why the average experimental meridional wind response does not vary between quiet and disturbed conditions. A more complete analysis would require other first principal models currently used in the space science community.

Recent investigations by *Fejer* [1993] described the coupling between the F-region nighttime zonal neutral winds and plasma drifts over Arecibo during magnetically quiet conditions. Besides the experimental results, *Blanc and Richmond* [1980] describe model predictions of the neutral winds and plasma drifts during magnetically disturbed conditions. A recent paper by *Coley et al.* [1994] uses measurements of the zonal neutral wind and zonal ion drifts by the DE 2 satellite to conclude that on average the zonal ion drift speed exceeds the zonal neutral wind speed. These DE 2 data were collected during April 1981 through February 1983, a period characterized by high solar flux conditions. The data were collected in the 300 - 400 km altitude range near the dip equator. During 2000 - 0500 LT, *Coley et al.* [1994] showed the ion drift is more strongly eastward than the neutral wind. This result is not consistent with the experimental results in *Fejer* [1993] and model predictions by *Blanc and Richmond* [1980]. This discrepancy could be further explored using the FPI measurements at Arecibo and Arequipa and zonal drifts measured by the ISRs at Arecibo and Jicamarca. A detailed comparison of the neutral winds and zonal drifts for quiet and disturbed conditions would be useful for investigating the results by *Coley et al.* [1994].

Our magnetic activity analysis study showed that storm-time events affect the neutral winds over Arecibo before Arequipa. This analysis also indicated that the response of the Arecibo neutral winds to disturbed conditions occur within 3 hours of the storm onset. At Arequipa, we showed that it takes longer than 3 hours after the storm onset for the neutral winds to respond to storm-time effects. We require a magnetic activity index with a smaller time resolution than the 3-hour K_p to provide a more precise short-term disturbed analysis. The 1-hour AE index is a possible candidate for enhancing the short-term disturbed study. The main drawback is the limiting of neutral wind statistics because thus far AE index has routinely been calculated only up to September 1987.

REFERENCES

Anderson, D.N., and R.G. Roble, The effect of vertical $\vec{E} \times \vec{B}$ ionospheric drifts on F region neutral winds in the low-latitude thermosphere, *J. Geophys. Res.*, 79, 5231-5236, 1974.

Berrington, K.A., and P.G. Burke, Effective collision strengths for forbidden transitions in e -N and e -O scattering, *Planet. Space Sci.*, 29, 377-381, 1981

Bilitza, D., *The Worldwind Ionospheric Data Base*, National Space Science Data Center/World Data Center A for Rockets and Satellites publication, New York, 1989.

Biondi, M.A., J.W. Meriwether, Jr., B.G. Fejer, S.A. Gonzalez, and D.C. Hallenbeck, Equatorial thermospheric wind changes during the solar cycle: measurements at Arequipa, Peru, from 1983 to 1990, *J. Geophys. Res.*, 96, 15917-15930, 1991.

Biondi, M.A., J.W. Meriwether, Jr., B.G. Fejer, and S.A. Gonzalez, Seasonal variations in the equatorial thermospheric measured at Arequipa, Peru, *J. Geophys. Res.*, 95, 12243-12250, 1990.

Blanc, M., and A.D. Richmond, The ionospheric disturbance dynamo, *J. Geophys. Res.*, 85, 1669-1689, 1980.

Bone, N., *The Aurora Sun-Earth Interactions*, pp. 1-150, Ellis Horwood Limited, New York, 1991.

Buonsanto, M.J., and J.C. Foster, Effects of magnetospheric electric fields and neutral winds on the low-middle latitude ionosphere during the March 20-21, 1990, storm, *J. Geophys. Res.*, 98, 19133-19140, 1993.

Burnside, R.G., C.A. Tepley, M.P. Sulzer, T.J. Fuller-Rowell, D.G. Torr, and R.G. Roble, The neutral thermosphere at Arecibo during geomagnetic storms, *J. Geophys. Res.*, 96, 1289-1301, 1991.

Burnside, R.G., and C.A. Tepley, Optical observations of thermospheric neutral winds at Arecibo between 1980 and 1987, *J. Geophys. Res.*, 94, 2711-2716, 1989.

Burnside, R.G., J.C.G. Walker, and M.D. Sulzer, Kinematic properties of the F-region ion velocity field inferred from incoherent scatter radar measurements at Arecibo, *J. Geophys. Res.*, 92, 3345-3355, 1987.

Burnside, R.G., R.A. Behnke, and J.C.G. Walker, Meridional winds in the thermosphere at Arecibo: Simultaneous incoherent scatter and airglow observations, *J. Geophys. Res.*, 88, 3181-3189, 1983.

Burnside, R.G., F.A. Herrero, J.W. Meriwether, Jr., and J.C.G. Walker, Optical observations of thermospheric dynamics at Arecibo, *J. Geophys. Res.*, 86, 5532-5540, 1981.

Burrage, M.D., C.G. Fesen, and V.J. Abreu, Low-latitude thermospheric neutral winds determined from AE-E measurements of the 6300-A nightglow at solar maximum, *J. Geophys. Res.*, 95, 10357-103644, 1990.

Chamberlain, J.W., *Theory of Planetary Atmospheres*, pp. 226-276, Academic Press, San Diego, 1987.

Chen, A., R. Johnson, and M.A. Biondi, Measurements of the $O^+ + N_2$ and $O^+ + O_2$ reaction rates from 300 to 900 K, *J. Chem. Phys.*, 69, 2688-2695, 1978.

Coley, W.R., R.A. Heelis, and N.W. Spencer, Comparison of low-latitude ion and neutral zonal drifts using DE 2 data, *J. Geophys. Res.*, 99, 341-348, 1994.

Dickinson, R.E., E.C. Ridely, and R.G. Roble, A three-dimensional general circulation model of the thermosphere, *J. Geophys. Res.*, 86, 1499-1512, 1981.

Fejer, B.G., F-region plasma drifts over Arecibo: Solar cycle, seasonal and magnetic activity effects, *J. Geophys. Res.*, 98, 13645-13652, 1993.

Fejer, B.G., Low latitude electro-dynamic plasma drifts: A review, *J. Atmos. Terr. Phys.*, 53, 677-693, 1991.

Fejer, B.G., The equatorial ionospheric electric fields: A review, *J. Atmos. Terr. Phys.*, 43, 377-386, 1981.

Fejer, B.G., E.R. DePaula, S.A. Gonzalez, and R.F. Woodman, Average vertical and zonal F region plasma drifts over Jicamarca, *J. Geophys. Res.*, 96, 13901-13906, 1991.

Fesen, C.G., M.E. Hagan, C.A. Tepley, and R.G. Roble, On the coupling between the lower and the upper thermosphere during the first lower thermosphere coupling study, *Geophys. Res. Lett.*, 98, 1545-1558, 1993.

Fesen, C.G., G. Crowley, and R.E., Roble, Ionospheric effects at low latitudes during the March 22, 1979, geomagnetic storm, *J. Geophys. Res.*, 94, 5405-5417, 1989.

Forbes, J.M., R.G. Roble, and C.G. Fesen, Acceleration, heating, and compositional mixing of the thermosphere due to upward propagating tides, *J. Geophys. Res.*, 98, 311-321, 1993.

Forbes, J.M., and F. Vial, Semidiurnal tidal climatology of the E-region, *J. Geophys. Res.*, 96, 1147-1157, 1991.

Forbes, J.M., and F. Vial, Monthly simulations of the solar semidiurnal tide in the mesosphere and lower thermosphere, *J. Atmos. Terr. Phys.*, 51, 663-677, 1989.

Fowles, G.R., *Introduction to Modern Optics.*, pp. 86-102, Dover Publications, New York, 1975.

Fuller-Rowell, T.J., and D.S. Evans, Height integrated pedersen and hall conductivity patterns inferred from the TIROS-NOAA satellite data, *J. Geophys. Res.*, 92, 7606-7618, 1987.

Gornall, W.S., The world of Fabry-Perots, *Lasers & Applications*, 47-52, 1983.

Haregreaves, J.K., *The Solar-Terrestrial Environment*, pp. 98-362, Cambridge Univ. Press, Cambridge, 1992.

Harper, R.M., Nighttime meridional neutral winds near 350 km at low to mid-latitudes, *J. Atmos. Terr. Phys.*, 35, 2023-2034, 1973.

Hecht, E. and A. Zajac, *Optics*, pp. 276-323, Addison-Wesley Publishing Co., London, 1979.

Hedin, A.E., Extension of the MSIS thermosphere model into the middle and lower Atmosphere, *J. Geophys. Res.*, 96, 11159-1172, 1991.

Hedin, A.E., E.L. Fleming, A.H. Manson, F.J. Schmidlin, S.K. Avery, R.R. Clark, S.J. Franke, G.J. Fraser, T. Tsuda, F. Vial, and R.A. Vincent, Empirical wind model for the middle and lower atmosphere, *J. Geophys. Res.*, in press, 1993.

Hedin, A.E., M.A. Biondi, R.G. Burnside, G. Hernandez, R.M Johnson ,T.L Killeen , C. Mazaudier, J.W. Meriwether, J.E. Salah , R.J. Sica, R.W. Smith, N.W. Spencer, V.B. Wickwar , and T.S. Virdi, Revised global model of thermosphere winds using satellite and ground-based observations, *J. Geophys. Res.*, 96, 7657-7688, 1991.

Hedin, A.E., N.W. Spencer, and T.L. Killeen, Empirical global model of upper thermosphere winds based on atmosphere and dynamics explorer satellite data, *J. Geophys. Res.*, 93, 9959-9978, 1988.

Heelis, R.A., P.C. Kendall, R.J. Moffett, D.W. Windle, and H. Rishbeth, Electrical coupling of the E and F-regions and its effects on F-region drifts and winds, *Planet. Space Sci.*, 22, 743-756, 1974.

Heelis, R.A., J.K. Lowell, and R.W. Spiro, A model of the high-latitude ionospheric convection pattern, *J. Geophys. Res.*, 87, 6339-6345, 1982.

Hernandez, G., *Fabry-Perot Interferometers*, pp. 1-150, Cambridge University Press, 1986.

Higgins, T., Etalons: A basic overview of Fabry-Perot resonators, *Lasers & Optronics*, 57-60, 1987.

Hinteregger, H.E., Representations of solar EUV fluxes for aeronomical applications, *Adv. Space Res.*, 39, 1-15, 1981.

Holton, J.R., *An Introduction to Dynamic Meteorology*, pp. 434-468, Academic Press, San Diego, 1992.

Hornbeck, R.W., *Numerical Methods*, pp. 121-130, Dover Publications, New York, 1983.

Jacka, F., Application of Fabry-Perot spectrometer for measurement of upper atmosphere temperature and winds, *Middle Atmos. Program*, 10, 19-40, 1984.

Kelley, M.C., *The Earth's Ionosphere*, pp. 4-259, Academic Press, San Diego, 1989.

Killeen, T.L., R.G. Roble, and N.W. Spencer, A computer model of global thermospheric winds and temperatures, *Adv. Space Res.*, 7, 10207-10215, 1987.

Killeen, T.L. and R.G. Roble, An analysis of the high-latitude thermospheric wind pattern calculated by a thermospheric general circulation model 1. Momentum forcing, *J. Geophys. Res.*, 89, 7509-7522, 1984.

Link, R., and L.L. Cogger, Correction to "A reexamination of the OI 6300-A nightglow", *J. Geophys. Res.*, 94, 1556, 1989.

Link, R., and L.L. Cogger, A reexamination of the OI 6300-A nightglow, *J. Geophys. Res.*, 93, 9883-9892, 1988.

Meriwether, Jr., J.W., J.W. Moody, M.A. Biondi, and R.G. Roble, Optical interferometric measurements of nighttime equatorial thermospheric winds at Arequipa, Peru, *J. Geophys. Res.*, 91, 5557-5566, 1986.

Raghavarao, R., L.E. Wharton, N.W. Spencer, H.G. Mayr, and L.H. Brace, An equatorial temperature and wind anomaly (ETWA), *Geophys. Res. Lett.*, 18, 1193-1196, 1991.

Richmond, A.D., Thermospheric heating in a magnetic storm: Dynamic transport of energy from high to low latitudes, *J. Geophys. Res.*, 84, 5259-5266, 1979.

Richmond, A.D., E.C. Ridley, and R.G. Roble, A thermosphere/ionosphere general circulation model with coupled electrodynamics, *Geophys. Res. Lett.*, 19, 601-604, 1992.

Richmond, A.D., M. Blanc, B.A. Emery, R.H. Wand, B.G. Fejer, R.F. Woodman, S. Ganguly, P. Amayenc, R.A. Behnke, C. Caleron, and J.V. Evans, An empirical model of quiet-day ionospheric electric fields at middle and low latitude, *J. Geophys. Res.*, 85, 4658-4664, 1980.

Richmond, A.D., and S. Matsushita, Thermospheric response to a magnetic substorm, *J. Geophys. Res.*, 80, 2839-2850, 1975.

Rishbeth, H., Thermospheric winds and the F-region: A review, *J. Atmos. Terr. Phys.*, 34, 1-47, 1972.

Roble, R.G., The polar lower thermosphere, *Planet. Space Sci.*, 40, 271-297, 1992.

Roble, R.G., E.C. Ridley, A.D. Richmond, and R.E. Dickinson, A coupled thermosphere/ionosphere general circulation model, *Geophys. Res. Lett.*, 15, 1325-1328, 1988.

Sahai, Y., H. Takahashi, P.R. Fagundes, B.R. Clemesha, N.R. Teixeira, and J.A. Bittencourt, Observations of thermospheric neutral winds at 23°S, *Planet. Space Sci.*, 40, 767-773, 1992.

Salah, J.E., and J.M. Holt, Mid-latitude thermospheric winds from incoherent scatter radar and theory, *Radio Sci.*, 9, 301-313, 1974.

Schunk, R.W., and J.C.G. Walker, Minor ion diffusion in the F2-region of the ionosphere, *Planet. Space Sci.*, 18, 1319-1344, 1970.

Sobral, J.H., H. Takahashi, M.A. Abdu, P. Muralikrishna, Y. Sahai, C.J. Zamlutti, E.R. DePaula, and P.P. Batista, Determination of the quenching rate of the O(1D) by O(3P) from rocket-borne optical (630 nm) and electron density data, *J. Geophys. Res.*, 98, 7791-7798, 1993.

Streit, G.E., C.J. Howard, A.L. Schmeltekopf, J.A. Davidson, and H.I. Schiff, Temperature dependence of O(¹D) rate constants for reactions with O₂, N₂, CO₂, O₃ and H₂O, *J. Chem. Phys.*, 65, 4761-4769, 1976.

Tascione, T.F., *Introduction to the Space Environment*, pp. 59-84, Orbit Book Co., Miami, 1988.

Tohmatsu, T., *Compendium of Aeronomy*, pp. 195-256, Terra Scientific, Tokyo, 1990.

Vadnais, C.M., Mesopause Winds and OH intensities at Mid-Latitudes- Fabry-Perot Interferometer Observations of the OH Emission at 8430A from Bear Lake Observatory, Master's thesis, Utah State University, Logan, 1992.

Walker, J.C.G., The mid-latitude thermosphere, *Planet. Space Sci.*, 36, 1-10, 1988.

Wand, R.H., A model representation of the ionospheric electric field over Millstone Hill, *J. Geophys. Res.*, 86, 5901-5811, 1981.

Wickwar, V.B., J.W. Meriweather, Jr., P.B. Hays, and A.F. Nagy, The meridional thermospheric neutral wind measured by radar and optical techniques in the auroral region, *J. Geophys. Res.*, 89, 10987-10998, 1984.

Wu, Q., T.L. Killeen, and N.W. Spencer, Dynamics explorer 2 observations of equatorial thermospheric winds and temperatures: Local time and longitudinal dependences, *J. Geophys. Res.*, 99, 6277-6288, 1994.

**APPENDIX
PERMISSION LETTERS**

I hereby give permission to Ricardo C. Davila to reprint the following material in his thesis.

Bibliography Citation

Rishbeth, H., *Thermospheric Winds and the F-region: A Review*, J. Atmos. Terr. Phys., 34, 1-47, 1972.

Listed below is the figure I am requesting for my thesis:

Page 14, Figure 3. "Graphs of neutral acceleration time constants and F for midday at sunspot minimum. The upper scale applies to the acceleration due to the pressure gradient F. The lower scale refers to the ion drag parameter v_{hi} ; the Coriolis parameter for a latitude of 45°, f ; and the normalized kinematic viscosity parameter $\eta/\rho H^2$."

(Fee) _____

(Signed) _____

PTO →

17-3-94

We hereby grant you permission to reprint the material specified in your letter (see recto) for the purpose you have indicated therein, at no charge, provided that:

1. The material to be used has appeared in our publication without credit or acknowledgement to another source.

2. Suitable acknowledgement to the source is given as follows:

For Books: "Reprinted from (Author/Title), Copyright (Year), Pages No., with kind permission from Elsevier Science Ltd, The Boulevard, Langford Lane, Kidlington OX5 1GB, UK"

For Journals: "Reprinted from Journal title, Volume number, Author(s), Title of article, Pages No., Copyright (Year), with kind permission from Elsevier Science Ltd, The Boulevard, Langford Lane, Kidlington OX5 1GB, UK"

3. Reproduction of this material is confined to the purpose for which permission is hereby given.

For future permissions, please contact:

Anne-Cécile Junger (Ms)
Subsidiary Rights Manager
Elsevier Science Ltd
The Boulevard, Langford Lane
Kidlington OX5 1GB, U.K.

I hereby give permission to Ricardo C. Davila to reprint the following material in his thesis,

Bibliography Citation

Heelis, R.A., Kendall, P.C., Moffett, R.J., Windle, D.W., and Rishbeth, H.,
Electrical Coupling of the E and F-regions and its effect on F-region-Drifts and Winds., Planet. Space Sci., 22, 743-756, 1974.

Listed below is the figure I am requesting for my thesis:

Page 752, Figure 5. "Calculated vertical ion drift velocities for several driving wind components. The solid line includes only the tidal-driven E-region dynamo, while the dashed line includes the F-region dynamo as well. Typical measured vertical plasma drifts are indicated by the dotted line."

(Fee) _____

(Signed) _____

PTO →
 17-3-94

We hereby grant you permission to reprint the material specified in your letter (see recto) for the purpose you have indicated therein, at no charge, provided that:

1. The material to be used has appeared in our publication without credit or acknowledgement to another source.
2. Suitable acknowledgement to the source is given as follows:

For Books: "Reprinted from (Author/Title), Copyright (Year), Pages No., with kind permission from Elsevier Science Ltd, The Boulevard, Langford Lane, Kidlington OX5 1GB, UK"

For Journals: "Reprinted from Journal title, Volume number, Author(s), Title of article, Pages No., Copyright (Year), with kind permission from Elsevier Science Ltd, The Boulevard, Langford Lane, Kidlington OX5 1GB, UK"

3. Reproduction of this material is confined to the purpose for which permission is hereby given.

For future permissions, please contact:
 Anne-Cécile Junger (Ms)
 Subsidiary Rights Manager
 Elsevier Science Ltd
 The Boulevard, Langford Lane
 Kidlington OX5 1GB, U.K.

I hereby give permission to Ricardo C. Davila to reprint the following material in his thesis,

Bibliography Citation

Fowles, G.R., Introduction to Modern Optics, pp. 86-96, Dover Publications, New York, 1989.

Listed below are the figures I am requesting for my thesis:

1. Page 86, Figure 4.1. "Paths of light rays in multiple reflection between two parallel mirrors."
2. Page 87, Figure 4.2. "Diagram showing the path difference between two successive rays."
3. Page 91, Figure 4.4.(a) "Arrangement for the Fabry-Perot etalon."

X

(Fee)
Rosa Lopez
(Signed)
Dover Publications, Inc.
180 Varick St.
New York, N.Y. 10014

COPYRIGHT PERMISSION LETTERS



American Geophysical Union

2000 Florida Avenue, N.W.
Washington, D.C. 20009
Phone (202) 462-4500
TWX 710-822-9300
FAX 202-328-0566

AGU POLICY ON REPRODUCTION OF COPYRIGHT MATERIALS

AGU no longer requires that permission be obtained from AGU or the author(s) for the use of tables, figures, or short extracts of papers published in AGU journals or books, provided that the source be appropriately cited; however, the author's permission must be obtained for modifying the material in any way beyond simple redrawing.

We recommend that the credit line read "authors, journal or book title, volume number, page number(s), year, copyright by the American Geophysical Union." If an article was placed in the public domain, in which case the words "Not subject to U.S. copyright" appear on the bottom of the first page of the article, please substitute "published" for the word "copyright" in the credit line mentioned above.

Also, AGU policy requires that the article be published by AGU before any material may be reproduced therefrom.

AGU Publications

The American Geophysical Union encompasses the Earth and space sciences:
Geodesy, Seismology, Atmospheric Sciences, Geomagnetism and Paleomagnetism,
Ocean Sciences, Hydrology, Volcanology, Geochemistry, and Petrology,
Tectonophysics, Planetary Science, Solar-Planetary Relationships